UNIVERSITY OF OKLAHOMA

GRADUATE COLLEGE

ALGORITHMIC IMPROVEMENTS AND ANALYSES OF THE GENERALIZED
WAVE CONTINUITY EQUATION BASED MODEL, ADCIRC

A Dissertation

SUBMITTED TO THE GRADUATE FACULTY

in partial fulfillment of the requirements for the

degree of

Doctor of Philosophy

By

KENDRA MAY DRESBACK
Norman, Oklahoma
2005

UMI Number: 3219702

Copyright 2005 by
Dresback, Kendra May

All rights reserved.

UMI®

**ALGORITHMIC IMPROVEMENTS AND ANALYSES OF THE GENERALIZED
WAVE CONTINUITY EQUATION BASED MODEL, ADCIRC**

**A Dissertation APPROVED FOR THE
SCHOOL OF CIVIL ENGINEERING AND ENVIRONMENTAL SCIENCE**

BY

_____

Randall L. Kolar

_____

Baxter Vieux

_____

Cheryl Ann Blain

_____

Kanthasamy K. Muraleetharan

_____

S. Lakshmivarahan

Acknowledgments

I would like to take this opportunity to acknowledge several people who have helped in the completion of this work. First and most of all, I would like to thank my advisor and mentor, Dr. Randall L. Kolar for his guidance, friendship, patience and support throughout my dissertation and graduate work. Next, I would like to thank Dr. Cheryl Ann Blain for sponsoring my stay and work at the Naval Research Laboratory, Stennis Space Center, Mississippi and also for her guidance and support. I also thank my other committee members, Dr. Baxter E. Vieux, Dr. K. K. Muraleetharan and Dr. S. Lakshmivarahan. I appreciate the support and friendship of my fellow graduate students. A special thank you to J. Casey Dietrich, an undergraduate researcher, who helped me complete a lot of the simulations for this research.

Finally, I thank my family for their support. I dedicate this dissertation to my parents, who have always served as an inspiration to me throughout my life. I will always appreciate the sacrifices they have made in their lives to allow me the opportunities I have had in my education and life. To my brother, I appreciate your support and encouragement over the years.

Table of Contents

List of Tables

List of Figures

Abstract

Shallow water equations are based on conservation of mass and momentum and can be used to model the hydrodynamic behavior of oceans, coastal areas, estuaries and lakes. The model used in this research ADCIRC, an advanced three-dimensional circulation model, is based on the shallow water equations. ADCIRC provides elevation changes and velocity profiles that can be utilized by themselves or coupled with other models, such as water quality models, thus lending itself to a wide-variety of applications. Three research areas are investigated in this dissertation in an effort to improve the predictive capabilities of ADCIRC through improved numerics.

First, the current time marching algorithm is semi-implicit, with the nonlinear terms evaluated explicitly. It has been hypothesized that the explicit treatment of the nonlinear terms can lead to instabilities. An iterative, implicit treatment of the nonlinear terms is implemented and studied. Results show an increase in the maximum time step of at least eight-fold, depending on the domain, and an increase in temporal accuracy from first to second order. A parallel implementation of the algorithm scales as well as the original algorithm.

Second, nearly all GWC-based models utilize a velocity-based, non-conservative momentum equation (NCM) to obtain the depth-averaged velocity profile. It has been hypothesized that the conservative momentum equation (CM) may improve accuracy,

mass balance and stability. Results show that the CM equation improves mass balance, both globally and locally, especially in areas of steep bathymetry gradients, and improves local spatial accuracy in these same regions, yet does so without significantly impacting stability, temporal accuracy and global spatial accuracy.

Third, baroclinic models that are used to simulate density-driven flows require an accurate and stable computation of the baroclinic pressure gradient (BPG). In this study, four methods for computing the BPG are investigated, along with resolution requirements (horizontal and vertical). Numerical experiments thus far indicate that the z-coordinate method provides the least amount of error, and a hybrid method, which switches from sigma to z-coordinates at a prescribed depth, also shows promising results.

Chapter 1. Introduction

This dissertation addresses some algorithmic improvements to the ADCIRC (an ADvanced 3D CIRCulation, [59]) model and subsequent analyses of these improvements. ADCIRC uses the shallow water equations as its theoretical basis. These equations, based on the depth-averaged equations of motion, are utilized by researchers and engineers to model the hydrodynamic behavior of oceans, coastal areas, estuaries, lakes and impoundments [50]. ADCIRC gives elevation changes and velocity profiles, which can then be linked to other models to obtain water quality or pollutant transport information. ADCIRC is based on an algorithm with a 25 year history of research and applications; the present model was primarily coded by Luettich and Westerink [59], and its initial application was for the Coastal Dredging Research Program of the United States Army Corp of Engineers [59]. This model has been validated against analytical solutions and field data, e.g. the quarter annular harbor, North Sea, and the Western North Atlantic [59,85]. Currently, ADCIRC has a wide variety of users including the Navy, Army, State of Texas, private consultants and several universities. Applications of the model include, but are not limited to the following: the effects of dredging on circulation [5,74], hurricane storm surges [10,11], Naval fleet operations [13], transport of species, both chemical and biological [58], tidal and wind-driven circulation [85,86] and wave-driven flow [24]. A noteworthy example is modeling hurricane storm surges in Southern Louisiana/City of

New Orleans. As described in the June 2003 cover story of ASCE's <u>Civil Engineering</u> magazine, ADCIRC is being used to design levy heights in order to withstand future hurricanes of Category 4 or 5 [16]. Although the ADCIRC model has been used successfully in a variety of applications, it is desired to further enhance its predictive capabilities through improved numerics. With this in mind, we have identified three specific issues for study within this dissertation; the goal is to provide more accurate 2D and 3D simulations.

Regarding the first study, we know that the current version of ADCIRC has stability problems with nonlinear applications unless a Courant number restriction is imposed, which severely restricts the time step and increases the computational cost of the model. In practice, a practical upper bound for the Courant number is approximately 0.5 in order to maintain the stability of the model; an even tighter constraint must be imposed if the simulation includes barrier islands and constricted inlets due to the small elements in these areas. In order to relax the Courant number restriction, an alternative time marching procedure was proposed that treats all of the nonlinear terms implicitly [53]. Herein, we implement and evaluate the implicit time marching algorithm in 2D and rigorously assess any gains in stability and accuracy with the new algorithm.

ADCIRC and other finite element shallow water models based on the GWC equation suffer from local mass conservation problems, especially in flow regimes that are highly nonlinear [1,51,52,54]. Through the implementation of mass conserving boundary conditions, several studies [52,65] have found that global mass conservation errors decreased, while one study [52] also showed decreases in local mass conservation errors with the proper choice of a numerical parameter. Also, past investigations determined that

reformulating the advective terms in the GWC equation to follow the momentum equation provides gains in stability (as well as mass conservation); however, the resulting algorithm is awkward, since it involves mixed (space and time) derivatives [54]. As an alternative, the second study herein examines the form of the momentum equation used in the ADCIRC model, specifically non-conservative vs. conservative.

Third, as applications of ADCIRC expand to include density-driven flows, it has been observed that the computed baroclinic pressure gradient (BPG) can become either unstable or unrealistic in shelf regions due to the steep bathymetry gradients (e.g. [17,42]). These unstable or unrealistic values of the BPG are also influenced by the vertical coordinate system utilized in the calculation of the BPG, which lead to further problems in the velocity values. Several vertical coordinate systems and associated algorithms for determining the BPG exist in the literature of both finite difference and finite element models [17,34,42,83]. Herein, we investigate four approaches to compute the BPG in ADCIRC, and assess the impacts of grid resolution on each approach. In particular, the interplay between the vertical and horizontal resolution, bathymetry and density profiles is of interest.

This dissertation consists of six chapters, including this introductory chapter. Some of the chapters in this dissertation are extensions of published or in-press journal articles. As such, some of the background information is repeated between chapters. Chapter 2 provides background on the shallow water equations and the ADCIRC model that is used to perform the analyses herein. Chapter 3 discusses an implicit time-marching algorithm; it is an extension of a journal article published in the *International Journal of Numerical Methods in Fluids* [30]. Chapter 4 provides results from an implementation of the

conservative form of the momentum equation; it is an extension of a journal article that is in-press in *Advances in Water Resources* [29]. Chapter 5 discusses the computation of the BPG using multiple coordinate frameworks and examines the effect of resolution, bathymetry and density structure on simulation results; it is a compilation of work published in two conference proceedings (references [31] and [32]). Chapter 6 discusses some future work to be done with ADCIRC that is a direct extension of what is reported in earlier chapters.

Chapter 2. Background on the Shallow Water Equations and the ADCIRC Model

This chapter presents the background of the model and grid structures used in future chapters. The first section addresses the basis of the shallow water equations for both 2D and 3D forms of the ADCIRC model. We present the equations and assumptions utilized in our evaluations with the model, along with the background on the development of the generalized wave continuity (GWC) equation. Section 2.2 covers some of the numerical methods that can be used in the solution of the shallow water equations. In Section 2.3, we discuss the ADCIRC model and the solution techniques for both 2D and 3D forms of the model. Lastly, we close with a section discussing the variety of grid generating techniques that are used in the subsequent chapters.

2.1 Shallow Water Equations - 2D and 3D

Shallow water models are based on the physical conservation laws, specifically the conservation of mass and momentum equations. The full 3D equations are averaged over a time scale of turbulent fluctuations, called Reynolds averaging, and then over the water column to develop the depth-averaged primitive equations for shallow water models [87]. For the shallow water equations used in the subsequent chapters of this dissertation, we present the assumptions used in the development of the equations along with a discussion of each assumption's implication:

- We assume a hydrostatic pressure distribution in the vertical. This assumption means that if we examine the magnitude of the terms in the horizontal and vertical momentum equations we find that the vertical velocity values are much smaller than the horizontal velocities and the distance in the horizontal direction is much greater than the depth. Based on a scaling analysis, the vertical momentum equation reduces to the pressure and gravity terms; a balance must exist between these two terms, which indicates a hydrostatic pressure distribution [25,72].

- We assume a static bed in the development of the shallow water equations. This assumption allows us to develop the depth-averaged form of the equations with bathymetry independent of time and assume that the bottom kinematic boundary condition is equal to zero.

- We assume that there is no exchange of mass with the environment other than specified boundary fluxes. This assumption means that there are no source or sink terms in the equations.

- Lastly, we assume the Boussinesq approximation in the development of the momentum equation. This means that density is taken to be constant except for the gravity terms [72]. This assumption allows for all of the density terms in the momentum equation, except for those of the gravity and pressure terms, to use a reference density, ρ_0 [72].

We also note that either standard Cartesian coordinates or spherical coordinates can be used in the shallow water equations.

2.1.1 2D Shallow Water Equations

The primitive equations are shown in Equations (2.1)-(2.3). Equation (2.1) is the conservation of mass (continuity equation); while Equations (2.2) and (2.3) are the conservation of momentum in conservative form and conservation of momentum in non-conservative form, respectively. Nomenclature is defined in Appendix 1.

$$L \equiv \frac{\partial \zeta}{\partial t} + \nabla \bullet (H\mathbf{v}) \; = \; 0 \tag{2.1}$$

$$\mathbf{M}^c \equiv \frac{\partial (H\mathbf{v})}{\partial t} + \nabla \bullet (H\mathbf{v}\mathbf{v}) + \tau H\mathbf{v} + H\mathbf{f} \times \mathbf{v} + H\nabla \left[\frac{p_a}{\rho} + g(\zeta - \alpha\eta) \right] -$$

$$\mathbf{A} - \frac{1}{\rho}\nabla \bullet (H\mathbf{T}) \; = \; 0 \tag{2.2}$$

$$\mathbf{M} \equiv \frac{\partial \mathbf{v}}{\partial t} + \mathbf{v} \bullet \nabla \mathbf{v} + \tau \mathbf{v} + \mathbf{f} \times \mathbf{v} + \nabla \left[\frac{p_a}{\rho} + g(\zeta - \alpha\eta) \right] - \frac{\mathbf{A}}{H} - \frac{1}{\rho H}\nabla \bullet (H\mathbf{T}) \; = \; 0 \tag{2.3}$$

Early finite element solutions based on the primitive form of the shallow water equations were plagued with spurious oscillations from short wave $(2\Delta x)$ noise that appeared superimposed on the true solution [80]. Spurious oscillations result from a folded dispersion relationship, meaning that there are two wavelengths (short wave noise and physical long waves) for each frequency. In a effort to eliminate the spurious oscillations, several researchers investigated using artificial damping or special numerical techniques, such as finding an algorithm that would propagate or dissipate these spurious oscillations [49]. Artificial damping techniques ranged from unrealistically large viscous terms [84] to large friction coefficients [76]. Numerical techniques included using time marching algorithms that offered dissipative qualities or a post-processing step that averaged or

smoothed the solution [49]. The drawback of all of these methods is that they tended to damp out some of the physical components in the solution.

In 1979, Lynch and Gray [64] introduced the wave continuity equation (WCE), shown in Equation (2.4), which eliminated the spurious oscillations in the solution without having to dampen the solution numerically or artificially.

$$W \equiv \frac{\partial L}{\partial t} + \tau L - \nabla \bullet \mathbf{M}^c = 0 \tag{2.4}$$

where the nomenclature is given in Appendix 1. The WCE provides a monotonic dispersion relationship, thus allowing only one wavelength for each frequency.

Kinnmark [48] determined in 1986 that there was no loss in the propagation characteristics of the WCE if the τ term was replaced with a numerical parameter, G, in order to obtain what he called the generalized wave continuity (GWC) equation, which is written as follows:

$$W^G \equiv \frac{\partial L}{\partial t} + GL - \nabla \bullet \mathbf{M}^c = 0 \tag{2.5}$$

This numerical parameter allows the equation to vary anywhere from a pure wave form of the equation to the primitive form of the continuity equation, if the parameter is chosen to be small or large, respectively. An expansion of the GWC equation for the case of barotropic flows and spatially-varying G is:

$$W^G \equiv \frac{\partial^2 \zeta}{\partial t^2} + G \frac{\partial \zeta}{\partial t} - H\mathbf{v} \bullet \nabla G - \nabla \bullet \left[\nabla \bullet (H\mathbf{v}\mathbf{v}) + H\nabla \left[\frac{p_a}{\rho} + g(\zeta - \alpha \eta) \right] - \frac{1}{\rho} \nabla \bullet (H\mathbf{T}) + $$

$$H\mathbf{f} \times \mathbf{v} + \tau H\mathbf{v} - \frac{\mathbf{A}}{H} - GH\mathbf{v} \bigg] = 0 \qquad\qquad\qquad\text{(2.6)}$$

The GWC equation presented above along with the momentum equations in either conservative or non-conservative forms, shown in Equations (2.2) and (2.3), respectively describe spatial and temporal elevation and velocity changes.

2.1.2 3D Shallow Water Equations

The three-dimensional (3D) shallow water equations utilize the same assumptions as the two-dimensional (2D) equations; in the 3D shallow water equations, the hydrostatic pressure distribution only applies if the vertical velocity is small in comparison to the horizontal velocity. Thus the flow must be weakly 3D for the model to remain accurate [81]. If such conditions are met, a 3D simulation can be obtained using pseudo-3D equations rather than the full 3D non-hydrostatic equations. The pseudo-3D equations still utilize a 2D depth-averaged form of the continuity equation for the elevation changes, and then use a 3D momentum equation to find the velocity changes. For the problems considered herein, such a model is appropriate.

Many prominent 3D shallow water models [15,41] invoke a mode splitting technique to solve the pseudo-3D equations. The mode splitting technique consists of two modes, external and internal, which can be delineated by the speed of the waves from the types of flows. Gravity waves, or barotropic flows, are defined from the external mode. These type of waves tend to be fast moving and change rapidly over time. The internal mode tends to be associated with the baroclinic flows. This type of flow tends to evolve more slowly over time. Based on this information, some 3D models solve the external mode equation more frequently than the internal mode equations [15].

The initial step of the mode splitting technique, the external mode, is to determine the elevation changes using a 2D depth-averaged continuity equation. In ADCIRC, we again use the GWC equation, as shown below.

$$W^G \equiv \frac{\partial^2 \zeta}{\partial t^2} + G\frac{\partial \zeta}{\partial t} - H\mathbf{v} \bullet \nabla G - \nabla \bullet \left[\nabla \bullet (H\mathbf{v}\mathbf{v}) + H\nabla \left[\frac{p_a}{\rho} + g(\zeta - \alpha\eta) \right] - \mathbf{M} + \right.$$

$$\left. H\mathbf{f} \times \mathbf{v} + \frac{\tau_b}{\rho_0} - \frac{\mathbf{A}}{H} - GH\mathbf{v} + \mathbf{B} + \mathbf{D} \right] = 0 \tag{2.7}$$

where the terms are defined in the nomenclature section in Appendix 1. Comparing Equations (2.6) and (2.7), one sees that two new terms, $\mathbf{B}$ and $\mathbf{D}$, were added to Equation (2.7). The $\mathbf{B}$ term is introduced in order to include baroclinic effects into the equations; it is computed by depth-averaging the baroclinic pressure gradient results over the vertical. Also the equation brings in momentum dispersion effects through the $\mathbf{D}$ term. This term can only be included in the 3D model because it requires knowledge of the vertical profile of the horizontal velocities in order to determine its magnitude [60]. Lastly, the bottom friction term $\frac{\tau_b}{\rho_0}$ in Equation (2.7) differs from the one in Equation (2.6) because it does not utilize a depth-averaged velocity value; instead it employs the velocity from the bottom layer in its evaluation. Also, note that the lateral stress term is represented by $\mathbf{M}$ instead of $\frac{1}{\rho}\nabla \bullet (H\mathbf{T})$.

Next, the internal mode solution is used to obtain the 3D velocity field. This solution is forced with the elevation changes given by the external mode solution. Full derivation of the 3D equations is given in reference [60]. We summarize some of the information from this reference and present the equations used in the 3D solution scheme.

The non-conservative momentum equation in Cartesian coordinates (x, y, z) is given as:

$$\mathbf{M} \equiv \frac{\partial \mathbf{v}}{\partial t} + \mathbf{v}_{3D} \bullet \nabla \mathbf{v} - f \times \mathbf{v} + \nabla_{xy}\left[\frac{p_a}{\rho_0} + g(\zeta - \alpha\eta)\right] - \frac{\partial}{\partial z}\frac{\tau_z}{\rho_0} - \mathbf{m} + \mathbf{b} = 0 \qquad \textbf{(2.8)}$$

where the variables are defined in Appendix 1. In order to determine the 3D velocity field, the 3D momentum equations utilize a vertical coordinate system based on a generalized sigma or stretched coordinate system, which varies from $\sigma = a$ at the free surface to $\sigma = b$ at the bottom. Both of these values are constant in ADCIRC, (i.e., $a = 1$ and $b = -1$) and the number of vertical nodes between these two values remains the same no matter the change in the bathymetry [81]. The mapping between the generalized stretched coordinate system and the Cartesian z-coordinate system is defined as:

$$\sigma = a + \left(\frac{a-b}{H}\right)(z - \zeta) \qquad \textbf{(2.9)}$$

where the variables are given in Appendix 1. In traditional sigma coordinates, the nodes are uniformly spaced over the vertical; however, in ADCIRC, the generalized sigma or stretched coordinates allow for variation in the vertical [60].

Based on the relationship between the generalized sigma or stretched coordinate and Cartesian z-coordinate systems given in Equation (2.9), derivatives between the two systems can be related to one another through the chain rule (a full derivation shown in Appendix 2) as follows:

$$\frac{\partial}{\partial x_z} = \frac{\partial}{\partial x_\sigma} - \left[\left(\frac{\sigma-b}{a-b}\right)\frac{\partial\zeta}{\partial x} + \left(\frac{\sigma-a}{a-b}\right)\frac{\partial h}{\partial x}\right]\frac{\partial}{\partial z} \qquad \textbf{(2.10)}$$

11

$$\frac{\partial}{\partial y_z} = \frac{\partial}{\partial y_\sigma} - \left[\left(\frac{\sigma - b}{a - b}\right)\frac{\partial \zeta}{\partial y} + \left(\frac{\sigma - a}{a - b}\right)\frac{\partial h}{\partial y}\right]\frac{\partial}{\partial z} \qquad (2.11)$$

$$\frac{\partial}{\partial z} = \left(\frac{a - b}{H}\right)\frac{\partial}{\partial \sigma} \qquad (2.12)$$

where the coordinate system in which the derivatives are evaluated is given by the subscript. By utilizing these relationships, the momentum equation in the generalized sigma or stretched coordinate system is as follows in operator notation:

$$\mathbf{M} \equiv \frac{\partial \mathbf{v}}{\partial t} + \mathbf{v} \bullet \nabla_{xy_\sigma}\mathbf{v} + w_\sigma\left(\frac{a - b}{H}\right)\frac{\partial \mathbf{v}}{\partial \sigma} - f \times \mathbf{v} + \nabla_{xy}\left[\frac{p_a}{\rho_0} + g(\zeta - \alpha\eta)\right] -$$

$$\left(\frac{a - b}{H}\right)\frac{\partial}{\partial \sigma}\left(\frac{\tau_z}{\rho_0}\right) - \mathbf{m}_\sigma + \mathbf{b} = 0 \qquad (2.13)$$

where

$$w_\sigma = w - \left(\frac{\sigma - b}{a - b}\right)\frac{\partial \zeta}{\partial t} - \mathbf{v} \bullet \left[\left(\frac{\sigma - b}{a - b}\right)\nabla_{xy}\zeta - \left(\frac{\sigma - a}{a - b}\right)\nabla_{xy}h\right] \qquad (2.14)$$

and w_σ represents the actual vertical velocity, w, combined with the coordinate transformations for the advective terms (a full derivation occurs in Appendix 2). Also

$$\mathbf{m}_\sigma = \nabla_{xy_\sigma} \bullet (E_l\nabla_{xy_\sigma}\mathbf{v}) \qquad (2.15)$$

The equations for the baroclinic pressure gradient, $\mathbf{b}$, are presented in Chapter 5. Note that the fifth term in Equation (2.13) is not a function of depth so whether it is evaluated in the Cartesian z-coordinates or generalized sigma or stretched coordinates it would produce identical results.

As a final step, after the horizontal velocities are found using Equation (2.13), the vertical velocity is determined using the 3D primitive continuity equation:

$$\nabla \bullet \mathbf{v}_{3D} = 0 \tag{2.16}$$

subject to kinematic boundary conditions at the free surface and bottom; and where the terms are defined in Appendix 1.

2.2 Numerical solutions

The shallow water equations presented in the previous section cannot be solved analytically except for the simplest problems; therefore we must use numerical methods in order to solve them. Some shallow water models use these equations in their primitive form ("native" form), while other manipulate these equations to obtain stable or non-oscillationary solutions for the numerical method they employ. Historically, finite difference and finite element methods are commonly used to solve the shallow water equations, but recently, a numerical method new to ocean modeling that uses the discontinuous Galerkin finite element method has begun to be investigated as a possible alternative [22,26]. We provide a short comparison of these methods and some of the pros and cons below.

The most commonly used numerical method to solve the shallow water equations is the finite difference method, which converts the continuum equations to difference expressions [19]. Over many years, models utilizing the finite difference numerical method on staggered grids have produced stable results [15,18,69]. By using staggered grids, this method excludes the shortwaves that can cause oscillations in the solutions, and these grids allow the use of the alternating direction implicit algorithm, which provides fast solutions

[15]. This method is also considered to be both globally and locally mass conservative. However the staggered grids make it difficult to accurately provide high levels of local refinement in portions of the shallow coastal areas or in areas of changing topography because the level of refinement used in these areas must extend throughout the entire grid. Also, it is difficult to accurately map an irregular coastal boundary due to the meshes using rectangular or square elements. Irregular coastal boundaries can be captured to a certain extent using orthogonal or non-orthogonal curvilinear coordinate transformation; however, they do not capture highly irregular coastal geometry, such as that around barrier islands or inlets [21].

Another numerical method used in shallow water equations is the finite element method, which approximates the form of the solution to the differential equation, while maintaining the original differential operator in weak form [19]. In contrast to the finite difference techniques, finite element models can use triangular, quadrilaterals or curved elements. These types of elements allow the user to describe irregular coastal boundaries, and they can be selectively refined in shallow coastal areas and in areas of changing topography. Also, the flux-type boundary conditions enter the weak form of the problem naturally in the finite element technique, thus allowing for an easy treatment of these boundary conditions. However, the finite element method needs to solve sparse, banded matrices to obtain solutions, which costs more in terms of computer memory and CPU time than the alternating direction implicit finite difference models [50]. Also, traditional finite element methods tend not to be locally mass conserving, an issue that is explored further in Chapter 4 of this dissertation.

Another successful algorithm for solving the shallow water equations using the

finite element method employs the quasi-bubble scheme [43] in the development of the equations. The quasi-bubble scheme obtains it name from the use of the linear approximation of the bubble function (a bubble function uses an additional quadratic interpolating function in discretization of the momentum equation), hence the name quasi-bubble [73]. One difference between this method and the typical finite element discretization is the extra information provided to the velocity solution from the additional node at the center of the triangle, and also by subdividing each triangle into three linear velocity subtriangles [4]. It provides undamped, well-behaved solutions; experimental tests done by Atkinson et al. [4] indicate that quasi-bubble and GWC-based codes produce similar results and have similar dispersion relations.

Over the past decade, another finite element method, called the discontinuous Galerkin (DG) method, has been applied to the shallow water equations; it uses discontinuous approximations of the shallow water equations [3,22,26]. The DG finite element method is similar to the finite volume methods and utilizes the primitive form of the equations [27]. This method can capture shocks or jumps that occur in the system, which are stabilized through upwinding schemes and stability post-processing ("slope-limiters") [27]. DG methods can use unstructured grids similar to the continuous finite element method, so they can still capture irregular coastal boundaries and provide selective refinement in areas of shallow coastal regions and in areas of changing topography. This method utilizes the shallow water equation in a weak sense on a element-wise basis, therefore it is also considered to be both globally and locally mass conservative [27]. The disadvantage to the DG method is its computational expense; DG equations have more degrees of freedom in the solution because they are based on the elements, not nodes like

the continuous finite element method, thus requiring more computational time to obtain a solution. Therefore, recent studies have looked at coupling the continuous and discontinuous finite element methods [26,27].

In this dissertation, we chose to use the finite element method over the finite difference method due to the grid flexibility that it offers in the coastal regions, which is important in expected applications. We note that there are several methods discussed in the previous paragraphs that use the finite element technique: one method using the GWC equation with the continuous Galerkin formulation; one using the quasi-bubble scheme with the continuous Galerkin formulation; and one that uses elements based on the discontinuous Galerkin formulations. In previous experimental studies by Atkinson et al. [4], they found that the dispersion relationship is the same for the quasi-bubble scheme and for the GWC-based model and that they produce similar results. In the case of the discontinuous Galerkin formulation, we note that the method is mass conservative globally and locally; however, the computational expense of the method does not make it a completely viable alternative to the other finite element methods. Because of the computational expense of the DG formulation, we seek to improve the GWC-based formulation by looking at some of the issues that need to be addressed, such as mass conservation and calculation of the baroclinic pressure gradient.

2.3 ADCIRC Model Development - 2D and 3D

ADCIRC, the model utilized in this dissertation, is a finite element model that solves the GWC equation to obtain elevation changes and the momentum equations to obtain velocities.

The development of the 2D ADCIRC model entails the following steps:

- Spatial discretization of the equations utilizes standard Galerkin finite elements with C^0 elements, which means only the functions, not their derivatives, are continuous between discrete points. We employ piece-wise linear functions in the model with exact quadrature rules. Product terms in the equations are simplified by linearly interpolating the products of the variables, not the individual variables. L_2 interpolation, which means that we use elemental averages, is applied to the non-conservative advective terms.

- Temporal discretization of the equations uses a three time-level scheme centered at k for the GWC equation, and a two time-level scheme centered at $k + 1/2$ for the non-conservative momentum equation (i.e., Crank-Nicholson treatment). Nonlinear terms are evaluated explicitly.

- This temporal solution strategy of ADCIRC allows a sequential technique, wherein the GWC equation is first solved to determine elevations and then the velocities are updated with the non-conservative momentum equation. This helps limit the size of the matrices that the computer must store and invert.

The development of the 3D ADCIRC model is as follows:

- Spatial discretization of the equations utilizes standard Galerkin finite elements with C^0 elements, which means only the functions, not their derivatives, are continuous between discrete points. We employ piece-wise linear functions in the model with exact quadrature rules. Product terms in

17

the equations are simplified by linearly interpolating the products of the variables, not the individual variables. L_2 interpolation, which means that we use elemental averages, is applied to the non-conservative advective terms. (same as 2D.)

- Temporal discretization of the equations uses a three time-level scheme centered at k for the GWC equation, and a two time-level scheme centered at $k + 1/2$ for the non-conservative momentum equation (i.e., Crank-Nicholson treatment). Nonlinear terms are evaluated explicitly. (same as 2D.)

- The solution strategy in the 3D ADCIRC code utilizes a mode splitting scheme to obtain the solution to the 3D equations. This technique defines the external mode as the 2D continuity equation; the GWC equation is used in ADCIRC to obtain the free surface elevation. These elevations are then fed into the internal mode solution of the 3D momentum equations to find velocities. By lumping some of the terms, the solution is allowed to take on an explicit-like character in the horizontal. Lumping occurs with matrices by putting all the emphasis on the diagonal terms and zeroing out the off-diagonal terms. Thus, the horizontal velocities are determined for every node at each layer in the vertical, avoiding globally-coupled matrices. The horizontal gradients given in Equation (2.13) are evaluated in the sigma coordinate system, except for the baroclinic pressure gradient, which is evaluated using a level or z-coordinate system in the current ADCIRC model configuration.

- To obtain the vertical velocities, we utilize Equation (2.16). In this step, matrices are unlumped (meaning that the evaluation of the matrices includes both the diagonal and off-diagonal terms) in the vertical, but the coupling results in easy-to-solve tridiagonal matrices for each string of vertical nodes associated with every horizontal node. Equation (2.16) has boundary conditions at both the bottom and at the water surface, but it is only a first order equation. The boundary condition at the bottom is used as a starting point for the calculations. Results are determined for the rest of the water column, and then the boundary condition at the water surface is used to correct the initial results. The correction for these results was developed by Muccino et al. [75] and Luettich et al. [57] and utilizes an adjoint method that adjusts the calculated results to produce an optimal solution. It was determined by Luettich et al. [57] that this correction is needed due to the errors in local mass conservation of the fluid.

Further explanation of the discretization of both the 2D and 3D equations occurs in Luettich et al. [59,60].

2.4 Development of Grids

Throughout this dissertation, we utilize grids developed using one of two techniques. The first technique employ a $\lambda / \Delta x$ ratio to determine node placement, where the ratio is defined as:

$$\frac{\lambda}{\Delta x} = \frac{\sqrt{gh} \times T}{\Delta x} \tag{2.17}$$

where the terms are discussed in Appendix 1. For constant nodal spacing, we divide the reach into N equal-sized elements, where N is chosen to produce the desired $\lambda/\Delta x$ ratio (e.g., $\lambda/\Delta x = 200$) for the M_2 wave, which is chosen as it is the dominate wave, in the shallowest (i.e., most critical due to the depth change) region. Of course, this means that in the deeper portions of these domains, the M_2 wave is even more finely resolved.

For variable node spacing, we keep the $\lambda/\Delta x$ ratio constant (e.g., $\lambda/\Delta x = 300$) and use that value to determine the Δx values for all of the domain. In this method, the initial node is placed at the land boundary, the wavelength is determined by the wave speed $\sqrt{gh}$, which is dependent only on depth for shallow water waves, and then a Δx value is calculated from the ratio shown in Equation (2.17).

Second, we use a grid development technique that employs local truncation errors of the linearized non-conservative momentum equation. This grid development technique was developed by Hagen et al. [39,40] and is abbreviated LTEA. This method places more nodes in areas where high local truncation error exists. These areas tend to be where there are steep topography changes, such as the continental rise or the shelf break. In most of the domains herein, the number of nodes between the $\lambda/\Delta x$ and LTEA grids varies only slightly, however the nodes are placed differently. In particular, for LTEA grids, more nodes are placed on the continental shelf break and less in the shallower regions of the domain, whereas the $\lambda/\Delta x$ grid places more nodes in the shallower region with the spacing increasing as the bathymetry increases. We note that in the following chapters of this dissertation, we utilize grids based on these aforementioned techniques and look at the impact of the grid generating techniques on algorithmic performance.

Chapter 3. Improving the Computational Efficiency of ADCIRC Through Implicit Time Marching and Its Parallel Implementation[a]

3.1 Introduction

In a previous article [33], we discussed and analyzed a predictor-corrector time-marching algorithm (abbreviated predictor-corrector algorithm or just PC, herein) in a one-dimensional (1D) setting, which utilizes the finite element framework and the generalized wave continuity (GWC) equation. This chapter builds upon that work and extends it to a two-dimensional (2D) setting, wherein it is assessed for stability, accuracy, parameter sensitivity, and parallel efficiency.

Herein, the finite-element code is based on Lynch and Gray's [64] wave continuity equation (WCE), which suppresses spurious oscillations without having to dampen the solution either numerically or artificially. Further studies by Kinnmark [48] determined that there was no loss in the wave propagation characteristics of the WCE if a numerical parameter, G, is introduced. This parameter expresses a balance between the primitive form and the pure wave form of the shallow water equations. The model utilized here, ADCIRC (an ADvanced three-dimensional CIRCulation model) [59] is based on the GWC equation.

Currently, nonlinear applications with ADCIRC have stability problems unless a

---

a. This chapter appears in an abbreviated form in the *International Journal of Numerical Methods in Fluids*. The reference is given in Chapter 7, number [30].

severe Courant number restriction is imposed. The Courant number is defined as

$$C_r = \frac{c \times \Delta t}{\Delta x}$$ (3.1)

where $c = \sqrt{gh}$ is the linear wave celerity, Δx is the node spacing and Δt is the time step. In practice, the Courant number varies over the grid, we assign a single value to a grid by choosing the smallest. We have found in practice that for deep ocean flows, a practical upper bound of the Courant number (C_r) is 0.5 in order to maintain the stability of the model; however, an even tighter constraint (e.g., $C_r \ll 0.1$) must be imposed if the simulation includes barrier islands, constricted inlets, or wetting and drying of near-shore elements. In order to relax this restriction, an alternative time-marching procedure was proposed that treats the nonlinear terms implicitly [53].

As reported in [33] (and repeated here for completeness), a number of earlier studies looked at time-marching, but often from a noise suppression point-of-view. For example, Lee and Froehlich [56] summarize several time-marching procedures in their shallow water equation review paper, which covers everything from the trapezoidal rule to three-level semi-implicit schemes. Lynch and Gray [37] showed several of the same time-marching procedures in greater detail. They indicate that the best scheme for finite element shallow water models is the three-level semi-implicit scheme. Several years later Kinnmark and Gray [47] examined a semi-implicit wave equation that produced accurate results, yet still treated the nonlinear terms explicitly. Most of the more recent work with GWC-based models has focused either on incorporating more physics or minimizing spatial error, e.g., alternative meshing criteria [10,11,39], wetting and drying [62], treatment of boundary conditions [52,65], 3D baroclinic simulations [66,68], and more accurate estimates of the

22

vertical velocity [75]. Furthermore, attempts to achieve timely simulations have led to parallel codes [23,46]. Little recent work with GWC-based models has been devoted to alternative time-marching algorithms. The intent of this study is to fill this gap, viz, an implicit treatment of nonlinear terms in both the GWC and momentum equations.

An implicit treatment can be realized by either simultaneous integration of the full nonlinear equations or a predictor-corrector algorithm. A predictor-corrector algorithm was chosen over the simultaneous integration for the following reasons: 1) it can be easily implemented within the framework of the existing ADCIRC code; 2) it minimizes the size of the matrices that must be stored and inverted; and 3) it is more computationally efficient than the simultaneous integration of the full nonlinear equations.

In this chapter, we examine the impact of the 2D predictor-corrector algorithm on stability, G sensitivity, and temporal accuracy, both globally and locally. Also, we implement a combined parallel/predictor-corrector algorithm and assess the scalability of the resulting code. In our earlier paper, we provided the background on the shallow water equations and indicated the proposed changes to the time-marching algorithm [33]; a summary of these sections is included below for completeness.

3.2 Shallow Water Equations

The full shallow water equations can be found in several sources [48,50,59,64,67] and in Chapter 2; the GWC equation and non-conservative form of the momentum (NCM) equation, which form the basis of the ADCIRC model, are given below. Using operator notation, where L represents the primitive continuity equation, and $\mathbf{M}^C$ the conservative form of the momentum equation, we present the GWC equation

$$W^G \equiv \frac{\partial L}{\partial t} + GL - \nabla \bullet \mathbf{M}^C \tag{3.2}$$

where G is a numerical parameter. Lynch and Gray's [64] WCE can be obtained by setting $G = \tau$, where τ is the bottom friction. It should be noted that the higher the value of G, the more the GWC equation approaches the primitive equation. Expanded versions of the GWC equation and NCM equation are shown below, Equations (3.3) and (3.4), respectively for the case of constant parameter G. All terms are described in Appendix 1, but the predominant variables are noted after the equations. The abbreviations appearing above certain terms in these equations will be discussed in subsequent sections.

$$W^G \equiv \frac{\partial^2 \zeta}{\partial t^2} + G\frac{\partial \zeta}{\partial t} + \overset{\text{``Gg''}}{G\nabla\bullet(H\mathbf{v})} - \nabla\bullet\{\overset{\text{``ag and at''}}{\nabla\bullet(H\mathbf{vv})} + \overset{\text{``cg''}}{H\mathbf{f}\times\mathbf{v}} + \overset{\text{``bg''}}{\tau H\mathbf{v}} +$$

$$H\nabla\left[\frac{p_a}{\rho} + \overset{\text{``fg''}}{g(\zeta - \alpha\eta)}\right] - \mathbf{A} - \frac{1}{\rho}\nabla\bullet(H\mathbf{T})\} = 0 \tag{3.3}$$

$$\mathbf{M} \equiv \frac{\partial\mathbf{v}}{\partial t} + \overset{\text{``am''}}{\mathbf{v}\bullet\nabla\mathbf{v}} + \overset{\text{``bm''}}{\tau\mathbf{v}} + \mathbf{f}\times\mathbf{v} + \nabla\left[\frac{p_a}{\rho} + g(\zeta - \alpha\eta)\right] - \frac{\mathbf{A}}{H} - \frac{1}{\rho H}\nabla\bullet(H\mathbf{T}) = 0 \tag{3.4}$$

where ζ is the elevation of the water surface above the datum, t is time, $\mathbf{v}$ is the depth-averaged velocity, and H is the total fluid depth, $h + \zeta$.

Algorithms based on these two equations result in solutions that compare well with analytical solutions and field data for both elevation and velocity. The codes typically use equal-order finite element interpolating functions (linear C^0 elements). As presently coded, semi-implicit time discretization of the GWC equation uses a three-time-level approximation centered at k, while time discretization of the NCM equation uses a lumped

two-time-level approximation centered at $k+1/2$. Equations are linearized by formulating the nonlinear terms explicitly. Exact quadrature rules are used. Product terms in the equations are simplified by linearly interpolating the products of the variables, not the individual variables. L_2 interpolation is applied to the advective terms. A time-splitting solution procedure is adopted wherein the GWC equation is first solved for nodal elevations and then the NCM equation is solved for the velocity field. Resulting discrete equations can be found in Luettich et al.[59]

3.3   Description of the Implicit Time-Marching Algorithm

As noted, the current semi-implicit algorithm evaluates the linear terms implicitly and the nonlinear terms explicitly. At the past and present time levels in ADCIRC, elevation and velocity values are known (either from initial conditions or previous calculations). The original algorithm takes the elevation and velocity values for the past (k-1) and the present (k) and uses them to calculate the values for the future ($k+1$) time level for the linear terms. However, the nonlinear terms are evaluated using only the elevation and velocity values at the present time level (k). Kolar et al. [53] hypothesized that the stability constraint stems primarily from this explicit evaluation of nonlinear terms.

In order to evaluate the nonlinear terms implicitly, a predictor-corrector time-marching algorithm is introduced. The predictor stage, which is equivalent to the original algorithm, evaluates the nonlinear terms using values from the present. Predicted future values, called k^*, and the already-known present (k) and past (k-1) values are then used to obtain corrected values for the future ($k+1$) time level. The corrector stage can be repeated as many times as necessary until convergence; however, previous studies [33] indicate that

one corrector iteration is sufficient.

Nonlinear terms exist in both governing equations for ADCIRC - the NCM and GWC equation. Our study focuses on all eight nonlinear terms identified in Equations (3.3) and (3.4). Six reside in the GWC equation: advective (abbreviated "ag and at"), in which "ag" is associated with the spatial derivative and "at" is associated with the temporal derivative[b], finite amplitude (abbreviated "fg"), Coriolis (abbreviated "cg"), GWC equation flux times G (abbreviated "Gg") and GWC equation flux times τ (abbreviated "bg") and two are from the NCM equation, the advective term (abbreviated "am") and the bottom friction term (abbreviated "bm").

Through the use of time weight coefficients, we have the option to distribute the relative contribution of the nonlinear terms over the three time levels. Exhaustive 1D studies [33] showed that optimal coefficients are problem dependent, but that near-optimal results for any domain are found by centering the GWC equation time weights at k (meaning that the time weights for the nonlinear terms are weighted equally between $k+1$ (or k^*), k, k-1) and centering NCM time weights at $k+1/2$ (meaning that the terms are weighted equally between k and $k+1$ (or k^*)). This near-optimal time weighting scheme is used for all studies herein. Also from the 1D studies, we determined that significant gains in the time step could be realized when just one or two nonlinear terms were treated implicitly; however, the increases were not as large as when all of the nonlinear terms were treated implicitly. Therefore, studies herein look at treating all nonlinear terms implicitly.

---

b. Earlier modifications to the ADCIRC code converted the advection term in the GWC equation to non-conservative form by using the primitive continuity equation to split it into two terms, one involving a spatial derivative and one involving a temporal derivative. See [54] for full details.

3.4 Two-Dimensional Domains

In this chapter, we examine algorithm behavior on a number of domains: the quarter annular harbor (denoted "quarter annular"), a fictional grid that has a well-documented analytical solution, and several application domains - Bight of Abaco (denoted "Bahamas"), Western North Atlantic (denoted "Eastcoast"), and Gulf of Mexico.

The quarter annular harbor grid is shown in Figure 3.1. Boundaries are marked on
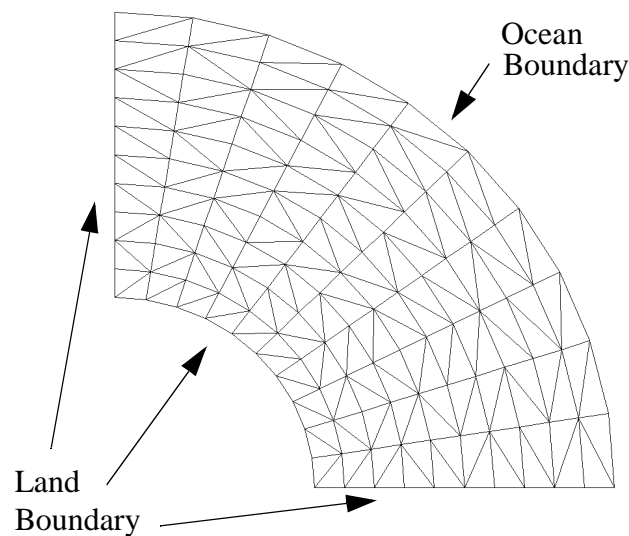
Figure 3.1 Quarter annular harbor domain (10 x 10 resolution).

the figure, with either ocean or land indicated. The boundary condition for the open ocean boundary is the M_2 tidal constituent, while the land boundaries are no flow. Resolutions used in comparison studies include 5x5, 10x10, 15x15, 20x20, 25x25 and 30x30 (radial divisions x θ divisions).

The application domains (Eastcoast, Gulf of Mexico and Bahamas) are shown in Figure 3.2; boundary conditions are indicated on the figure. Table 3.1 contains information

Eastcoast
Domain

Bahamas Domain

Land
Boundary

Land
Boundary

Ocean
Boundary

Ocean
Boundary
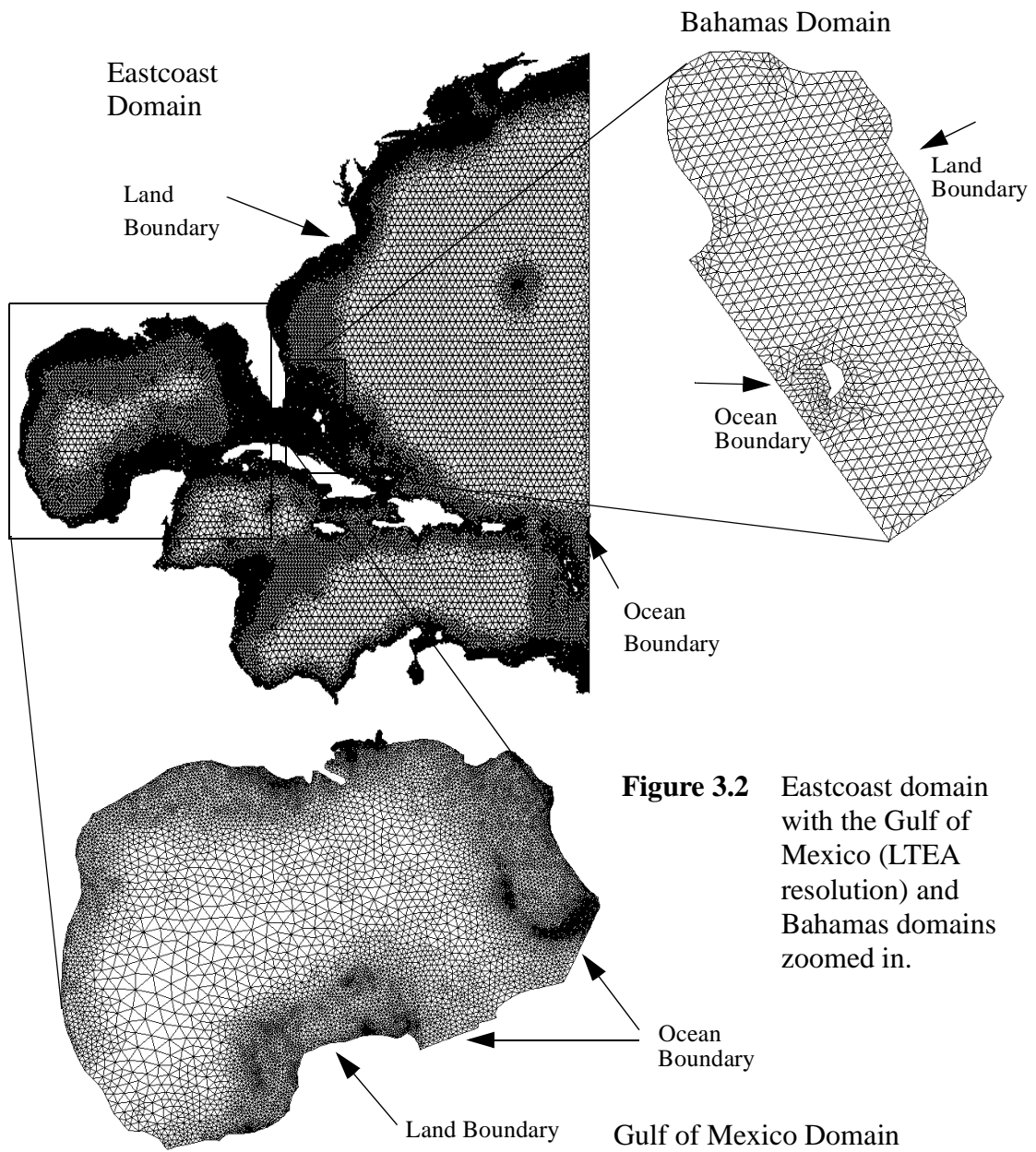
Figure 3.2 Eastcoast domain
with the Gulf of
Mexico (LTEA
resolution) and
Bahamas domains
zoomed in.

Ocean
Boundary

Land Boundary

Gulf of Mexico Domain

28

Table 3.1 Application domain information.

	Bahamas	Gulf of Mexico		Eastcoast
Meshing Criteria	$\lambda/\Delta x$	$\lambda/\Delta x$	LTEA	$\lambda/\Delta x$
# nodes	926	11701	11934	32947
# elements	1696	21970	22870	61705
Min. Bathymetry (m)	1.0	1.0	0.7	3.0
Max. Bathymetry (m)	≈ 9.0	≈ 3600.0	≈ 3600.0	≈ 6000.0
original G value (sec^{-1})	0.009	0.009	0.009	0.005
M_2 amplitude (m)	0.395	0.07 - 0.173	0.07 - 0.173	0.0652-0.5580
O_1 amplitude (m)	0.075			
K_1 amplitude (m)	0.095			
S_2 amplitude (m)	0.06			
N_2 amplitude (m)	0.10			

regarding parameters, boundary, and grid information for each of the application domains. In all of the domains, the land boundaries are treated as no flow. Two meshing criteria are used in developing the Gulf of Mexico grids: $\lambda/\Delta x$, which is commonly used in grid development, and the Local Truncation Error Analysis (LTEA), developed by Hagen et al.[39,40] In the LTEA technique, nodes are placed in order to minimize spatial truncation error.

3.5 Numerical Experiments and Discussion

3.5.1 Stability

Dominant nonlinear terms preclude the use of traditional stability studies, such as Fourier analysis. Therefore, we utilize heuristic methods. In particular stability changes

with the new algorithm were determined from these steps: 1) Each domain was evaluated using the original algorithm to obtain the maximum stable time step (to the nearest five seconds) for each type of spatial discretization; 2) Each domain was evaluated using the predictor-corrector algorithm to obtain the maximum stable time step for each spatial discretization; 3) Results from the two previous steps were compared to one another and a percent change between the two resulting time steps was obtained. Because the corrector iteration requires another solution of the system matrix, we need to achieve more than a $n \times 100\%$ change for the predictor-corrector algorithm to be considered cost-effective, where n is the number of corrector steps. This is a conservative estimate because it assumes the entire load vector is re-evaluated with each iteration, while in reality, only the $k*/k+1$ portion of the nonlinear terms needs to be updated. Previous results showed no significant gains in performing more than one iteration of the corrector step, therefore only one iteration is considered herein.

Results for each of the domains are summarized in Table 3.2 with the maximum allowable time steps shown along with the maximum Courant number. In all the domains, results show that the Courant number restriction relaxes with the predictor-corrector algorithm. Generally, Courant numbers with the original algorithm are less than 0.5, while Courant numbers greater than 1.0 can be realized with the predictor-corrector algorithm. All domains obtain the needed 100% increase (single corrector iteration) for the new algorithm to be cost-effective, with the greatest increase in the maximum stable time step occurring with the Eastcoast domain, which shows an eight-fold increase.

For the different spatial discretizations, results from the quarter annular and Gulf of Mexico domains indicate that resolution changes do affect the stability results. In particular

Table 3.2 Numerical stability experiments - maximum stable time step and associated
Courant number for various domains.

Domains	Original Δt, sec. (C_r)	Predictor-Corrector Δt, sec. (C_r)	Percent Increase
Quarter annular			
5x5	2205 (0.50)	7095 (1.50)	222%
10x10	1120 (0.47)	5140 (2.14)	359%
15x15	730 (0.45)	4250 (2.47)	482%
20x20	550 (0.45)	3685 (3.00)	569%
25x25	445 (0.45)	3400 (3.40)	664%
30x30	370 (0.45)	3060 (3.74)	727%
Bahamas			
$\lambda/\Delta x$	245 (0.57)	885 (2.06)	261%
Gulf of Mexico			
$\lambda/\Delta x$	200 (0.52)	580 (1.54)	190%
LTEA	100 (0.17)	360 (0.62)	260%
Eastcoast			
$\lambda/\Delta x$	55 (0.032)	470 (0.27)	754%

for the quarter series, the maximum Courant number with the original algorithm remains

constant with increasing resolution; however, the maximum Courant number with the

predictor-corrector algorithm increases with increasing resolution. For the Gulf of Mexico

domain, we evaluated two different meshing techniques, the typical $\lambda/\Delta x$ and the LTEA.

The LTEA method adds refinement in the grid where truncation errors are high, which

usually coincided with the continental rise and shelf break. For these two refinements, we

analyzed the spatial variability of the Courant number over the domain. From these studies,

we found that the LTEA grid tends to even out the magnitude of the Courant number over

the break, with the most restrictive Courant number occurring in the shallow, near-shore region; in contrast, the $\lambda/\Delta x$ grid shows a limiting Courant number at the shelf break.

3.5.2 G Sensitivity

Sensitivity studies provide information on how parameter changes impact algorithm performance. Herein, we are especially interested in how *G*, the numerical parameter in the GWC equation, impacts the maximum stable time step. Sensitivity analyses were conducted on three domains, with several spatial resolutions: quarter annular domain with two spatial resolutions, 10x10 and 30x30; Bahamas domain; Gulf of Mexico domain with two meshing techniques, $\lambda/\Delta x$ and LTEA and Eastcoast domain. In each of these domains, we analyzed a range of *G* values between 0.00001 sec^{-1} and 0.1 sec^{-1}. Using the PC algorithm, for each *G* parameter value we obtained the maximum stable time step, which we compared to the maximum stable time step from the original algorithm with the *G* parameter fixed at its original value.

Percent changes between these two scenarios are shown in Figure 3.3. Figure 3.3a shows that the quarter annular domain (two resolutions), along with the Bahamas domain. For the quarter annular domains, the greatest increase in stability occurs with *G* between 0.001 to 0.0001 sec^{-1}, with peaks at $G=0.0004 \text{ sec}^{-1}$ for the 10x10 resolution and $G=0.0007$ sec^{-1} for the 30x30 resolution. For the Bahamas domain, the greatest increase occurs with *G* between 0.01 and 0.001 sec^{-1}, with the peak at $G=0.0025 \text{ sec}^{-1}$. Figure 3.3b shows the results from the two Gulf of Mexico meshes and the Eastcoast domain. For the $\lambda/\Delta x$ grid, the greatest increase in stability occurs when *G* is between 0.001 to 0.0001 sec^{-1} with the peak occurring at $G=0.00068 \text{ sec}^{-1}$, while for the LTEA grid, the greatest increase in stability occurs between 0.01 to 0.0001 sec^{-1} with two peaks - one at a $G=0.002 \text{ sec}^{-1}$ and
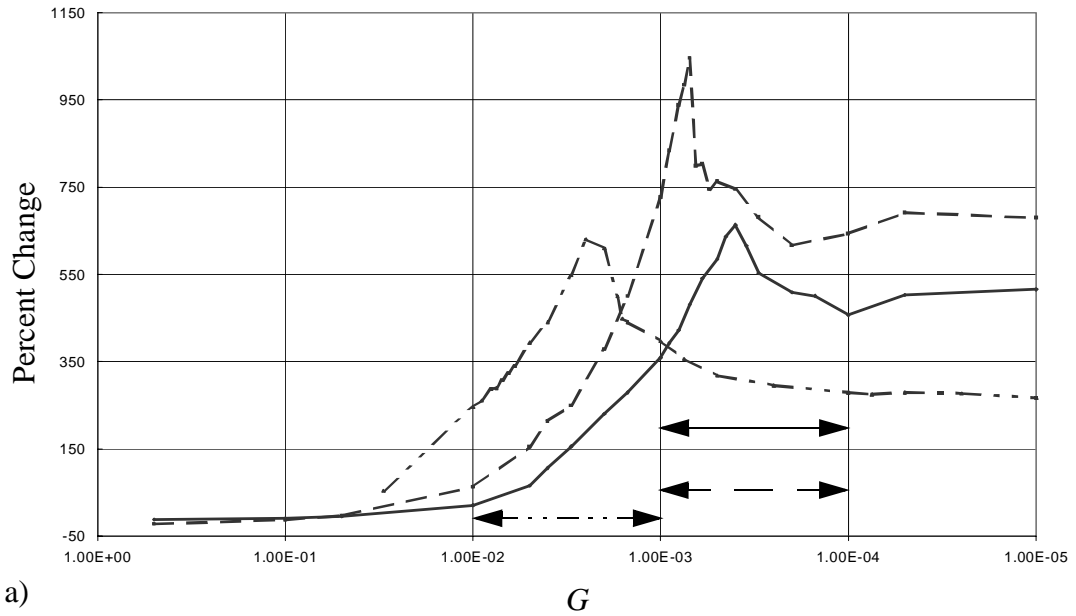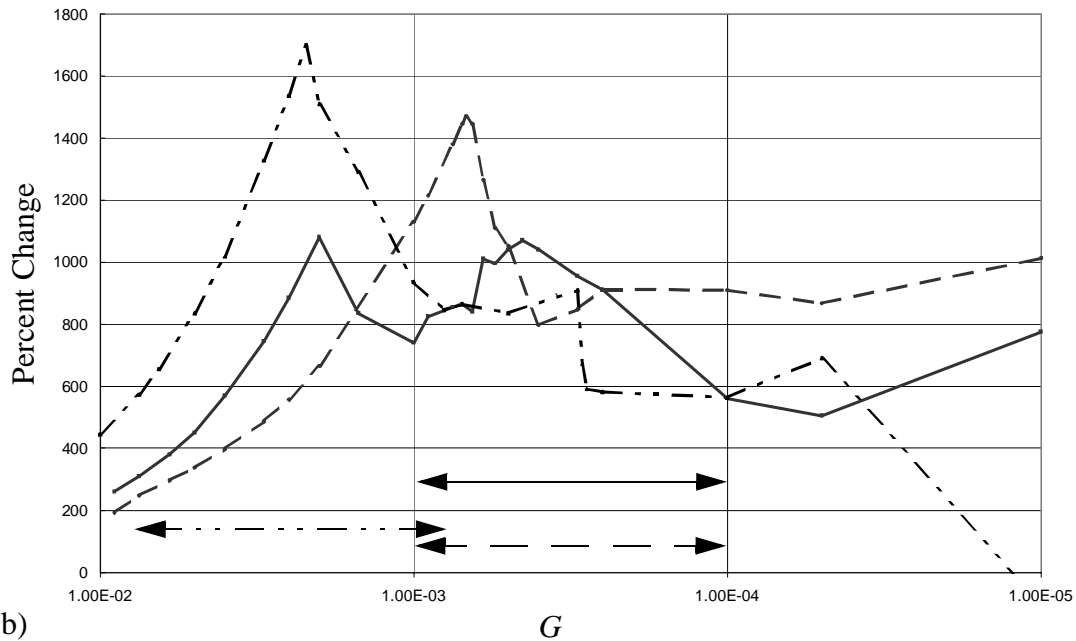
Figure 3.3 Sensitivity of the G parameter to stability for two-dimensional bathymetry: a) quarter annular domains (10x10 (solid line) and 30x30 (dashed line) resolution) and Bahamas domain (dot-dash line), b) Gulf of Mexico, $\lambda/\Delta x$ (dashed line) and LTEA (solid line) resolution and the Eastcoast domain (dot-dashed line). Arrows, using the same line styles, indicate where $1 \leq G/\tau_{max} \leq 10$ for each domain.

the other at G=0.00045 sec^{-1}. In the Eastcoast domain, the greatest increase in stability occurs between 0.01 and 0.001 sec^{-1} with the peak at 0.0022 sec^{-1}. A common feature of all is that stability is highly sensitive to the value of G used in the simulation.

An optimum range for G/τ_{max} should lie between 1 and 10 in order to minimize the mass balance errors and errors in the generation of nonlinear constituents, as indicated in previous work by Kolar et al. [54] They also indicated that when G/τ_{max} increases above 10, oscillations can appear in the solution. We looked at this ratio for each of the domains analyzed herein to determine if the stability peak lies within this recommended range. In Figure 3.3, we indicate where $1 \leq G/\tau_{max} \leq 10$ for each domain. In short, for all domains tested, the maximum increase in stability coincides with the recommended range that minimizes the mass balance errors and errors in the generation of nonlinear constituents. Thus, a single value of G can meet both criteria.

3.5.3 Temporal Accuracy

In this section, we investigate the influence of the predictor-corrector algorithm on temporal accuracy, both globally and locally. Globally, we analyze the temporal accuracy using L_2 and L_∞ error measures and determine the changes to the order of accuracy (convergence rate) between the two algorithms. L_2 error measures are obtained by comparing a fine ("true") solution to the coarse solution at the same point using the following:

$$L_2 \text{ error } = \sqrt{\frac{\sum_{i=1}^{N}(c_i - f_i)^2}{N}} \qquad\qquad (3.5)$$

where c_i is the coarse solution, f_i is the fine solution and N is the number of node in the

coarse grid. The L_∞ error is defined as the magnitude of the maximum difference of the coarse and fine solutions over the entire domain. Discussion of these results occurs in the first subsection. In the second subsection, CAFE (Cumulative Area Fraction Errors) analysis [61] is used to study the local behavior of temporal accuracy.

3.5.3a Global Temporal Accuracy (Convergence Rates)

In order to evaluate the global behavior of temporal accuracy, including the overall convergence rate, we compare solutions from a coarse temporal resolution to a "true" (fine Δt) solution of 10 seconds. Spatial resolution is kept the same. Accuracy changes were quantified by analyzing the global error, as measured by the L_2 norm and the L_∞ norm. For all domains, we evaluated both norms at 120 discrete times covering 10 complete tidal cycles of the M_2 tide, which is the dominant tidal signal. For the L_2 norm, we averaged the results over time, while for the L_∞ norm, we determined the maximum absolute value over time. We performed the temporal accuracy experiments on all of the domains: quarter annular (30x30 resolution), Bahamas, Gulf of Mexico ($\lambda/\Delta x$ grid) and Eastcoast. Figure 3.4 shows the elevation L_2 norms for each of these domains: quarter annular (Figure 3.4a), Bahamas (Figure 3.4b), Gulf of Mexico (Figure 3.4c), and Eastcoast (Figure 3.4d).

In all domains, results show that the error for the predictor-corrector algorithm plots below the original algorithm (less absolute error). Also, we determined the slope of the line (i.e., order of accuracy) for each of the time-marching algorithms, which is shown in Table 3.3. In all the domains analyzed, we find that the order of accuracy increases from approximately first order for the original algorithm to second order for the predictor-corrector algorithm (see Table 3.3). Results using either the L_∞ norm or the velocity field
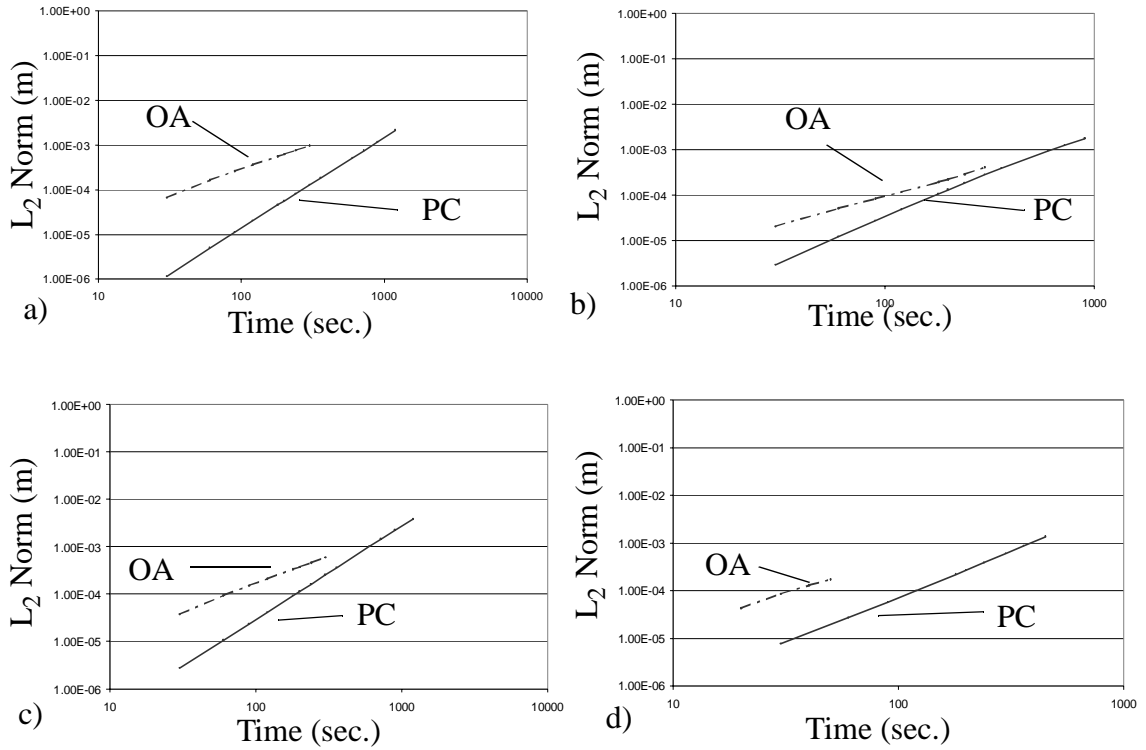
Figure 3.4 Temporal accuracy results for: a) quarter annular b) Bahamas, c) Gulf of Mexico and d) Eastcoast. All results are based on the L_2 norm of elevation (dot-dash line - original algorithm (labeled OA), solid line - predictor-corrector algorithm (labeled PC)).

Table 3.3 Order of accuracy from slope of L_2 norm.

Domains	Original	Predictor-Corrector
Quarter annular (30x30)	1.15	2.03
Bahamas	1.27	1.89
Gulf of Mexico	1.19	1.97
Eastcoast	1.53	1.92

are similar.

These results mimic what we found with the 1D experiments [33]. Noteworthy is that the predictor-corrector algorithm shows the greatest increase in accuracy for domains where the bathymetry gradients are significant over much of the domain, such as the Gulf of Mexico. In contrast, the least gains are seen with the Eastcoast domain, which may be due to the fact that the majority of domain is deep water, where the wave propagation is more nearly linear. In these instances, updating the nonlinear terms does not provide as much improvement to the accuracy.

3.5.3b Local Temporal Accuracy

Next, we evaluated the behavior of the temporal accuracy over the spatial domain utilizing CAFE plots [61]. CAFE plots provide both absolute and relative errors between two simulations of the same domain with the same spatial resolution, but different temporal resolutions. Absolute errors are obtained from: $\varepsilon_a = |(c_i - f_i)|$ where c_i is the coarse solution and f_i is the fine solution; while relative errors (%) are determined from: $\varepsilon_r = \left(\frac{|c_i - f_i|}{f_i}\right) 100$ [40]. A frequency graph is developed based on these differences, viz, for each error level, the cumulative area fraction is computed, which is calculated as the ratio of area of the grid associated with a certain difference compared to the total area of the grid.

Elevation, being a scalar field, can be represented by amplitude and phase errors. However the velocity field is a vector field, so direction needs to be quantified. If one considers that the velocity vector at a point in space and maps its position as time evolves, an ellipse is traced out, as Figure 3.5 shows. The five components of the velocity error are:
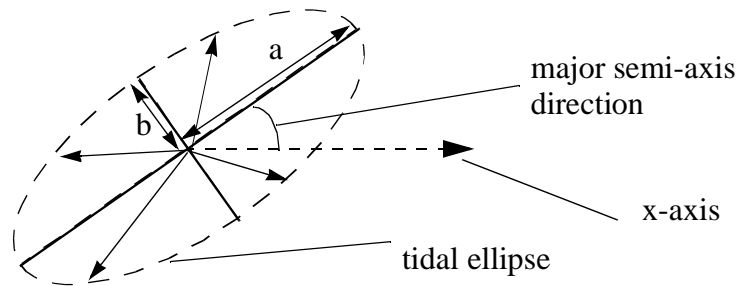
Figure 3.5 A schematic of the velocity tidal ellipse that describes the coarse or fine velocity fields and their components.

the major and minor semi-axis velocity is obtained from lengths of the maximum and minimum current vector over a tidal cycle (a and b in Figure 3.5, respectively); the major semi-axis phase difference is determined from the phase lag that the major semi-axis velocity makes with the tidal forcing; eccentricity is obtained from the ratio of the major and minor semi-axis velocity results (eccentricity $= a/b$ where a and b are defined in Figure 3.5) and the major semi-axis direction difference is determined from the angle of the major semi-axis current and the positive x-axis [40].

The following steps are used to develop the CAFE curves for this study: 1) Harmonic data is recorded for the original algorithm over several tidal cycles for coarse and fine temporal resolutions; 2) Harmonic data is recorded for the predictor-corrector algorithm over several tidal cycles for coarse and fine temporal resolutions; 3) Absolute and relative errors are calculated for each algorithm; 4) Cumulative errors for both algorithms are computed; 5) Results from the original and predictor-corrector algorithms are plotted against each other to determine the percent area exceeding a certain criteria for

convergence.

Figure 3.6 shows two sample CAFE plots. To read these plots, one must first realize that a perfect solution (no error) would plot as a vertical line located at $x = 0$, indicated by the vertical solid line in Figure 3.6. Any deviations from this line represent errors in the simulation; the further the graph is from $x = 0$, the more the error. For a given convergence criteria, one finds the associated percent of cumulative area in the domain that exceeds the given criteria. For example in Figure 3.6a, one first selects a convergence criteria (in this case, +/- 0.02 cm.) then follows that value to where it intersects the CAFE plot and obtains the cumulative area that exceeds this convergence criteria (in this case, 0.095% overprediction and 0.02% underprediction). Note that in Figure 3.6a, the short-dashed line plots underneath the curve of the long-dashed line, indicating less error. Also, by examining the shape of the CAFE plots, we can infer the spatial distribution of the temporal error, e.g., if the curves are "skinny" (narrow at the top), the temporal error is confined to a small portion of the domain, but if the curves are "fat" (wider at the top - shown in Figure 3.6b), temporal error permeates the domain

Figures 3.7-3.12 show CAFE plots for three domains: quarter annular (30x30 resolution), Eastcoast and Gulf of Mexico ($\lambda / \Delta x$). Tables 3.4-3.9 present the error levels obtained from the CAFE results for the same three domains: Results are representative of the accuracy changes for all the domains. These tables show the error levels for all of the velocity and elevation components for the indicated temporal resolutions. The criteria used in these tables are based on tolerance levels that exceed required accuracy for most applications. In the tables, the bold values indicate the lowest error. In analyzing the results shown in these tables, we observe that when the time step is the same between the two
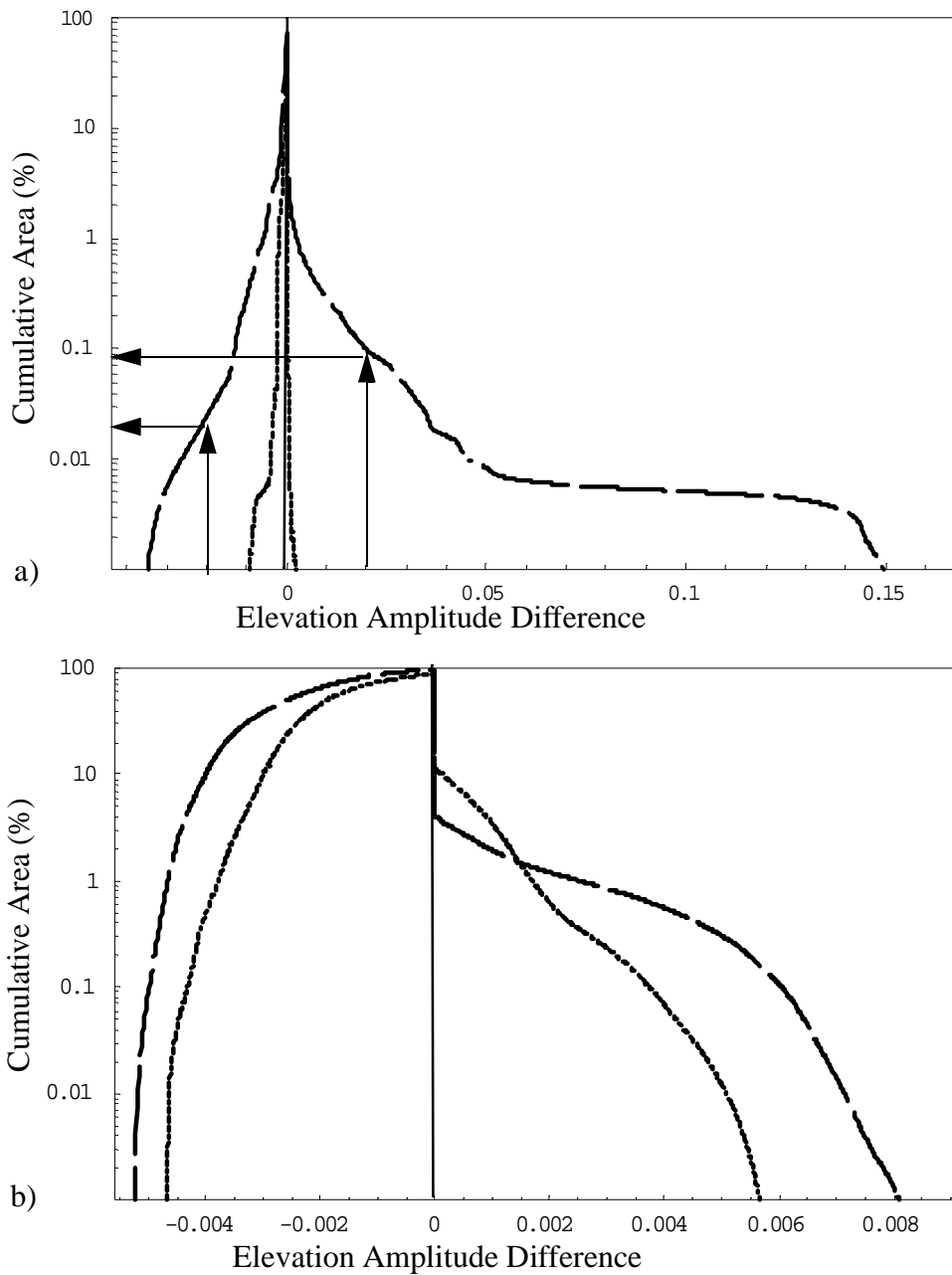
Figure 3.6 Sample CAFE plots. Vertical solid line at $x = 0$ represents a "perfect" solution (no error). Axes for these figures are: error values for a given component are shown on the x-axis while the y-axis shows the cumulative area of the domain. The two line styles indicate two different simulations.
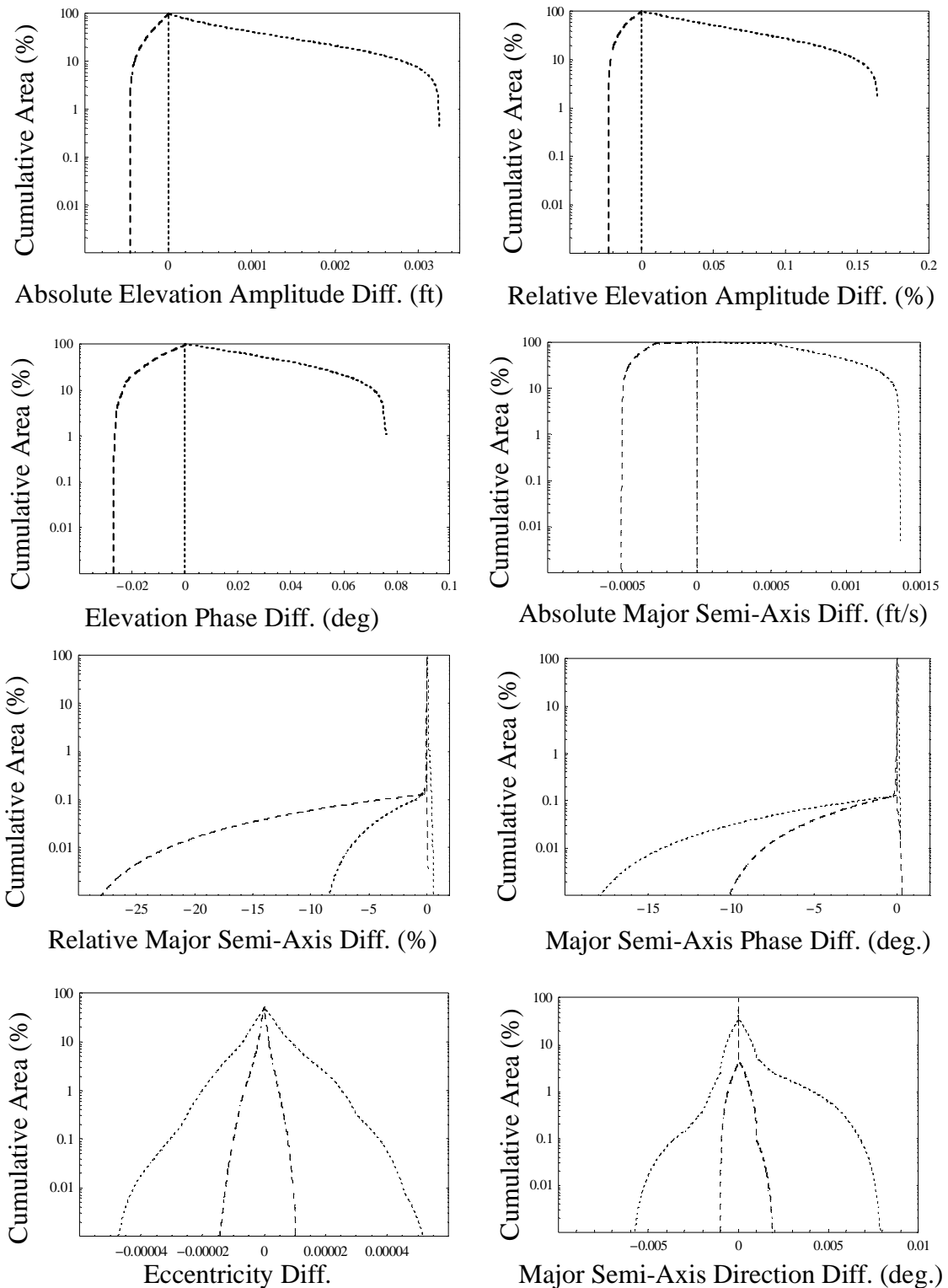
Figure 3.7   CAFE plots for quarter annular domain - different time step for both time-marching algorithms (orig Δt = 150 sec, PC Δt = 300 sec). Dotted line - original time-marching algorithm and dashed line - predictor-corrector time-marching algorithm.
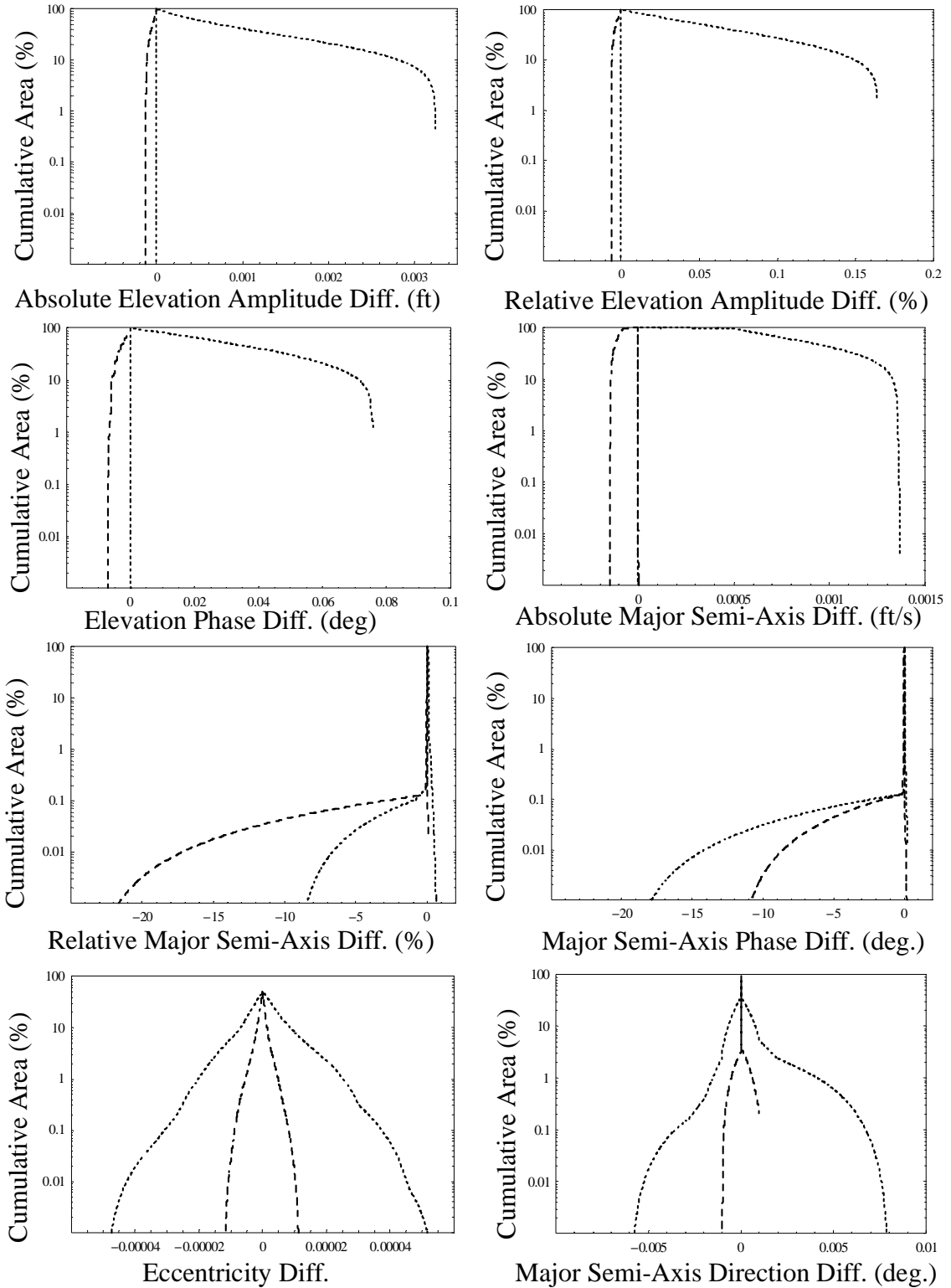
Figure 3.8   CAFE plots for quarter annular domain - same time step for both time-marching algorithms (Δt = 150 sec). Dotted line - original time-marching algorithm and dashed line - predictor-corrector time-marching algorithm.
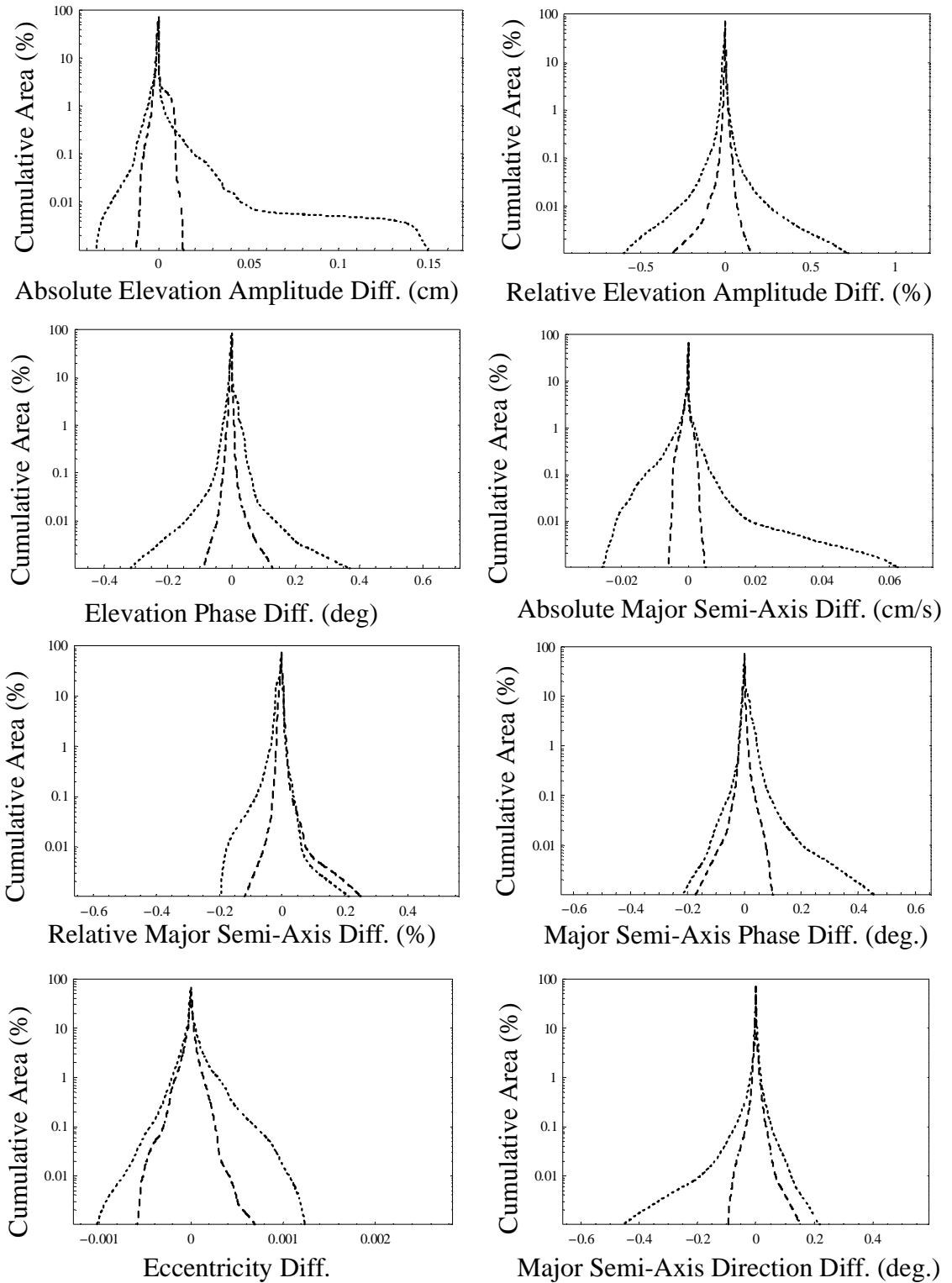
Figure 3.9 CAFE plots for Eastcoast domain - different time step for both time-marching algorithms (orig Δt = 40 sec, PC Δt = 100 sec). Dotted line - original time-marching algorithm and dashed line - predictor-corrector time-marching algorithm.
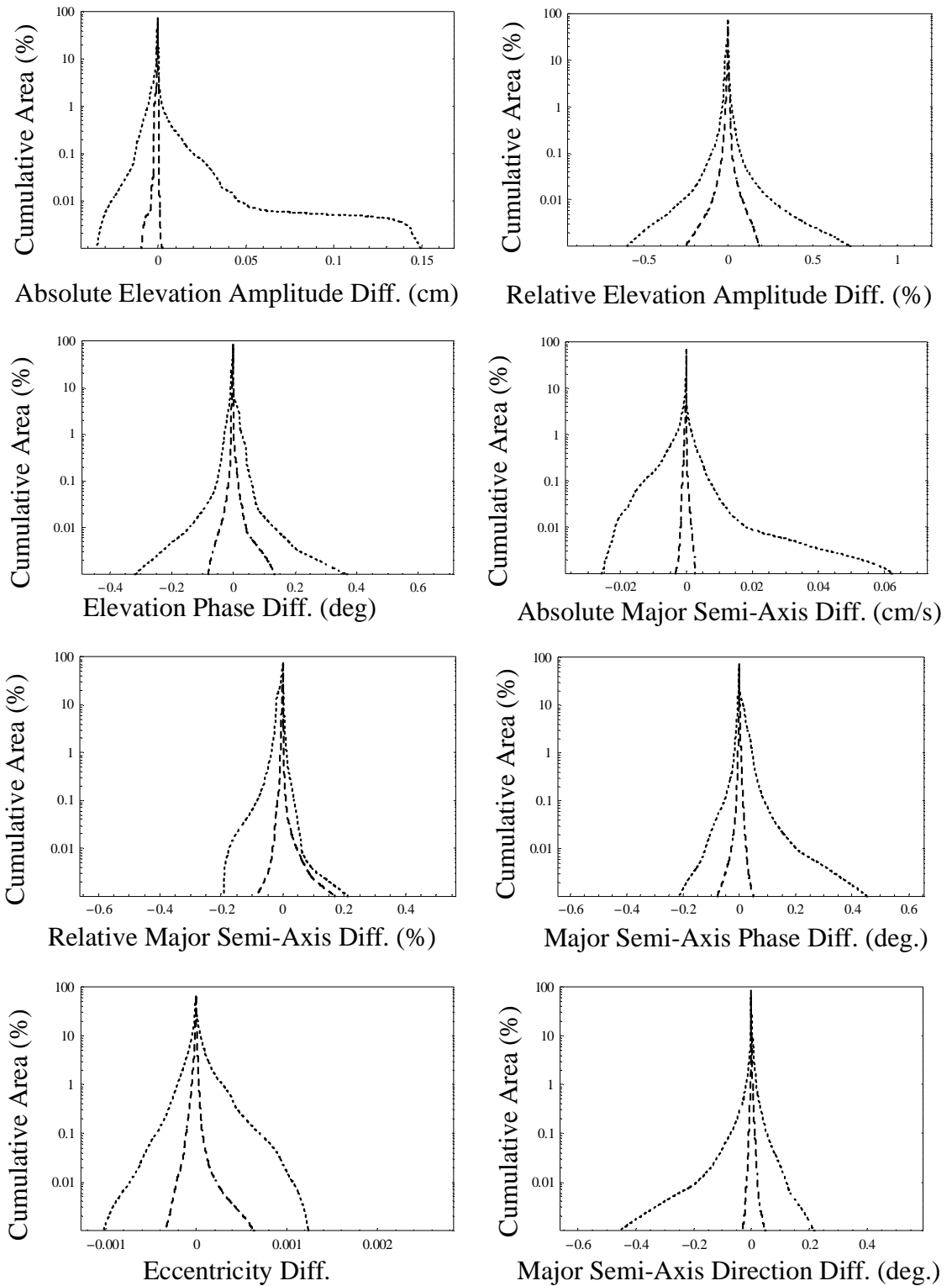
Figure 3.10 CAFE plots for Eastcoast domain - same time step for both time-marching algorithms ($\Delta t = 40$ sec). Dotted line - original time-marching algorithm and dashed line - predictor-corrector time-marching algorithm.
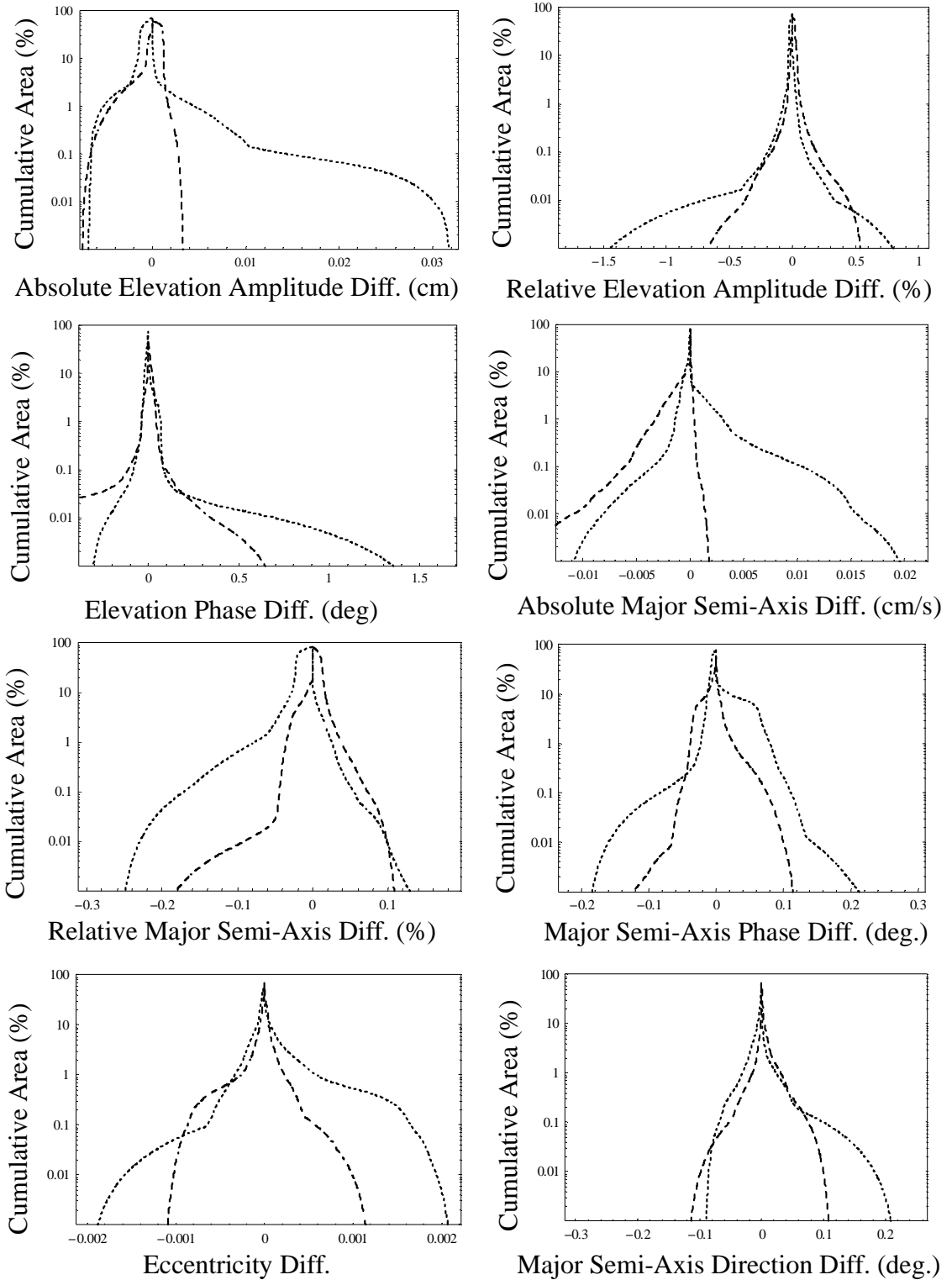
Figure 3.11 CAFE plots for Gulf of Mexico domain - different time step for both time-marching algorithms (orig Δt = 50 sec, PC Δt = 150 sec). Dotted line - original time-marching algorithm and dashed line - predictor-corrector time-marching algorithm.
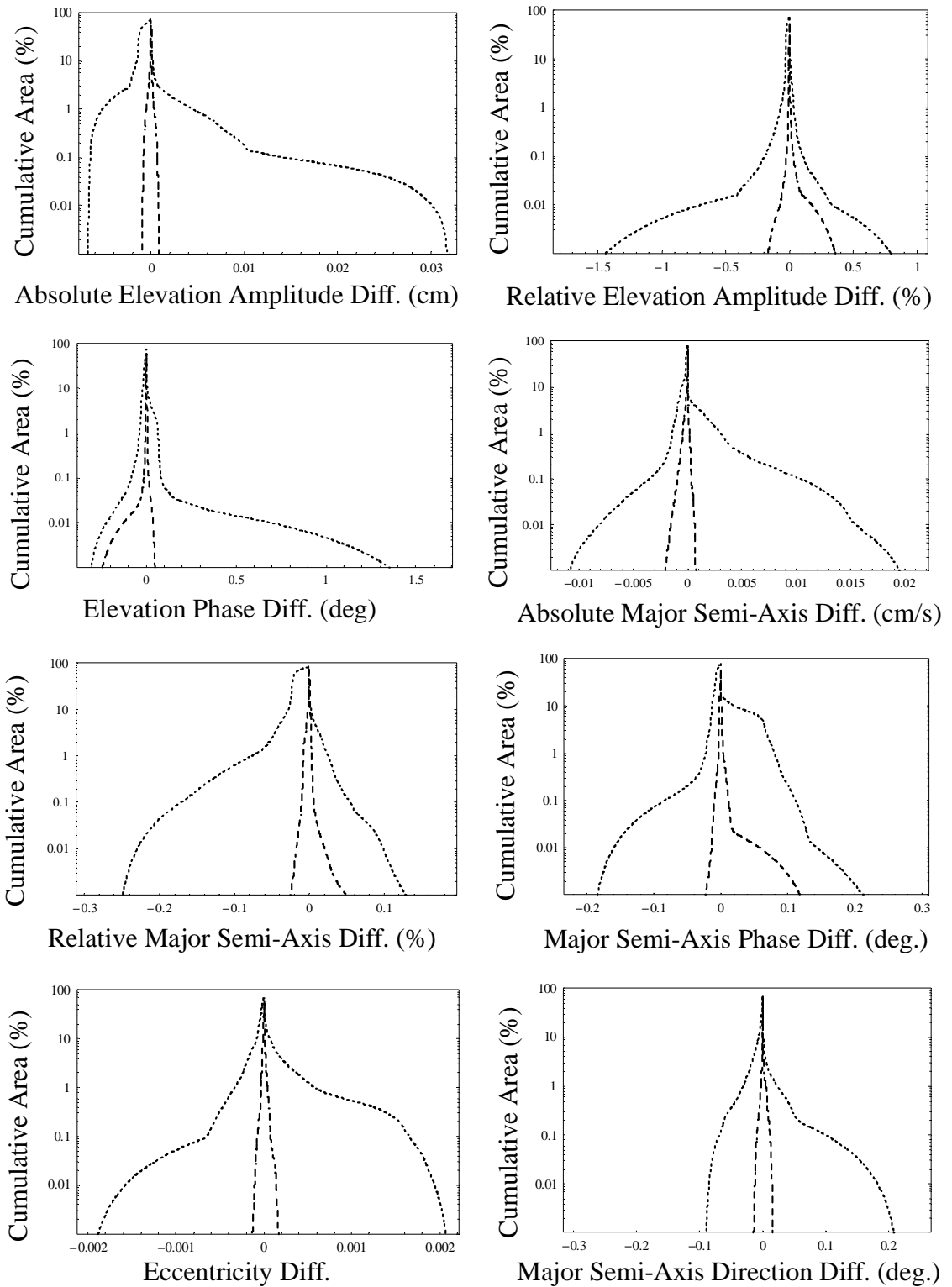
Figure 3.12 CAFE plots for Gulf of Mexico domain - same time step for both time-marching algorithms (Δt = 50 sec). Dotted line - original time-marching algorithm and dashed line - predictor-corrector time-marching algorithm.

Table 3.4 Elevation error measures for quarter annular domain.

	Quarter annular (same Δt)		Quarter annular (different Δt)	
	Original	PC	Original	PC
Time step (sec)	150	150	150	300
Elevation Amplitude (Absolute)				
% exceeding -0.001 ft	<0.0001	<0.0001	<0.0001	<0.0001
% exceeding 0.001 ft	40	**<0.0001**	40	**<0.0001**
% exceeding +/-0.001 ft	40	**<0.0002**	40	**<0.0002**
Elevation Amplitude (Relative)				
% exceeding -0.02%	<0.0001	<0.0001	**<0.0001**	20
% exceeding 0.02%	80	**<0.0001**	80	**<0.0001**
% exceeding +/-0.02%	80	**<0.0002**	80	**20**
Elevation Phase Difference				
% exceeding -0.02 °	<0.0001	<0.0001	**<0.0001**	20
% exceeding 0.02 °	60	**<0.0001**	60	**<0.0001**
% exceeding +/-0.02 °	60	**<0.0002**	60	**20**

Table 3.5 Velocity error measures for quarter annular domain.

	Quarter annular (same Δt)		Quarter annular (different Δt)	
	Original	PC	Original	PC
Time step (sec.)	150	150	150	300
Major Semi-Axis (Absolute)				
% exceeding -0.0005 ft s^{-1}	<0.0001	<0.0001	**<0.0001**	10
% exceeding 0.0005 ft s^{-1}	95	**<0.0001**	95	**<0.0001**
% exceeding +/-0.0005 ft s^{-1}	95	**<0.0002**	95	**10**
Major Semi-Axis (Relative)				
% exceeding -5%	**0.03**	0.09	**0.03**	0.1
% exceeding 5%	<0.0001	<0.0001	<0.0001	<0.0001
% exceeding +/-5%	**0.03**	0.09	**0.03**	0.1
Major Semi- Axis Phase Difference				
% exceeding -0.05 °	0.08	**0.04**	0.08	**0.04**
% exceeding 0.05 °	<0.0001	<0.0001	<0.0001	<0.0001
% exceeding +/-0.05 °	0.08	**0.04**	0.08	**0.04**
Eccentricity				
% exceeding -0.0002	1	**<0.0001**	1	**<0.0001**
% exceeding 0.0002	2.5	**<0.0001**	2.5	**<0.0001**
% exceeding +/-0.0002	3.5	**<0.0002**	3.5	**<0.0002**
Major semi-axis direction				
% exceeding -0.1 °	0.02	**<0.0001**	0.02	**<0.0001**
% exceeding 0.1 °	0.6	**<0.0001**	0.6	**<0.0001**
% exceeding +/-0.1 °	0.62	**<0.0002**	0.62	**<0.0002**

Table 3.6 Elevation error measures for Eastcoast domain.

	Eastcoast (same Δt)		Eastcoast (different Δt)	
	Original	PC	Original	PC
Time step (sec)	40	40	40	100
Elevation Amplitude (Absolute)				
% exceeding -0.01 cm	0.3	**0.001**	0.3	**0.03**
% exceeding 0.01 cm	0.3	**<0.0001**	0.3	**0.04**
% exceeding +/-0.01 cm	0.6	**<0.0011**	0.6	**0.07**
Elevation Amplitude (Relative)				
% exceeding -0.1%	0.1	**0.0009**	0.1	**0.01**
% exceeding 0.1%	0.08	**0.007**	0.08	**0.004**
% exceeding +/-0.1%	0.18	**0.0079**	0.18	**0.014**
Elevation Phase Difference				
% exceeding -0.1 °	0.025	**<0.0001**	0.025	**0.0008**
% exceeding 0.1 °	0.02	**0.003**	0.02	**0.002**
% exceeding +/-0.1 °	0.045	**<0.0031**	0.045	**0.0028**

Table 3.7 Velocity error measures for Eastcoast domain.

	Eastcoast (same Δt)		Eastcoast (different Δt)	
	Original	PC	Original	PC
Time step (sec.)	40	40	40	100
Major Semi-Axis (Absolute)				
% exceeding -0.01 cm s^{-1}	0.2	**<0.0001**	0.2	**<0.0001**
% exceeding 0.01 cm s^{-1}	0.04	**<0.0001**	0.04	**<0.0001**
% exceeding +/-0.01 cm s^{-1}	0.24	**<0.0002**	0.24	**<0.0002**
Major Semi-Axis (Relative)				
% exceeding -0.1%	0.08	**0.0009**	0.08	**0.002**
% exceeding 0.1%	0.003	**0.002**	**0.003**	0.006
% exceeding +/-0.1%	0.083	**0.0029**	0.083	**0.008**
Major Semi- Axis Phase Difference				
% exceeding -0.05 °	0.14	**0.003**	0.14	**0.04**
% exceeding 0.05 °	0.9	**0.001**	0.9	**0.04**
% exceeding +/-0.05 °	1.04	**0.004**	1.04	**0.08**
Eccentricity				
% exceeding -0.0002	1	**0.015**	1	**0.8**
% exceeding 0.0002	2	**0.012**	2	**0.4**
% exceeding +/-0.0002	3	**0.027**	3	**1.2**
Major semi-axis direction				
% exceeding -0.1 °	0.07	**<0.0001**	0.007	**0.0005**
% exceeding 0.1 °	0.016	**<0.0001**	**0.0016**	0.004
% exceeding +/-0.1 °	0.086	**<0.0002**	0.0086	**0.0045**

Table 3.8 Elevation error measures for Gulf of Mexico domain.

	Gulf of Mexico (same Δt)		Gulf of Mexico (different Δt)	
	Original	PC	Original	PC
Time step (sec.)	50	50	50	150
Elevation Amplitude (Absolute)				
% exceeding -0.002 cm	4	**<0.0001**	4	**3**
% exceeding 0.002 cm	2	**<0.0001**	2	**0.7**
% exceeding +/-0.002 cm	6	**<0.0002**	6	**3.7**
Elevation Amplitude (Relative)				
% exceeding -0.1%	0.4	**0.007**	0.4	**0.25**
% exceeding 0.1%	0.15	**0.02**	**0.15**	0.4
% exceeding +/-0.1%	0.55	**0.027**	**0.55**	0.65
Elevation Phase Difference				
% exceeding -0.1 °	0.07	**0.015**	**0.07**	0.1
% exceeding 0.1 °	0.08	**<0.0001**	**0.08**	0.1
% exceeding +/-0.1 °	0.15	**<0.0151**	**0.15**	0.2

Table 3.9 Velocity error measures for Gulf of Mexico domain.

	Gulf of Mexico (same Δt)		Gulf of Mexico (different Δt)	
	Original	PC	Original	PC
Time step (sec.)	50	50	50	150
Major Semi-Axis (Absolute)				
% exceeding -0.001 cm s^{-1}	2.5	**0.08**	**2.5**	6
% exceeding 0.001 cm s^{-1}	3.5	**<0.0001**	3.5	**0.04**
% exceeding +/-0.001 cm s^{-1}	6	**<0.0801**	**6**	6.04
Major Semi-Axis (Relative)				
% exceeding -0.02%	60	**0.005**	60	**5**
% exceeding 0.02%	2	**0.01**	**2**	5
% exceeding +/-0.02%	62	**0.015**	62	**10**
Major Semi- Axis Phase Difference				
% exceeding -0.02 °	2	**0.002**	**2**	8
% exceeding 0.02 °	10	**0.022**	10	**1.5**
% exceeding +/-0.02 °	12	**0.024**	12	**9.5**
Eccentricity				
% exceeding -0.0002	3.5	**<0.0001**	3.5	**1.5**
% exceeding 0.0002	4	**<0.0001**	4	**1.25**
% exceeding +/-0.0002	7.5	**<0.0002**	7.5	**2.75**
Major semi-axis direction				
% exceeding -0.02 °	2	**0.0004**	2	**0.8**
% exceeding 0.02 °	1.5	**<0.0001**	**1.5**	2
% exceeding +/-0.02 °	3.5	**<0.0005**	3.5	**2.8**

algorithms, the predictor-corrector algorithm produces less error for all of the components except for one in the quarter annular domain. (Note that all bold numbers are under the "PC, same Δt" column.) And in the figures for the same time step (Figures 3.8, 3.10, and 3.12), the predictor-corrector algorithm plots underneath the curve of the original algorithm in nearly all instances, thus indicating less error. Noteworthy is that the error measure is often two orders of magnitude less. When the time step for the predictor-corrector algorithm is 2.5 times that of the original algorithm for Eastcoast, 3 times that of the original algorithm for the Gulf of Mexico and 2 times that of the original algorithm for the quarter annular domain, the tables show that the predictor-corrector algorithm still produces less error than the original algorithm at a lower time step in most ($\approx 83\%$) of the cases. (Note in the tables that the majority of bold numbers are still under the "PC, different Δt" column.) Moreover, many of these predictor-corrector errors for the Eastcoast domain are still an order of magnitude less than the original algorithm. Also note that in a majority ($\approx 70\%$) of the CAFE plots (Figures 3.7, 3.9, and 3.11), the predictor-corrector algorithm plots underneath the original algorithm.

3.5.4 Testing of the Combined Parallel/Predictor-Corrector Algorithm

Complex applications on larger, more intricate domains require that we utilize parallel computing to obtain results in a time-efficient manner. Therefore, the last component of this work with the predictor-corrector algorithm was to code and analyze the algorithm in parallel. The original parallel code is reported in Dawson et al. [28], and it uses the METIS algorithm [45] to decompose grids. Ghost nodes and MPI (Message Passing Interface) [38] are used to pass information between the subdomains at each iteration. Further information on the parallel code can be found in Dawson et al. [28] We adapted this
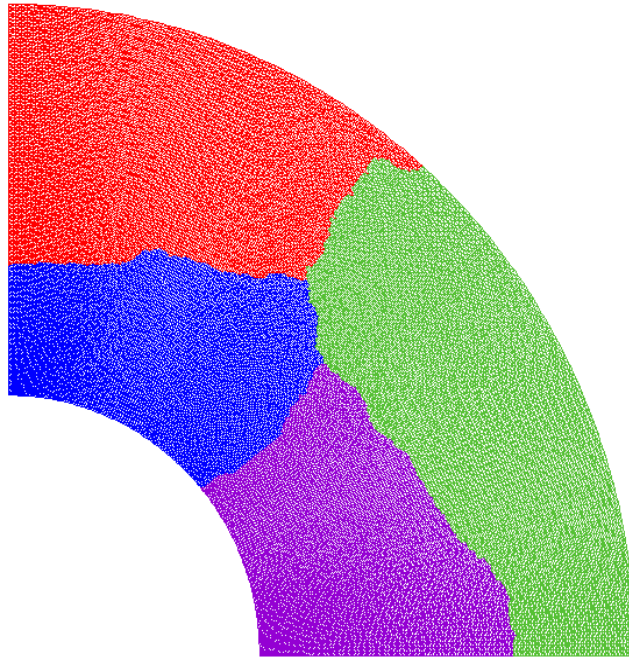
Figure 3.13 Example of the domain decomposition. The quarter annular domain with 100,000 nodes is shown for a 4 processor decomposition.

paradigm for the combined predictor-corrector/parallel code.

Figure 3.13 shows an example of the decomposition of the quarter annular grid (100x100 resolution) on four processors. Figure 3.14 shows the surface to volume ratio (computed as the ratio of the number of nodes on the boundary of the subdomain to the total number of nodes in the subdomain) versus the number of processors for two applications discussed herein, quarter annular and Eastcoast. For computational efficiency, this ratio should be kept as low as possible in order to keep communication cost low. Here, for the quarter annular domain, an ideal surface to volume ratio can be computed because it is topologically similar to a square, which, of all rectangular figures, is the one that has the maximum area for given perimeter. Thus, if a larger square is divided so that each subdomain is square, it will maintain the minimum possible surface to volume ratio. Such a computation for a square with the same number of nodes as the quarter annular domain
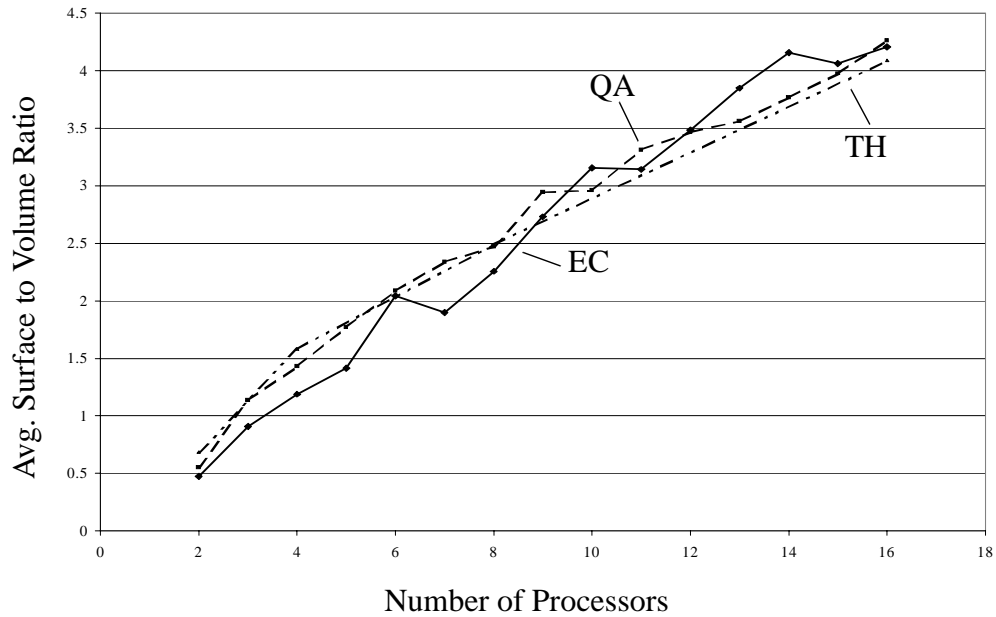
Figure 3.14 Surface to volume ratio for various subdomains. Dashed line - quarter annular domain (100x100 resolution) - labeled QA, Solid line with diamonds - Eastcoast domain - labeled EC. Theoretical values are shown with the dashed-dot-dot line - labeled TH.

is shown as the dashed-dot line in Figure 3.14. As can be seen, the actual surface to volume ratio for the quarter annular domain (see the dashed line in Figure 3.14) nearly matches the ideal curve for the square. Surprisingly, the Eastcoast domain also shows very good surface to volume behavior even though it is a very irregular domain (see the solid line in Figure 3.14). Thus, the METIS algorithm appears to be producing near-optimal subdomains.

3.5.4a Methodology and Domains Evaluated for the Benchmarking Studies

The parallel code was benchmarked on two platforms. Table 3.10 describes the characteristics of the two parallel computing environments, which are two 16-processor clusters: one consisting of Sun UltraSparc IIe processors, and another consisting of Intel Pentium III processors.

In order to determine the performance of the new combined algorithm, we

Table 3.10 Comparison of the two computer architectures.

Attributes	Sun Ultra Sparc IIe	Intel Pentium III
Speed	500 MHz	1 GHz
Operating System	Solaris 8	Linux
Cache	256 KB	256 KB
Memory	128 MB	256 MB
Communication	100 Mb/s	100 Mb/s
Compiler	Sun Forte 6.0	NAG
MPI	Sun ClusterTools	MPIch

Table 3.11 Benchmarking studies - parameters.

Parameters/ Domains {study}	Quarter annular (100x100) {1}	Eastcoast {1}	Quarter annular {2}	Quarter annular {3}
number of nodes	100000	32947	5000 - 80000	50 - 280000
avg. number of nodes/ processor	varies	varies	5000	varies
time step (original)	30	60	25	varies
time step (predictor-corrector)	180	515	25	NA

investigated three scenarios, which are presented in Table 3.11. Two scenarios (quarter annular - 100x100 resolution and Eastcoast domains) provide information on scaling and the effects of the additional stability associated with the predictor-corrector algorithm. In the third study, we want to minimize the impact of communication overhead on scaling by keeping the number of nodes per processor constant, as indicated in the table. Under this scenario, the computational workload per processor is kept constant.

3.5.4b Results of the Benchmarking Studies

In this section, we focus on three main comparisons: 1) results when the global number of nodes remains constant; 2) results when the average number of local nodes per processor remains constant; and 3) results when the global number of nodes varies on one processor.

Results from the first study are shown in Figure 3.15. Figure 3.15a shows the actual run time information and Figure 3.15b shows the scaling results for the quarter annular domain. For the timing information, wall-clock times were obtained for both algorithms at the time step indicated in Table 3.11 for the Sun and Intel platforms. To develop the scaling results, we compared the timing results from each processor to the two processor simulation, which served as the baseline. In theory, the four processor simulation should run twice as fast as the two processor simulation, etc.; this theoretical speed-up is shown in Figure 3.15b as a solid line. From these figures, we observe the following:

- As expected, the parallel version of the predictor-corrector algorithm also shows significant stability gains. For example, with the quarter annular domain, we found a six-fold increase in the maximum time step with both serial and parallel versions.

- Results for both the Sun and Intel platforms indicate the predictor-corrector algorithm significantly reduces wall-clock time because of the gains in stability. Comparing the two platforms, we see that Intel results show a slightly faster wall-clock time as compared to the Sun results, which is most
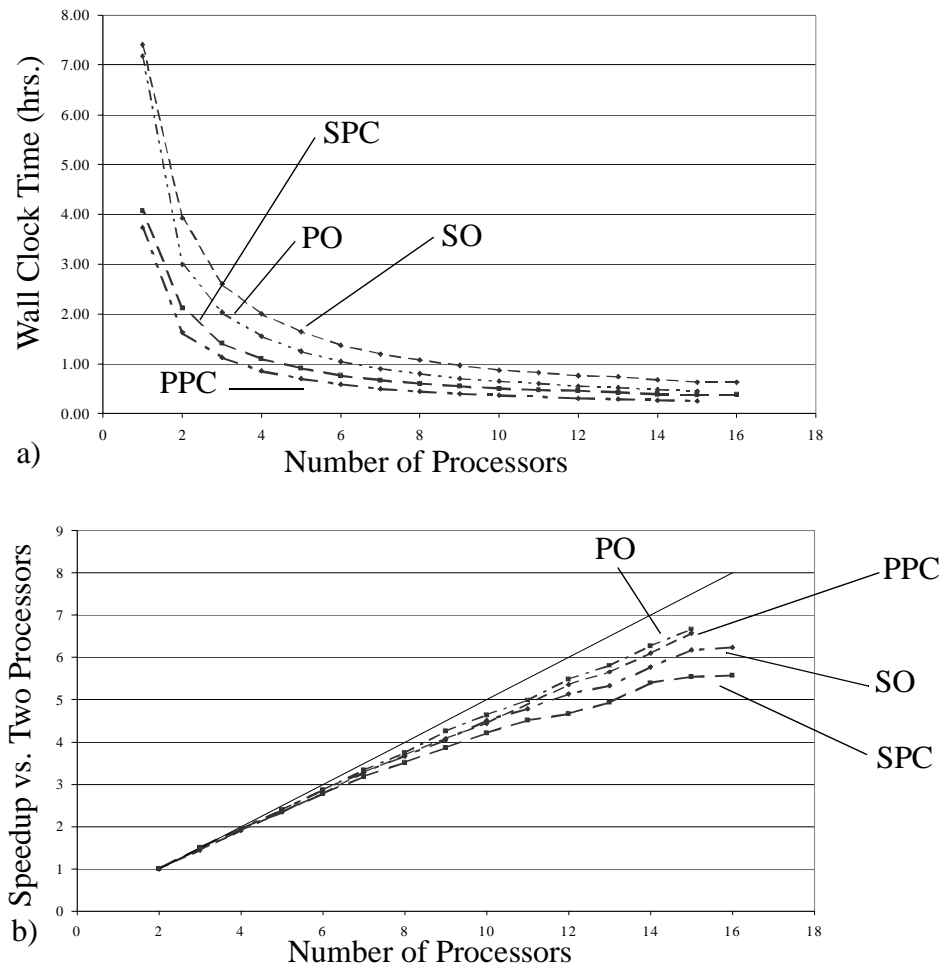
Figure 3.15 Benchmarking results for the quarter annular scenario with a) showing the wall-clock time while b) shows the speed-up vs. two processors. (PO - original time-marching algorithm (Pentium), PPC - predictor-corrector time-marching algorithm (Pentium), SO - original time-marching algorithm (Sun) and SPC - predictor-corrector time-marching algorithm (Sun)). Solid line on b) indicates the theoretical speed-up (linear).

likely due to the higher cpu speed of the Intel processors.

• Scalability results for both platforms show a near linear speed-up through the six-processor simulation, with a slight decrease as the number of processor increases. For both algorithms, we find the same trend with a slight decrease at the higher number of processors being more pronounced
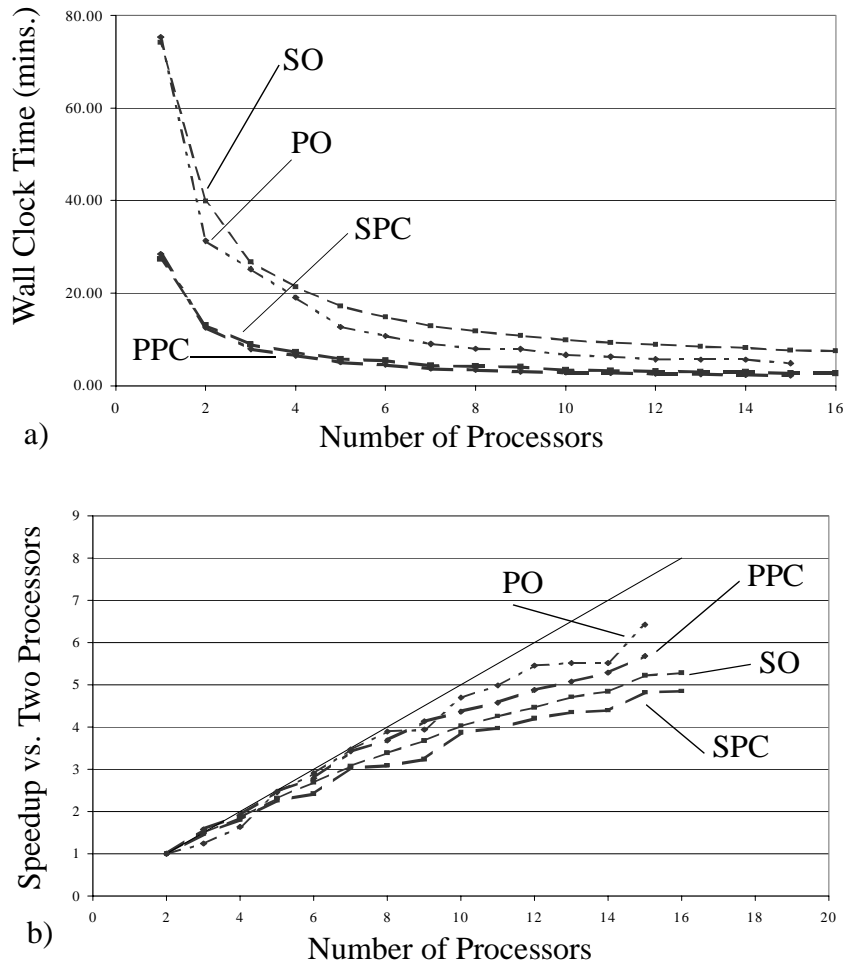
Figure 3.16 Benchmarking results for the Eastcoast scenario with a) showing the wall-clock time while b) shows the speed-up vs. two processors. (PO - original time-marching algorithm (Pentium), PPC - predictor-corrector time-marching algorithm (Pentium), SO - original time-marching algorithm (Sun) and SPC - predictor-corrector time-marching algorithm (Sun)). Solid line on b) indicates the theoretical speed-up (linear).

for the predictor-corrector algorithm.

- We also evaluated the Eastcoast domain (shown in Figure 3.16) with the combined parallel, predictor-corrector algorithm and observed similar behavior, e.g. an eight-fold increase in the maximum time step with both serial and parallel versions, good scaling, and lower wall-clock time for the

59

predictor-corrector algorithm.

Figure 3.17 shows the timing results for the second study, where the quarter annular
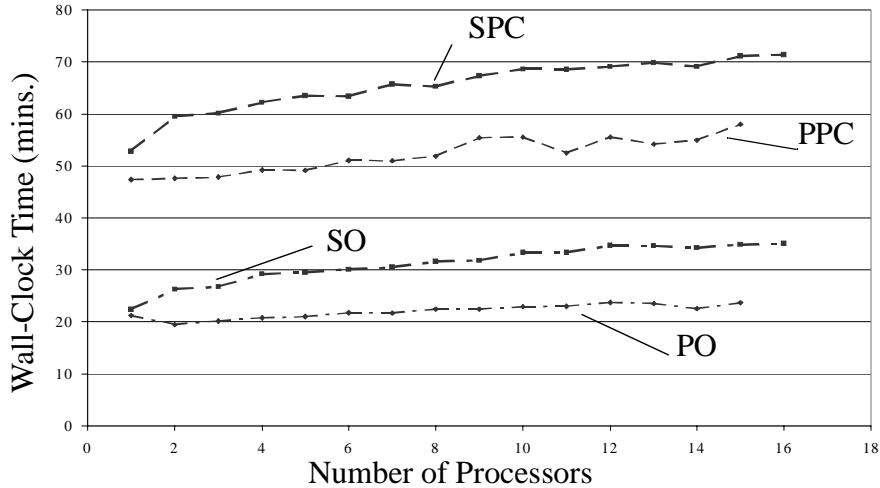
Figure 3.17 Benchmarking study results for the two time-marching
algorithms where the time step is constant between the two
algorithms in the quarter annular domain. (PO - original time-
marching algorithm (Pentium), PPC - predictor-corrector time-
marching algorithm (Pentium), SO - original time-marching
algorithm (Sun) and SPC - predictor-corrector time-marching
algorithm (Sun)).

domain is used and the average number of nodes per processor is held constant. Significant

differences in wall-clock time between the two algorithms exist because we use the same

time step for both algorithms (recall the predictor-corrector algorithm requires twice the

computation time per time step, thus causing the simulation to take approximately twice as

long). In this study, the wall-clock time should theoretically remain constant as the number

of processors increases because the average workload per processor remains constant.

Results indicate the Sun platform has a significant increase in the wall-clock time from one

to two processors, which does not occur for the Intel platform. This deviation from the

constant theoretical results indicates communication overhead is greater for the Sun

platform than for the Intel platform. For the Sun platform, wall-clock time continues to increase through the ten processor simulation, then levels out. For the Intel platform, the wall-clock times show less increase as the number of processors increases. Differences between the two platforms may be due to the communication configurations and MPI implementation.

Lastly, Figure 3.18 shows the results for the third study, where the quarter annular
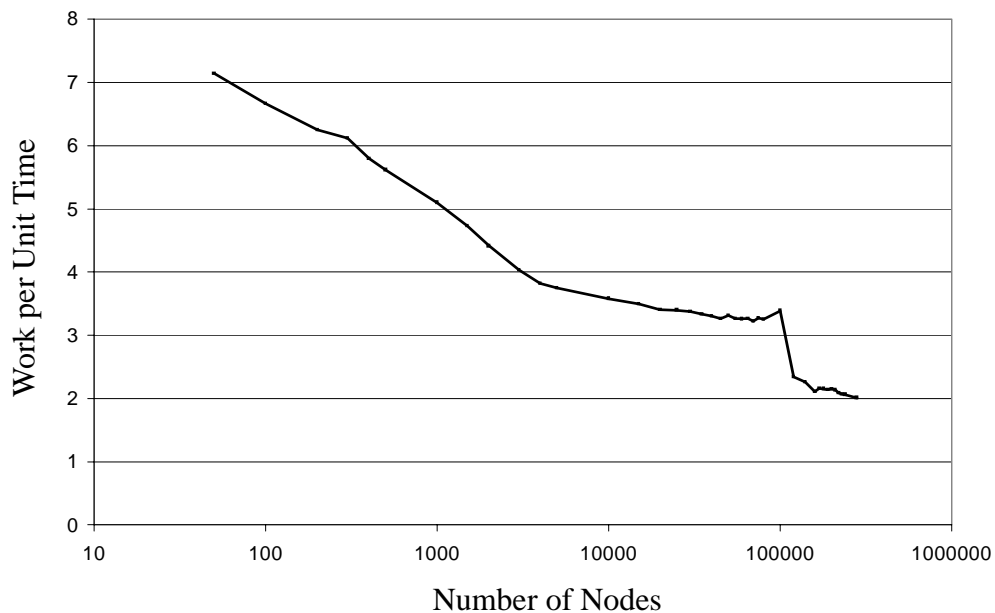
Figure 3.18 Benchmarking study results for the single processor experiment utilizing the original time-marching algorithm in the quarter annular domain on the Sun cluster.

domain is used, the number of nodes varies, but the study utilizes only one processor. For this study, the number of time steps in the simulation remains constant but the size of time step varies with the increasing number of nodes in order to maintain stability. Here, we are interested in determining the number of nodes that can be processed on one processor

without having to utilize swap memory. These experiments use the original algorithm, however, the predictor-corrector algorithm should provide similar results with a slight increase in the work per unit time (if analyzed with the same time step). Work per unit time is determined from calculating the total memory used for all the arrays for each grid and then dividing that total by the wall-clock time for each of grids. As shown in Figure 3.18, the results show a steady decrease in the work per unit time as the number of nodes increases with a sharp decline occurring near 100000 nodes mark. This indicates where the computer starts swapping information in and out of cache in order for one processor to be able to complete the simulation. Thus, for this cluster, the analysis indicates that we should decompose our big domains into enough subdomains so that we have less than 100000 nodes per processor in order to complete the simulation utilizing only cache memory. We would expect to see similar results for the Pentium platform since both machines have the same size cache.

3.6 Conclusions

In this chapter, we develop and analyze a predictor-corrector algorithm for 2D, GWC-based shallow water models. We quantify the effects of this new time-marching algorithm with respect to the stability and temporal accuracy (both globally and locally) for a wide variety of 2D domains and also looked at the influence of mesh generating techniques ($\lambda/\Delta x$ versus LTEA) on the results for the Gulf of Mexico domain. Lastly, we evaluate the computational performance of the combined parallel/predictor-corrector algorithm, as compared to the original algorithm. The hypothesis put forth in Kolar et al. [53] suggest that the stability constraint stems primarily from the explicit evaluation of

nonlinear terms. From the results presented in this chapter, it is evident that the stability

constraint relaxes with the implicit evaluation of the nonlinear terms, therefore confirming

this hypothesis. Other major findings from this 2D study are listed below.

- With all of the nonlinear terms treated implicitly, stability shows dramatic improvement, ranging from a minimum of a three-fold increase with the Gulf of Mexico domain ($\lambda/\Delta x$ resolution) to a maximum of an eight-fold increase with the Eastcoast domain. As mentioned earlier, for this algorithm to be considered cost-effective, we must obtain at least a 100% change between the two algorithms.

- Mesh generating techniques influence the allowable Courant number in the Gulf of Mexico. In particular, the LTEA mesh evens out the allowable Courant number over the shelf break region, which coincides with the area where the extra refinement occurs in this mesh.

- Resolution studies for the quarter annular domain show that the allowable Courant number with the original algorithm remains constant with increasing resolution; however, allowable Courant numbers increase with resolution for the predictor-corrector algorithm.

- From the G sensitivity study, we see that the G values that produce minimal mass balance errors and errors in the generation of the nonlinear constituents coincide with those that allow the maximum stable time step (i.e., $1 \le G/\tau_{max} \le 10$).

- Global temporal accuracy (convergence rate) studies show that the predictor-corrector algorithm reduces absolute error and increases the order

of accuracy from approximately first order to nearly second order.

- From the local temporal accuracy studies, we determined the predictor-corrector algorithm decreases errors by approximately two orders of magnitude, as compared to the original algorithm at the same time step.

- When evaluating the predictor-corrector algorithm with a time step that is at least twice that of the original algorithm, we found that the predictor-corrector algorithm still produces less error in most of the components (approximately 81%) than the original algorithm.

- Results from the combined parallel/predictor-corrector algorithm show that it significantly reduces simulation time as compared to the parallel algorithm that does not use predictor-corrector time marching. For example, suppose a scalar simulation of a hurricane storm surge application on the eastcoast of the United States using the original time marching algorithm takes approximately 80 hours to obtain results. The same simulation on an ideal 10-node cluster using the parallel algorithm and the original time marching algorithm would take approximately 8 hours to obtain results, but with the predictor-corrector time marching algorithm, we could obtain results on the same cluster in approximately 3 hours. Thus, the enhanced stability allows us to produce results more quickly for time-sensitive applications.

- For both computing platforms (Intel and Sun) the combined algorithm achieves nearly ideal speedup through six processors, with slight tapering-off as the number of processors is increased. More importantly, when the

workload per processor is kept nearly constant, the scaling at a higher number of processors is more ideal.

Chapter 4. Form of the Momentum Equation in ADCIRC[a]

4.1 Introduction

Shallow water equations are used to describe the hydrodynamic behavior of oceans, estuaries, coastal regions, lakes and impoundments. The depth-averaged versions of the conservation of mass and momentum form the basis of the shallow water equations in their native or primitive form. Early finite-element based shallow water models that utilized the primitive form of the shallow water equation suffered from stability problems due to spurious oscillations in the solutions. In 1979, Lynch and Gray [64] introduced the wave continuity equation (WCE), which eliminated the spurious oscillations in the solution without having to dampen the solution numerically or artificially. Kinnmark [48] determined in 1986 that there was no loss in the propagation characteristics of the wave continuity equation if a numerical parameter, G, was introduced, thus obtaining the generalized wave continuity (GWC) equation (see Section 4.2 and Chapter 2 for more details on the GWC).

Finite element shallow water models based on the GWC equation may be prone to errors in local mass conservation [1,48,51,52,54,65], as measured by direct integration of the continuity equation, also referred to in the literature as a "finite volume" approach.We

---

a. This chapter appears in an abbreviated form in *Advances in Water Resources*. The reference is given in Chapter 7, number [29].

acknowledge the recent work of Hughes et al. [44] and Berger et al. [8], who argue that continuous Galerkin finite elements are locally conservative, provided that the external flux is computed in a method consistent with the discretization, e.g., weighted residual boundary integral. A full comparison of the two approaches (finite volume vs. weighted residual) is beyond the scope of this dissertation, but our experience with the "consistent flux" approach of Hughes and Berger indicates it is not sensitive to grid resolution (mass balance error does not change with decreasing resolution). Hence, it does not provide a measure of solution accuracy. On the other hand, the finite volume approach can provide such information, which is an issue that we explore later in this chapter.

Keeping with the finite volume method of computing mass balance errors, we note that the errors are particularly large for highly nonlinear flows, which include shallow, converging sections around barrier islands and flood waves propagating onto dry land [51,54]. Kinnmark provided the first theoretical analysis of the mass conserving properties of the GWC equation [48]. The GWC equation, which is part of the class of derivative equations, allows for a larger solution space than does the primitive form of the equations. In order to restrict this solution space, Kinnmark determined that several auxiliary conditions must be met. He obtained the auxiliary conditions by determining the equivalence between the primitive form of the shallow water equations, including the conservative form of the momentum and continuity equations, and other formulations, such as the wave continuity equation. Kinnmark determined that the continuity equation, including its boundary conditions, must be exactly satisfied during spin-up (for most applications, the model is ramped up from at-rest conditions) in order for mass to be conserved. However, because of roundoff errors and other noise that occurs during spin-up

of a numerical model, this can not always be guaranteed. Supporting this observation were Walters and Carey, who hypothesized that the vanishing of the derivative of the continuity equation with respect to time alone is not sufficient to ensure that mass is conserved [82]. Because the first condition cannot be satisfied, Kinnmark investigated two other auxiliary conditions, of which one must be met. First, if the non-conservative momentum (NCM) equation is used, then $G > \nabla \bullet \mathbf{v}$ (where G is the GWC equation numerical parameter and $\mathbf{v}$ is the depth-averaged velocity field). In practice, because an upper bound exists on G above which spurious modes are generated, one cannot guarantee that this requirement is satisfied for a time-dependent velocity field. Second, if the conservative form of the momentum equation (CM) is used, then $G > 0$, which is a condition that can always be met [48].

Aldama et al. analyzed mass conservation of the GWC equation and NCM equation in their continuous and discrete forms, using both a Taylor-Frechet and Fourier series analysis [1]. In their analysis for the discrete form of the equations, they found that the GWC formulation is not consistent with the mass conservation principle, and the mass conservation error was proportional to e^{-Gt}. For a given time, as $G \rightarrow \infty$, the error approaches zero. A balance between the choice of G and the amount of residual error must be obtained, because, as $G \rightarrow \infty$, the GWC equation approaches the primitive form of the continuity equations and produces spurious oscillations.

In concurrent studies, Kolar et al. [51,52,54] examined the sensitivity of mass conservation to the G parameter and boundary conditions. In two of these studies, they determined that implementing mass conserving boundary conditions improves global mass balance errors without increasing G and improves local mass balance errors with a lesser

values of G [51,52]. Also, Lynch and Holboke analyzed the mass conservation boundary conditions in a 3D framework and determined the boundary conditions could be implemented differently to improve the global mass conservation; however, local mass conservation was not analyzed [65].

In another study, Kolar et al. also examined recasting the advective term in the GWC equation into non-conservative form so that it mimics the formulation of the NCM equation [54]. They found that the global mass conservation is improved; however, local mass conservation errors persisted. In summary, they recommended that GWC models match the form of the advective terms and that the ratio of G/τ_{max} is: $1 \leq G/\tau_{max} \leq 10$, where τ is the bottom friction coefficient as determined from a quadratic friction law:

$$\tau = C_f \frac{\sqrt{(u^2 + v^2)}}{H} \tag{4.1}$$

and τ_{max} is the largest magnitude of τ over the spatial domain. In Equation (4.1), u and v are depth-averaged velocities, H is the total water depth, and C_f is the bottom friction parameter. When the ratio falls within this range, the nonlinear constituent errors and the global and local mass balance errors are both minimized without introducing spurious modes [54].

Several studies examined the relationship between the meshing criteria and convergence [11,39,40,61]. In particular, Hagen et al. [39,40] developed a meshing technique that examines the local truncation error associated with the linearized form of the NCM equation. This study showed that refinement in areas where truncation error is large (e.g., in areas where steep bathymetry gradients occur) and coarsening in areas where

truncation error is small, improves the overall accuracy of the solution without increasing the computational burden. These areas correspond to where the velocity-based NCM solution changes rapidly.

From the literature cited above, we observe the following about NCM-based GWC equation models: 1) local mass balance errors (as measured by direct integration of the continuity equation) and instabilities can occur, particularly in regions with highly nonlinear flows; 2) numerical and analytical studies demonstrate that the problem can be lessened, but not eliminated, by proper choice of G, by reformulating the advective terms, and by proper treatment of the boundary conditions; and 3) high levels of grid refinement are needed in areas with steep bathymetry gradients to minimize truncation errors. Based on these observations, we hypothesize that changing to the conservative form of the momentum equation, which is flux-based and not velocity-based, will improve both global and local mass conservation, eliminate the need to reformulate the advective term between the governing equations, and lessen the need for extensive refinement in areas with steep bathymetry gradients due to flux varying more slowly than velocity in these regions. Also, use of the conservative form of the momentum equation makes it more natural to bring in flux boundary conditions and facilitates coupled models (e.g., discontinuous and continuous Galerkin methods [26,27]). Thus, the primary objective of this chapter is to assess the impact of the conservative form of the momentum equation on mass conservation, stability, temporal and spatial accuracy for GWC-based finite element models. Numerical simulations will be conducted with the ADCIRC (ADvanced CIRCulation model [59]) family of models. In this chapter, some assessments utilize a combined predictor-corrector (see Chapter 3)/conservative momentum code in the

evaluation.

4.2 Background

Testing of the conservative form of the momentum equation (CM) was done with both the 1D and 2D version of ADCIRC. If the operator L represents the primitive continuity equation and $\mathbf{M}^c$ the conservative form of the momentum equation, then the GWC equation is obtained from the following operation.

$$W^G \equiv \frac{\partial L}{\partial t} + GL - \nabla \bullet \mathbf{M}^c = 0 \tag{4.2}$$

In Equation (4.2) G controls the relative weight of the primitive continuity equation, such that if $G \to 0$, the equation becomes a pure wave continuity equation, whereas if $G \to \infty$, the equation is a pure primitive continuity equation.

In the 1D, we neglect atmospheric and tidal potential forcings and assume the eddy viscosity is constant; the standard form of the ADCIRC model equations (GWC, NCM and CM, Equations (4.3), (4.4) and (4.5), respectively) are as follows:

$$W^G \equiv \frac{\partial^2 \zeta}{\partial t^2} + G\frac{\partial \zeta}{\partial t} - q\frac{\partial G}{\partial x} - \frac{\partial}{\partial x}\left[\frac{\partial(qu)}{\partial x} + (G-\tau)q + gH\frac{\partial \zeta}{\partial x} - \varepsilon\left(\frac{\partial^2 q}{\partial x^2}\right) \right] = 0 \tag{4.3}$$

$$\mathbf{M} \equiv \frac{\partial(u)}{\partial t} + u\frac{\partial(u)}{\partial x} + \tau u + g\frac{\partial \zeta}{\partial x} - \frac{\varepsilon}{H}\left(\frac{\partial^2 q}{\partial x^2}\right) = 0 \tag{4.4}$$

$$\mathbf{M}^c \equiv \frac{\partial(q)}{\partial t} + \frac{\partial(qu)}{\partial x} + \tau q + gH\frac{\partial \zeta}{\partial x} - \varepsilon\left(\frac{\partial^2 q}{\partial x^2}\right) = 0 \tag{4.5}$$

where $q = Hu$ is the depth-averaged flux, u is the depth-averaged velocity, τ is determined

from the following $\tau = C_f(|u|/H)$, ε is the eddy viscosity, t is time, ζ is the elevation of the water surface above the datum, x is the distance, G is the GWC numerical parameter and $H = h + \zeta$ is total water column depth.

In the 1D studies with the GWC-NCM model, the advective terms in the GWC equation takes on two different forms, consistent or inconsistent. The inconsistent form develops from Equations (4.3) and (4.4) because the advective term in the GWC equation is in conservative form and the advective term in the NCM equation is in non-conservative form. In the consistent formulation, the advective term in the GWC equation is altered to the non-conservative form (as reported in [54]) by introducing the primitive continuity equation so that a second-order space derivative is replaced by a mixed space and time derivative.

Equations for the 2D ADCIRC model (GWC, NCM and CM, Equations (4.6), (4.7) and (4.8), respectively) with a constant eddy viscosity are as follows:

$$W^G \equiv \frac{\partial^2 \zeta}{\partial t^2} + G\frac{\partial \zeta}{\partial t} - \mathbf{q}\nabla\bullet(G) - \nabla\bullet[\nabla\bullet(\mathbf{qv}) + \mathbf{f}\times\mathbf{q} + (G-\tau)\mathbf{q} + H\nabla\left[\frac{p_a}{\rho} + g(\zeta - \alpha\eta)\right] -$$

$$\mathbf{A} - \varepsilon(\nabla^2(\mathbf{q}))\,] \ = \ 0 \tag{4.6}$$

$$\mathbf{M} \equiv \frac{\partial(\mathbf{v})}{\partial t} + \mathbf{v}\nabla\bullet(\mathbf{v}) + \tau\mathbf{v} + \mathbf{f}\times\mathbf{v} + \nabla\left[\frac{p_a}{\rho} + g(\zeta - \alpha\eta)\right] - \frac{\mathbf{A}}{H} - \frac{\varepsilon}{H}(\nabla^2(H\mathbf{v})) = 0 \tag{4.7}$$

$$\mathbf{M}^c \equiv \frac{\partial(\mathbf{q})}{\partial t} + \nabla\bullet(\mathbf{qv}) + \tau\mathbf{q} + \mathbf{f}\times\mathbf{q} + H\nabla\left[\frac{p_a}{\rho} + g(\zeta - \alpha\eta)\right] - \mathbf{A} - \varepsilon(\nabla^2(\mathbf{q})) = 0 \tag{4.8}$$

New terms in these equations are as follows: $\mathbf{q} = H\mathbf{v}$ is the depth-averaged flux, $\mathbf{v}$ is the depth-averaged velocity, $\mathbf{f}$ is the Coriolis parameter, given by $2\Omega\sin\phi$, Ω is the angular velocity of the earth and ϕ is latitude, g is gravity, α is the Earth elasticity factor, $\mathbf{A}$ is the

wind stress on the water surface, η is the Newtonian equilibrium tidal potential, ρ is density, and p_a is barometric pressure.

In ADCIRC, linear finite elements are used for the spatial discretization, while for the temporal discretization, a three time-level scheme centered at k is used in Equations (4.3) and (4.6), and a two time-level scheme centered at $k + 1/2$ is used in Equations (4.4), (4.5), (4.7) and (4.8). Flux-based (CM equation) solutions are obtained by first solving Equations (4.3) or (4.6) for the elevation changes and then using Equations (4.5) or (4.8), depending on 1D or 2D; in either case, new velocity values are obtained by dividing the nodal flux by the total water depth at that point. Velocity-based (NCM equation) solutions substitute Equation (4.4) for (4.5) and Equation (4.7) for (4.8). Ocean boundaries are treated as essential conditions in the continuity equation, while flux boundaries are treated as natural in the continuity equation and essential in the momentum equation. This implementation is often referred to as "conventional" treatment. In order to keep the focus on the form of the momentum equation, we did not examine alternative treatments of the boundary conditions.

4.3 Procedures

4.3.1 Mass Conservation

In order to evaluate the changes to mass balance errors (see second paragraph in Section 4.1), we compared the accumulation of mass to the net flux of the mass leaving the element or domain by directly integrating the primitive continuity equation, which is similar to studies by Kolar and others [54]. For completeness, we summarize their algorithm and provide a modified algorithm suitable for use with the CM equation.

First, the primitive continuity is integrated over space and time to obtain

$$\int_{t_0}^{t}\int_{\Omega}\left[\frac{\partial \zeta}{\partial t}+\nabla\bullet(H\mathbf{v})\right]d\Omega dt = 0 \tag{4.9}$$

Next, the first term in Equation (4.9) is integrated over time and the divergence theorem is applied to the second term to obtain

$$\int_{\Omega}(\zeta_t - \zeta_{t_0})d\Omega + \int_{t_0}^{t}\left[\int_{\Omega}H\mathbf{v}\cdot\mathbf{n}d(\partial\Omega)\right]dt = 0 \tag{4.10}$$

Next, the dependent variables in Equation (4.10) were evaluated by approximating with linear basis functions to obtain

$$\int_{\Omega}(\zeta_t - \zeta_{t_0})d\Omega = \sum_{e}[\bar{\zeta}_t - \bar{\zeta}_{t_0}]_e A_e \tag{4.11}$$

where A_e is the area of the element, $\bar{\zeta}$ is the arithmetic average of the nodal values of ζ over the element, and the sum is over all elements in the domain of interest. Next evaluate the boundary integral in Equation (4.10), which represents the net flux into the domain when $\mathbf{n}$ is taken as the unit outward normal. When expanding H and $\mathbf{v}$ in terms of their linear basis functions, they can be evaluated exactly for linear triangular elements as follows

$$Q^{net} \equiv \int_{\Omega}H\mathbf{v}\cdot\mathbf{n}d(\partial\Omega) = \sum_{e_b}\frac{w_e}{6}[2H_1 v_{n1} + H_1 v_{n2} + H_2 v_{n1} + 2H_2 v_{n2}] \tag{4.12}$$

where w_e is the length of the boundary segment of element e_b, $v_n = \mathbf{v}\cdot\mathbf{n}$, the sum is over

all elements on the boundary, and subscripts 1 and 2 refer to the nodes (numbered locally) at the end of the boundary segment. Now the time integral of Q^{net} is approximated using the trapezoidal rule, i.e,

$$\int_{t_0}^{t}\left[\int_{\Omega} H\mathbf{v}\cdot\mathbf{n}d(\partial\Omega)\right]dt = \int_{t_0}^{t} Q^{net}dt \approx \sum_{k}\frac{1}{2}[Q_{t_0}^{net} + Q_{t}^{net}]\Delta t \qquad \textbf{(4.13)}$$

where k is the time-step index. This formation is used to evaluate the original algorithm, which uses the non-conservative momentum equation.

For the new algorithm based on the conservative momentum equation, we evaluate Equation (4.10) again and replaced the $H\mathbf{v}$ term with the $\mathbf{q}$ flux term, which is the natural dependent variable. All terms remain the same except Equation (4.14) replaces Equation (4.12).

$$Q^{net} = \int_{\Omega}\mathbf{q}\cdot\mathbf{n}d(\partial\Omega) = \sum_{e_b}\frac{w_e}{2}[q_{n_1} + q_{n_2}] \qquad \textbf{(4.14)}$$

where w_e is the length of the boundary segment of element e_b, $q_n = \mathbf{q}\cdot\mathbf{n}$, the sum is over all elements on the boundary, and subscripts 1 and 2 refer to the nodes (numbered locally) at the end of the boundary segment.

In this chapter, we present the mass balance errors as the average absolute error over the simulation time. We average these errors over time for both the local and global results and plot these errors on a log scale. The derivation given above is in 2D, however we can evaluate the 1D results in a similar fashion because the flux at the boundary reduces to a point evaluation, and the accumulation calculations in Equation (4.11) are evaluated on a

length basis. As noted in Section 4.1, we are purposely using the finite volume approach of checking mass balance because of the diagnostics it provides (see Section 4.4.6).

4.3.2 Stability

To evaluate stability heuristically, we obtain the maximum stable time step from the following procedures: 1) Find the maximum allowable time step with the NCM equation to the nearest five seconds; 2) Find the maximum allowable time step with the CM equation to the nearest five seconds; 3) Compare the results from both equations and determine the percent change between the two results.

4.3.3 Accuracy

4.3.3a Analytical

By using the Taylor Series expansion, we can expand the dependent variables of the discrete equations around a common point to evaluate them on a theoretical basis and to determine the accuracy of the equations. The full equations are given in Appendix 3. From these truncation errors, we determined that the GWC equation is first-order accurate in time if the advective terms are in non-conservative form, while it is second-order accurate in time if the advective terms are in conservative form. In space, the GWC equation is first-order accurate for variable spacing; while, it is second-order accurate for constant spacing. For the NCM and CM equations, we found that they are first-order accurate in time and space if we use variable spacing while it is second-order accurate in space if we use constant spacing. Also, both momentum equations become second-order accurate in time if the equations are linearized.

4.3.3b Numerical

Temporal

Numerically, temporal accuracy is determined by comparing a coarse solution using a larger time step to a 'true' solution, i.e., one based on a fine time step. For the true solutions, we used a one second time step for the 1D experiments, while a ten second time step was used in the 2D experiments. These were chosen based on previous temporal accuracy experiments that evaluated a new time-marching algorithm, described in Chapter 3 and in [30,33]. Changes in the temporal accuracy are then quantified by evaluating the error vs. step size, as measured by both the L_2 norm and L_∞ norm. An L_2 norm evaluates the errors over several discrete times during the simulation and averages the error, while an L_∞ norm looks at the error over several discrete times during a simulation and finds the maximum error.

Spatial

Global Spatial Accuracy

Numerically, the "true solutions" for the 1D experiments were chosen by performing a grid convergence test where refinement of the grid occurred until a chosen convergence criterion (errors on the order of 10^{-6} m or m/s) was met. We then compared fine and coarse grid results to measure the errors, as expressed by L_2 norm and L_∞ norm. For the L_2 errors, we averaged these errors over time to provide one point value for every grid resolution studied.

Local Spatial Accuracy

For 1D, we utilized the same grid convergence procedures outlined under global

accuracy to establish the "true solution". We then compared fine and coarse grid results to measure the errors, as expressed by the average nodal error over the number of tidal cycles. In this case, the errors are averaged over time but not over space, so the results are shown on a nodal basis. For the 2D spatial accuracy experiments, CAFE (Cumulative Area Fraction Error) [61] plots provide the information on local accuracy changes. CAFE plots produce absolute and relative errors between two simulations of the same domains with the same temporal resolution, but different spatial resolutions. A discussion of the CAFE plots and how to read them can be found in reference [30,40] and the previous chapter. To develop CAFE plots for this study, we used the following steps: 1) Harmonic data is recorded for the NCM equation over several tidal cycles for both a coarse and fine spatial resolution; 2) Harmonic data is recorded for the CM equation over several tidal cycles for both a coarse and fine spatial resolution; 3) Absolute and relative errors are calculated for each equation; 4) Cumulative errors for both equations are computed; and 5) Results are plotted on the same graph to determine the percent area exceeding a certain criteria for convergence.

4.4 One-Dimensional Numerical Experiments

4.4.1 Domains Evaluated

Four 1D domains were used to evaluate the effects of the conservative form of the momentum equation (CM equation): a constant bathymetry of 5 m (Figure 4.1a); a parabolic bathymetry (Figure 4.1b, also denoted "quadratic"), which has a rate of rise that varies as a second-order polynomial; the Western North Atlantic bathymetry (Figure 4.1c, also denoted "eastcoast"), which is a 1D slice of the eastern United States seaboard out into
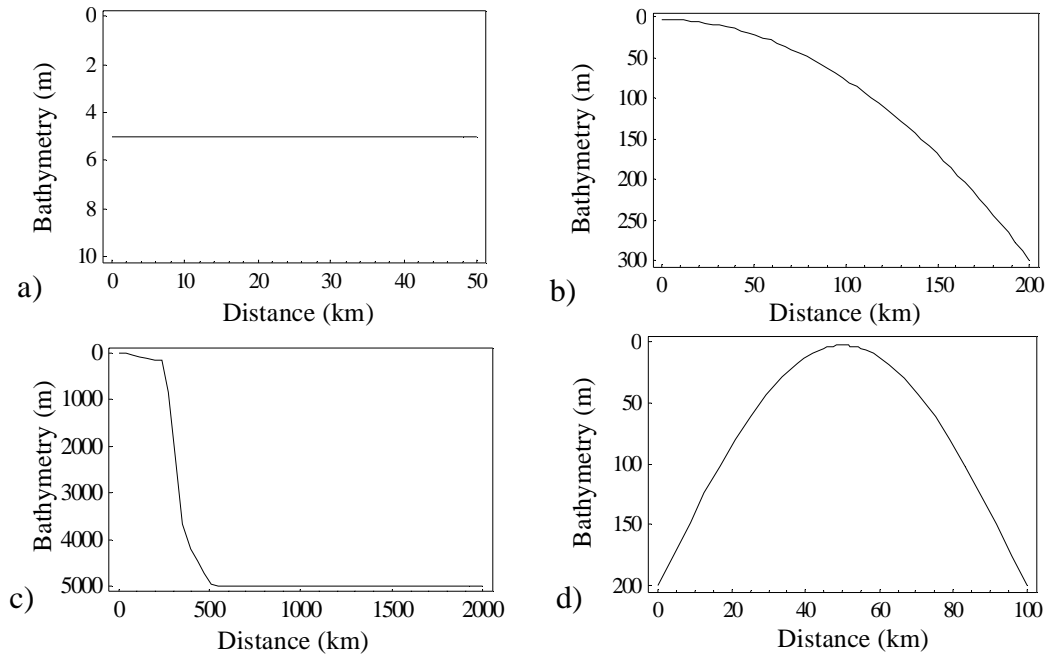
Figure 4.1 Schematics of the 1D domains. a - constant, b - quadratic, c - eastcoast and d - sinusoidal.

the Atlantic Ocean; and a sinusoidal varying bathymetry (Figure 4.1d, also denoted "sinusoidal"). The sinusoidal bathymetry induces diverging and converging flow fields in a 1D setting. Each of the domains use the following simulation conditions: an eddy visocity parameter of zero, a 1-meter M_2 tidal forcing at the ocean boundary (a forcing that we have found through experience to produce critical responses in the system), and no normal flux at the land boundary. Maximum and minimum bathymetry values for the parabolic domain are 300 and 3 meters, respectively; for the Western North Atlantic, the maximum and minimum bathymetry values are 5000 and 20 meters, respectively; for the sinusoidal domain, the maximum and minimum bathymetry values are 200 and 2.5 meters, respectively, with the minimum depth occurring in the center of the domain. Discussion of the grid generation techniques can be found in Chapter 2. In the following 1D experiments, the bottom friction parameter varies from a constant value of 0.0001 sec^{-1}, which was used

for the constant, quadratic and eastcoast domains, to a variable value used for the sinusoidal domain where the coefficient of the equation is 0.003. The eddy viscosity parameter, ε, remains zero and the numerical parameter of the GWC equation is $G = 0.001 \ \text{sec}^{-1}$ throughout all of these experiments.

A summary of the meshing criteria for all the 1D numerical experiments is provided in Table 4.1. For each of the 1D experiments, we indicate the nodal spacing technique used and the meshing criteria, which is either the number of nodes for constant nodal spacing or the $\lambda / \Delta x$ ratio for variable nodal spacing. Multiple values are included when the experiment called for multiple grids, such as an analysis of spatial accuracy.

4.4.2 Mass Conservation

We first investigated the impacts of the CM equation on mass conservation, an issue that has been noted to plague nonlinear applications when measured using a finite volume approach [1,48,51,52,54,65] (also see second paragraph in Section 4.1). Experiments in this section utilize the procedures presented in Section 4.3.1. In the studies herein, we computed mass conservation errors for the NCM equation using the following formulations: 1) the inconsistent form of the advective terms, which means that both the GWC equation advective terms are in conservative form and the NCM advective terms are in non-conservative form; and 2) the consistent form of the advective terms, which means the GWC equation and NCM advective terms are in the non-conservative form (requires manipulation of the GWC equation, as reported in [54]). We evaluated the errors in global and local mass conservation for six M_2 tidal cycles for all domains utilizing a 5-second time step.

Table 4.1 Meshing criteria for the 1D numerical experiments.

		Numerical Experiments				
		Mass Conservation		Spatial Accuracy		Stability
Domains	Spacing Criteria	Global	Local	Global	Local	
Constant	Constant[a]	51	NA[b]	NA	NA	51
Quadratic	Constant	201	76[c]	varies- 11 to 1001	NA	201
Quadratic	Variable[d]	300	300	varies - 25 to 5000	NA	300
Eastcoast	Constant	201	101	varies - 11 to 2001	101, 201, 401, 801	201
Eastcoast	Variable	300	300	varies - 25 to 5000	300, 1200, 5000	300
Eastcoast	LTEA	NA	46	NA	46	NA
Sinusoidal	Constant	100	41	varies - 11 to 1001	NA	43
Sinusoidal	Variable	300	300	varies - 100 to 10000	300, 1000, 5000	300

a. Number of nodes is given for constant spacing.
b. NA - experiments were not performed with this domain and nodal spacing.
c. Chosen to have approximately same # of nodes as the variable spacing criteria.
d. The $\lambda/\Delta x$ ratio is given for variable spacing.

4.4.2a Global Mass Conservation

Figure 4.2 presents the absolute average error in the global mass balance for the NCM and CM equations for all domains, using two types of meshing, constant (C) and variable (V). All parameter values are the same within each domain.Results show that

Global mass error (10^4 m^3)

1
0.1
0.01
0.001

Const-C   Quad-C   Quad-V   EC-C   EC-V   Sin-C   Sin-V

Domains

Domain Name
Abbreviations:
Const- constant
Quad- quadratic
EC - eastcoast
Sin- sinusoidal
Nodal Spacing:
C- constant
V- variable
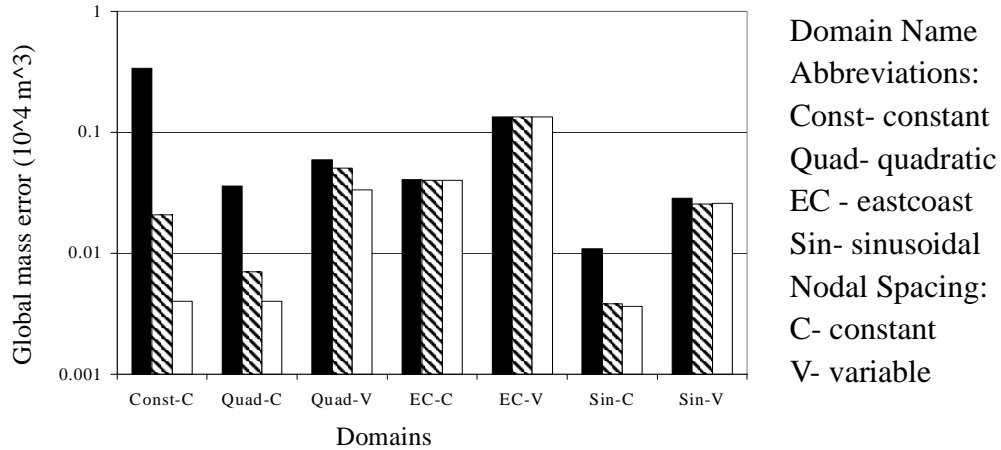
Figure 4.2   Errors in the global mass conservation for all the domains; NCM equation
- no changes to GWC advective formulation (filled bars), NCM equation
- changes to GWC advective formulation (striped bars), CM equation
(open bars).

adopting the CM equation improves global mass balance in most of the domains.

Improvement in the global mass balance errors for the CM algorithm is less evident with

the variable nodal spacing than with the constant nodal spacing (for a given domain); the

latter shows up to two orders of magnitude improvement, except for the eastcoast domain.

The behavior of the eastcoast results can be explained by noting the large percentage of the

domain with deep bathymetry where the nonlinear terms are not significant, thus the form

of the advective terms is insignificant. (We will further explore this issue in Section 4.4.6.)

A consistent treatment of the advective terms (striped bars) partially offsets the mass

balance improvement realized by the CM equation, thus indicating that both the form of the

advective terms and the choice of dependent variable plays a role. This is also explored

further in Section 4.4.6.

4.4.2b Local Mass Conservation

For local mass conservation, we looked at three domains with steep bathymetry

gradients: the quadratic (Figure 4.1b), the eastcoast (Figure 4.1c) and the sinusoidal (Figure

4.1d). All three cases use both constant and variable nodal spacing. Results using the

variable nodal spacing are shown in Figure 4.3, while Figure 4.4 shows results using the

constant nodal spacing. A schematic of the bathymetry for each domain is also shown by
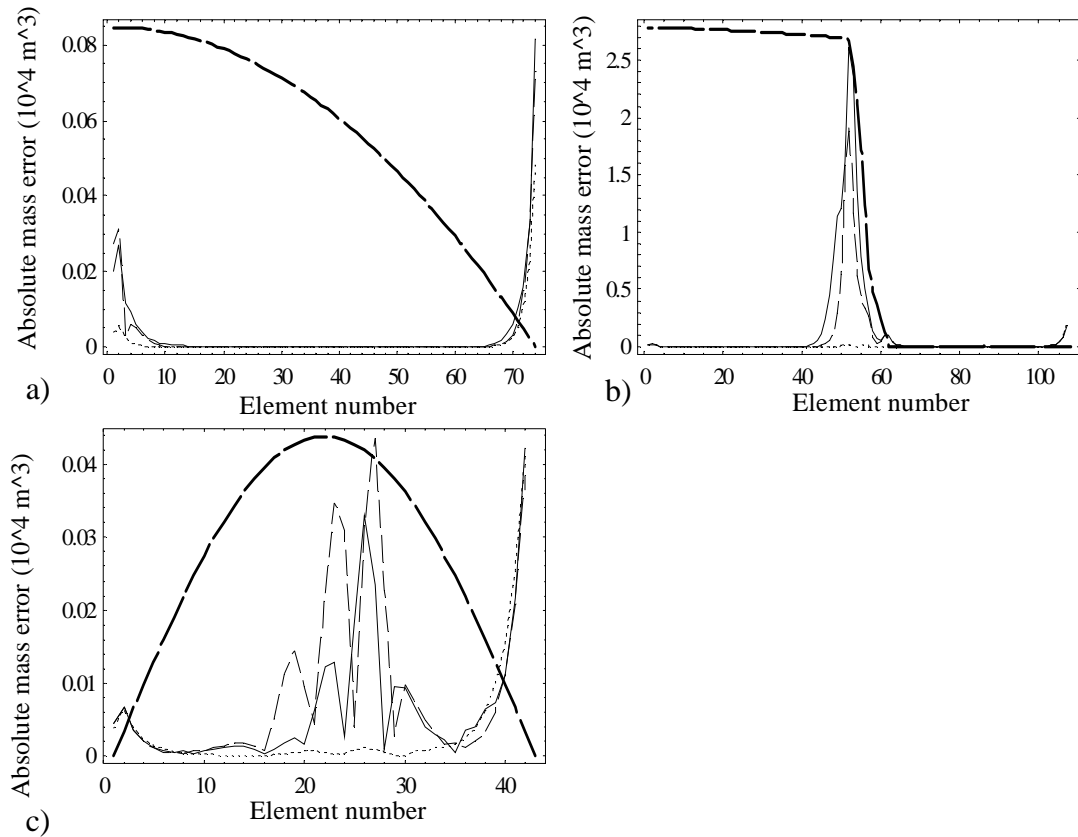
Figure 4.3 Local mass conservation results for two formulations of the momentum
equation using variable spacing for a) quadratic, b) eastcoast, c)
sinusoidal. (Longer dashes - bathymetry (not to scale), Solid line - NCM
(no changes to the GWC advective formulation), medium dashes -
NCM (changes to the GWC advective formulation) and short dashes -
CM).

the longer dashed line in the figures. In these experiments, we evaluated local mass balance

errors for the NCM equation with two forms of the GWC advective terms; the inconsistent

form and the consistent (see Section 4.2). As can be seen, the CM formulation provides a

significant error reduction in areas where there is a steep bathymetry gradient. In contrast,

we find that the NCM results show large local mass balance errors where a steep
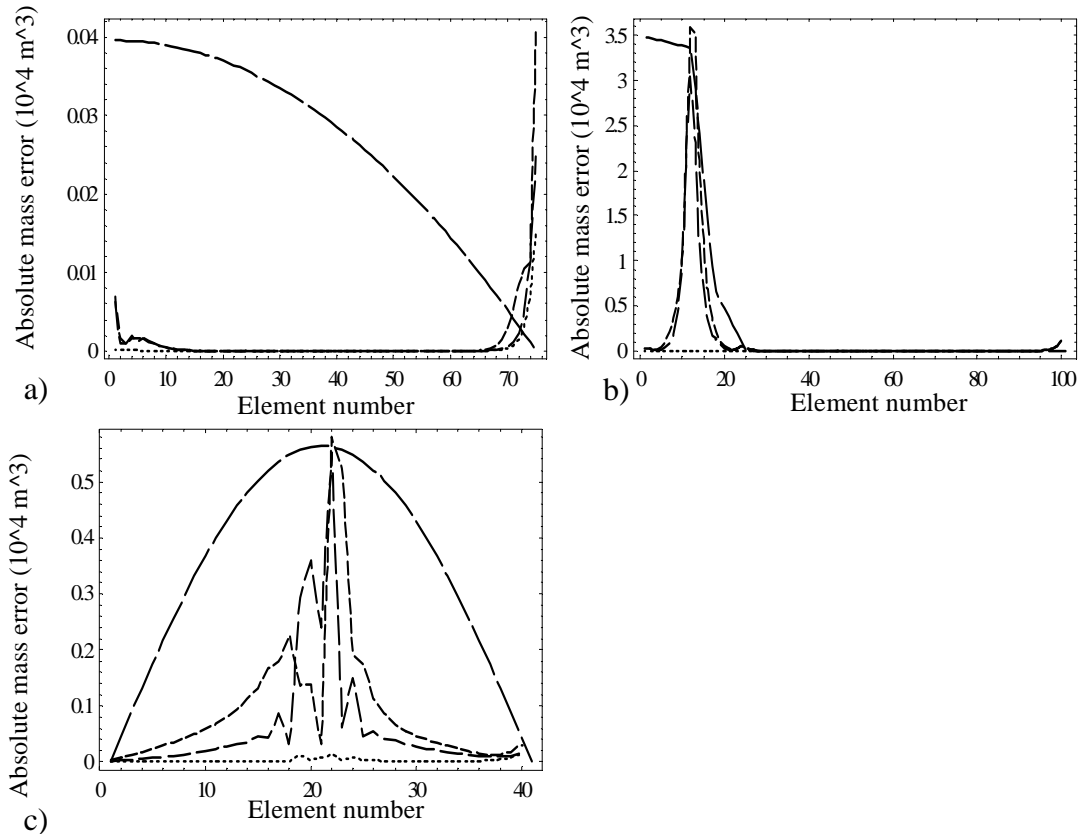
Figure 4.4 Local mass conservation results for two formulations of the momentum equation using constant spacing for a) quadratic, b) eastcoast, c) sinusoidal. (Longer dashes - bathymetry (not to scale), Solid line - NCM (no changes to the GWC advective formulation), medium dashes - NCM (changes to the GWC advective formulation) and short dashes - CM).

bathymetry gradient occurs, regardless of the treatment of the advective terms. For the eastcoast domain, we determined from numerical experiments that the grid spacing for the NCM simulation would have to be decreased by a factor of 20 (consistent advective terms) or 115 (inconsistent advective terms) in order to have the same level of local mass balance error as the CM equation.

In Figure 4.3, note that the open boundary (element 74 in Figure 4.3a, 107 in Figure 4.3b, 40 in Figure 4.3c) shows larger local mass balance errors than the land boundary, which corresponds to earlier findings for "conventional" treatment of boundary conditions

[54]. As mentioned, because this chapter focuses on the form of the momentum equation, we did not revisit the boundary condition issue. Also, note that for the quadratic bathymetry, we observed a decrease in the local mass errors at the land boundary for the CM equation as compared to the NCM equation. Overall, the CM equation improves the local mass balance errors in the domains evaluated, with the greatest gains seen in areas of steep bathymetry changes, which correspond to areas where the nonlinear terms are dominant.

We also examined the influence of type of spatial discretization (constant vs. variable node spacing) on local mass conservation. Similar results as shown in Figure 4.3 were found for constant nodal spacing (results shown in Figure 4.4) using approximately the same number of nodes, but with higher differences between the local mass balance errors for the two forms of the momentum equations. For example in the eastcoast domain, the errors increased by approximately 30% for the NCM equation in the area of the steep bathymetry change. In all cases, the local mass balance errors for the CM equation are much less than the local mass balance errors for NCM equation.

4.4.3 Stability

Several numerical experiments were set up to examine the impact of the CM equation on stability, following the procedures discussed in Section 4.3.2. In all of the domains evaluated, results show no significant change in stability between the two algorithms, thus indicating that the CM equation does not influence stability. Similar results were found when comparing the two predictor-corrector time-marching versions.

4.4.4 Accuracy

4.4.4a Temporal Accuracy

We evaluated the CM algorithm's impact on temporal accuracy following the procedures presented in Section 4.3.3. To quantify temporal accuracy, we recorded 50 discrete times over two complete M_2 tidal cycles for all four domains with the following parameters: the constant bathymetry domain used a constant nodal spacing (51 nodes) and the time step ranged from 1 to 100 sec with the original time-marching algorithm and 1 to 50 sec with the predictor-corrector time-marching algorithm; the quadratic domain used variable nodal spacing with $\lambda/\Delta x = 300$ and the time step ranged from 1 to 80 sec with the original time-marching algorithm and 1 to 400 sec with the predictor-corrector time-marching algorithm; the eastcoast domain also used variable node spacing with $\lambda/\Delta x = 300$ and the time step ranged from 1 to 125 sec with the original time-marching algorithm and 1 to 1000 sec with the predictor-corrector time-marching algorithm; and the sinusoidal domain used variable node spacing with $\lambda/\Delta x = 300$ and the time step ranged from 1 to 125 sec with the original time-marching algorithm and 1 to 250 sec with the predictor-corrector time-marching algorithm. In these experiments, the bottom friction parameter varies from a constant value of 0.0001 sec^{-1}, which was used for the constant, quadratic and eastcoast domains, to a variable value used for the sinusoidal domain where the coefficient of the equation is 0.003. Results of these accuracy studies are shown in Figure 4.5 for the original time-marching algorithm; while, Figure 4.6 shows results for the predictor-corrector time-marching algorithm described in Chapter 3.

In Figure 4.5, results show that the NCM equation has a slightly lower absolute
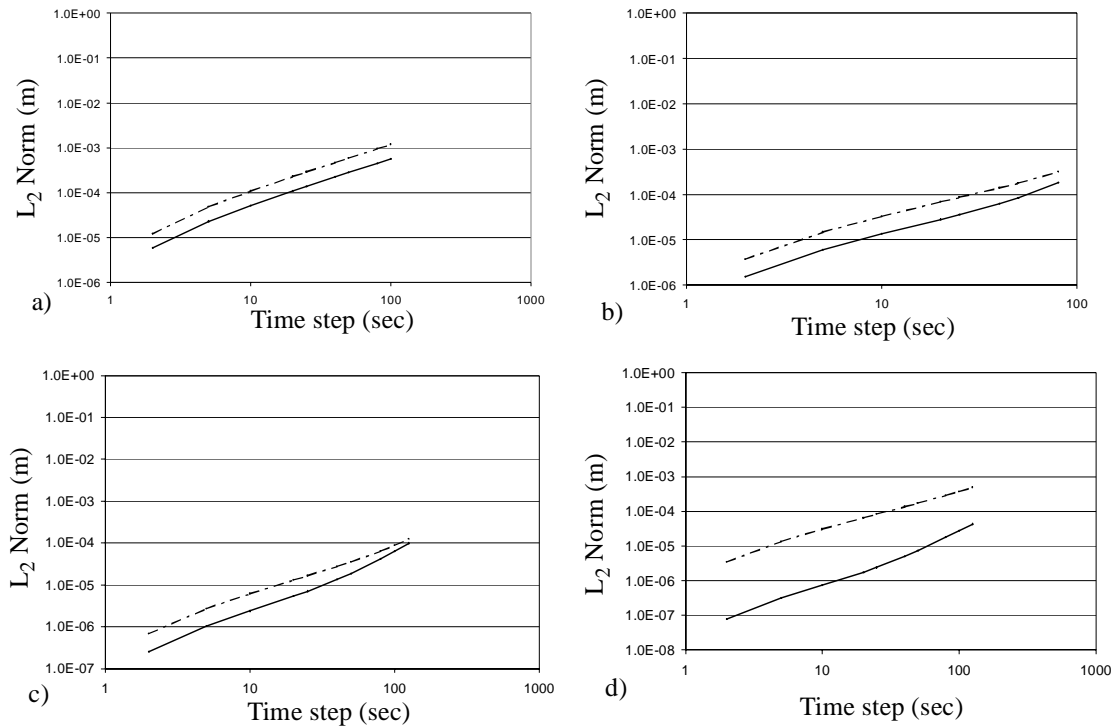
Figure 4.5 Temporal accuracy results (elevation) for all four domains using the original time-marching algorithm: a) constant (constant), b) quadratic (variable), c) eastcoast (variable) and d) sinusoidal (variable). Solid line - NCM, Dot-dash - CM. (Note: first three results use a constant bottom friction while the last result uses a variable bottom friction.)

Table 4.2 Convergence rates for the 1D temporal accuracy.

	original time marching algorithm		predictor-corrector time marching algorithm	
	NCM	CM	NCM	CM
constant bathymetry	1.14	1.14	1.53	2.06
quadratic bathymetry	1.23	1.17	1.81	1.96
eastcoast bathymetry	1.39	1.21	1.83	2.02
sinusoidal bathymetry	1.49	1.17	1.73	1.10
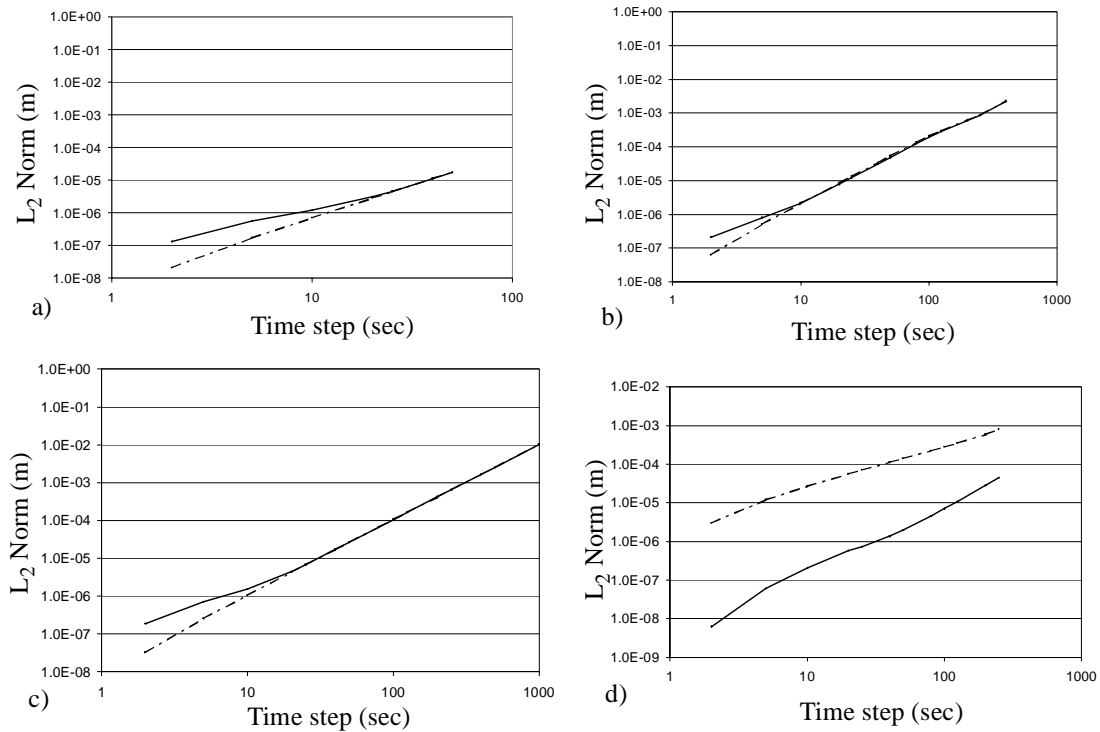
Figure 4.6 Temporal accuracy results (elevation) for all four domains using the predictor-corrector algorithm: a) constant (constant), b) quadratic (variable), c) eastcoast (variable) and d) sinusoidal (variable). Solid line - NCM, Dot-dash - CM. (Note: first three results use a constant bottom friction while the last result uses a variable bottom friction.)

error in all the domains than the CM equation. We determined the order of accuracy or convergence rate for the original time-marching algorithm via a least squares fit to the data. Results, shown in Table 4.2, show that the results are similar for the constant, quadratic and eastcoast domains while they are different sinusoidal domain. The results in Figure 4.6 indicate that for three of the domains the NCM equation and CM equation have the same errors at the larger time steps; while, at smaller time steps the CM equation produces lower absolute error than the NCM equation. The convergence rates for these domains are given in Table 4.2, which shows that the CM equation provides higher convergence rates than the NCM equation except for the sinusoidal domain; of the first three, the rates are

approximately second order. In the sinusoidal domain, the results indicated that a higher absolute error is present in the CM equation than in the NCM equation results, with the convergence rates showing that the CM equation is first order accurate while the NCM equation is almost second order accurate. Note that these results are only for the elevation changes; however, velocity and L_∞ norm results show similar trends. Therefore, the different form of the momentum equation does not significantly influence the convergence rates for the temporal accuracy whether using the original or the predictor-corrector time-marching algorithms, except for the sinusoidal domain. This is also evident in the Taylor Series expansions of the discrete equations (given in Appendix 3), in which both momentum equations are first order accurate in time for nonlinear problems.

4.4.4b Spatial Accuracy

Global Spatial Accuracy

We evaluated the CM algorithm's impact on global spatial accuracy following the procedures presented in Section 4.3.3. For the 1D experiments, we looked at two techniques of obtaining the "true solution", one based on the $\lambda/\Delta x$ ratio and one based on successively refining Δx on a uniform mesh by a factor of two. For the $\lambda/\Delta x$ approach, we found that a ratio of 5000 provided the desired convergence criteria for all the domains evaluated; while for the other method, we found that a resolution of $\Delta x = 61$ m for eastcoast domain, $\Delta x = 25$ m for the sinusoidal domain, and $\Delta x = 24$ m for the quadratic domain meets the convergence criteria. A cross comparison of these "true solutions" shows that the results were nearly identical, so the $\lambda/\Delta x$ ratio is used in the remainder of this subsection. The global spatial accuracy experiments used both constant and variable nodal spacing, with the ranges of grid refinement shown in Table 4.1, and a time step of one
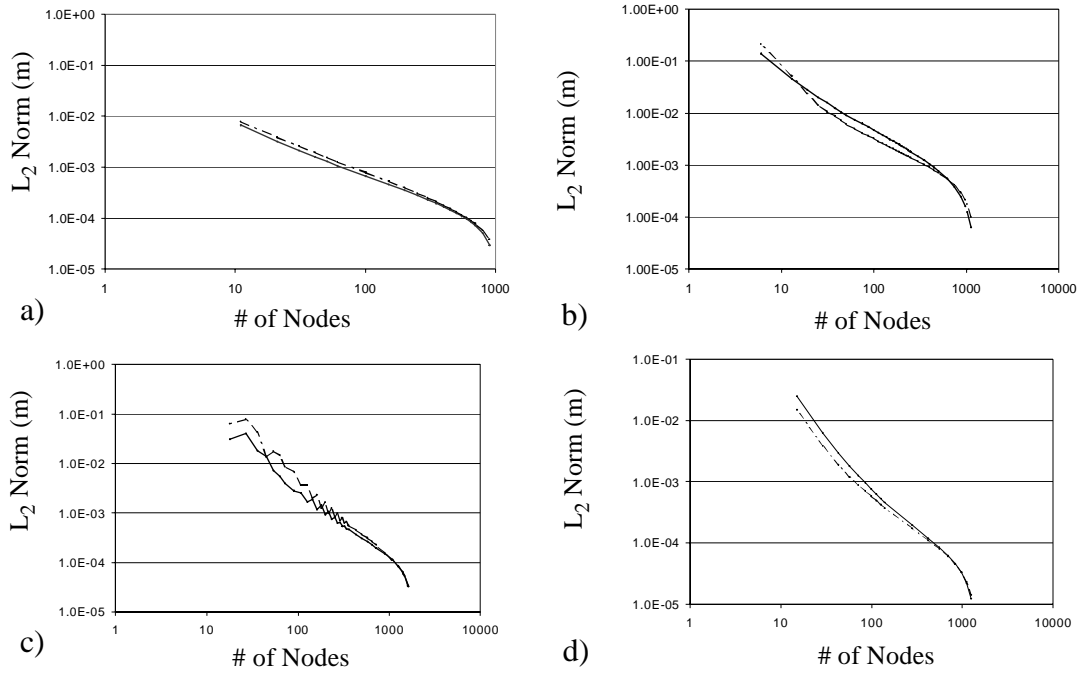
Figure 4.7 Spatial accuracy results (elevation) for all four domains using the original time-marching algorithm: a) constant (constant), b) quadratic (variable), c) eastcoast (variable) and d) sinusoidal (variable). Solid line - NCM, Long dashes - CM. (Note: first three results used a constant bottom friction while the last result used a variable bottom friction.)

second. Results using both the original and predictor-corrector time-marching algorithms (Figures 4.7 and 4.8, respectively) produced similar convergence rates for both forms of the momentum equation. Therefore, no significant effect is seen on the global spatial accuracy results when utilizing the conservative form of the momentum equation.

Local Spatial Accuracy

Next, we looked at the CM algorithm's impact on local spatial accuracy following the procedures presented in Section 4.3.3. Based on the local mass conservation results, we focused on the eastcoast and sinusoidal domains, as these show the greatest change in local mass conservation errors. The "true solution" based on a uniform mesh was employed for both domains. The grid resolution parameters are shown in Table 4.1.
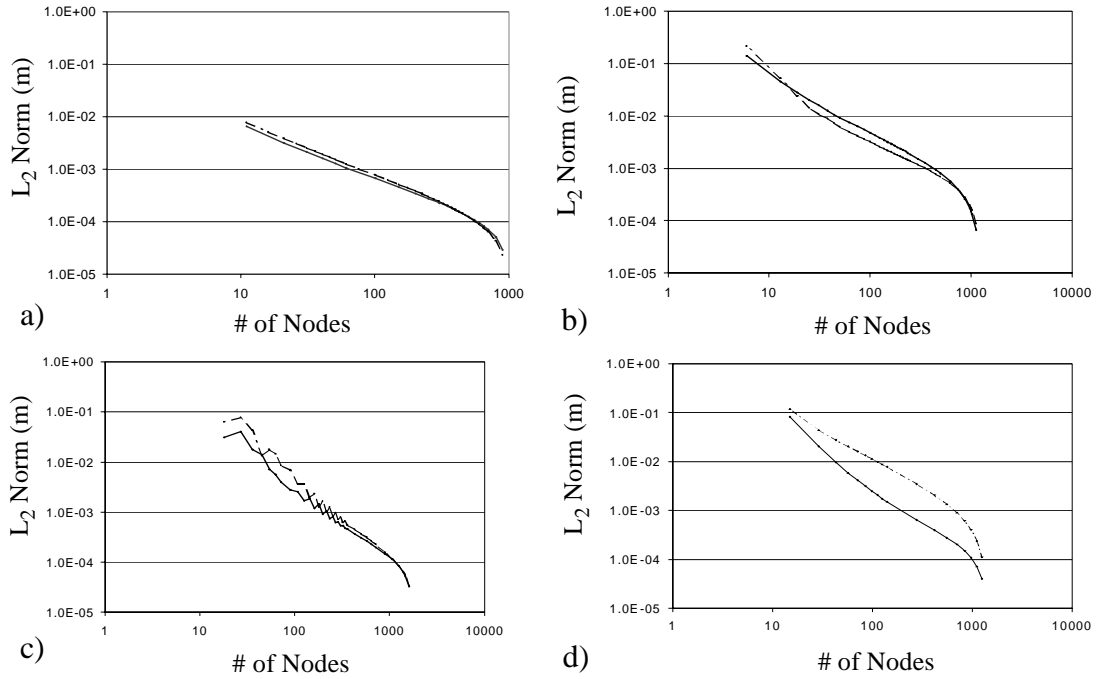
Figure 4.8 Spatial accuracy results (elevation) for all four domains using the predictor-corrector time-marching algorithm: a) constant (constant), b) quadratic (variable), c) eastcoast (variable) and d) sinusoidal (variable). Solid line - NCM, Long dashes - CM. (Note: first three results used a constant bottom friction while the last result used a variable bottom friction.)
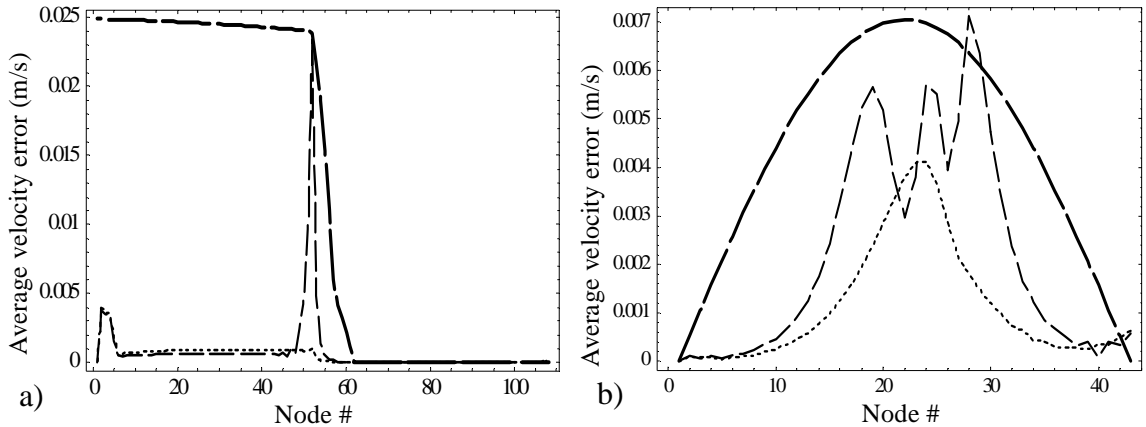
Figure 4.9 Local spatial accuracy results (average velocity errors) for the: a) eastcoast and b) sinusoidal domains. Long dashes - NCM (inconsistent GWC advective terms), Short dashes - CM, Longer dashes - bathymetry. Node spacing is given in Table 4.1. Results utilize a variable nodal spacing with $\lambda / \Delta x = 300$.

Results for the variable-spaced grids for these domains are shown in Figure 4.9, with a schematic of the bathymetry shown by the longer dashed lines. The figures indicate that the CM equation increases the local spatial accuracy, particularly along areas of steep topography changes. The highest error with the non-conservative form of the momentum equation occurs at the top of the continental shelf area for the eastcoast domain. In the sinusoidal domain, we find that the non-conservative momentum equation has higher errors before and after the bathymetry rise than the conservative momentum equation results; while, the conservative momentum equation shows an increase in error at the peak of the bathymetry. In Figure 4.9b, it is interesting and important to note that the NCM local spatial errors show a similar 3-peak pattern as the local mass errors of Figure 4.3c. Note that both momentum equations show an error near the land boundary in both domains. Local accuracy results differ from global accuracy because the latter averages the errors over the domain, which tends to smooth out the local errors.

Finally, we looked at the interaction of the meshing criteria with the form of the
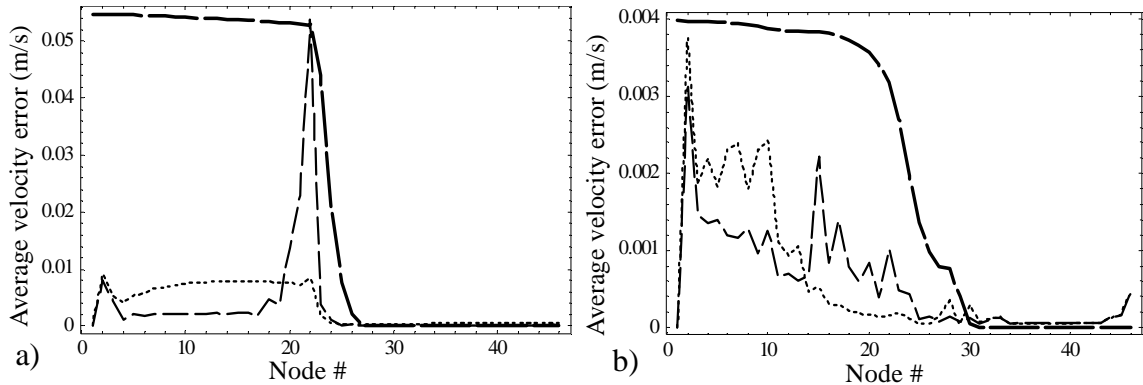
Figure 4.10 Local spatial accuracy results (average velocity errors) for the eastcoast domain: a) $\lambda/\Delta x$ and b) LTEA. Long dashes - NCM (inconsistent GWC advective terms), Short dashes - CM, Longer dashes - bathymetry. Node spacing is given in Table 4.1. Results utilize a variable nodal spacing with $\lambda/\Delta x = 125$.

momentum equation. In particular, for the eastcoast domain, we analyzed two variable meshes with the same number of nodes; one using the $\lambda / \Delta x$ ratio and one based on the LTEA (see Chapter 2). In Figure 4.10, results show that the CM formulation is less sensitive to the meshing criteria, but that the LTEA reduces peak errors in the NCM formulation by two orders of magnitude (i.e., reduces it to the same as the CM formulation). Such a result is not surprising in that the LTEA method uses truncation error estimates from the velocity-based NCM equation.

4.4.5 Impact of Changing the Tidal Constituents

All previous experiments utilize a M_2 tidal constituent as the elevation boundary condition; however, in 2D applications there can be several tidal constituents included in the simulation. Therefore, we investigated this by changing the amplitude in the 1D eastcoast domain in order to simulate other tidal constituents. Figure 4.11 shows the results
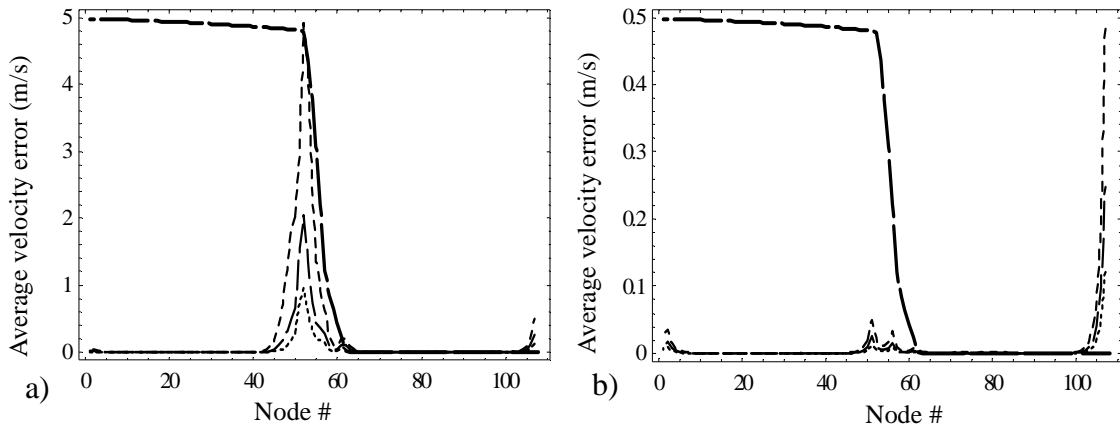
Figure 4.11   The effect of changing the amplitude on local spatial accuracy. a) NCM (inconsistent GWC advective terms) and b) CM. Medium dashes - 2 m amplitude, long dashes - 1 m amplitude, short dashes - 0.5 m amplitude and longer dashes - bathymetry.

from these tests for both formulations of the momentum equations. The errors decrease or increase based on how the amplitude of the tidal constituent is changed in the simulation. However, the important thing to note is that the CM equation is less sensitive to amplitude changes than the NCM equation, thus indicating that when other tidal constituents are present, we will still obtain a decrease in the local spatial accuracy results with the CM equation.

4.4.6 Discussion

A broader look at the results of the previous sections suggests two trends. First, both the CM and NCM equations produce similar results in parts of the domain, e.g., in the deep water portion of the eastcoast domain, where the flow physics is nearly linear, neither the CM or NCM show large local mass balance errors (see Figure 4.3b). But in regions of sharp bathymetric gradients, they differ significantly. In particular, note that the CM equation does not show the same local mass balance error spikes in these regions as does the NCM algorithm, as can been seen in Figure 4.3b over the continental rise and Figure 4.3c over the rise in bathymetry. It is precisely in these same regions where the nonlinear advective terms are significant, so we will look for a correlation through simulation and analyses.

Second, the parallel behavior of the error in the local mass balance graph and the error in the local accuracy graph (cf Figures 4.3b and 4.9a) and the similar 3-peak pattern of the NCM results between Figures 4.3c and 4.9b suggests that the two are related. In other words, can the finite volume method of computing mass balance serve as a surrogate variable for truncation error? This issue is also explored in this section.

To examine the behavior of the local truncation error for the advective terms further,

we present the truncation error expressions for the advective terms in the NCM and CM

equations below, as obtained from a Taylor Series expansion of the discrete equations. (The

full expansion is too lengthy to be repeated here, but the interested reader can find the

results in reference [55] and in Appendix 3)

$$
\text{TE}_{\text{NCM}}^{\text{advective}} = \frac{1}{2}(\Delta x_{i+1} - \Delta x_i)\left[\left(\frac{\partial u_i}{\partial x}\right)^2 + \left(u_i\frac{\partial^2 u_i}{\partial x^2}\right)\right] -
$$

$$
(\Delta x_i^2 - \Delta x_i \Delta x_{i+1} + \Delta x_{i+1}^2)\left[\frac{1}{2}\left(\frac{\partial u_i}{\partial x}\frac{\partial^2 u_i}{\partial x^2}\right) + \frac{1}{6}\left(u_i\frac{\partial^3 u_i}{\partial x^3}\right)\right] + \text{H.O.T} \qquad (4.15)
$$

$$
\text{TE}_{\text{CM}}^{\text{advective}} = (\Delta x_{i+1} - \Delta x_i)\left[\left(\frac{\partial q_i}{\partial x}\frac{\partial u_i}{\partial x}\right) + \frac{1}{2}\left(u_i\frac{\partial^2 q_i}{\partial x^2} + q_i\frac{\partial^2 u_i}{\partial x^2}\right)\right] -
$$

$$
\frac{1}{2}(\Delta x_i^2 - \Delta x_i \Delta x_{i+1} + \Delta x_{i+1}^2)\frac{\partial q_i}{\partial x}\frac{\partial^2 u_i}{\partial x^2} - \frac{1}{2}(\Delta x_i^2 - \Delta x_i \Delta x_{i+1} + \Delta x_{i+1}^2)\frac{\partial u_i}{\partial x}\frac{\partial^2 q_i}{\partial x^2} -
$$

$$
\frac{1}{6}(\Delta x_i^2 - \Delta x_i \Delta x_{i+1} + \Delta x_{i+1}^2)u_i\frac{\partial^3 q_i}{\partial x^3} -
$$

$$
\frac{1}{6}(\Delta x_i^2 - \Delta x_i \Delta x_{i+1} + \Delta x_{i+1}^2)q_i\frac{\partial^3 u_i}{\partial x^3} + \text{H.O.T.} \qquad (4.16)
$$

Note that the truncation error for each is formally first order accurate for unequal nodal

spacing, but is second order accurate for constant grid spacing, as would be expected for

linear Galerkin finite elements. Because the flux varies more slowly than velocity in

regions where the topography is changing rapidly, one would expect the magnitude of the

derivatives of q, which appear in the CM truncation error expression, to be less than the

corresponding derivatives of u, which appear in the NCM equation. To verify this, we

carried out a scaling analysis of the leading error terms shown in Equations (4.15) and

(4.16) using elevation and velocity values taken from eastcoast results over the continental

rise (i.e., a region of high advection). After correcting for the differences in units between

Equations (4.15) and (4.16) by dividing by the water column depth, we found that the

truncation error for the CM advective terms is two orders of magnitude less than the

corresponding terms for the NCM equation. In addition, when the scaling analysis is

repeated for the deep water portion of the eastcoast domain, where the NCM and CM

equations give similar results (i.e., a region of low advection, small flux and velocity

gradients, and nearly linear physics), the two truncation error expressions scale to nearly

identical values.

Physical arguments, simulations, and analysis thus lead us to believe that local

truncation error is less for the CM equation than the NCM equation in regions of high

advection. It then follows that the local mass balance error must also be less for the CM

equation in these regions. To wit, in the limit as Δx and Δt tend toward zero, truncation

error disappears and the discrete solution approaches the continuum solution (sans roundoff

errors), so one would expect that local mass balance errors, *as computed from direct

integration of the continuum equations*, would also tend toward zero. This is indeed the

case. Increasing the resolution for simulation results shown in Figures 4.3b and 4.9a

decreases both the local spatial truncation error and the local mass balance error *at the same

rate*. Figure 4.12 shows results for both local spatial accuracy and local mass balance errors

for two refined grid resolutions from these shown in Figures 4.3b and 4.9a.

If the advective terms do indeed dominate the error behavior (mass balance or

spatial accuracy), one would expect less error if they were omitted from the equation (a

quasi-linear simulation). The simulations used to produce Figure 4.3b were re-run without
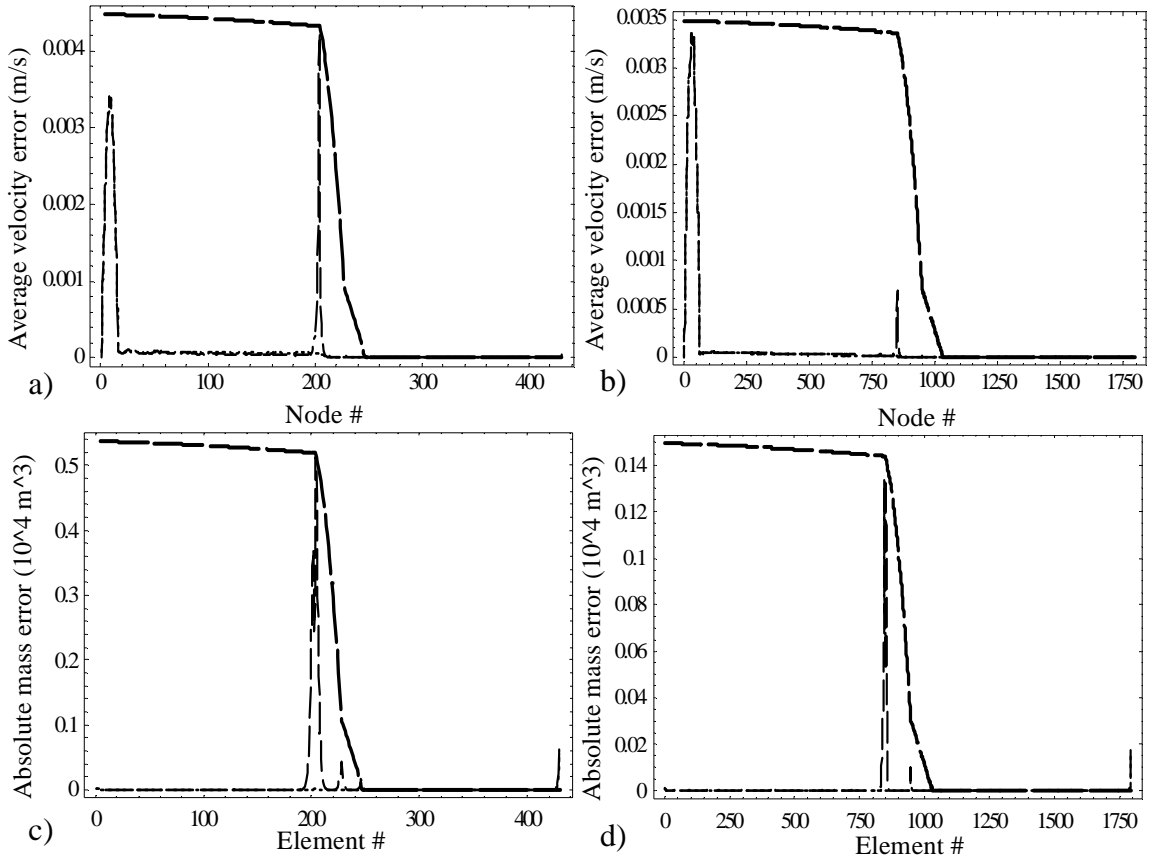
Figure 4.12 The effects of spatial resolution on local spatial accuracy and mass conservation. a) local spatial accuracy where $\lambda/\Delta x = 1200$, b) local spatial accuracy where $\lambda/\Delta x = 5000$, c) local mass conservation where $\lambda/\Delta x = 1200$ and d) local mass conservation where $\lambda/\Delta x = 5000$. Long dashes - NCM (inconsistent GWC advective terms), short dashes - CM, longer dashes - bathymetry. (Note that the scale in d) is less than c).

these advective terms; the results (see Figure 4.13) show that the peak local mass balance errors for the quasi-linear run are 40% less than those shown in Figure 4.3b. In addition, if one removes the remaining nonlinear terms from the equations and runs a full linear simulation, the local mass balance errors diminish only slightly from simulations with just the advective terms excluded, thus suggesting that the advective terms are the primary contributor to errors in these regions.

All of this leads us to conclude that the choice of dependent variable (flux vs.
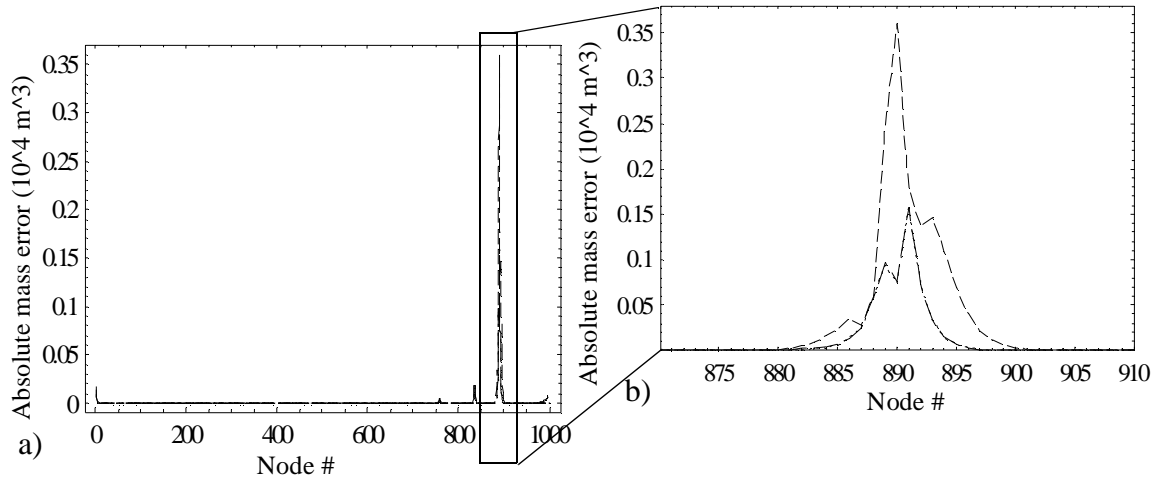
Figure 4.13 Local mass conservation errors for fully nonlinear simulation (medium dashes), quasi-linear, i.e. no advective terms (long dashes) and fully linear simulation (short dashes). Results here are only for the NCM equation with inconsistent treatment of the advective terms. Results for the quasi-linear and fully linear simulations have similar errors. a) full results and b) zoomed in on a section of the results.

velocity) and the form of the advective terms (conservative vs. non-conservative) in the discrete equations are the primary causes for the difference in behavior between the NCM and CM simulations, with the CM equation offering increased accuracy in areas with high advective gradients. Furthermore, local mass balance error, when measured by direct integration of the continuity equation, parallels local truncation error and can thus be used as a surrogate variable for local truncation error. As such, among other applications, it can be used to identify regions where mesh refinement is necessary. Such a conclusion is also consistent with earlier studies [54]. It remains to be demonstrated in this chapter that these 1D observations carry over to 2D simulations.

4.5 Two-Dimensional Numerical Experiments

4.5.1 Domains Evaluated

In 2D, we examined behavior of the two formulations of the momentum equation

98

on the quarter annular harbor (denoted "quarter annular"), a fictional grid that has a well-documented analytical solution, and several application domains - Bight of Abaco (denoted "Bahamas"), Western North Atlantic (denoted "WNAT"), Gulf of Mexico, and Persian Gulf.
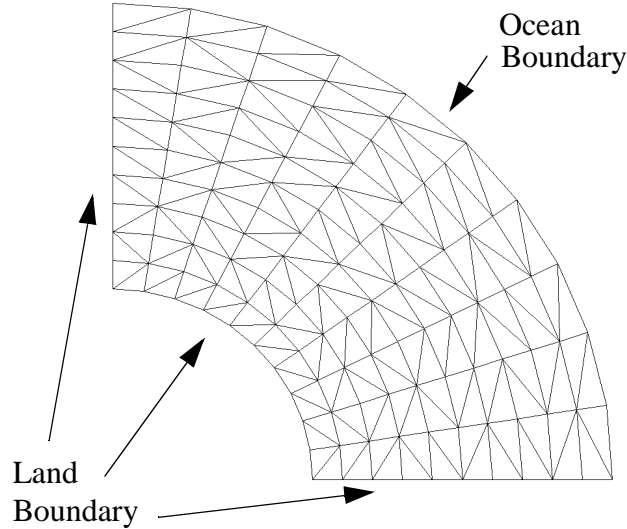
Figure 4.14 Quarter annular harbor domain (10 x 10 resolution).

The quarter annular grid is shown in Figure 4.14. Boundaries are marked on the figure, with either ocean or land indicated. The boundary condition for the open ocean boundary is the M_2 tidal constituent with a 1-meter amplitude, while the land boundaries are no flow. For the experiments herein, we utilized a 10x10 resolution (radial divisions x θ divisions), which gives a $\lambda/\Delta x$ of 26, an accepted value in practice [59]. Bathymetry varies from a minimum of 3 m to a maximum of 19 m with inner radius at a distance of 60690 m and the outer radius at a distance of 152400 m. The following parameters were used in these experiments: eddy viscosity, ε, is set to zero, $C_f = 0.003$ and $G = 0.001 \text{ sec}^{-1}$.
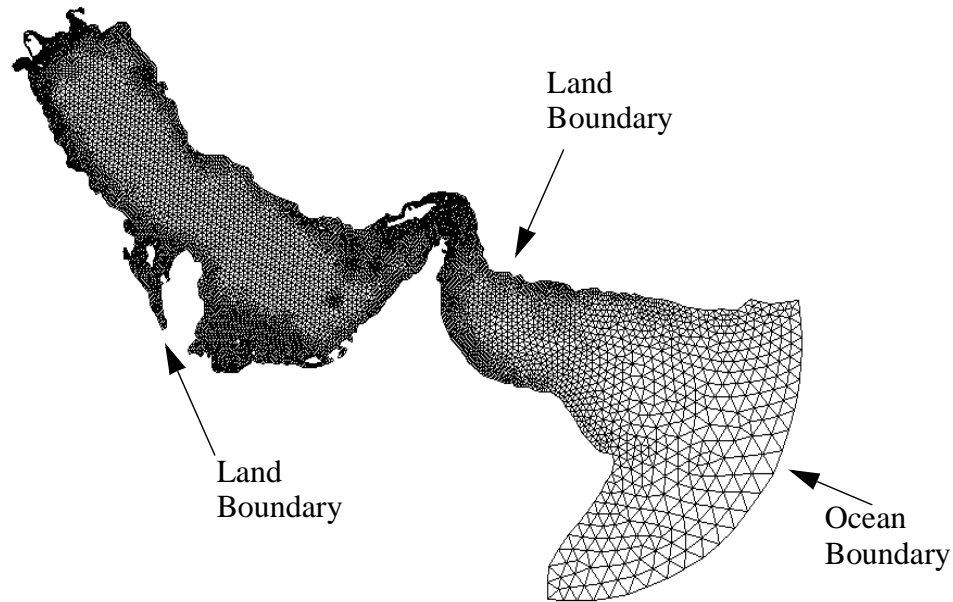
Figure 4.15 Persian Gulf domain.

Figure 4.15 shows the Persian Gulf domain, while the three other application domains (WNAT, Gulf of Mexico and Bahamas) are shown in Figure 4.16. Boundary conditions are indicated on the figures. Table 4.3 contains information regarding parameters, boundary and grid data for each of the application domains (i.e., number of nodes, range of nodal spacing, etc.). In all of the domains, the land boundaries are treated as no flow and the ocean boundaries utilize the tidal constituents presented in Table 4.3. In these domains, we set the eddy viscosity term, ε, to zero except for the WNAT domain where a eddy viscosity value of 10 m^2/s is used.

4.5.2 Mass Conservation

4.5.2a Global Mass Conservation

We analyzed the impact of the CM equation on the global mass balance errors

WNAT
Domain

Bahamas Domain

Land
Boundary

Land
Boundary

Ocean
Boundary

Ocean
Boundary

Gulf of Mexico
Domain
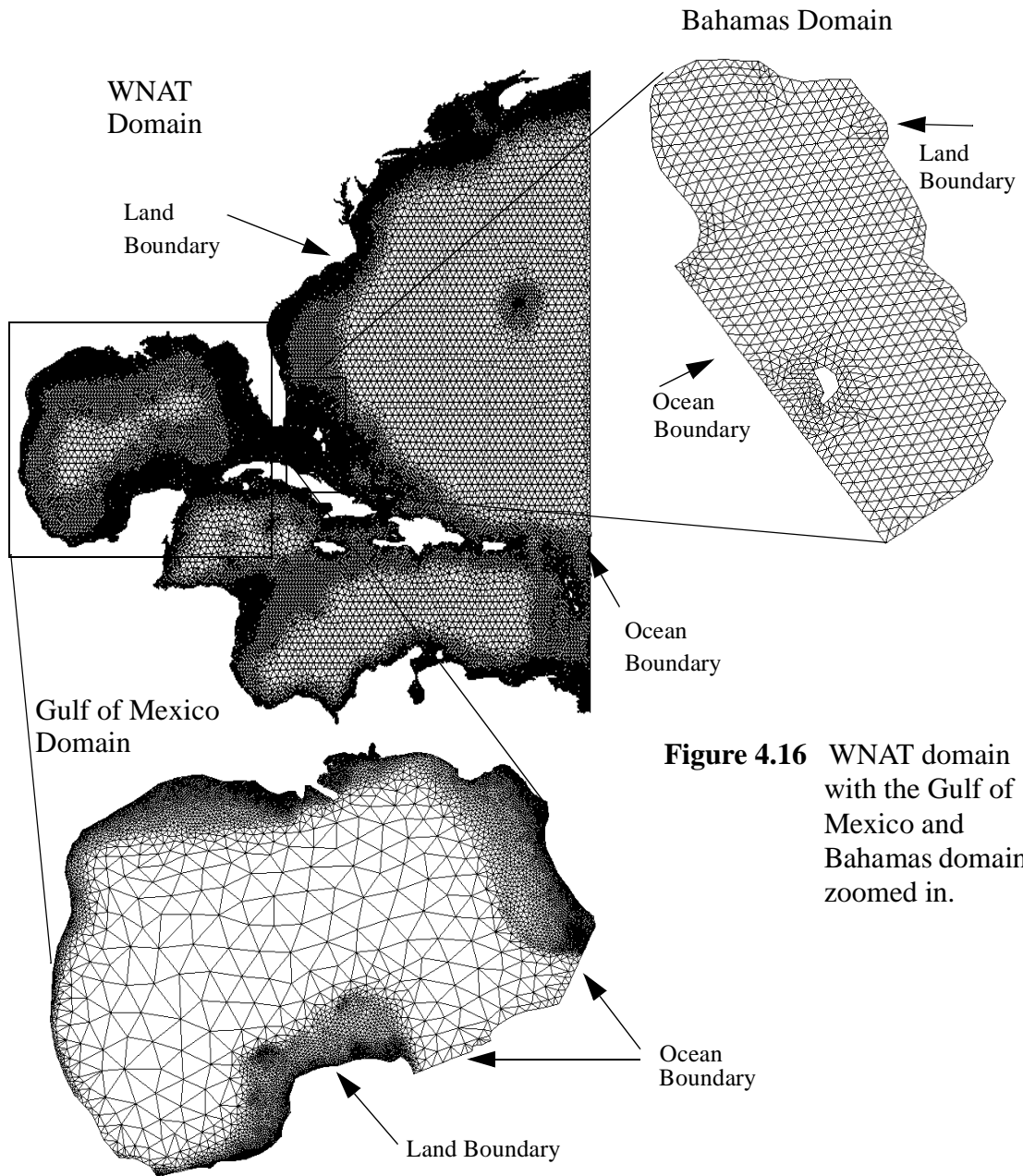
Figure 4.16 WNAT domain
with the Gulf of
Mexico and
Bahamas domains
zoomed in.

Ocean
Boundary

Land Boundary

Table 4.3 Application domain information.

	Bahamas	Gulf of Mexico		WNAT	Persian Gulf
Meshing Criteria	$\lambda/\Delta x$	$\lambda/\Delta x$	LTEA	$\lambda/\Delta x$	$\lambda/\Delta x$
# nodes	926	11701	11934	32947	8550
# elements	1696	21970	22870	61705	15724
Min. Bathymetry (m)	1.0	1.0	0.7	3.0	1.0
Max. Bathymetry (m)	≈ 9.0	≈ 3600.0	≈ 3600.0	≈ 6000.0	≈ 3700.0
C_f value (-)	0.009	0.003	0.003	0.003	0.0015
G value (sec^{-1})	0.009	0.009	0.009	0.005	0.01
M_2 amplitude (m)	0.395	0.07 - 0.173	0.07 - 0.173	0.0652 - 0.5580	0.496 - 0.6517
O_1 amplitude (m)	0.075				0.185 - 0.194
K_1 amplitude (m)	0.095				0.35 - 0.37
S_2 amplitude (m)	0.06				0.193 - 0.256
N_2 amplitude (m)	0.10				0.115 - 0.149
Q_1 amplitude (m)		N.A.			0.0036 - 0.0037
P_1 amplitude (m)					0.113 - 0.118
K_2 amplitude (m)					0.0042 - 0.0058

utilizing the procedures presented in Section 4.3.1. Results are shown in Figure 4.17, which shows the average over time for both formulations of the momentum equation. (Recall that throughout this 2D section, the NCM advective terms are consistent with the GWC equation.) The CM results show slight to moderate decreases in the global mass conservation errors in four of the domains. In two domains, the WNAT and the Gulf of Mexico (LTEA resolution), we observe that the NCM equation produces slightly better or similar results to the CM equation. In the WNAT domain, the similar error behavior is due to the fact that the majority of the domain is in deeper water where the nonlinear terms do not play a significant role; these 2D WNAT results parallel the 1D results for the eastcoast slice (cf Figure 4.2) with the consistent treatment of the advective terms.

Regarding the Gulf of Mexico results, we note that the LTEA method provides extra resolution on the shelf break [39,40]. The extra shelf resolution decreases the global mass error in the NCM equation results. On the other hand, the CM equation results are only slightly less than the $\lambda/\Delta x$ resolution (Figure 4.17, Gulf of Mexico open bars), which indicates that the CM equation is less sensitive to the method of node placement on the shelf break. Such behavior is consistent with the 1D experiments and consistent with the fact that the LTEA uses the velocity-based NCM truncation errors to determine node placement.

4.5.2b Local Mass Conservation

Next we analyzed the impact of the CM equation on the local mass conservation utilizing the procedures presented in Section 4.3.1. Results are presented as contour plots in Figures 4.18-4.23 with the scales showing the log of the errors. Note that the scales for any given pair of NCM and CM graphs are the same. We also present in Figure 4.24 the
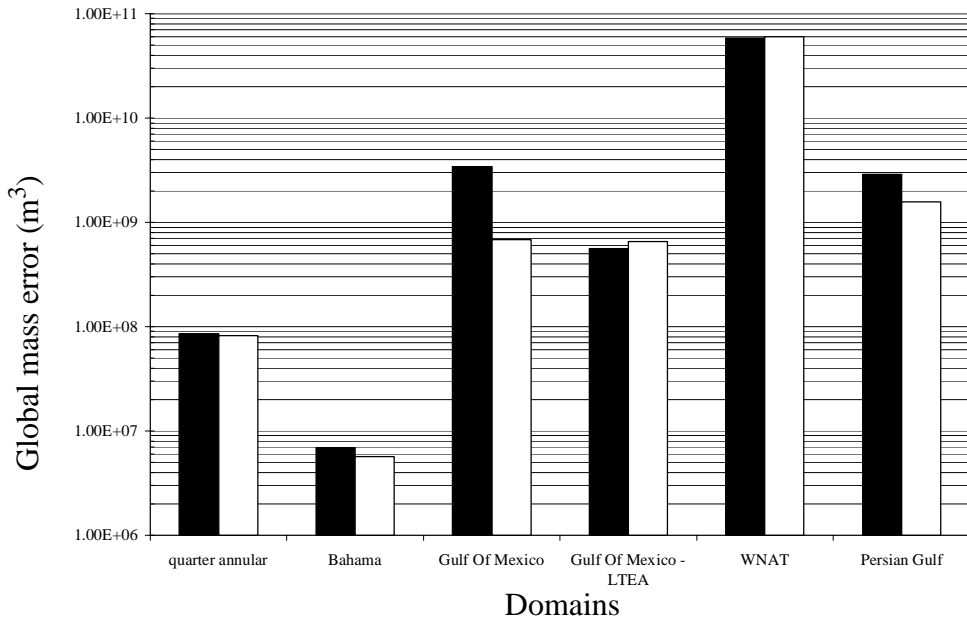
Figure 4.17   Global mass conservation results for the domains analyzed. Plot of the average global mass errors for both forms of the momentum equation (open bars - conservative momentum, filled bars - non-conservative momentum).

differences in the mass balance errors where the scale shows the log of the errors. In Figures

4.20-4.23, we include the bathymetric contours to indicate where the steep bathymetry

gradients occur. Results indicate that the CM equation reduces the local mass balance errors

over a significant portion of the domain, with the largest gains occurring in the shelf and

shelf break regions. (Observe the relative amount of blue and light pink between graph

pairs or the amount of blue in the difference graphs in Figure 4.24.) This is most evident in

Figures 4.22 and 4.24c (WNAT), where we see decreases in local mass balance errors

(changes from pink to light blue or the blue area in Figure 4.24) with the CM equation along

the continental shelf and shelf break region in the Gulf of Mexico and along the eastern

seaboard of the United States. In the WNAT and Gulf of Mexico (LTEA resolution)

domains, we find that the differences in local mass balance errors between the two

formulations indicate NCM local mass balance errors are less along the ocean boundaries;

Conservative Momentum　　　　　　　　Non-Conservative Momentum
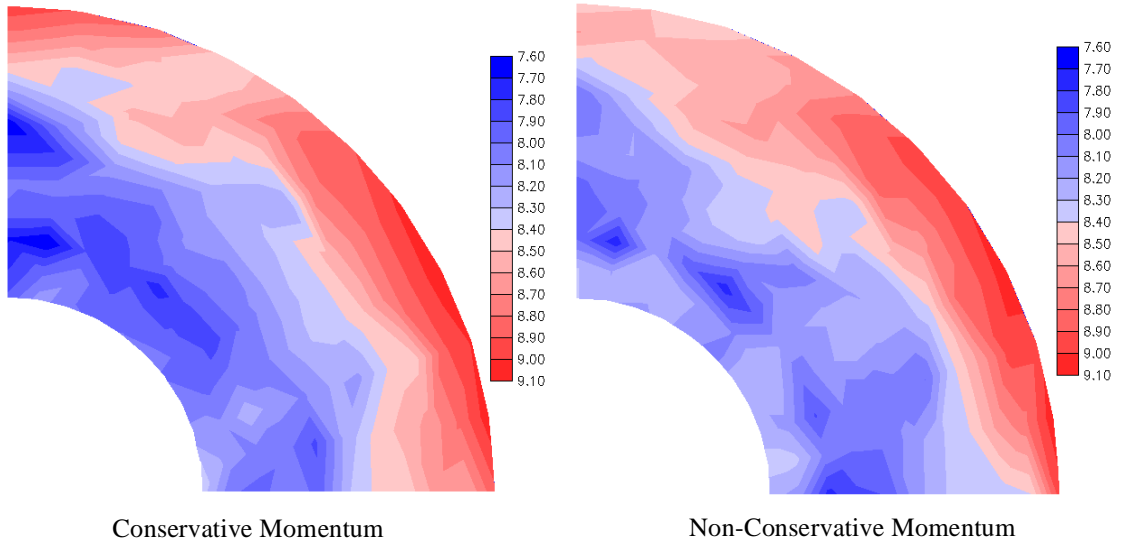
Figure 4.18　Local mass conservation results for the quarter annular domain. Red coloring indicates higher mass balance errors while the blue coloring indicates the lower mass balance errors. Conservative momentum results are shown on the left with the non-conservative momentum results shown on the right. The legend shows the log of the errors for the CM and NCM results.

Conservative Momentum　　　　　　　　Non-Conservative Momentum
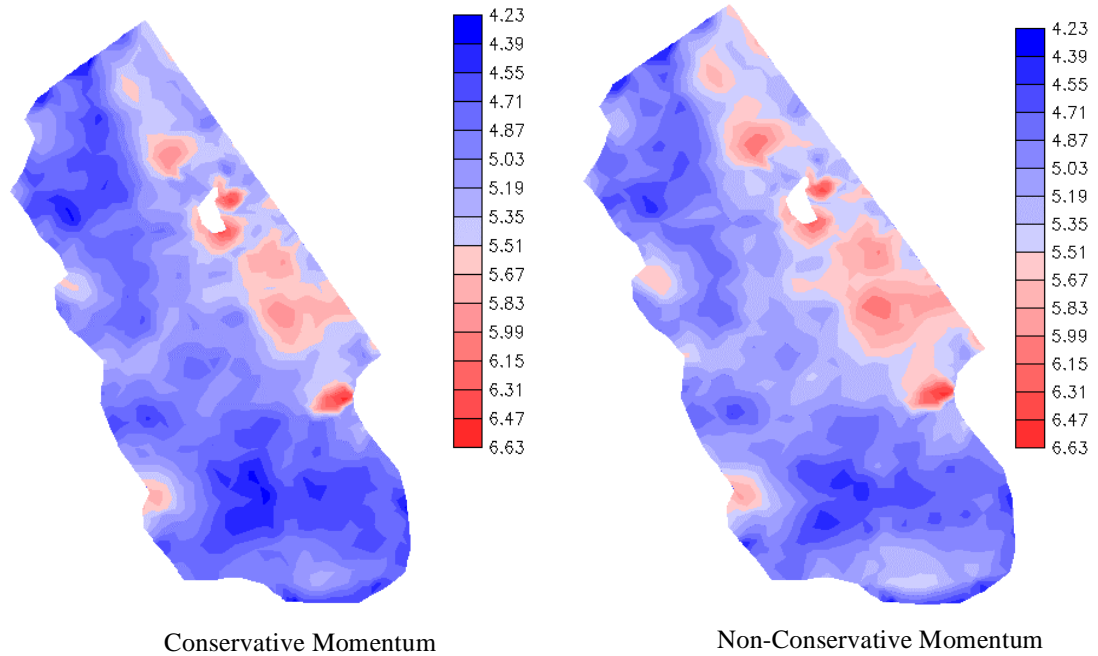
Figure 4.19　Local mass conservation results for the Bahamas domain. Red coloring indicates higher mass balance errors while the blue coloring indicates the lower mass balance errors. Conservative momentum results are shown on the left with the non-conservative momentum results shown on the right. The legend shows the log of the errors for the CM and NCM results.

Conservative Momentum

Non-Conservative Momentum
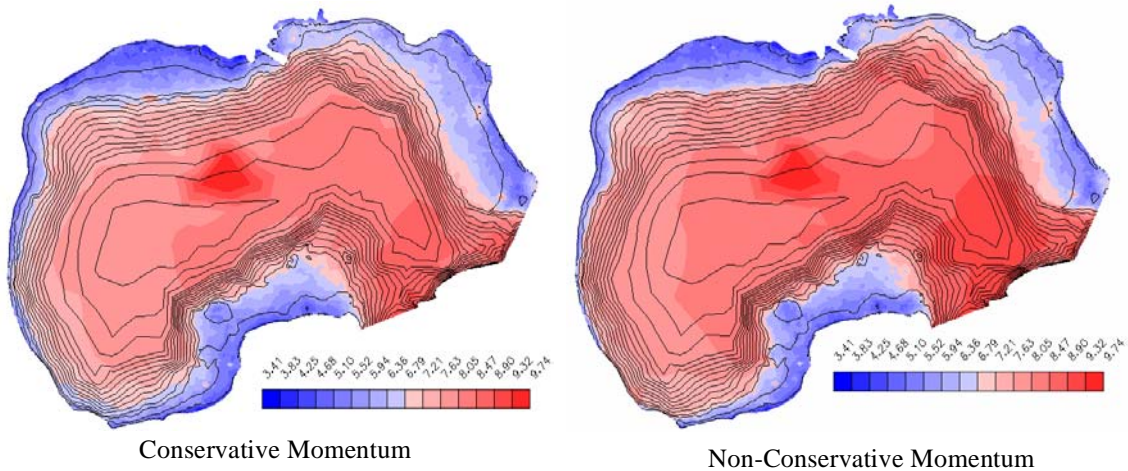
Figure 4.20 Local mass conservation results for the Gulf of Mexico domain - $\lambda/\Delta x$. Red coloring indicates higher mass balance errors while the blue coloring indicates the lower mass balance errors. Conservative momentum results are shown on the left with the non-conservative momentum results shown on the right. The legend shows the log of the errors for the CM and NCM results.

Conservative Momentum

Non-Conservative Momentum
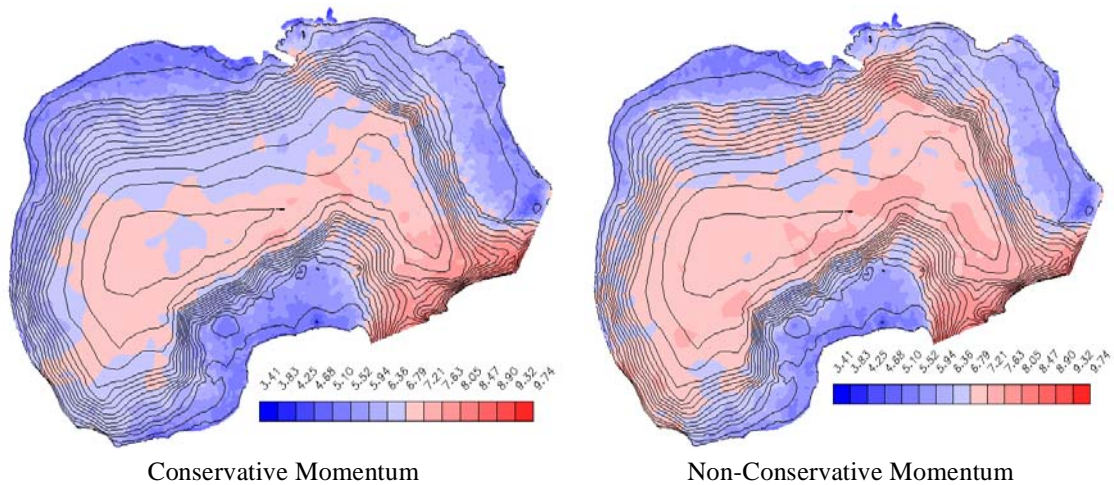
Figure 4.21 Local mass conservation results for the Gulf of Mexico domain - LTEA. Red coloring indicates higher mass balance errors while the blue coloring indicates the lower mass balance errors. Conservative momentum results are shown on the left with the non-conservative momentum results shown on the right. The legend shows the log of the errors for the CM and NCM results.

106

Conservative Momentum   Non-Conservative Momentum
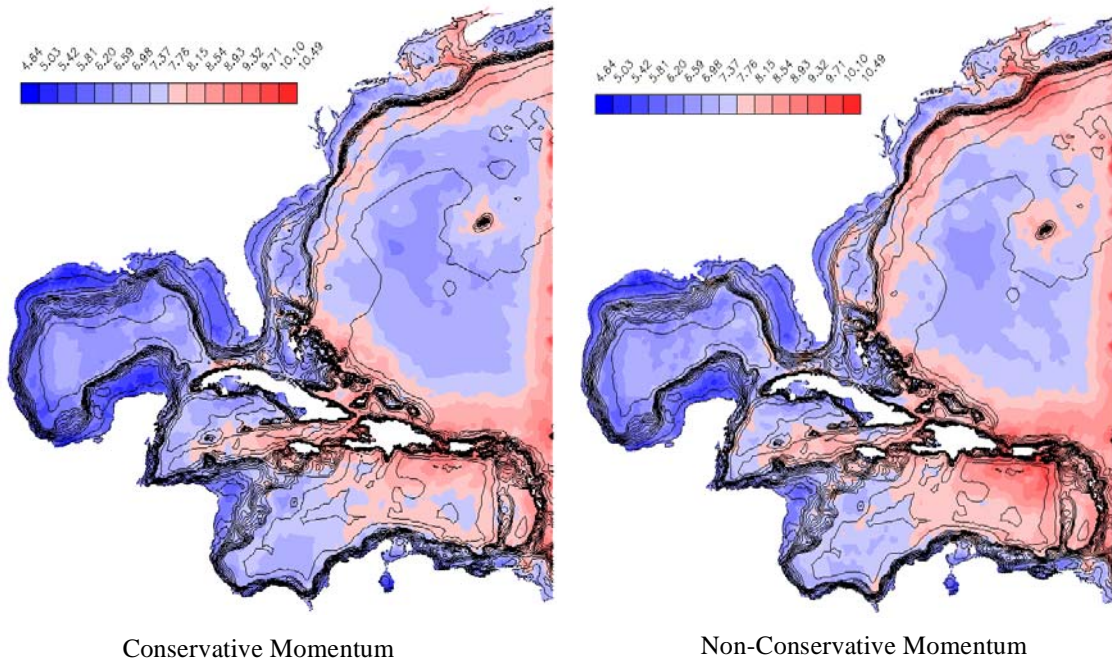
Figure 4.22 Local mass conservation results for the WNAT domain. Red coloring indicates higher mass balance errors while the blue coloring indicates the lower mass balance errors. Conservative momentum results are shown on the left with the non-conservative momentum results shown on the right. The legend shows the log of the errors for the CM and NCM results.

Conservative Momentum   Non-Conservative Momentum
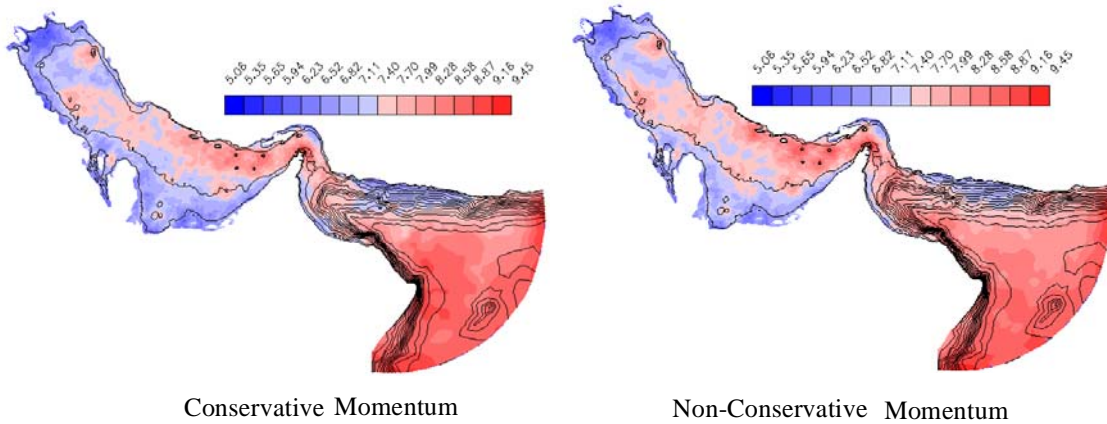
Figure 4.23 Local mass conservation results for the Persian Gulf domain. Red coloring indicates higher mass balance errors while the blue coloring indicates the lower mass balance errors. Conservative momentum results are shown on the left with the non-conservative momentum results shown on the right. The legend shows the log of the errors for the CM and NCM results.
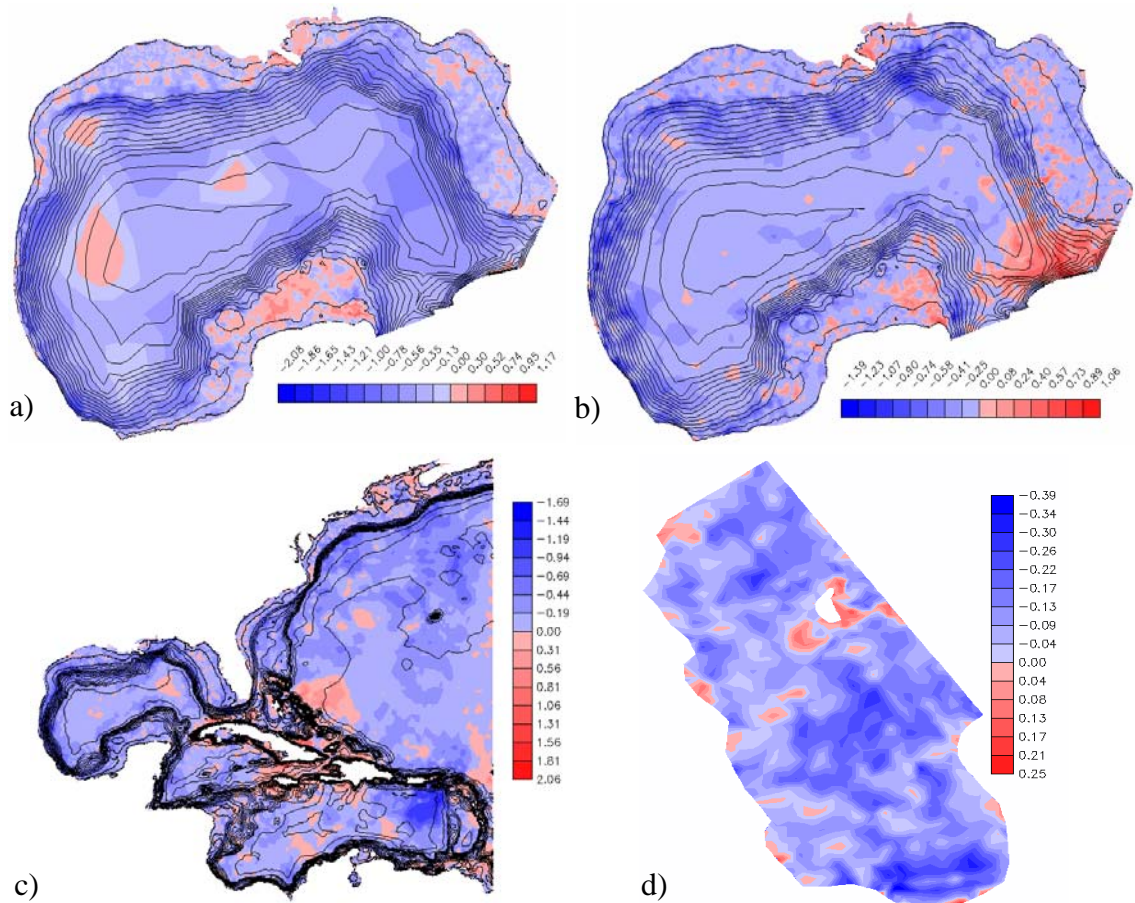
Figure 4.24 Local mass conservation results for the Gulf of Mexico and WNAT domains: a) GOM - $\lambda/\Delta x$, b) GOM - LTEA, c) WNAT - $\lambda/\Delta x$ and d) Bahamas - $\lambda/\Delta x$. Red coloring indicates where the NCM equation results are better while the blue coloring indicates where the CM equation results are better. The legend shows the difference in the log of the errors between the CM and NCM results.

land boundaries near the ocean boundary also have high mass balance errors that decrease as one moves away from the ocean boundary. These results parallel the 1D observations.

We analyzed the influence of the meshing criteria on the local mass balance errors in the Gulf of Mexico domain by using the LTEA method to provide extra resolution at the shelf break. (Recall from Table 4.3 that the total number of nodes is approximately the same.) As can be seen in Figures 4.24a and 4.24b or between Figures 4.20 and 4.21, the CM equation produces less error than the NCM equation, regardless of meshing techniques.

This is notable because the LTEA method is designed to reduce truncation errors for velocity-based sections.

4.5.3 Stability

We analyzed the impact of the CM equation on stability using the procedures presented in Section 4.3.2. Results in all of the domains show no impact on stability due to the CM equation. In fact, we found that the two momentum equations produced a nearly identical maximum allowable time step. Therefore, the CM equation does not influence stability, a result that is similar to the 1D findings.

4.5.4 Accuracy

4.5.4a Temporal Accuracy

We utilized the procedures presented in Section 4.3.3 to determine the impact of the CM equation on temporal accuracy. For these experiments, we evaluated 120 discrete timesteps over several M_2 tidal cycles. The timestep varied from 10 to 900 sec for the quarter annular domain (10x10 resolution), while for the Gulf of Mexico ($\lambda/\Delta x$ resolution) the timestep varied from 10 to 180 sec. With the predictor-corrector algorithm included, the timestep varied from 10 to 3600 sec for the quarter annular domain and from 20 to 360 sec for the Gulf of Mexico.

Figure 4.25 shows the temporal accuracy results for the original time-marching algorithm. For both domains, results using the original time-marching algorithm indicate that the two momentum equations provide the same error behavior, and both show a first order convergence rate (shown in Table 4.4). For the case of the predictor-corrector time-
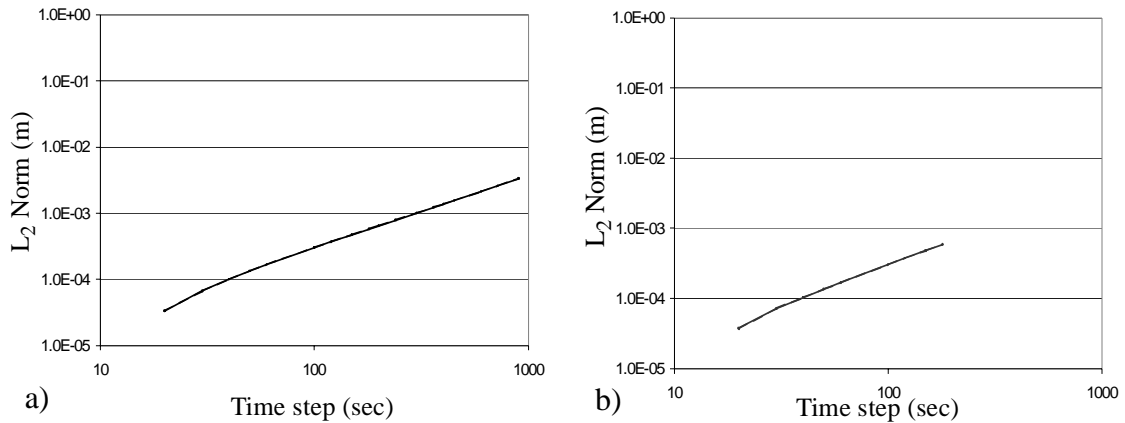
Figure 4.25   Temporal accuracy results (elevation) for two domains using the original time-marching algorithm: a) quarter annular (10x10 resolution), b) Gulf of Mexico - $\lambda/\Delta x$. Solid line - NCM, Long dashes - CM.

Table 4.4 Convergence rates for the 2D temporal accuracy.

	quarter annular		Gulf of Mexico	
	NCM	CM	NCM	CM
original time marching algorithm	1.16	1.16	1.23	1.23
predictor-corrector time marching algorithm	1.72	2.06	1.89	1.31

marching algorithm, the quarter annular results (shown in Figure 4.26) indicate that the NCM equation has less temporal error in the smaller time steps; however, as the time step increases, the results between the two momentum equations converge. As for the Gulf of Mexico domain, we find that the NCM equation errors are less than for the CM equation when using the predictor-corrector time-marching algorithm. Convergence rates (shown in Table 4.4) for the predictor-corrector time-marching algorithm shows mixed results, with the quarter annular domain providing second order accuracy for both forms of the momentum equation, while the Gulf of Mexico is second order accurate with the NCM

110

equation, but only first order accurate with the CM equation. In three out of the four 1D domains and one of the 2D domains, the form of the momentum equation does not significantly influence the convergence rates for the temporal accuracy whether using the original or predictor-corrector time-marching algorithm, which is similar to the 1D findings.
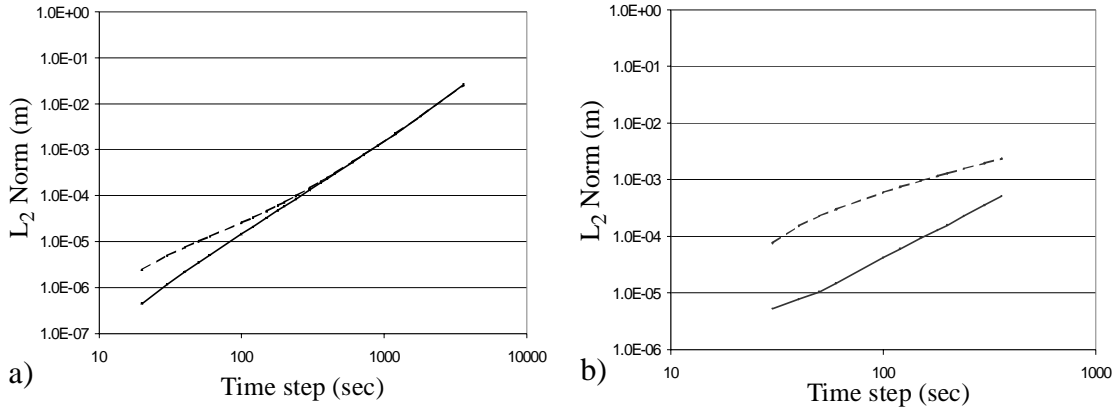
Figure 4.26 Temporal accuracy results (elevation) for two domains using the predictor-corrector time-marching algorithm: a) quarter annular (10x10 resolution), b) Gulf of Mexico - $\lambda/\Delta x$. Solid line - NCM, Long dashes - CM.

4.5.4b Spatial Accuracy

Results from the 1D spatial accuracy experiments indicate that the CM equation does not impact the global spatial accuracy significantly; therefore, we only analyze local spatial accuracy for the 2D domains.

We evaluate the effect of the CM equation on local spatial accuracy using CAFE (Cumulative Area Fraction Errors) curves [61]. Procedures followed in this section are presented in Section 4.3.3. To obtain the "true solution", we refined the quarter annular domain until the convergence criteria was met, which resulted in a resolution of 200x200. Note that CM vs. NCM solutions are nearly indistinguishable at this fine resolution ($\lambda/\Delta x$

Table 4.5 Elevation error measures for quarter annular and Gulf of Mexico domains.

	quarter annular		Gulf of Mexico	
	NCM	CM	NCM	CM
Resolution Comparison	10x10 vs. 200x200	10x10 vs. 200x200	$\lambda/\Delta x$ vs. split by 4 $(\lambda/\Delta x)$	$\lambda/\Delta x$ vs. split by 4 $(\lambda/\Delta x)$
Elevation Amplitude (Absolute)				
% exceeding -0.005 ft (quarter) % exceeding -0.005 cm (GOM)	8.4	**1.2**	88	**67**
% exceeding 0.005 ft (quarter) % exceeding 0.005 cm (GOM)	1.3	**0.56**	**10**	31
% exceeding +/-0.005 ft (quarter) % exceeding +/-0.005 cm (GOM)	9.7	**1.8**	98	98
Elevation Amplitude (Relative)				
% exceeding -0.5%	0.12	**<0.001**	84	**65**
% exceeding 0.5%	0.51	**0.051**	**7**	25
% exceeding +/-0.5%	0.63	**0.051**	91	**90**
Elevation Phase Difference				
% exceeding -0.2 °	14	**0.0083**	**25**	33
% exceeding 0.2 °	2.6	**2.5**	64	**60**
% exceeding +/-0.2 °	17	**2.5**	**89**	93

ratio over 500).

Tables 4.5-4.6 present a snapshot of the error levels obtained from the CAFE analysis for two domains: the quarter annular and Gulf of Mexico, while Figures 4.27-4.28 show the CAFE plots for the same two domains comparing coarse and fine ("true") resolution. Spatial resolution is indicated in the tables. The values in bold type highlight which form of the momentum equation provides the least error. This data, combined with an analysis of the full CAFE plots, reveals that the CM equation significantly improves the

Table 4.6 Velocity error measures for quarter annular and Gulf of Mexico domains.

	quarter annular		Gulf of Mexico	
	NCM	CM	NCM	CM
Resolution	10x10 vs. 200x200	10x10 vs. 200x200	$\lambda/\Delta x$ vs. split by 4 ($\lambda/\Delta x$)	$\lambda/\Delta x$ vs. split by 4 ($\lambda/\Delta x$)
Major Semi-Axis (Absolute)				
% exceeding -0.05 ft s^{-1} (quarter) % exceeding -0.05 cm s^{-1} (GOM)	**0.66**	1.0	**15**	20
% exceeding 0.05 ft s^{-1} (quarter) % exceeding 0.05 cm s^{-1} (GOM)	**0.0062**	0.054	**9.2**	15
% exceeding +/-0.05 ft s^{-1} (quarter) % exceeding +/-0.05 cm s^{-1} (GOM)	**0.67**	1.1	**24**	35
Major Semi-Axis (Relative)				
% exceeding -1%	**75**	78	**49**	57
% exceeding 1%	19	**15**	**23**	28
% exceeding +/-1%	94	**93**	**72**	85
Major Semi- Axis Phase Difference				
% exceeding -10 °	**0.086**	0.092	1.3	1.3
% exceeding 10 °	0.14	**0.13**	1.1	**0.66**
% exceeding +/-10 °	0.23	**0.22**	2.4	**2.0**
Eccentricity				
% exceeding -0.1	0.29	**0.23**	2.3	**1.2**
% exceeding 0.1	**0.040**	0.19	1.0	**0.92**
% exceeding +/-0.1	**0.33**	0.42	3.3	**2.1**
Major semi-axis direction				
% exceeding -5 °	**1.3**	1.4	3.7	**3.0**
% exceeding 5 °	0.23	**0.19**	4.4	**3.7**
% exceeding +/-5 °	**1.5**	1.6	8.1	**6.7**
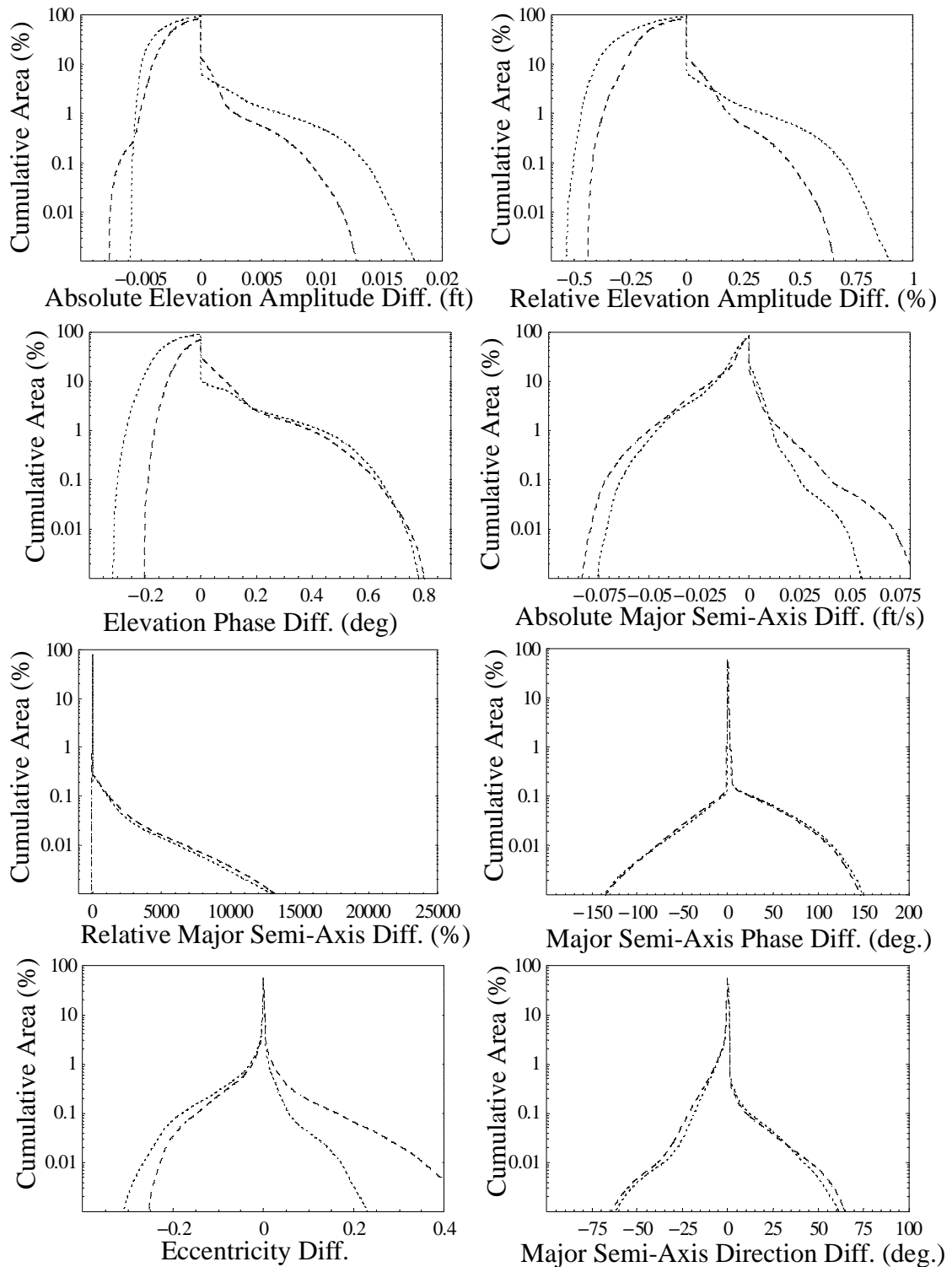
Figure 4.27 CAFE plots for quarter annular domain comparing the two momentum equations using the original time-marching algorithm. Dotted line - NCM equation and dashed line - CM equation.

114
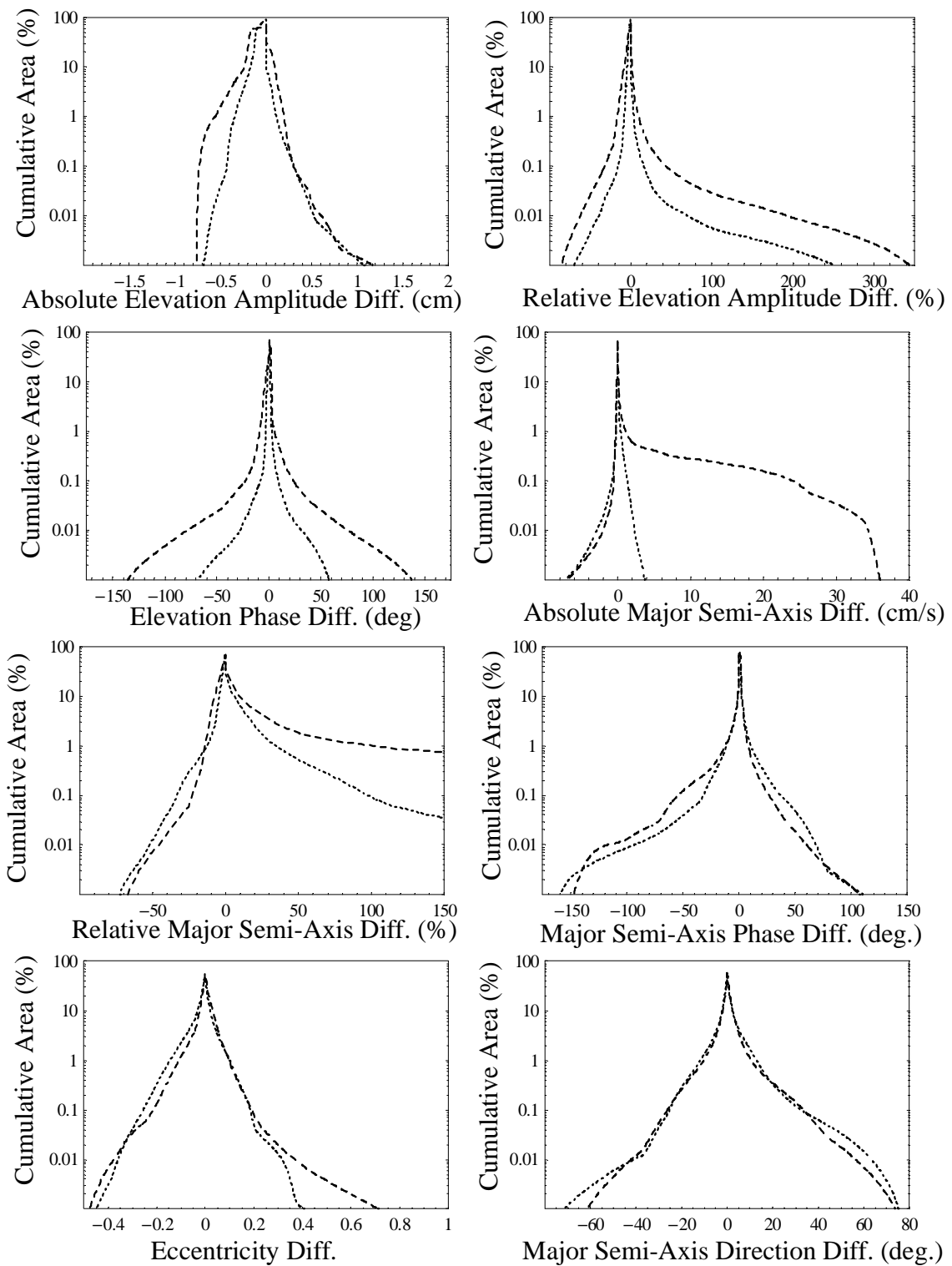
Figure 4.28 CAFE plots for Gulf of Mexico domain comparing the two momentum equations using the original time-marching algorithm. Dotted line - NCM equation and dashed line - CM equation.

elevation response over the entire domain for the quarter annular. For four of the five velocity components, the CM and NCM algorithms have very similar errors, while for one velocity component (major semi-axis, absolute), NCM is better over much of the quarter annular domain.

As for the Gulf of Mexico domain, we find mixed results, which is most likely due to how the fine grid was developed. For real domains, bathymetry is known only at discrete points from field measurements. To interpolate between these as the grid is refined ("triangles split by 4") introduces additional errors besides truncation errors into the measured response, so that spatial resolution studies are inconclusive for the Gulf of Mexico.

In contrast, for the fictitious quarter annular domain, one can refine the grid indefinitely because the bathymetry and coastline can be determined from known analytical equations at all spatial locations. Lastly, we evaluated the spatial accuracy with the predictor-corrector time-marching algorithm for quarter annular domain and found similar results. Altogether, the CM algorithm shows improved local spatial accuracy.

4.6 Conclusions

Herein, we analyzed the impact of using the flux-based, conservative form of the momentum equation instead of the velocity-based, non-conservative form to compute the depth-averaged velocities in 1D and 2D shallow water models. Our hypothesis in this study was that the use of the conservative momentum equation would improve both global and local mass conservation, eliminate the need to reformulate the advective terms between the GWC and NCM equations, and lessen the need for extensive refinement in areas with steep

bathymetry gradients. Through a set of extensive numerical experiments, supported with truncation error analysis, we show that the use of the conservative momentum equation does improve global mass conservation in most simulations, and it greatly improves local mass conservation in regions of steep topography for all of the domains, as measured in the finite volume sense. Paralleling the local mass balance results, local spatial accuracy also improves. The analysis in Section 4.4.6 demonstrates that both the choice of dependent variable and the form of the advective terms in the discrete equations causes a difference in behavior between the NCM and CM simulations, with the CM equation offering increased accuracy in areas of high advective gradients. Also, local mass balance error, when measured by direct integration of the primitive continuity equation, parallels local truncation error and can thus be used as a surrogate variable for local truncation error. As such, among other applications, it can be used to identify regions where mesh refinement is necessary. Furthermore, the use of the conservative form of the momentum equation eliminates the need for reformulating the advective terms between the governing equations. However, results are inconclusive regarding the third hypothesis, that is, for some simulations the LTEA mesh does not impact the CM results, while in others the LTEA mesh reduces both NCM and CM local mass balance errors.

In the end, the significant decrease in local mass balance error and corresponding increase in local spatial accuracy for the CM formulation, with no loss of global spatial accuracy and stability, provides sufficient evidence for its use in GWC-based, finite element shallow water models.

Chapter 5. Algorithmic and Resolution Influences on Diagnostic Baroclinic Simulations[a]

5.1 Introduction

Ocean flows are frequently categorized by one of two different dynamic modes, barotropic and baroclinic, that describe different wave speeds. Barotropic flows include motion driven by the tides and wind and only take into account pressure differences with respect to depth. Baroclinic flows include motion driven by density changes caused by temperature and salinity differences in the ocean [72]. These density variations create pressure gradients that vary with depth, thus creating a driving force called the baroclinic pressure gradient.

In areas where the topography changes rapidly, such as a seamount or continental rise region, many three-dimensional hydrodynamic models have problems computing a stable and realistic baroclinic pressure gradient (BPG). An initial study into the calculation of the BPG term serves as the main topic of this chapter. The motivation for this work stems, in part, from anomalous results observed by Blain [12] in baroclinic Arabian Gulf simulations using a wave continuity based FE model. Figure 5.1 illustrates the problem, where the source of error was identified as an unrealistic (and unstable) BPG computed by the model in a region of steep bathymetry and density gradients. This is shown by the large

a. This chapter has appeared as two abbreviated conference proceedings, the Estuarine and Coastal Modeling conference and Computational Methods in Water Resources. The references for these two proceedings are given in Chapter 7, numbers. [32] and [31], respectively.
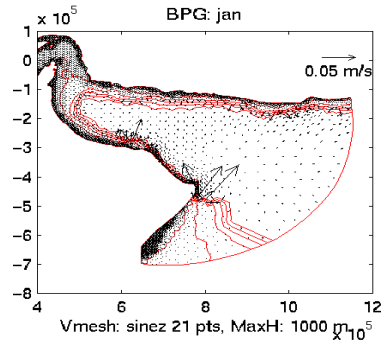
Figure 5.1   Instabilities caused by errors in the calculation of the BPG during simulations of the Arabian Gulf [12].

arrows in the area of steep contour changes in Figure 5.1.

Four common vertical coordinate systems utilized in ocean models are as follows: sigma coordinates, which are terrain-following [17]; z-coordinates (also called level coordinates), which follow a fixed depth [9]; isopycnal, which follow lines of constant density [14]; and hybrid, which includes any combination of sigma coordinates, z-coordinates or isopyncal coordinates [20,69]. Advantages and disadvantages exist for all of these coordinate systems, which several investigators have mentioned in their studies (e.g., [9,17,69]). To summarize, sigma coordinates provide a constant number of vertical layers, regardless of depth, and capture the bottom and free moving surfaces, thus allowing the boundary conditions to be implemented easily. One disadvantage of the sigma coordinate system involves the "hydrostatic inconsistency" condition, first discussed in the context of oceanographic models by Haney [42]. Figure 5.2 shows one set of vertical nodes that are considered hydrostatically inconsistent (Figure 5.2a) and one set of vertical nodes that are hydrostatically consistent (Figure 5.2b). This condition indicates that in areas of steep topography, there needs to be an appropriate amount of horizontal resolution in order to obtain stable and realistic BPG results. However, in some cases, the amount of horizontal
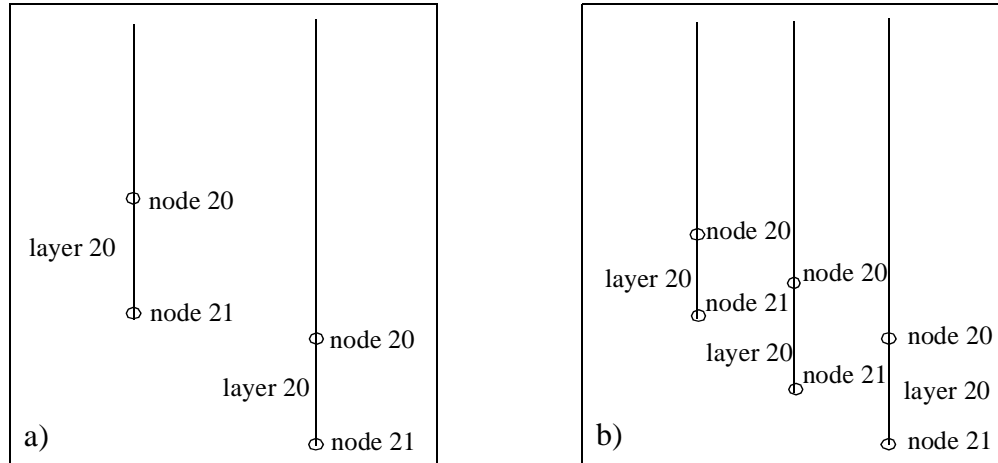
Figure 5.2 Schematic of vertical nodes that are a) hydrostatically inconsistent and b) hydrostatically consistent. Graphically, in a) we can tell the vertical nodes are hydrostatically inconsistent because node 21 does not fall in layer 20 in the adjacent vertical string of nodes, whereas in b), node 21 does fall in layer 20 in the adjacent vertical string of nodes.

resolution needed to produce accurate results leads to excessive computational costs. If the hydrostatic inconsistency condition is not met, then spurious modes tend to be introduced into the solution through truncation errors obtained from the transformation of the BPG term to the sigma coordinate system. Thus in the areas of steep bathymetry gradients, large truncation errors can mask the true BPG [17]. Suggestions from some researchers have reduced these errors, but the problem has not been completely solved. In some models, this problem has been reduced by subtracting off a mean vertical density gradient or an area-averaged density from the initial density field [69-71]. Stelling and van Kester introduced a finite volume approach that first switches from sigma coordinates to a redefined (similar to z-coordinates) system, where the BPG results are calculated, and then utilizes a simple filter to correct the BPG results. Results showed that they could obtain stable results for simulations that had steep bottom slopes [79]. However, further studies by Slordal [77] determined that this method tended to underestimate the BPG results so a modified method

120

was introduced. The modification makes it equivalent to linearly interpolating the density values in the vertical and then computing the gradients. Slordal [77] found that this improved the results but was more computationally time consuming than the traditional sigma coordinate method. Another disadvantage of the modified evaluation is that errors still develop in the results when a sharp vertical change occurs in the density field, just as it does with traditional sigma coordinates [77].

As for the z-coordinates, they do not suffer from the truncation error problems that occur with the sigma coordinate and its transformation. They also tend to be able to capture steep pynocline changes or maintain layered density fields better. However, the disadvantage of the z-coordinate system is its inability to properly resolve the flow around the bottom topography in areas of sloping bathymetry ("stair-step" resolution), and the correct flow at the surface is often not captured [17]. To obtain an accurate BPG where sloping bathymetries come into play for z-coordinates, several researchers suggest using extrapolation techniques. e.g. Beckmann and Haidvogel utilized a Chebyshev polynomial [7]. Beckmann and Haidvogel found that the use of Chebyshev polynomials to extrapolate BPG values at the bottom helped reduce the errors in the BPG values as compared to the traditional sigma coordinates. However, they indicated that the results tend not to be as stable as the results using traditional sigma coordinates. They suggest that this instability is due to the extrapolation of the results using the Chebyshev polynomials because these types of polynomials tend to have oscillation problems if they are not extrapolating values over a "small" distance [7].

Another method that has been used in global ocean models is the isopycnal coordinates, which follows lines of constant density [14]. This type of coordinate system

does well in the deeper parts of the ocean because the density profile tends to be stably stratified. However, this coordinate system does not do well in shallower parts of the ocean, such as the continental shelf, due to the mixing and advection processes that tend to be dominant in this part of the ocean [17]. It also has the same "stair-step" resolution problem at the bottom boundary that the z-coordinate method has because the lines of constant density do not follow the topography changes [14]. Thus, the method is not widely used for near-coastal models, such as ADCIRC.

Hybrid methods have been suggested that take advantage of the strengths of sigma and z-coordinate methods and have been used in several models (e.g, NCOM [69] and Spall and Robinson [78]). The degree of hybridization between the two coordinate systems and the technique of the hybridization can both vary in the model. For example, Beckers [6] examined a hybrid scheme that only used one z-coordinate (fixed) with sigma coordinates above and below it. Also, Spall and Robinson [78] analyzed a hybrid scheme that used z-coordinates in the upper layers and sigma coordinates in the bottom layers. Another hybrid scheme, which is used by NCOM (Navy Coastal Ocean Model) [69], applies sigma coordinates in the upper layers and the z-coordinates in the bottom layers. We also note that other types of hybrid methods have been developed, such as HYCOM [20], which switches from isopycnal in deep water to sigma coordinates in the coastal areas and then switches to z-coordinates in the surface mixed layer/unstratified sea areas. In a study with the HYCOM model, researchers found that the hybrid model using multiple coordinate systems provided better results than only using one coordinate system [20]. Burchard and Petersen [17] also mentioned that the hybrid methods may provide better results than those of the sigma coordinates or z-coordinates. However, hybrid methods can suffer from problems in the

areas where the coordinate systems switch from one method to another [78]. Finally, an additional issue is the depth at which to switch between coordinate systems.

Several researchers have investigated the unstable or unrealistic results of the BPG term in the context of finite difference models (e.g., [17,42,70]), however, only a few studies have been done in the context of finite element or unstructured grid models. Finite element formulations using triangular elements of the BPG term differ from finite difference formulations using square elements because they include more information from neighboring nodes. In contrast finite difference formulations tend to include only the neighboring nodes that are forward, behind or next to the node being evaluated. Using a finite element model, Walters and Foreman looked at the influence of resolution on the velocity field using sigma coordinates, first varying the horizontal resolution for a fixed vertical resolution and then vice versa [83]. They determined that the sigma coordinate system produced either second- or first-order accurate solutions, depending on the density profile, for the continental shelf region. From their studies, they suggested that the sigma coordinate system should be replaced with z-coordinates. Alternatively, they suggest post-processing the BPG field in order to minimize the sigma coordinate transformation errors.

Fortunato and Baptista evaluated the vertical placement of nodes in sigma coordinates within the framework of finite elements for a barotropic model [36]. They found that an efficient placement of the vertical nodes may take care of the strong dependence of errors on the local flow properties. In order to realize this, they introduced localized sigma coordinates, which allow for more flexibility in the placement of nodes. These localized sigma coordinates differ from a nonuniform sigma coordinate system in the fact that they allow for the vertical nodes to be placed independently for each horizontal

node, while the nonuniform sigma coordinates use the same placement algorithm at each horizontal node. Fortunato and Baptista found that the localized sigma coordinates provide a strong alternative to the traditional sigma coordinates and z-coordinates.

Another investigation by Fortunato and Baptista evaluated all of the horizontal gradients in the momentum equation in either sigma coordinates or z-coordinates in a 2D (width-averaged) barotropic and baroclinic (diagnostic) model [34]. They determined that evaluating all of the horizontal gradients in the sigma coordinate system provided the best approach in most cases; however, in certain cases the z-coordinates proved to be better, in particular for the case study presented in Walters and Foreman [83]. They also provided some guidelines to obtain the proper horizontal resolution for a sigma coordinate model near steep bathymetry gradients [34].

Herein, we build on this earlier work and investigate BPG calculations using several of these coordinate system in the context of a finite element model. This study will only look at different coordinate systems to calculate the BPG term; while all other horizontal gradients in the momentum equation will use sigma coordinates. In this respect, it differs from the work done by Fortunato and Baptista [34], since their work analyzed all the gradients in the momentum equation with either sigma or z-coordinates, independently. We are only analyzing the BPG term with these different coordinate systems since this term has been shown in the applications to be problematic [12]. This study also extends the work done by Walters and Foreman [83] by looking at other coordinate systems for calculating the BPG term besides the sigma coordinates. In this study, we will investigate four different coordinate systems for determining the BPG results: sigma coordinates, z-coordinates and two hybrid systems composed of these two coordinate systems. We look at these coordinate

systems and the effect of grid resolution (horizontal, vertical, and combined) on diagnostic simulation results.

5.2 Background Of The Model

The model utilized in this study is a 2D laterally-averaged (x-z) shallow water model that uses the finite element method; it follows the same development steps as the 3D ADCIRC model [60], as discussed in Chapter 2. We also employ a mode splitting scheme in the solution technique, similar to that of the 3D ADCIRC, in which the external mode solves a 1D (depth-averaged) continuity equation for the elevation field and a 2D (x-z) momentum equation to resolve the velocity field. The depth-averaged velocity values utilized in the continuity equation are obtained from the integration of the 2D momentum equation results. As a final step, we calculate the vertical velocity values using the 2D (x-z) continuity equation.

We replace the primitive continuity equation with the generalized wave continuity (GWC) equation to eliminate the spurious modes that occur with finite element models using the primitive equations [e.g., 48,59,60,64]. The GWC equation is as follows:

$$W^G \equiv \frac{\partial^2 \zeta}{\partial t^2} + G\frac{\partial \zeta}{\partial t} - HU\frac{\partial G}{\partial x} - \frac{\partial}{\partial x}\left[\frac{\partial(HUU)}{\partial x} + gH\frac{\partial \zeta}{\partial x} - M_x - \frac{\tau_{sx}}{\rho_0} + \right.$$

$$\left. \frac{\tau_{bx}}{\rho_0} - GHU - B_x - D_x\right] = 0 \tag{5.1}$$

where ζ is surface elevation above a datum, H is the total fluid depth, and U is the depth-averaged velocity, g is gravity, D_x is the depth-integrated momentum dispersion (momentum transfer due to a non-uniform velocity profile), B_x is the depth-integrated

baroclinic forcing, M_x is the depth-averaged lateral stress term, which is determined from

$M_x = E_l \dfrac{\partial^2 (Hu)}{\partial x^2}$ where E_l is the eddy viscosity coefficient, $\dfrac{\tau_{bx}}{\rho_0} = K_{\text{slip}} u_b$ is the bottom

friction term, where K_{slip} is the linear slip coefficient and u_b is the velocity at the bottom

boundary, and $\dfrac{\tau_{sx}}{\rho_0}$ is atmospheric forcing. In Equation (5.1), G is a numerical parameter

that allows either a pure wave form of the equation when the parameter is small or the

primitive form of the continuity equation if the parameter is large. This code does not

include the Coriolis forcing terms. We currently utilize a constant eddy viscosity

coefficient, E_l, in the lateral stress term.

The current model employs the non-conservative form of the momentum equation,

which is as follows:

$$\mathbf{M} \equiv \frac{\partial u}{\partial t} + u\frac{\partial u}{\partial x} + w\frac{\partial u}{\partial z} + g\frac{\partial \zeta}{\partial x} - \frac{\partial}{\partial z}\left(\frac{\tau_{zx}}{\rho_o}\right) + b_x - m_x = 0 \qquad (5.2)$$

where $\dfrac{\tau_{zx}}{\rho_o} = E_z\left(\dfrac{\partial u}{\partial z}\right)$ is the constitutive law for vertical stress gradient with vertical eddy

viscosity E_z; $m_x = \dfrac{\partial}{\partial x}\left(E_l\dfrac{\partial u}{\partial x}\right)$ is the constitutive law for the lateral stress gradient with a

horizontal eddy viscosity parameter, E_l, which is the same as that used in Equation (5.1).

We are using the non-conservative form of the momentum equation because the current

production code of ADCIRC utilizes this form. In Equation (5.2), we define

$$b_x = g\frac{\partial}{\partial x}\int_z^{\zeta}\frac{(\rho - \rho_0)}{\rho_0}dz \qquad (5.3)$$

which is the BPG.

To evaluate Equation (5.2), we map the terms in the equation onto a generalized

sigma or stretched coordinate system (referred to hereafter as either sigma coordinates or sigma coordinate system), where σ ranges from a at the surface (a is set to 1 herein) to b at the bottom (b is set to -1 herein) and these values remain the same regardless of the change in the bathymetry. The relationship between the sigma coordinate system and the z-coordinate system (referred to hereafter as either z-coordinates or z-coordinate system) is determined from the following:

$$\sigma = a + \left(\frac{a-b}{H}\right)(z - \zeta) \tag{5.4}$$

Based on this relationship between the sigma coordinate system and z-coordinate system, derivatives from the two systems can be related to one another, as shown in Chapter 2 and Appendix 2. The momentum equation in the sigma coordinate system thus becomes:

$$\mathbf{M} \equiv \frac{\partial u}{\partial t} + u \frac{\partial u}{\partial x_\sigma} + w_\sigma \left(\frac{a-b}{H}\right) \frac{\partial u}{\partial \sigma} + g \frac{\partial \zeta}{\partial x} - \left(\frac{a-b}{H}\right) \frac{\partial}{\partial \sigma} \left(\frac{\tau_{zx}}{\rho_o}\right) + b_x - m_x = 0 \tag{5.5}$$

where $m_x = \frac{\partial}{\partial x_\sigma}\left(E_l \frac{\partial u}{\partial x_\sigma}\right)$ and w_σ incorporates terms from the variable transformation (see reference [60] and Chapter 2 for more details). The evaluation of the m_x term occurs along the stretched surfaces directly with no coordinate transformation.

These equations use C^0 linear finite elements for the horizontal and vertical spatial discretization with the exact quadrature rules. For the temporal discretization, a three time-level scheme centered at k is used in Equation (5.1), and a two time-level scheme centered at $k + 1/2$ is used in Equation (5.5). Except for the BPG, all of the horizontal derivatives are evaluated in the sigma coordinate system; the BPG term uses different coordinate systems, as described below.

In this work, we have isolated the BPG term (b_x in Equation (5.5)) and only implement this term differently in accordance with the different coordinate systems. We isolate this term because it has been shown to cause unstable or unrealistic results (as discussed in Section 5.1). Initially, we define a buoyancy term, β (shown in Equation (5.6)), which is then used to evaluate the horizontal gradient in the appropriate coordinate system:

$$\beta = g \int_z^{\zeta} \frac{(\rho - \rho_0)}{\rho_0} dz \tag{5.6}$$

In z-coordinates, the BPG is given as

$$b_{x_z} = \frac{\partial \beta}{\partial x_z} \tag{5.7}$$

while in the sigma coordinate system, the BPG is given as

$$b_{x_z} = \frac{\partial \beta}{\partial x_\sigma} - \frac{\partial z}{\partial x} \frac{\partial \beta}{\partial z} \tag{5.8}$$

Using the coordinate transformations presented in Chapter 2, Equation (2.10), Equation (5.8) becomes the following:

$$b_{x_z} = \overbrace{\frac{\partial \beta}{\partial x_\sigma}}^{(a)} - \overbrace{\left[\left(\frac{\sigma - b}{a - b}\right)\frac{\partial \zeta}{\partial x} + \left(\frac{\sigma - a}{a - b}\right)\frac{\partial h}{\partial x}\right]\left(\frac{a - b}{H}\right)\frac{\partial \beta}{\partial \sigma}}^{(b)} \tag{5.9}$$

In this study, we utilize Equations (5.7) and (5.9), along with a combination of the two, to develop the two hybrid systems investigated in this study. One of the hybrid systems
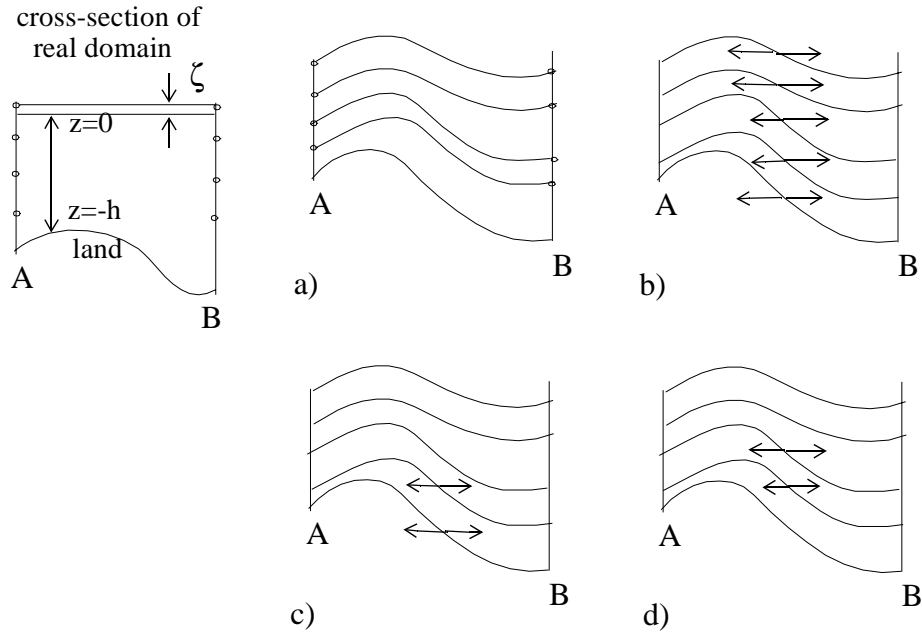
Figure 5.3   Schematic of the four coordinate systems utilized in calculating the BPG term in the momentum balance for the cross-section shown to the left: a) sigma coordinates, b) z-coordinates c) NCOM, and d) SZS. Arrows indicate z-coordinate system calculation of the BPG.

employed in this study follows the system used in NCOM [69], which switches from the sigma coordinates to z-coordinates as the depth increases. In what follows, we refer to this hybrid system as NCOM system or NCOM. The second hybrid system switches from sigma coordinates to z-coordinates at a specific depth then back to sigma coordinates at a second deeper depth. This system is referred to as the SZS (sigma coordinates, z-coordinates, sigma coordinates) system or SZS and is similar to the system for computing the BPG used by Beckers [6].

Figure 5.3 shows a schematic of each coordinate system. In the z-coordinate system BPG implementation, we compute horizontal gradients by interpolating values between adjacent vertical sigma nodes in Figure 5.3b [7,35]. Near bottom boundaries a linear extrapolation technique is used in regions where gradients based on z-coordinates "run into
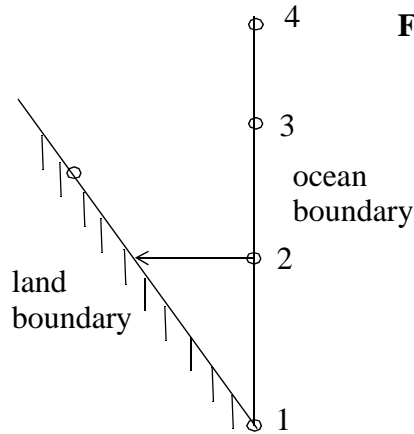
Figure 5.4 Schematic of the "run into the ground" problem with the z-coordinates. In the extrapolation technique, we utilize the two prior vertical node results (i.e., nodes 3 and 4) to obtain the result for node 2 because it has the "run into the ground" problem.

the ground." This linear extrapolation technique can be described using Figure 5.4. For example, if we are computing the gradient at node 2, then we look to the left and right (or all neighbors in 3D) of that node to obtain the density values in the adjacent string of nodes. In this case, when we look to the left and the right we find that there are no adjacent nodes because the ocean is on the right and the horizontal extension to the left runs into the bottom boundary. In this case, the gradient is determined using the previously calculated gradients for the nodes above it. Therefore, we take the gradient values from nodes 3 and 4 in Figure 5.4, and use them to extrapolate a gradient value for node 2. Note that we obtain the gradients for nodes 3 and 4 by using information from the nodes to the left of the ocean boundary.

5.3 Model Validation

The domain used for the model validation is an idealized basin, which provides a good check on the numerical algorithms since, for simple density fields, it has an analytic solution. The idealized basin is 48 km long with 51 nodes in the horizontal ($\Delta x = 960$ m) and 21 layers ($\Delta\sigma = 0.05$) in the vertical. We use a constant bathymetry of 10 m depth ("flat bottom"). Boundary conditions on both ends of the ideal basin are land boundaries

with no-flux boundary conditions. Other conditions of this simulation are as follows: horizontal eddy viscosity mixing processes are neglected (negligible horizontal velocity gradients), vertical eddy viscosity utilizes a constant value of 0.0011 m^2/s, cold start with a 0.1 day ramp, 1-day simulation time with a one second time step which allows the simulation to reach a steady state, G in the GWC solution set to 0.001/sec, linear slip bottom condition with a coefficient of 0.001/sec, and all the nonlinear terms turned on. The density field for this idealized basin varies horizontally from 1024 to 1028 kg/m^3 (left to right) and is constant over depth at each x-location. In this test case, the BPG simplifies to

$$b_x = \frac{g}{\rho_0}\frac{\partial}{\partial x}\int_{-z}^{\zeta}(\rho - \rho_0)dz = \frac{g}{\rho_0}\frac{\partial}{\partial x}\int_{-z}^{0}(\rho - \rho_0)\,dz = \frac{g}{\rho_0}\frac{\partial}{\partial x}(\rho z - \rho_0 z) = \frac{gz}{\rho_0}\frac{\partial\rho}{\partial x} \qquad \textbf{(5.10)}$$

where ρ is a known function of x only, ρ_0 is the reference density, which remains constant at 1000 kg/m^3, and it is assumed that the elevation set-up is small when evaluating this integral (i.e., ζ is set to zero). Numerical tests subsequently verified this assumption.

For the conditions of this idealized basin, Luettich and Westerink [63] derived an analytic solution for the surface elevation and velocity, as given below

$$\frac{\partial\zeta}{\partial x} = -\frac{h}{2}\frac{\partial\rho}{\partial x}\frac{\left(1 + \frac{kh}{4E_z}\right)}{\left(1 + \frac{kh}{3E_z}\right)} \qquad \textbf{(5.11)}$$

$$u = -\frac{g}{6E_z}\frac{\partial\rho}{\partial x}\left(z^3 + \frac{h^3}{4}\right) + \frac{g}{2E_z}\frac{\partial\zeta}{\partial x}\left(z^2 - \frac{h^2}{3}\right) \qquad \textbf{(5.12)}$$

where k is the slip condition, h is the bathymetry, z is the depth and E_z is the vertical eddy
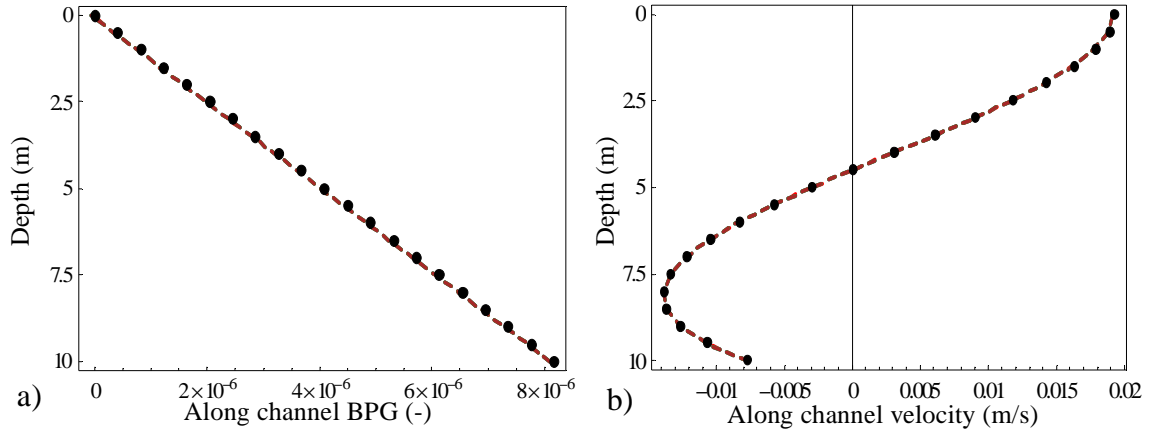
Figure 5.5 Model validation results with the analytical solution shown as black dots and all four coordinate systems used in the calculation of the BPG shown as plots laying on top of the analytical solution. (a-BPG, b-horizontal velocity)

viscosity. A full derivation of the analytical solution occurs in Appendix 4. Figure 5.5 shows the results from this model validation test case for both the BPG and horizontal velocity field. As can be seen all the coordinate system results match the analytical solution. This identical behavior from all of the coordinate systems is expected because of the constant bathymetry of the problem. In such a case, the sigma coordinates and z-coordinates are nearly identical because the coordinate transformation terms (Equation 5.9b) do not play a significant role because $\frac{\partial h}{\partial x}$ is 0 and $\frac{\partial \zeta}{\partial x}$ is very small, thus Equation (5.9a) is like Equation (5.7).

5.4 Procedures

Recall that for this study, all test cases were conducted utilizing the diagnostic mode of the baroclinic model.

5.4.1 Global Spatial Accuracy

The "true solutions" for these 2D x-z experiments were determined either by performing a grid convergence test, where the grid is refined until a chosen convergence

criterion (errors on the order of 10^{-6} m/s) was met, or from known analytical solutions. A discussion of what constitutes a true solution for each domain occurs in the subsequent section. We compared the results from these true solutions to the coarse grid results to measure the errors utilizing the L_2 norm (refer to Equation (3.5)). These errors are determined for the BPG, horizontal velocity and vertical velocity. For each of the domains analyzed, we chose twelve different stations (shown in Figure 5.7) at which to compare results. These twelve stations are representative of the entire domain because we placed them across the domain and in areas where there are significant changes in the bathymetry or density fields. For a measure of global accuracy, we averaged the L_2 errors over time for each of the twelve stations and then averaged the results over the twelve stations to provide one data point for every grid resolution studied. For each of the domains, we analyzed the effects of both horizontal and vertical resolution on the BPG, horizontal and vertical velocities. Horizontal resolution studies hold the number of vertical nodes constant and vary the number of horizontal nodes; while, the vertical resolution studies hold the number of horizontal nodes constant and vary the number of vertical nodes.

5.4.2 Local Spatial Accuracy

To analyze the local spatial accuracy, we followed the same procedures for obtaining a true solution as described in the previous section. We obtain the errors from: $\varepsilon = |c_i - f_i|$ where c_i is the coarse solution and f_i is the fine or true solution. These errors are determined for the BPG, horizontal velocity and vertical velocity. We find the errors at every vertical node for all twelve stations, which are the same stations used in the global spatial accuracy, and average the errors over time. These errors are then graphed for each

vertical node at the twelve stations in the form of a density plot. For two of the domains analyzed, we first hold the vertical resolution constant and then look at the errors for two horizontal resolutions, coarse and fine. Next, we hold the horizontal resolution constant and then look at the errors for two vertical resolutions, coarse and fine. For each of the domains, we also show a plot of the density field and the location of the twelve stations for discussion purposes.

5.4.3 Horizontal/Vertical Resolution Interplay

Next, we analyzed the interplay between horizontal and vertical resolution by varying the number of nodes and looking at the global spatial accuracy results. For each of the domains analyzed, we utilize the resolution matrix presented in Table 5.1, which is

Table 5.1 Matrix for the interplay of horizontal and vertical resolutions.

Vertical nodes	Horizontal nodes				
	9	17	33	65	129
5	x	x	x	x	x
9	x	x	x	x	x
17	x	x	x	x	x
33	x	x	x	x	x
65	x	x	x	x	x
129	x	x	x	x	x

based on interval halving. We evaluated L_2 errors for the BPG, horizontal velocity and vertical velocity by comparing simulation results to the true solution for the domains analyzed. Here again we averaged the L_2 errors over time and then averaged over the

134

twelve stations in order to obtain one point for each grid resolution. For some of the grid resolutions, we found that stable results could not be obtained, and we note this in the results (presented in Section 5.6.2 and Section 5.6.3).

5.4.4 Depth for Hybrid Systems

Last, we examined the best placement for the depth changes for each of the hybrid systems by looking at how the placement impacts global spatial accuracy. For example in the NCOM scheme, we vary the interface between the sigma coordinates and z-coordinates from a shallow depth to a deeper depth in order to determine how the placement of the interface affects the accuracy of the solution.

5.5 Numerical Experiments

Three domains and two different density profiles serve as the test cases for this portion of the study.

5.5.1 Linear Sloping Bathymetry

For this test case, we employ a 48 km long domain with a constant bottom slope varying from 10 m at the shallow end to 100 m at the deep end (approximately a 2% slope), and the density profile varies linearly from 1026 kg/m^3 (shallow) to 1028 kg/m^3 (deep) in the horizontal direction, with no variation in the vertical direction. Boundary conditions are no-flux land boundaries on both sides of the domain. This study utilizes all the nonlinear terms in the equations. Eddy viscosity parameters in both the lateral and vertical directions remain constant at 0 and 0.051 m^2/s, respectively, and bottom friction utilizes a linear slip condition with a K_{slip} value of 0.05 m/s. In this test case, the GWC equation numerical

135

parameter, G, is set to 0.001 sec^{-1}, the time step set to 0.1 sec, and the simulation time set

to 1 day which allows the simulation to reach a steady state. Results were recorded 90 times

over the course of the simulation.

A "true solution" for this test case was obtained by refining the grid in the horizontal

direction until the L$_2$ error changes were within machine accuracy and had reached

convergence, which occurred with a constant nodal spacing of approximately 180 m. This

served as the true solution for the horizontal resolution study. Similarly, for the vertical

resolution study, we refined the grid in the vertical until the L$_2$ error showed that the

solution had converged, which occurred with 129 ($\Delta\sigma = 0.016$) uniformly distributed

vertical nodes. For the interplay study, a horizontal nodal spacing of approximately 180 m

with 129 vertical nodes provided the true solution. The true solution was obtained using the

z-coordinate system for calculating the BPG term; however, we also looked at the results

with the sigma coordinate system and found that results were similar (BPG/velocity error

difference is on order of magnitude 10^{-8}/10^{-6}, respectively.

5.5.2 Idealized Shelf

The second test case, adapted from both Walters and Foreman [83] and Fortunato

and Baptista [34], mimics the shelf break region with bathymetry that varies linearly in

three different regions along a 50 km coastal slice, as shown in Figure 5.6. Density varies

only in the vertical and depends on depth, as shown in Figure 5.6 (equations also shown).

Boundary conditions were no-flux land boundaries on both sides of the domain. Note that

if we change the boundary conditions to a no-flux land boundary on one side and a zero

elevation boundary condition on one side, the magnitude of the results change; however the

$$h(x) = \begin{cases} 10 + 2\left(\dfrac{x}{1000}\right) & \text{if} \quad 0 \leq x \leq 20000 \\[2mm] 50 + 10\left(\dfrac{x - 20000}{1000}\right) & \text{if} \quad 20000 \leq x \leq 25000 \\[2mm] 100 + 20\left(\dfrac{x - 25000}{1000}\right) & \text{if} \quad 25000 \leq x \leq 50000 \end{cases}$$

$$\rho(z) = \begin{cases} 1001 - \cos\left(\dfrac{\pi z}{100}\right) & \text{if } z \geq -100 \\[2mm] 1002 & \text{if } z \leq -100 \end{cases}$$
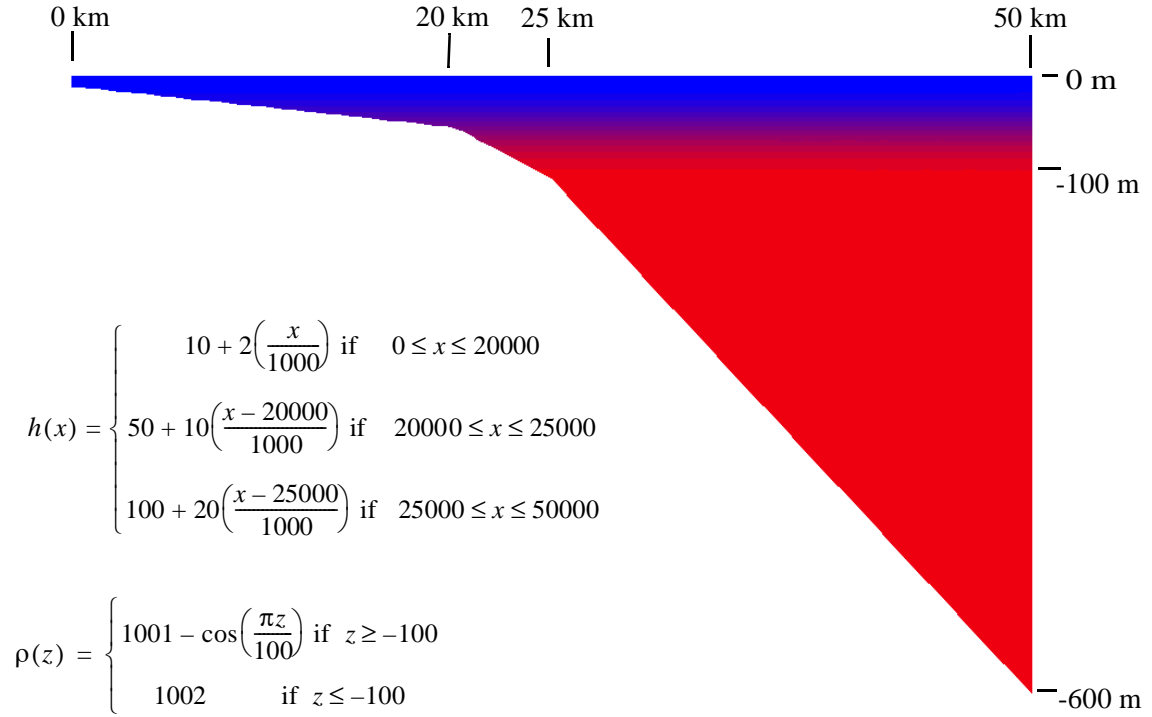
Figure 5.6   Bathymetry and density profiles for the idealized shelf test case. Density values are shown changing from blue in the lighter water to red in the heavier water.

trends are the same. This study utilized all the nonlinear terms in the equations, in particular, we included the advective terms; however, results were similar whether including or excluding the advective terms. Eddy viscosity parameters in both the lateral and vertical directions remained constant at 0 and 0.051 m^2/s, respectively, and bottom friction utilized a linear slip condition with a K_{slip} value of 0.001 m/s. In this test case, the GWC equation numerical parameter, G, was set to 0.001 sec^{-1}, the time step set to 0.1 sec, and the simulation time set to 1 day which allows the simulation to reach a steady state. Results were recorded 90 times over the course of the simulation.

For this test case, we compared the results to an analytical solution. As noted by Walters and Foreman [83] and Fortunato and Baptista [34], the analytical solution for this test case is zero for the BPG and velocity field because there are no boundary forcings, and
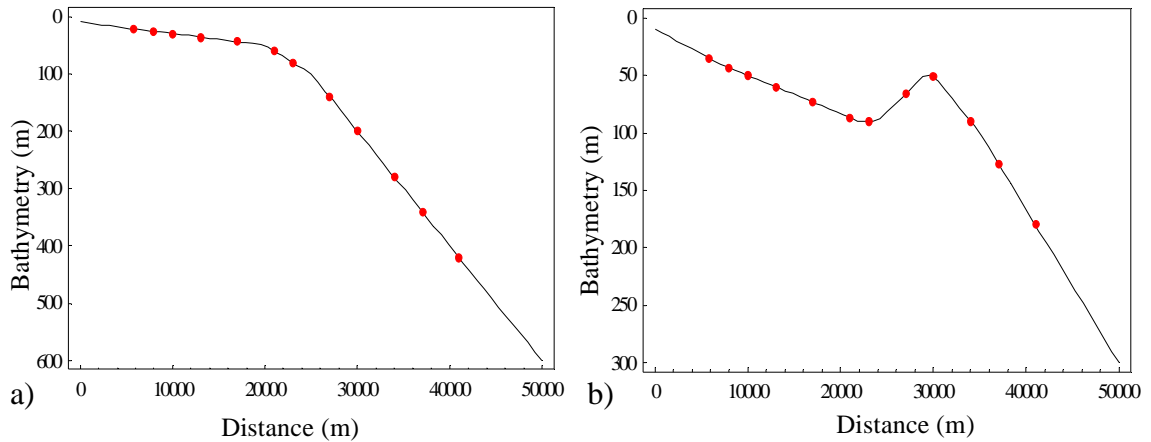
Figure 5.7 Schematic of the bathymetry (shown as a black line) for: a) the idealized shelf test case and b) the seamount test case along with the 12 points (shown as the red dots) used as the comparison stations.

the density varies only in the vertical direction (stable stratification) and not horizontally. The location of the twelve stations for this test case are given in Figure 5.7a.

5.5.3 Seamount

In this test case, we analyzed a different bathymetry with the same density profile as the idealized shelf test case. For the bathymetry, we developed a domain that includes a seamount, along with a change in topography that mimics the continental shelf region (see Figure 5.8). We utilized the following boundary conditions: a no-flux land boundary and elevation boundary of zero on the opposite side of the domain. This study utilized all the nonlinear terms in the equations. Eddy viscosity parameters in both the lateral and vertical directions remained constant at 0 and 0.051 m^2/s, respectively, and bottom friction utilized a linear slip condition with a K_{slip} value of 0.001 m/s. Here again, the GWC equation numerical parameter, G, was set to 0.001 sec^{-1}, the time step set to 0.1 sec, and the simulation time set to 1 day which allows the simulation to reach a steady state. Results were recorded 90 times over the course of the simulation.

$$h(x) = \begin{cases} 10 + 0.0042857x & \text{if} & 0 \le x \le 7000 \\ 40 + 0.00333(x - 7000) & \text{if} & 7000 \le x \le 22000 \\ 90 & \text{if} & 22000 \le x \le 24000 \\ 90 + (-0.008)(x - 24000) & \text{if} & 24000 \le x \le 29000 \\ 50 & \text{if} & 29000 \le x \le 30000 \\ 50 + 0.01(x - 30000) & \text{if} & 30000 \le x \le 35000 \\ 100 + 0.013333(x - 35000) & \text{if} & 35000 \le x \le 50000 \end{cases}$$

Density field same as in Figure 5.6
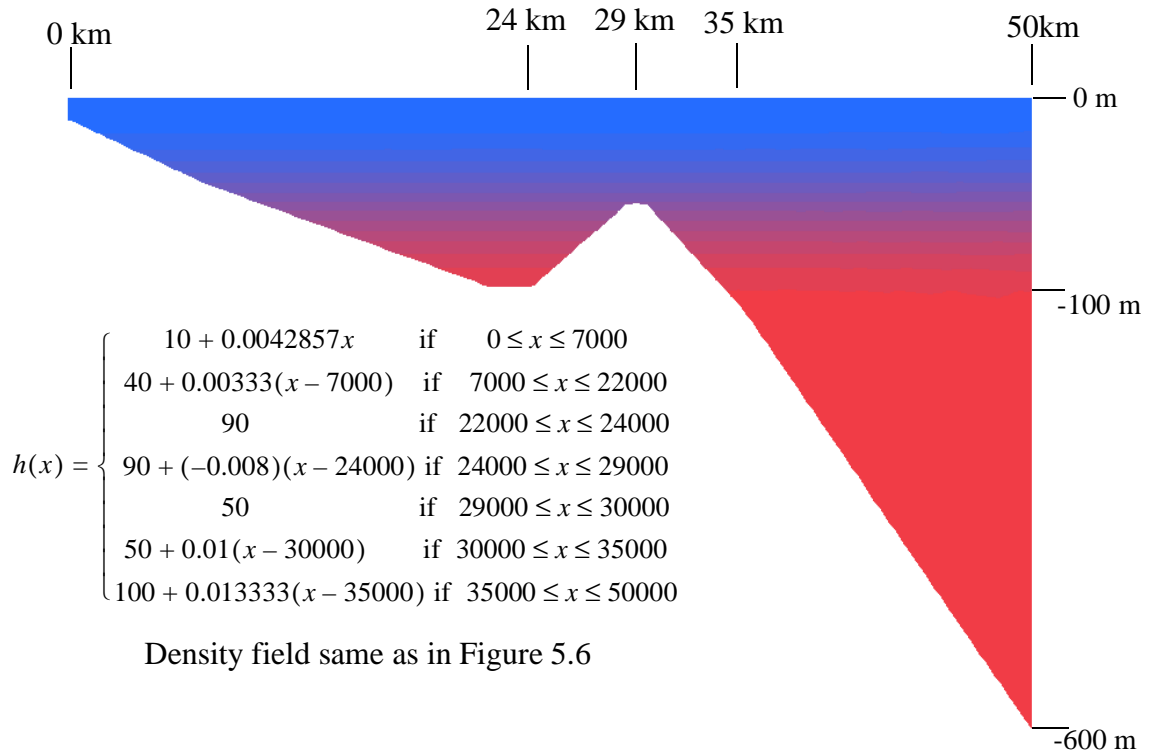
Figure 5.8   Bathymetry and density profiles for seamount test case. Density values are shown changing from blue in the lighter water to red in the heavier water.

As with the idealized shelf test case, we compared the results from this test case to an analytical solution of zero for the BPG and velocity fields, since there are no boundary forcings and the density varies only in the vertical direction (stable stratification) and not horizontally. The locations of the twelve stations for this test case are given in Figure 5.7b.

5.6 Experimental Results

5.6.1 Linear Sloping Bathymetry

Figure 5.9 shows the results of the horizontal resolution study for the BPG, horizontal velocity and vertical velocity. The results of this horizontal resolution study show that the only significant difference between the three coordinate systems for
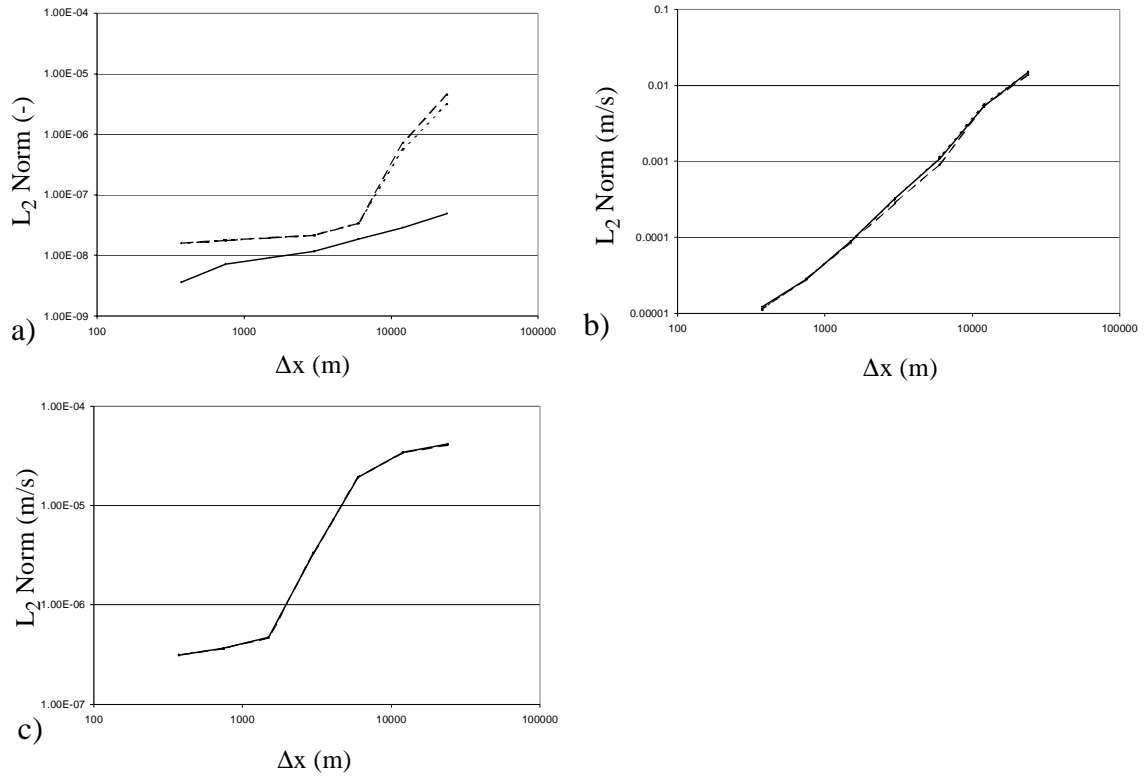
Figure 5.9   Global accuracy results for the linear sloping bathymetry test case for horizontal resolution (vertical number of nodes held constant at 65 nodes or $\Delta\sigma = 0.031$): a) BPG, b) horizontal velocity and c) vertical velocity. Long dashes indicate sigma coordinates, solid line indicates the z-coordinates and short dashes or dots indicate the NCOM system. (SZS system not evaluated for this test case.)

calculating the BPG was in the value of the BPG itself. For all the refinements in the horizontal, the z-coordinate system exhibits nearly constant rate of decrease in the BPG error; however, the sigma coordinates and hybrid schemes show that the BPG errors decreases rapidly until the nodal spacing is approximately 6000 m and then decreases slowly for the more refined grids. These trends in the BPG errors for the sigma coordinates can be explained by looking at the terms in Equation (5.9). For the coarse horizontal resolution, we note that in the sigma coordinates the BPG errors develop more from the truncation errors associated with the coordinate transformation term (Equation 5.9b), but as we refine the horizontal resolution this term in the equation becomes less significant and

the errors are driven more from the truncation errors associated with the derivative of the pressure field over the sigma surface, given by Equation 5.9a. As for the z-coordinates, the errors change more uniformly as the grid is refined because of the nature of the density field, specifically, the density field changes only in the horizontal direction. The average L_2 errors for the horizontal and vertical velocity fields do not show any appreciable changes based on the different coordinate systems for calculating the BPG. We believe this is due to other driving forces besides the BPG values influencing the velocity field, such as changes in the surface gradient. Note that the velocity fields show second order convergence, the theoretical maximum for linear Galerkin schemes.

The vertical resolution study shows that all coordinate systems for computing the BPG produce nearly identical results, as was expected since the variation of the density field is only in the horizontal direction. Similarly, for this model problem, there are no observable changes between the different coordinate systems when looking at the interplay of the horizontal and vertical resolution.

5.6.2 Idealized Shelf

5.6.2.a Horizontal Resolution Studies

Global Spatial Accuracy

Figure 5.10 shows the global spatial accuracy results of the horizontal resolution study for the BPG, horizontal velocity and vertical velocity for the idealized shelf. As can be seen, evaluating the BPG with z-coordinates produce the lowest errors, while sigma coordinates produce the highest errors. Results for the z-coordinates produce the lowest
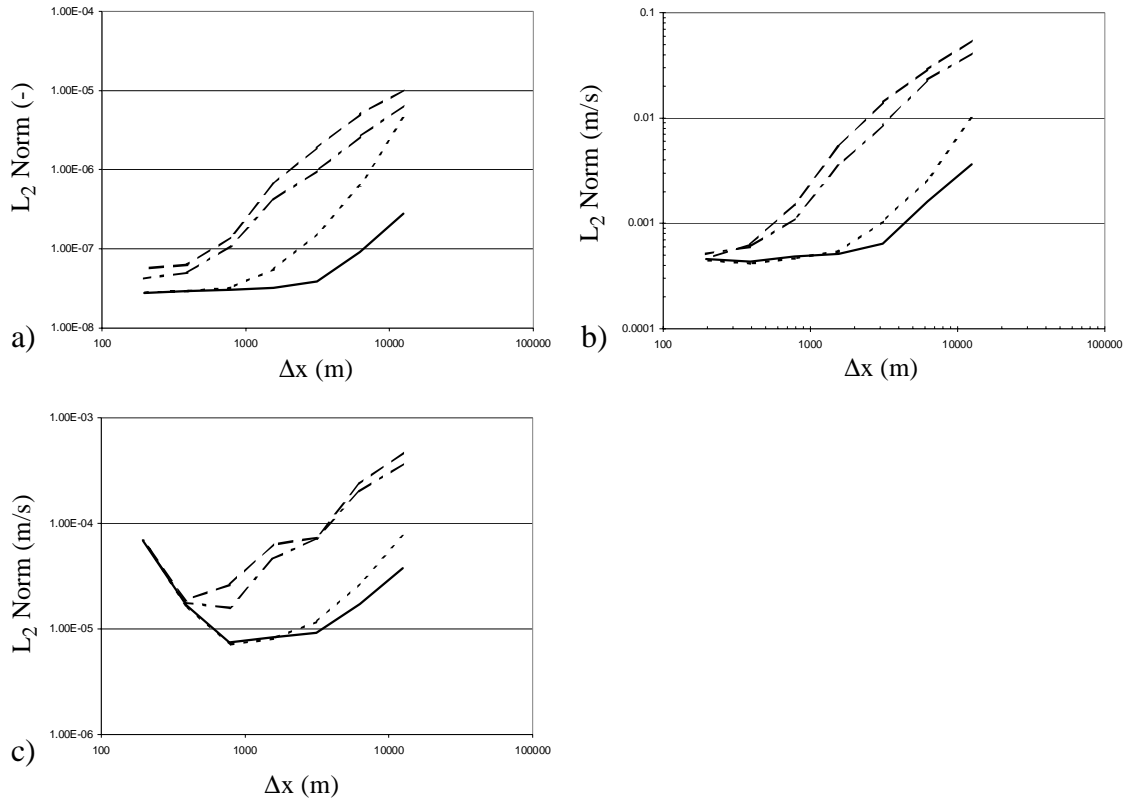
Figure 5.10   Global accuracy results for the idealized shelf test case for horizontal resolution (vertical number of nodes held constant at 65 nodes or $\Delta\sigma = 0.031$): a) BPG, b) horizontal velocity and c) vertical velocity. Long dashes indicate sigma coordinates, dot-dashes indicate the SZS system, solid line indicates the z-coordinates and short dashes or dots indicate the NCOM system.

errors due to the density field varying in a stably stratified nature, thus the changes occur

in layers. Thus derivatives evaluated on a level surface show the minimum error. On the

other hand, the higher sigma error is expected because sigma coordinates are more prone

to errors in evaluating the BPG when the fluid is stably stratified. For the sigma

coordinates, we find high errors at the coarse horizontal resolutions due to the truncation

errors associated with coordinate transformation terms (Equation 5.9b). As we refine the

horizontal resolution, the errors associated with this term decrease (the numerical

approximation of the x-derivatives improve) and truncation errors associated with the

142

derivatives of the pressure terms (Equation 5.9a) along the sigma surfaces begin to dominate. In evaluating the term given in Equation (5.9a), the stretching of the coordinate system in the vertical causes there to be two different density values between two adjacent sigma nodes [34], which leads to nonzero gradients. We also note that errors for the sigma coordinates reach an asymptotic value above the z-coordinate asymptote, which is probably due to the sigma coordinates inability to effectively capture a stably stratified density field because of the stretching of the coordinate system and straddling of interfaces. For the z-coordinates, we find that higher errors also exist at the coarser resolutions, which is due to truncation errors that develop with this system; however, we note that these errors are less than with the sigma coordinates by approximately two orders of magnitude. At the finer horizontal resolutions, we find that the errors for the z-coordinates reach also an asymptotic value, and these errors develop from the interpolation errors that occur in the z-coordinates, that is no matter how much we refine the grid horizontally, we still have vertical nodes that straddle an interface.

Looking at the NCOM results, we notice that when grid resolution is low, the results are closer to the sigma coordinate system since the grid contains more sigma coordinates than z-coordinates. But as we increase the grid resolution, this allows for more horizontal nodes, thus increasing the number of z-coordinates and causing the results to approach that of the pure z-coordinate system. To illustrate this, we examined the z/σ ratio for two different horizontal resolutions, 9 and 33 nodes, with a constant vertical resolution of 17 nodes. We found that for the coarse resolution, the ratio is 1.31, while for the fine resolution, we obtain a ratio of 1.41; thus indicating that adding horizontal resolution increases the relative number of z-coordinates used in the NCOM system. The NCOM

system in this test case switches from sigma coordinates to z-coordinates in an upper layer (at $z = -25$ m), just before there are large changes in density field. Note that the depth at which we switch the coordinate system and bathymetry of the problem also plays a role, an issue that is examined in Section 5.6.2d. Finally as expected, the SZS scheme produces results that fall between the NCOM and sigma coordinate systems, as more of the layers utilize sigma coordinates instead of z-coordinates. However, we should note that the results improve relative to full sigma coordinates by including some z-coordinates. In this scheme, we switch from sigma coordinates to z-coordinates at $z = -25$ m and change back to sigma coordinates at $z = -75$ m; these two depths are where there are large changes in the density fluid. These results follow that of Fortunato and Baptista [34] in indicating that z-coordinates provide the best solution to this test case; however, the NCOM scheme shows promising results.

Also, note that errors in the BPG produce corresponding errors in the horizontal velocity field (as shown in Figure 5.10b). The horizontal velocity results approach nearly the same value for all four coordinate systems for a highly resolved horizontal grid.

Finally, we looked at the vertical velocity errors (shown in Figure 5.10c), which follow a similar pattern as the horizontal velocity errors; however, we find that when looking at the results of the fine resolution there is a upward trend in the results. This upward trend could be due to mass balance errors with the horizontal velocity field.

Local Spatial Accuracy

Next, we examined local spatial accuracy for one coarse horizontal resolution and one fine horizontal resolution to determine where in space the errors occur. The number of

vertical layers was kept constant at 65 nodes or $\Delta\sigma = 0.031$.

First, we analyzed the coarse grid ($\Delta x = 3125\text{ m}$ or 17 nodes) results for the BPG errors, which are shown in Figure 5.11. In this figure, we include results from all four coordinate systems used in the calculation of the BPG; while Figure 5.12 shows a plot of the diagnostic density field and the location of the twelve stations. As with the global spatial accuracy analysis, results show that the z-coordinate system always has the lowest error values by two orders of magnitude (note the scale), while sigma coordinates produce the highest error values. The two hybrid scheme results fall in-between the results for sigma coordinates and z-coordinates.

In the sigma coordinates, we find that most of the errors (red regions) occur over the shelf break region (stations 5-8) where the density field is changing rapidly along with the bathymetry. The errors in the sigma coordinates results occur in this region due to the truncation errors associated with the coordinate transformation terms (see Equation 5.9b), which are approximated over the region with significant changes in the bathymetry between the coarse grid nodes. As for errors in the z-coordinates, we see that most of the errors occur in the same area as the errors in the sigma coordinates but are clustered near the bottom for stations 5-9 and near the upper layers for stations 9-12. The errors with the z-coordinates for stations 5-9 are due to the fact that we must extrapolate the values from some of the results in the upper portion of the water column, since we encounter the "run into the ground" problem shown in Figure 5.4. Regarding the errors at stations 9-12, we see that this is an area where the density values are changing rapidly, which means that we run into interpolation errors. These errors exist whenever we have vertical sigma nodes that straddle an interface between two density values, from which we must interpolate to z-
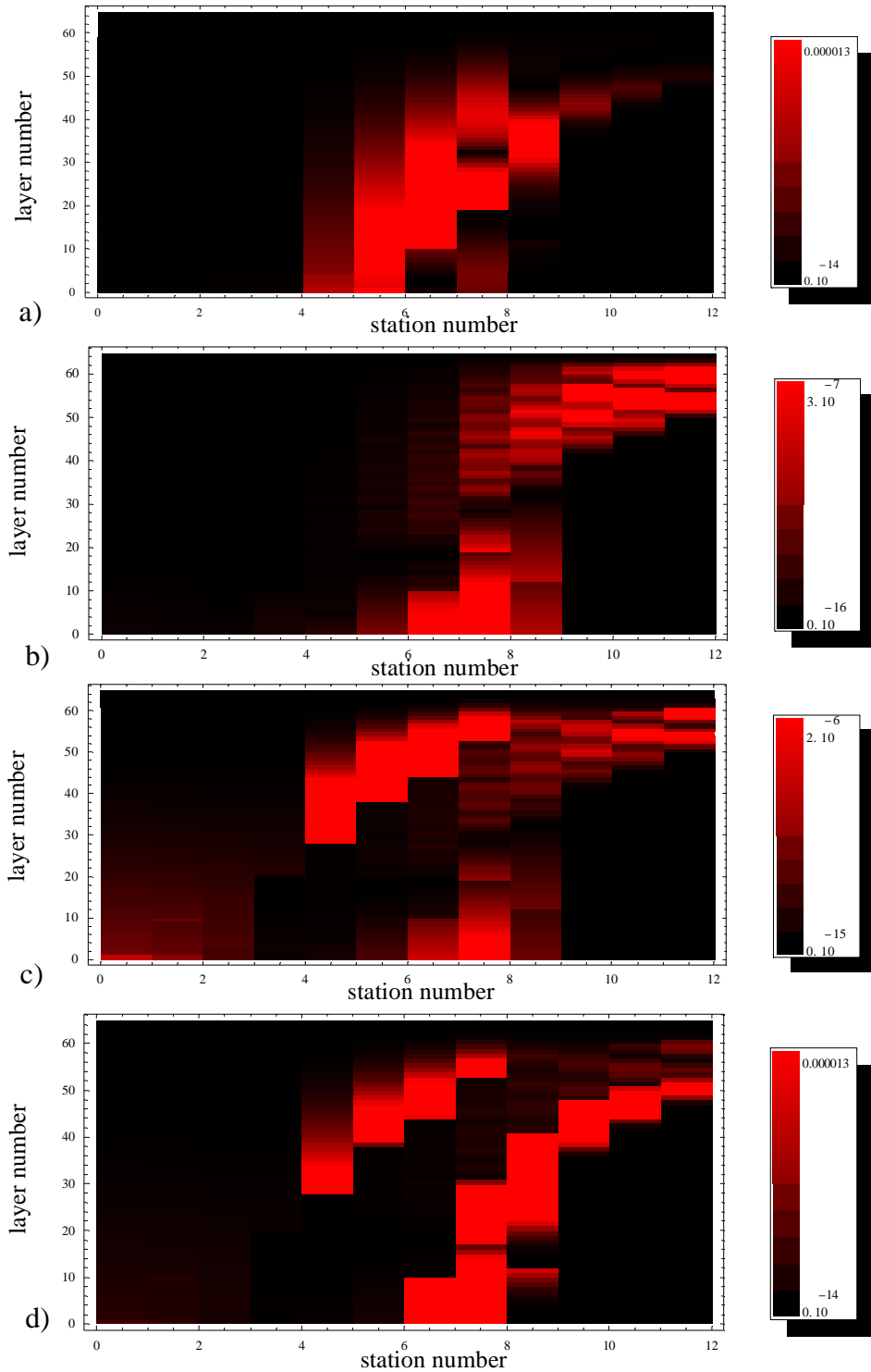
Figure 5.11 BPG error results for the idealized shelf test case for coarse horizontal resolution (vertical number of nodes held constant at 65 nodes or $\Delta\sigma = 0.031$): a) sigma coordinates, b) z-coordinates, c) NCOM system, and d) SZS system.

146
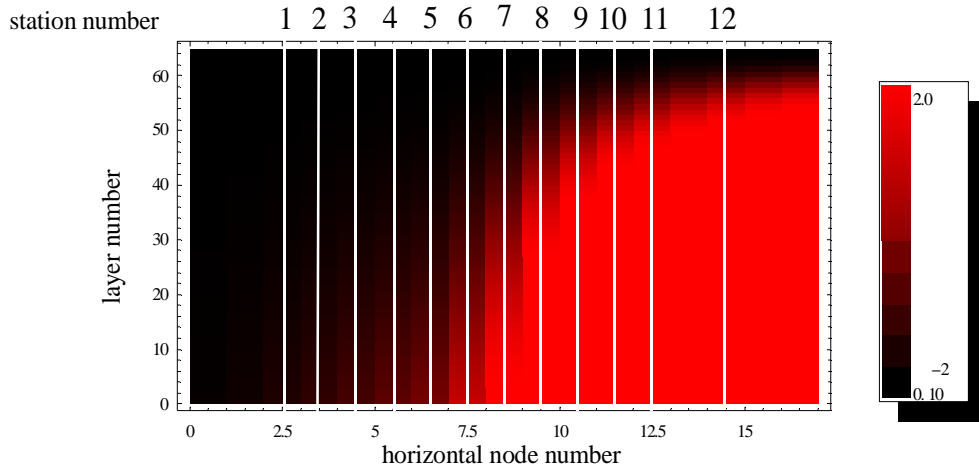
Figure 5.12 Schematic of the density field of the idealized shelf test case for the coarse horizontal resolution with the twelve stations represented by the white lines (see also Figure 5.7).

coordinates.

The NCOM and SZS systems incorporate the errors of both the sigma coordinates and z-coordinates. In the areas that have more sigma coordinates, the results follow those of the sigma coordinates, while in areas that have more z-coordinates, the results are similar to the z-coordinate results. Similar patterns are found for the horizontal and vertical velocity errors (not shown), since these errors result from errors in the BPG field.

Next, we looked at the fine grid ($\Delta x = 391$ m or 129 nodes) results for the BPG errors, which are shown in Figure 5.13. In Figure 5.14, we show a plot of the diagnostic density field and the location of the twelve stations. In these results, we find that the magnitude of the errors for all four coordinate systems are within one order of magnitude difference (note the scales) with z-coordinates and NCOM being the lowest. In sigma coordinates, we find that the errors now occur mostly in the regions where the density field changes (stations 5-12, cf to density field in Figure 5.14). We note that these errors are due to the truncation errors associated with the derivative of the pressure term (Equation 5.9a)

147
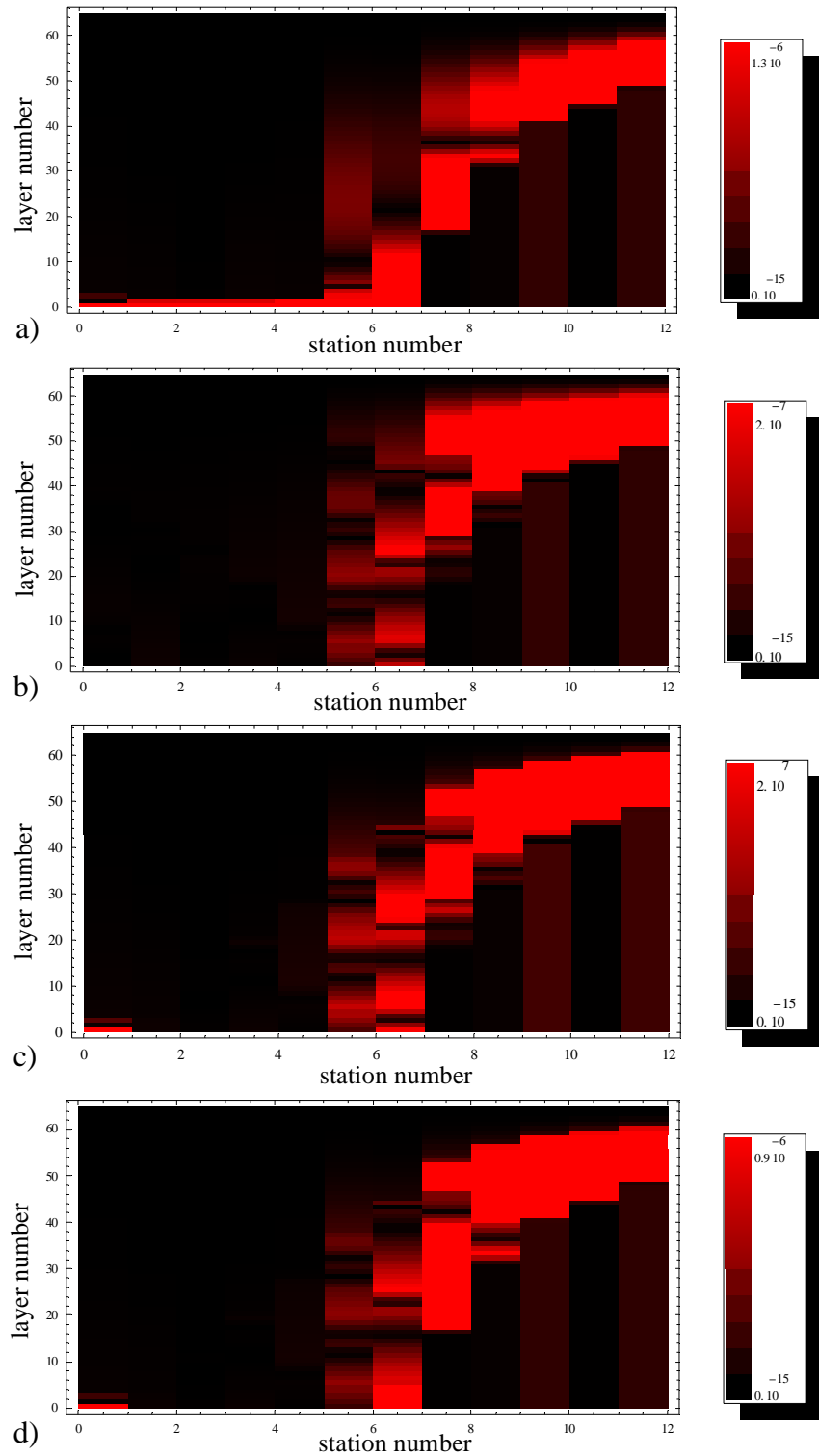
Figure 5.13 BPG error results for the idealized shelf test case for fine horizontal resolution (vertical number of nodes held constant at 65 nodes or $\Delta\sigma = 0.031$): a) sigma coordinates, b) z-coordinates, c) NCOM system, and d) SZS system.
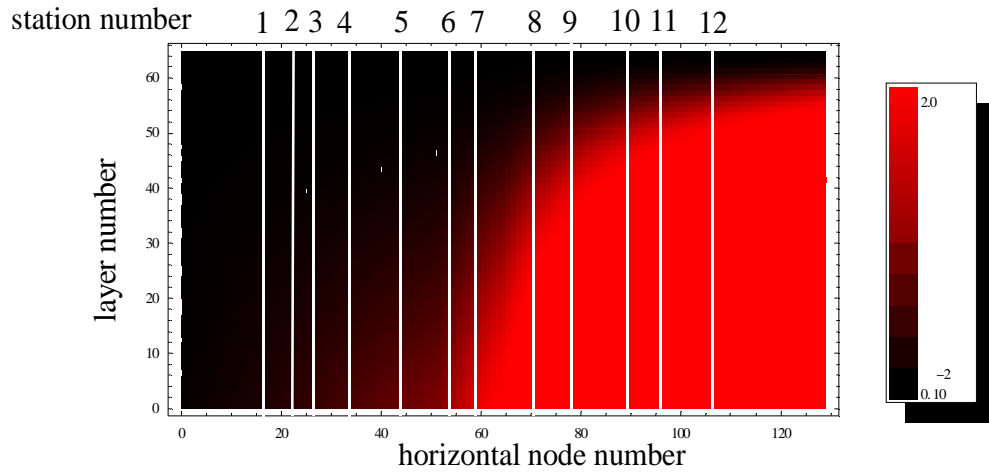
Figure 5.14   Schematic of the density field of the idealized shelf test case for the fine horizontal resolution with the twelve stations represented by the white lines (see also Figure 5.7).

along the sigma surfaces. For the z-coordinates, we find that errors occur in the same location as the sigma coordinates (stations 5-12) and also occur where the density field changes. These errors result from the aforementioned interpolation errors. The behavior of NCOM and SZS systems is similar to the behavior in the coarse resolution study in that they incorporate patterns from both the sigma coordinates and z-coordinates. The horizontal and vertical velocity errors (not shown) are similar to the BPG results since these errors result from errors in the BPG field.

When comparing the fine and coarse grid results, we note that adding more horizontal resolution decreases the magnitude of errors for all coordinate systems. However, we find that the errors decrease in the sigma coordinates more than the z-coordinates because the z-coordinates are not as significantly influenced by the addition of horizontal resolution for this type of density field (use of z-coordinates on a level density field results in small gradient errors). Such behavior is similar to the results from the global spatial accuracy study. As mentioned in that analysis, the errors for the sigma coordinate

system decrease rapidly as more horizontal resolution is added due to the decrease in the influence of the truncation errors associated with the coordinate transformation (see Equation 5.9b).

5.6.2.b Vertical Resolution Studies

Global Spatial Accuracy

We next evaluated the influence of vertical resolution on the BPG and velocity fields. Figure 5.15 shows the results for the BPG, horizontal velocity and vertical velocity.
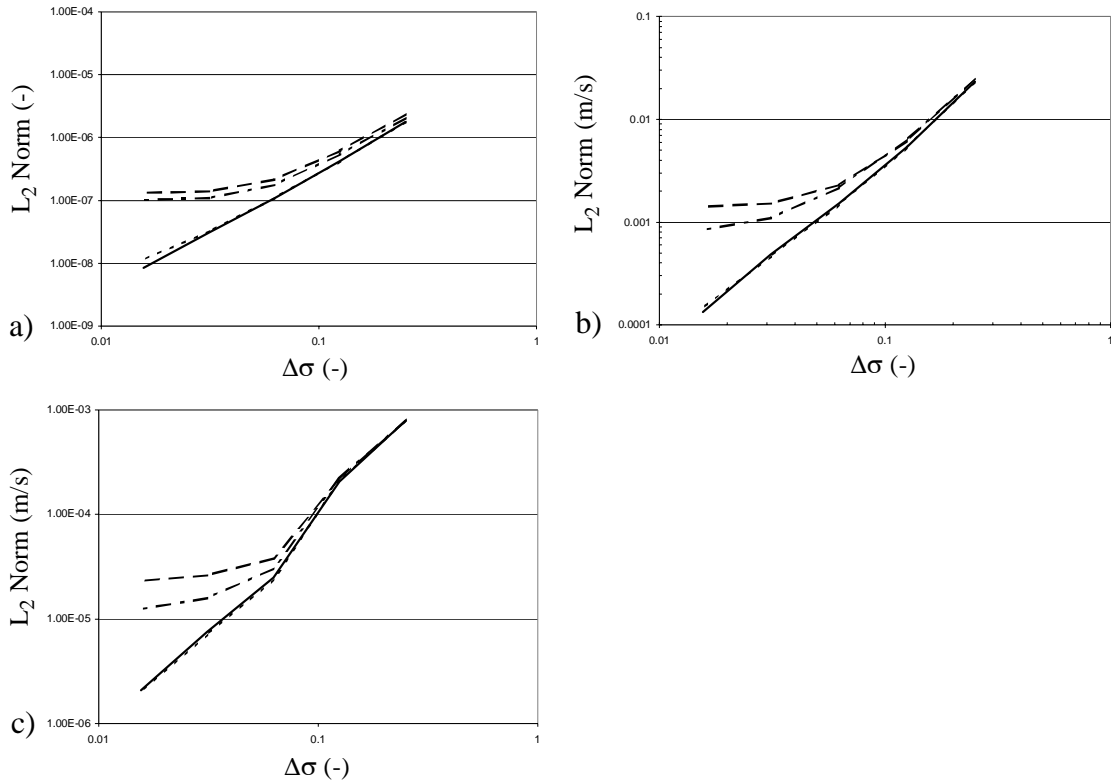
Figure 5.15 Global accuracy results for the idealized shelf test case for vertical resolution (horizontal number of nodes held constant at 65 nodes or $\Delta x = 781$ m): a) BPG, b) horizontal velocity and c) vertical velocity. Long dashes indicate sigma coordinates, dot-dashes indicate the SZS system, solid line indicates the z-coordinates and short dashes or dots indicate the NCOM system.

As can be seen, the errors in the z-coordinate and NCOM systems continue to decrease when more vertical resolution is added; however, for the sigma coordinate and SZS systems, as further vertical resolution is added, the errors start to separate from the other methods (z-coordinates and NCOM) and appear to reach an asymptotic value. For the sigma coordinates, we note that the errors at the coarse vertical resolution develop from the truncation errors associated with both of the terms in Equation (5.9); however, as vertical resolution is added the truncation errors associated with the derivative of the pressure term along the sigma surfaces (Equation 5.9a) decreases, but the errors from the truncation errors associated with the coordinate transformation terms (see Equation 5.9b) plateau out due to the presence of the $\frac{\partial}{\partial x}$ terms in the transformation (remember Δx is held constant). The errors in the z-coordinate continue to decrease as we add more vertical resolution because the coordinate field starts to coincide with the density field. Also, this system relies on interpolation of density values to a level surface and the interpolation error decreases as the vertical spacing is reduced. In theory, we should be able to approach zero with the errors for the z-coordinate system as we continually refine the vertical grid; however, numerically we cannot because of roundoff errors introduced in the interpolation and extrapolation techniques. The NCOM results lay near to the results using z-coordinates due to the relative amount of z-coordinates used in the vertical, while the SZS results lay near the results using sigma coordinates due to the amount of sigma coordinates used in the vertical. Similar trends are found in the horizontal and vertical velocity errors since the BPG is the driving force in this test case.

Local Spatial Accuracy

Next, we examined local spatial accuracy, where we look at one coarse vertical resolution and one fine vertical resolution, to determine where in space the errors occur. The number of horizontal nodes remains constant at 65 nodes or $\Delta x = 781$ m.

The coarse grid ($\Delta \sigma = 0.25$ or 9 nodes) results for the BPG errors are shown in Figure 5.16. In Figure 5.17, we show a plot of the diagnostic density field and the location of the twelve stations. In these results, we find that the magnitude of the errors for z-coordinates and NCOM are nearly identical, and that the magnitude of the errors for the sigma coordinates and SZS are very close to one another. Such behavior is not unexpected due to the relative number of z-coordinates and sigma coordinates in the respective hybrid methods. For sigma coordinates, we find that the highest errors occur near the shelf break region (stations 5-7) with other significant errors obtained in the regions where the density field is changing rapidly (stations 9-12). The errors located along the shelf break region and those located where the density field is changing are due to truncation errors that are associated with both terms in Equation (5.9). As for errors in the z-coordinates, we notice that they occur mostly in the region where the density field changes (stations 7-12), which is indicative of interpolation errors across stratified density fields. Note that the error patterns for the NCOM system more closely follows the pattern for z-coordinates since we have more z-coordinates in this hybrid system; however, the pattern for the SZS system tends to follow the pattern for sigma coordinates since we have more sigma coordinates in this hybrid system. An exception is that in the SZS system, we are able to see some of the influence of the z-coordinates in the lowering of the scale and the error pattern. Overall, we note that most of the errors for the sigma coordinates resides in areas where we have both
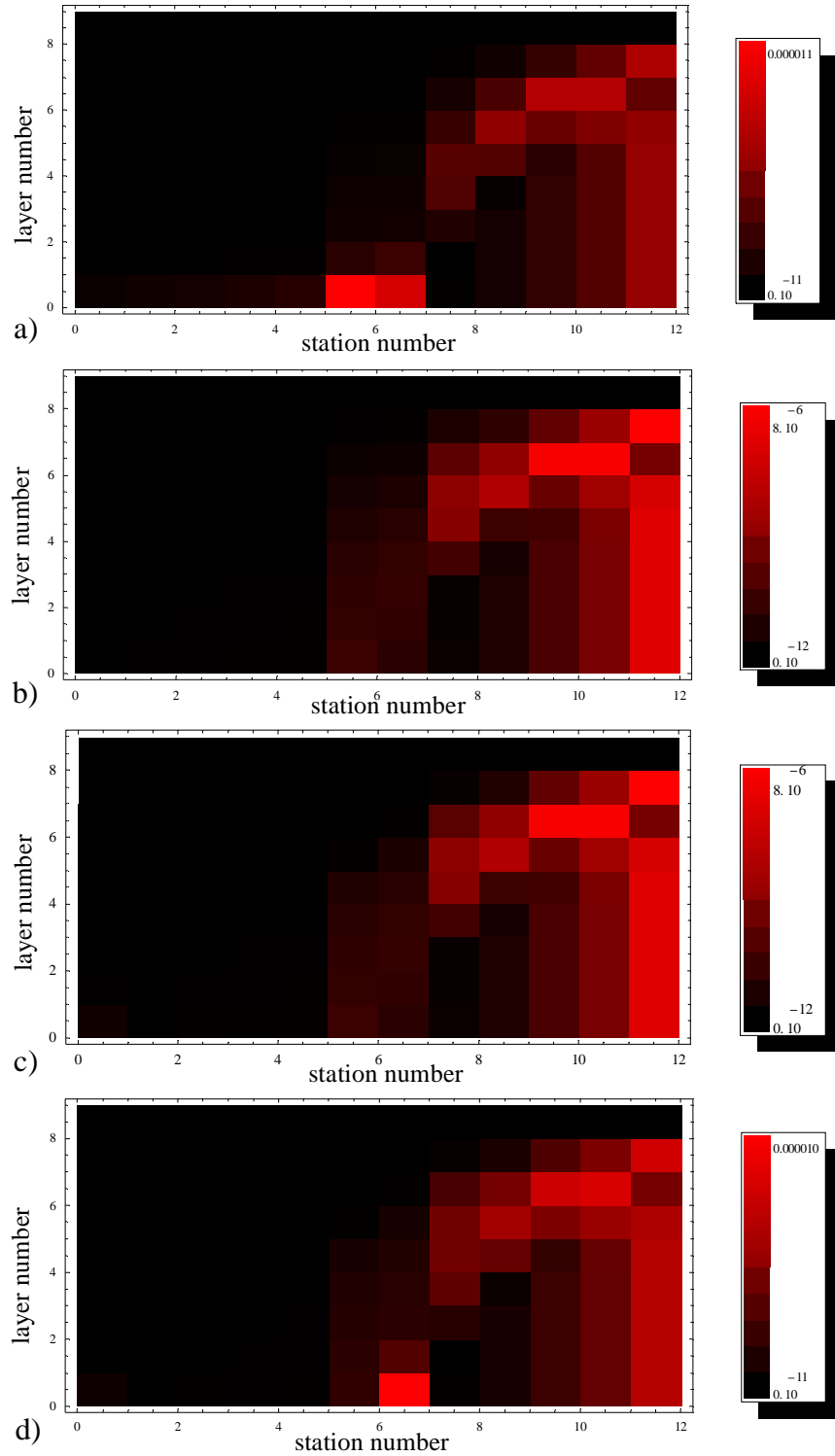
Figure 5.16 BPG error results for the idealized shelf test case for coarse vertical resolution (horizontal number of nodes held constant at 65 nodes or $\Delta x = 781$ m): a) sigma coordinates, b) z-coordinates, c) NCOM system, and d) SZS system.
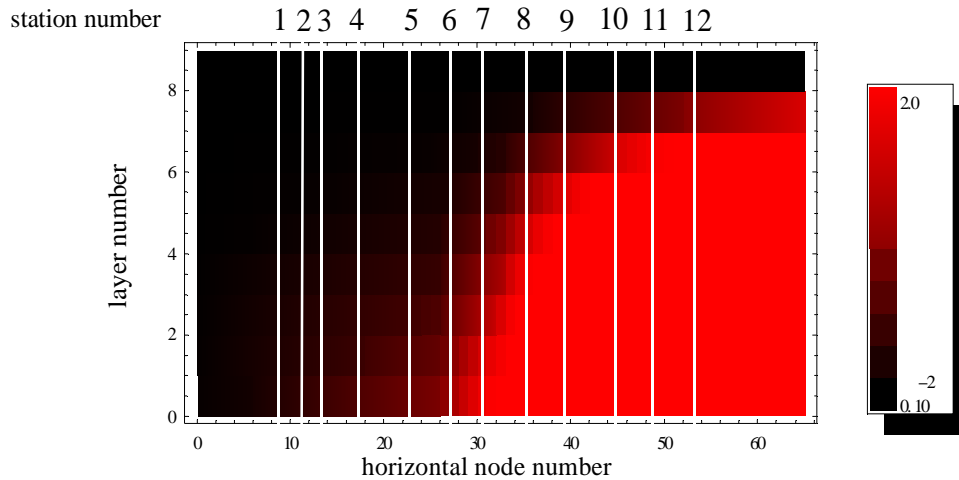
Figure 5.17   Schematic of the density field of the idealized shelf test case for the coarse vertical resolution with the twelve stations represented by the white lines (see also Figure 5.7).

density and bathymetry changes; while, the z-coordinate errors mostly develop in the regions where density changes occur. Similar patterns are found in the horizontal and vertical velocity errors (not shown) since the BPG is the driving force in this test case.

Next, we looked at the fine grid ($\Delta\sigma = 0.031$ or 65 nodes) results for the BPG errors, which is shown in Figure 5.18. In Figure 5.19, we show a plot of the diagnostic density field and the location of the twelve stations. As with the coarse results, we find that the magnitude of the errors are similar for the z-coordinate and NCOM systems, while the magnitude of the errors are similar for the sigma coordinate and SZS systems. In sigma coordinates, we find that errors occur in areas where the density field changes (stations 5-12) with the greatest errors occurring near the shelf break region (stations 5-7). In this shelf break region, the errors most likely come from the truncation errors associated with the coordinate transformation term (Equation 5.9b) because we are not changing the horizontal resolution. As for the z-coordinates, we notice that most of the errors also occur in the regions where the density field changes (stations 5-12, particularly the upper layers in
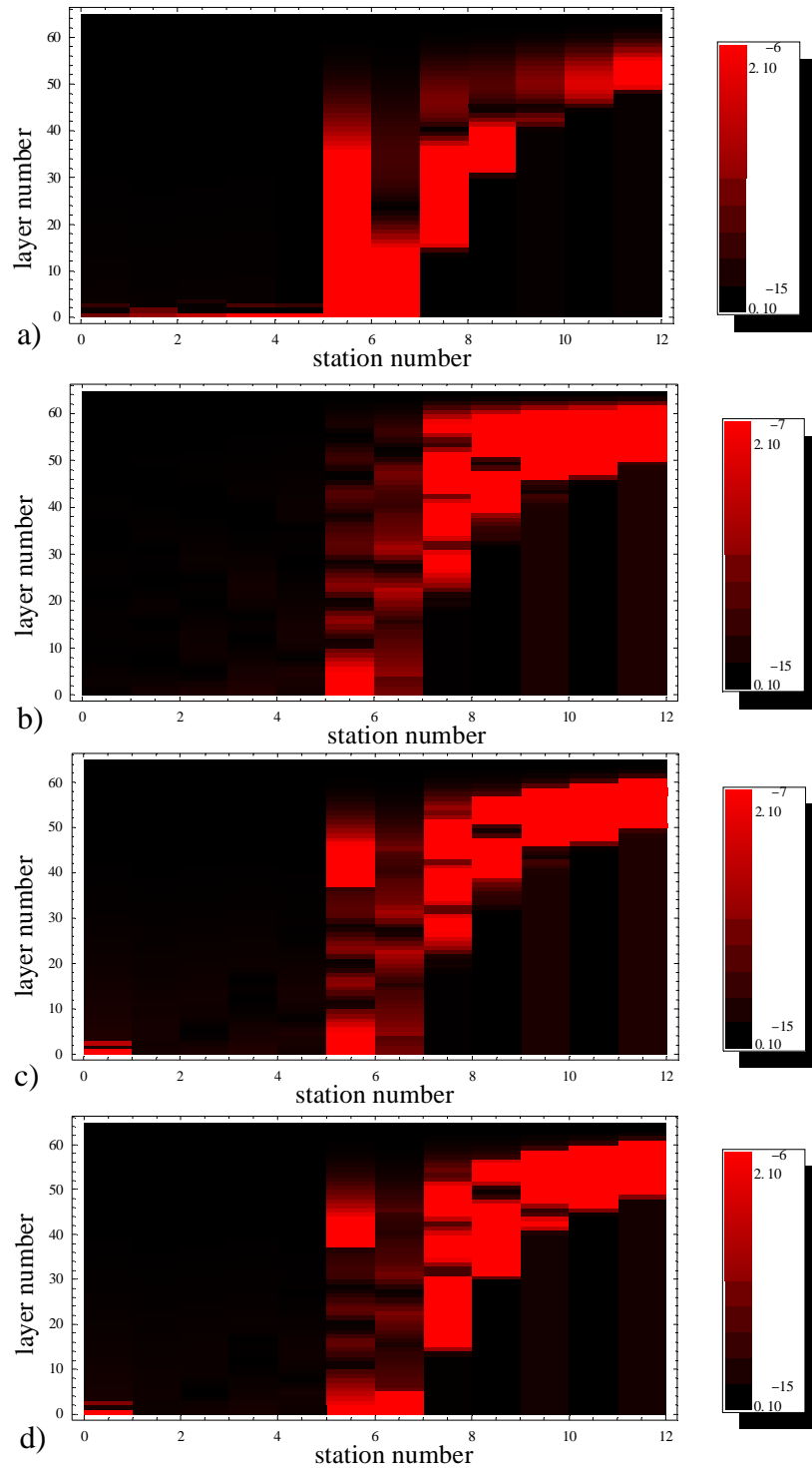
Figure 5.18 BPG error results for the idealized shelf test case for fine vertical resolution (horizontal number of nodes held constant at 65 nodes or $\Delta x = 781$ m): a) sigma coordinates, b) z-coordinates, c) NCOM system, and d) SZS system.
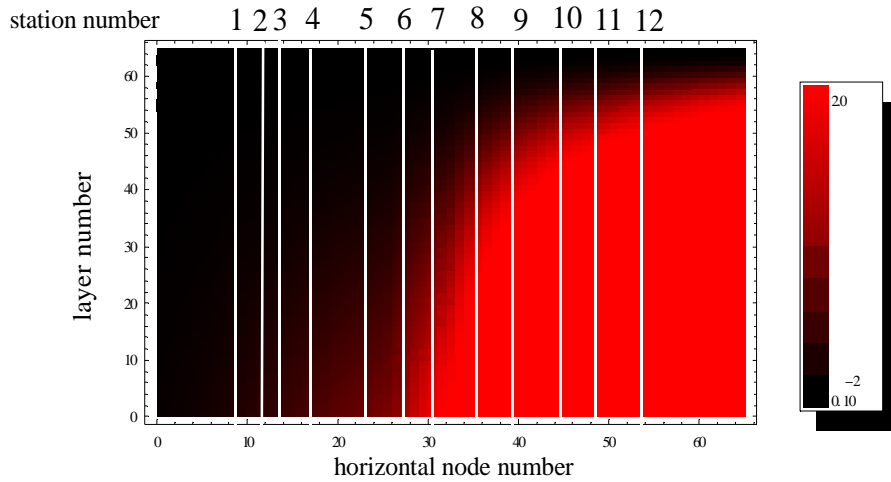
Figure 5.19 Schematic of the density field of the idealized shelf test case for the fine vertical resolution with the twelve stations represented by the white lines (see also Figure 5.7).

stations 8-12). These errors arise because of the aforementioned interpolation errors. In the NCOM system results, we find that the errors are similar to the errors for z-coordinates since this hybrid system uses more z-coordinates; however, we do see the influence of the sigma coordinate system with some of the higher errors over the shelf break region (red coloring at station 5, layers 38-54). In the SZS system, we find that the errors are more a combination of the patterns from sigma coordinates and z-coordinates. In particular, we notice the influence of the sigma coordinate system in the higher errors over the shelf break region (red coloring at station 5, layers 38-54); while the influence of the z-coordinate system is seen in errors that occur between stations 9 through 12 in layers 40 through 60. Similar patterns are found in the horizontal and vertical velocity errors (not shown) since the BPG is the driving force in this test case.

When comparing fine and coarse grid results, we notice that the magnitude of the errors decrease by approximately one order of magnitude for all four coordinate systems. Also, note that the magnitude of the errors are always less for the z-coordinates than the

156

sigma coordinates. At both resolutions, we find that most of the errors for all of the coordinate systems occur in regions where the density field changes the most.

5.6.2.c Horizontal/Vertical Resolution Interplay

We examined the interplay between horizontal and vertical resolution for BPG,
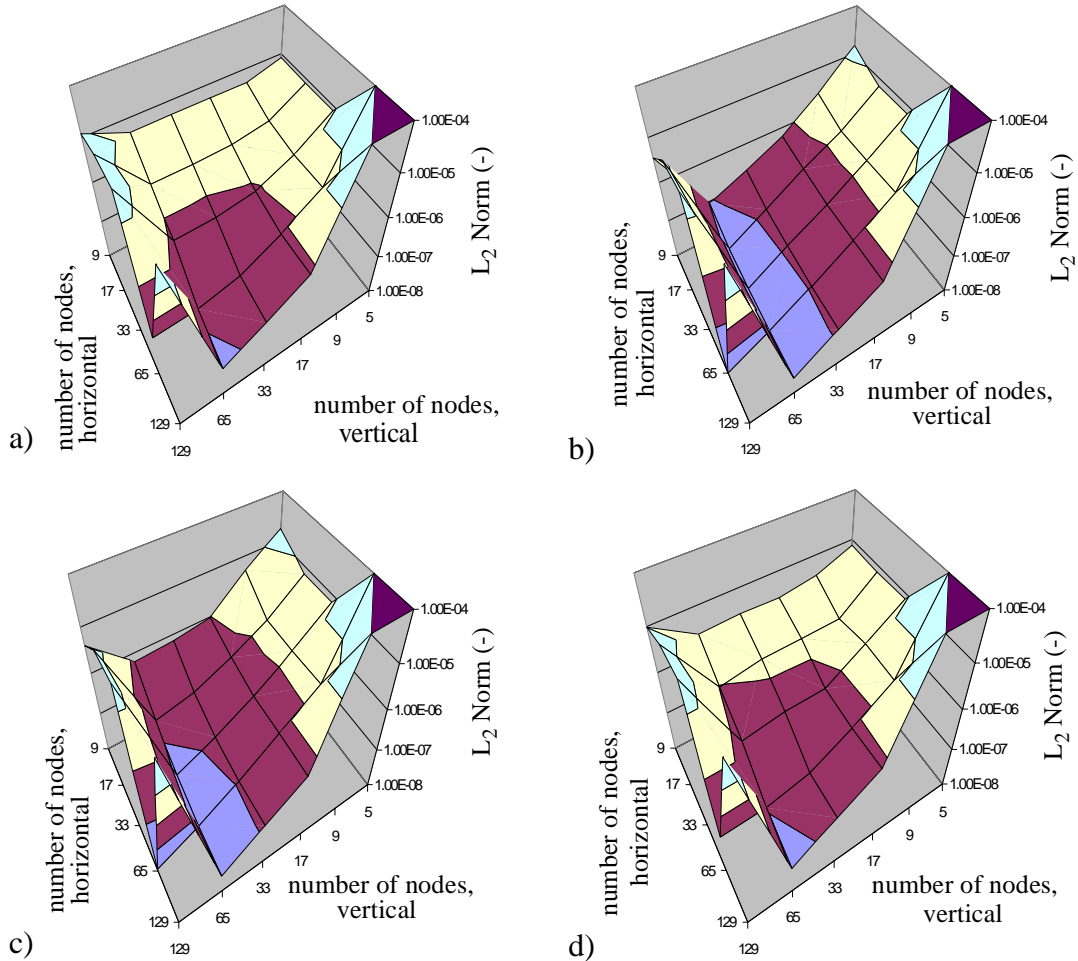
Figure 5.20 BPG errors for the idealized shelf test case for the interplay study. Results are from a) sigma coordinates, b) z-coordinates, c) NCOM system, and d) SZS system.

157
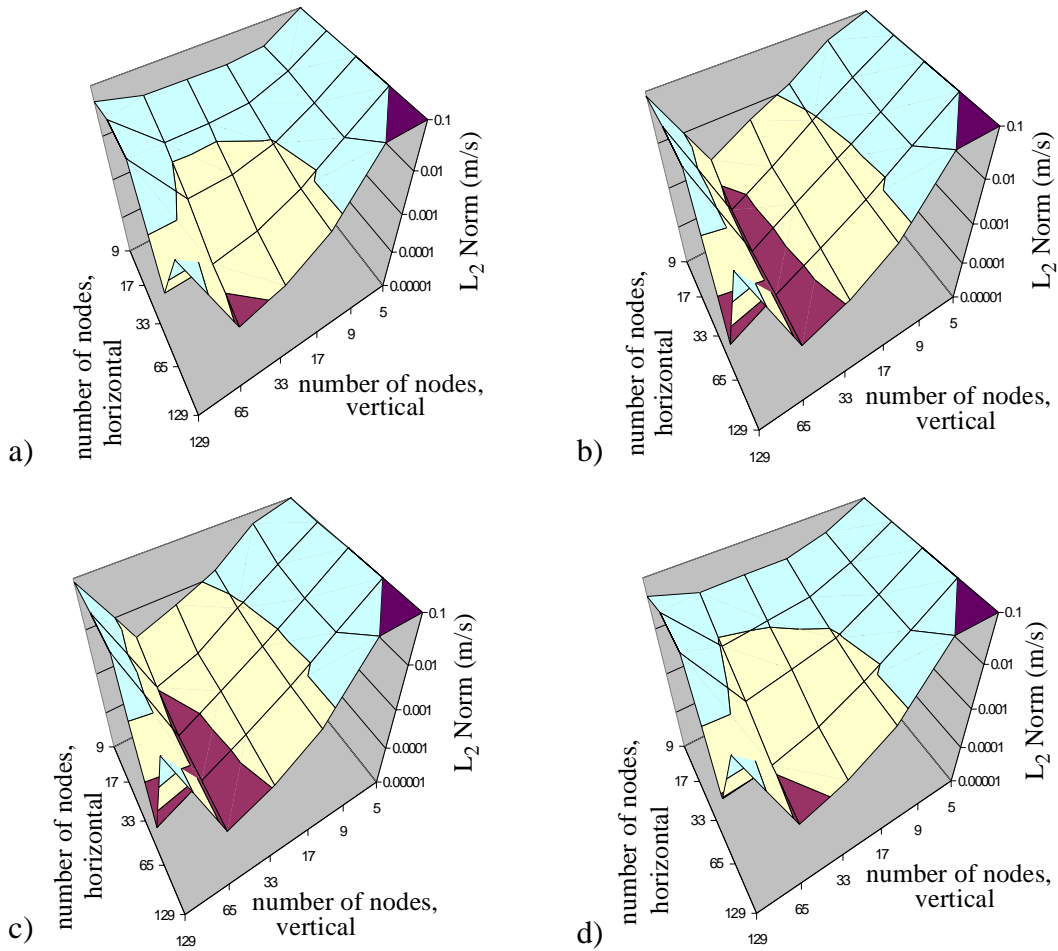
Figure 5.21 Horizontal velocity errors for the idealized shelf test case for the interplay study. Results are from a) sigma coordinates, b) z-coordinates, c) NCOM system, and d) SZS system.

horizontal velocity and vertical velocity errors, as shown in Figures 5.20-5.22, respectively. A matrix of the horizontal and vertical resolutions is given in Table 5.1. Note that if the simulation is unstable, then that result is noted with an arbitrarily high error value for plotting purposes. For example, the simulation using 129 nodes in the horizontal and vertical direction does not produce stable results, so a large error value (1 for BPG or 1 m/s for velocities) is assigned in order to generate Figure 5.20a. In Figures 5.20-5.22, the errors within a given figure are shown on the same scale.
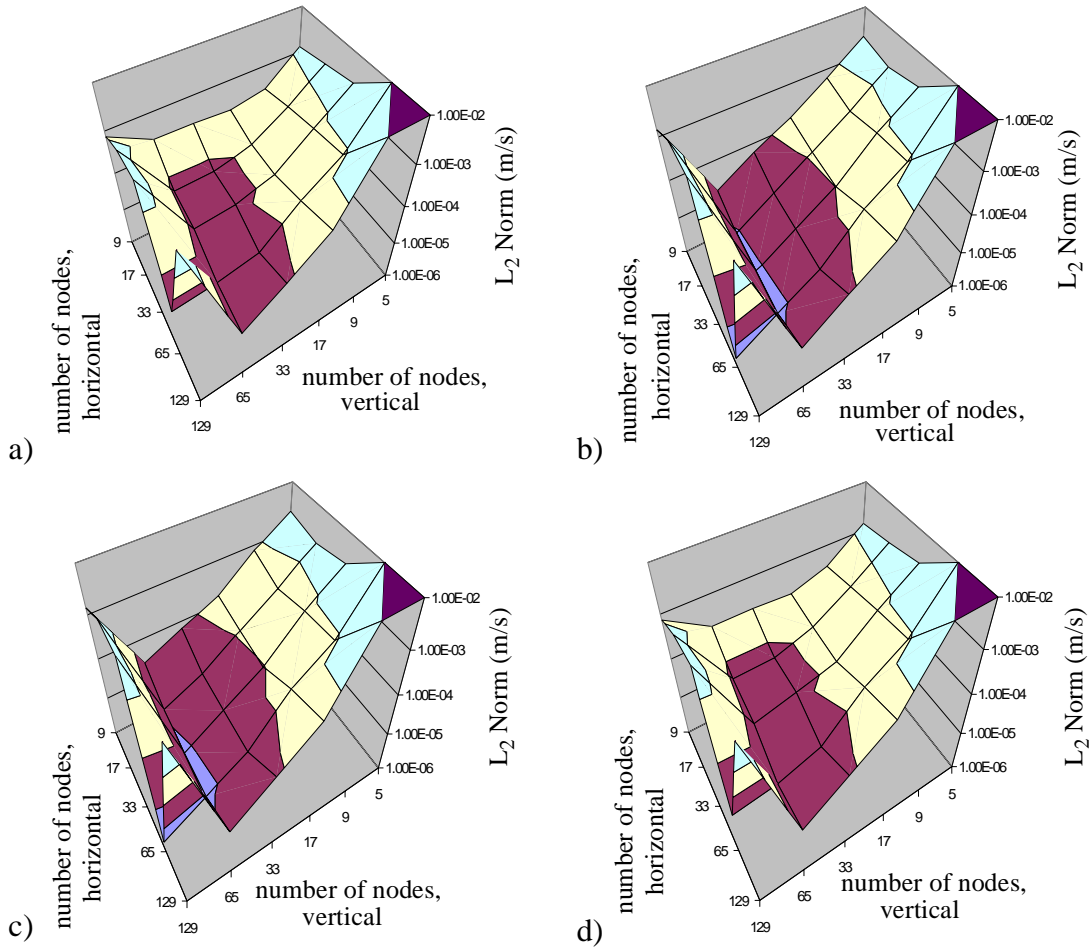
Figure 5.22 Vertical velocity errors for the idealized shelf test case for the interplay study. Results are from a) sigma coordinates, b) z-coordinates, c) NCOM system, and d) SZS system.

Errors in the sigma coordinate and the SZS systems are higher by approximately an order of magnitude than the z-coordinates and NCOM (lowest BPG errors for sigma coordinates and SZS are on the order of 10^{-7}, and for z-coordinates and NCOM they are on the order of 10^{-8}). Overall, we find that the z-coordinate system produces the least overall error. As discussed in the previous section, this is due to the density field being stably stratified, so the z-coordinate system more naturally describes the density changes than the sigma coordinate system. Results also indicate that the NCOM system and z-coordinates

have similar error patterns as refinement occurs in both horizontal and vertical directions. The NCOM system is similar due to the high number of z-coordinates; however, the results with the NCOM system differ from the pure z-coordinate system since it does contain some sigma coordinates particularly at the coarser horizontal resolutions. This is similar to our findings with the global spatial accuracy results for the horizontal resolution study. We also note that the SZS system results are similar to the pure sigma coordinates due to the significant number of sigma coordinates in the SZS system.

We also find that the results from the z-coordinates are influenced more by adding more vertical resolution than by adding horizontal resolution, which is similar to findings from the global spatial accuracy study (see discussion in Section 5.6.2a). As for the sigma coordinates, we notice that this coordinate system is influenced by adding horizontal resolution and vertical resolution. Horizontal and vertical velocity results (shown in Figures 5.21 and 5.22) show the same trends as the BPG because the BPG is the driving force in this test case.

5.6.2.d Depth for Hybrid Systems

Lastly for this test case, we evaluated the depth(s) at which the hybrid systems switch coordinate systems. An analysis of global spatial accuracy shows that for the NCOM scheme, the depth at which sigma coordinates are switched to z-coordinates should be between 20 m and 40 m to provide the lowest errors. This depth range corresponds to the region above the rapid change in the density field (see Figure 5.6). Based on previous discussions, this makes sense because z-coordinates are more adept at handling layered density fields. In the case of the SZS scheme, we found that the depth at which sigma

coordinates are switched to z-coordinates should be between 30 m to 40 m, while the switch back to sigma coordinates should be between 90 m to 100 m. These depth ranges correspond to the region above and below the rapid change in the density field, similar to the NCOM results.

5.6.3 Seamount

The major difference between this test case and the previous one is the bathymetry; the density field is the same. In this section, we present major results from each of the studies; reasons for observed patterns are given in Section 5.6.2 and are not repeated here for the sake of brevity.

5.6.3.a Horizontal Resolution Studies

Global Spatial Accuracy

For this test case, the horizontal resolution study shows similar results as the idealized shelf test case (Section 5.6.2a), with the sigma coordinates error being higher than the other three vertical coordinate systems (see Figure 5.23). BPG results indicate that errors in the NCOM scheme (which switches from sigma coordinates to z-coordinates at $z = -25$ m) coincide with those of the z-coordinates as the grid is refined, while the errors with the sigma coordinates are approximately one-half log cycle higher. The SZS (changes from sigma coordinates to z-coordinates at $z = -25$ m and switches back to sigma coordinates at $z = -75$ m, the depths correspond to the regions above and below the rapid change in the density field) results fall in-between the sigma coordinates and NCOM system. These BPG errors translate into similar error patterns in the horizontal velocity for
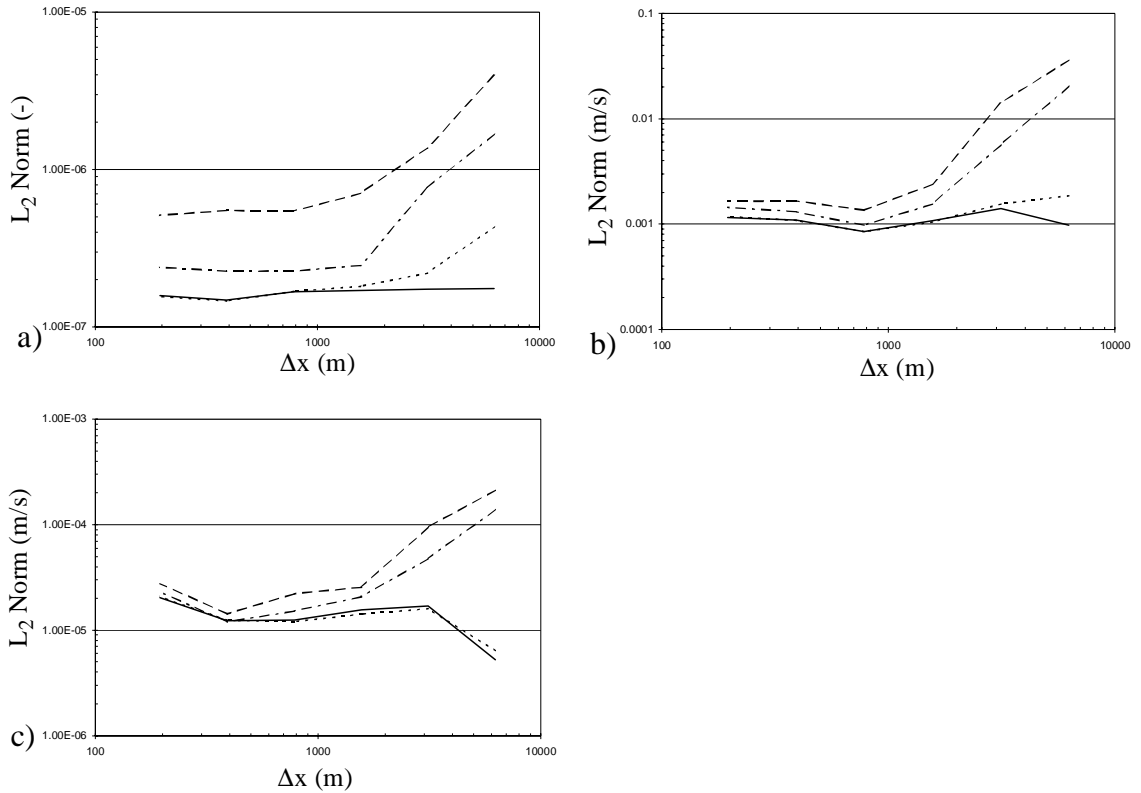
Figure 5.23 Global spatial accuracy results for the seamount test case for horizontal resolution (vertical number of nodes held constant at 17 nodes or $\Delta\sigma = 0.125$): a) BPG, b) horizontal velocity and c) vertical velocity. Long dashes indicate sigma coordinates, dot-dashes indicate the SZS system, solid line indicates the z-coordinates and short dashes or dots indicate the NCOM system.

all of the vertical coordinate systems (cf Figures 5.23a and 5.23b). We find that the vertical velocity errors have the same trends as the horizontal velocity errors.

Local Spatial Accuracy

Next, we examine local spatial accuracy, where we look at one coarse horizontal resolution and one fine horizontal resolution, to determine where in space the errors occur. The number of vertical nodes remains constant at 17 nodes or $\Delta\sigma = 0.125$.

Figure 5.24 shows the coarse grid ($\Delta x = 3125$ m or 17 nodes) results for the BPG errors, for all four coordinate systems. In Figure 5.25, we show a plot of the diagnostic

162
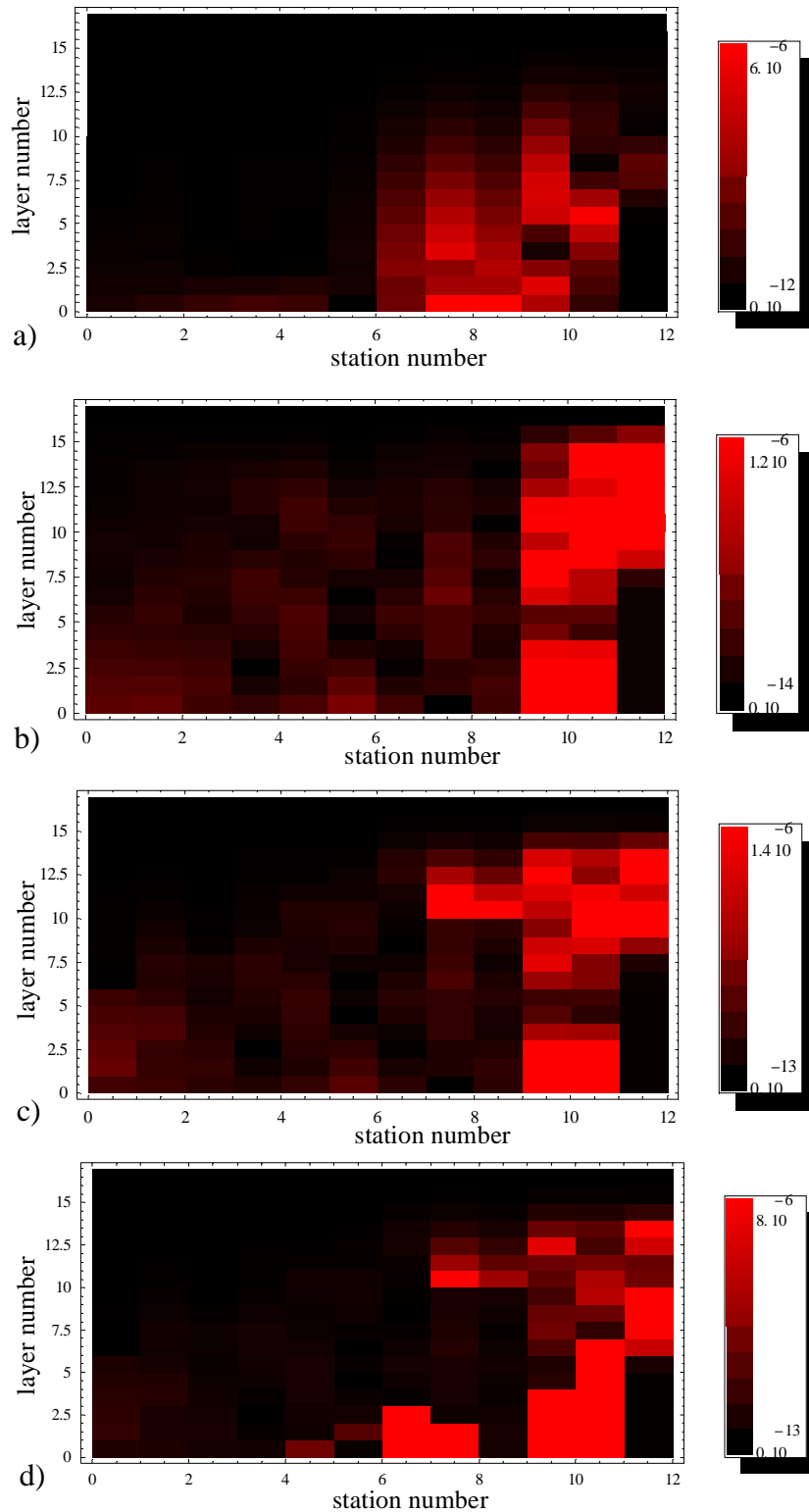
Figure 5.24 BPG errors for the seamount test case for coarse horizontal resolution (vertical number of nodes held constant at 17 nodes or $\Delta\sigma = 0.125$): a) sigma coordinates, b) z-coordinates, c) NCOM system, d) SZS system.
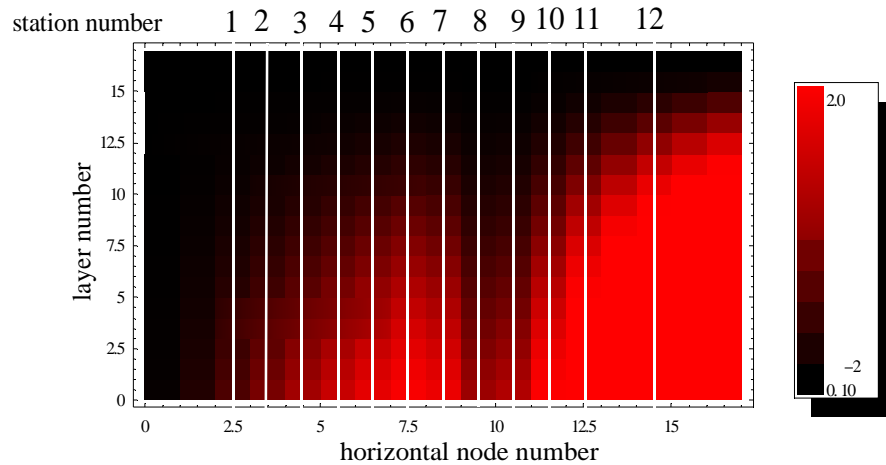
Figure 5.25 Schematic of the density field of the seamount test case for the coarse horizontal resolution with the twelve stations represented by the white lines (see also Figure 5.7).

density field and the location of the twelve stations. Results indicate that for the sigma coordinate system the largest errors appear in the trough and crest parts of the seamount region (stations 6-9); this changing bathymetry causes the truncation errors with the coordinate transformation term (see Equation 5.9b) to influence the errors more in the trough and crest regions than in other regions of the domain. In the z-coordinate system, we find the highest errors where the density field changes in the deeper water (stations 9-12); however, the magnitude of these errors are less than that of the sigma coordinate system. Errors in the calculation of the BPG are high in the deeper water because of the interpolation technique used in the upper layers and the extrapolation technique used in the lower layers. Note that the NCOM and SZS results show a combination of the sigma coordinate and z-coordinate results, as expected. However, it is interesting to note that some of the larger BPG errors that occur in these systems do not appear in the sigma coordinates and z-coordinates; for example, the errors in the middle layers in the trough and crest region of the bathymetry (stations 7-9). This phenomenon may arise because of the

switch in the coordinate schemes. We also find similar error patterns in the horizontal and vertical velocity (not shown) since the driving forcing is the BPG in this test case.

Next, we analyzed the fine grid ($\Delta x = 391\,\mathrm{m}$ or 129 nodes) results for BPG errors, which are shown in Figure 5.26. In Figure 5.27, we show a plot of the diagnostic density field and the location of the twelve stations. Results indicate that at this finer horizontal resolution the errors decrease for all four coordinate systems with z-coordinates and NCOM being lowest for reasons discussed in Section 5.6.2a. The errors with the sigma coordinates occur in areas where the density field and bathymetry changes rapidly as in the crest of the seamount (stations 7-9) and also in the deeper portion of the domain (stations 10-12). These errors are influenced by both the truncation errors associated with the pressure terms along the sigma surfaces and the coordinate transformation term (see Equation 5.9). As for the z-coordinates, we find that the errors exist mostly in the deep portion of the ocean (stations 10-12) where the density field changes. These develop from the interpolation errors in mapping the density values to z-coordinates, in calculating the BPG. The NCOM system shows similar results to the z-coordinate system since it uses more z-coordinates than the sigma coordinates. For the SZS system, we find that the errors are similar to those of the sigma coordinates since it uses more sigma coordinates. However, the influence of the z-coordinates can be seen in the reduction of the errors found near the crest of the seamount (stations 7-9). Finally, we find similar error patterns in the horizontal and vertical velocity (not shown) since the driving forcing is the BPG in this test case.
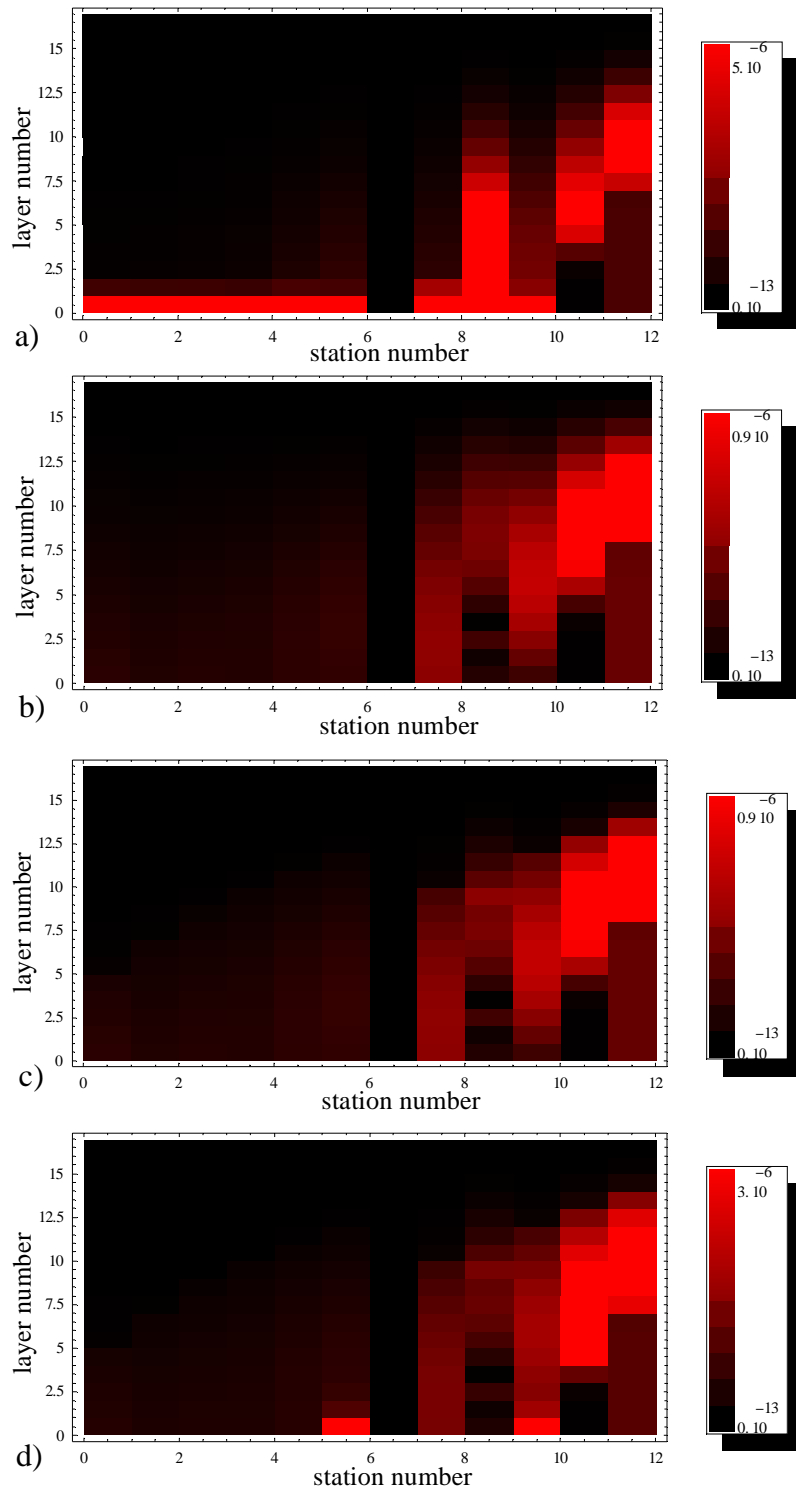
Figure 5.26 BPG errors for the seamount test case for fine horizontal resolution (vertical number of nodes held constant at 17 nodes or $\Delta\sigma = 0.125$): a) sigma coordinates, b) z-coordinates, c) NCOM system, and d) SZS system.
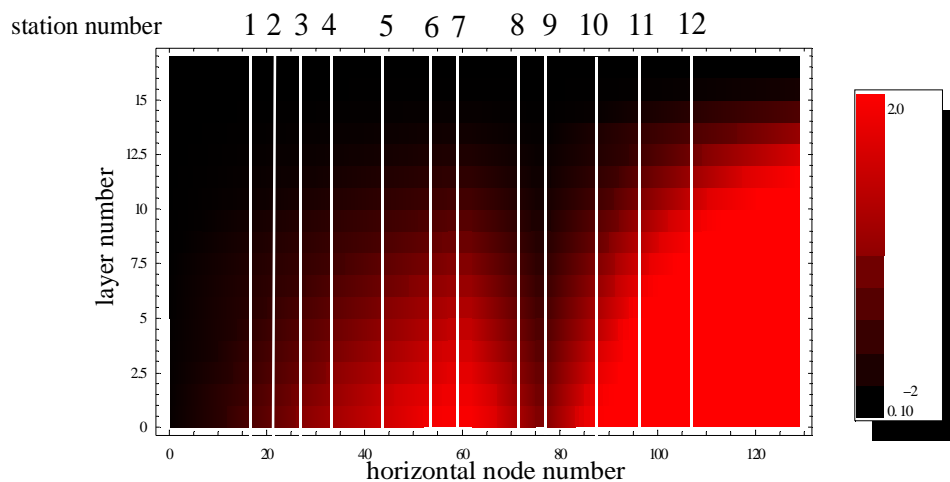
Figure 5.27   Schematic of the density field of the seamount test case for the fine horizontal resolution with the twelve stations represented by the white lines (see also Figure 5.7).

5.6.3.b Vertical Resolution Studies

Global Spatial Accuracy

Figure 5.28 indicates how vertical resolution affects the errors in the BPG, horizontal velocity and vertical velocity. Results from the z-coordinates and NCOM system have less error than the results from the sigma coordinates and SZS system. Also, the sigma coordinate and SZS systems tend toward an asymptote for the BPG. Horizontal and vertical velocity have similar errors due to the BPG being the driving force. The patterns are very similar to the idealized shelf case (Section 5.6.2b), and the reasons for this behavior are discussed therein.

Local Spatial Accuracy

Next, we examine local spatial accuracy, where we look at one coarse vertical resolution and one fine vertical resolution, to determine where in space the errors occur.

167
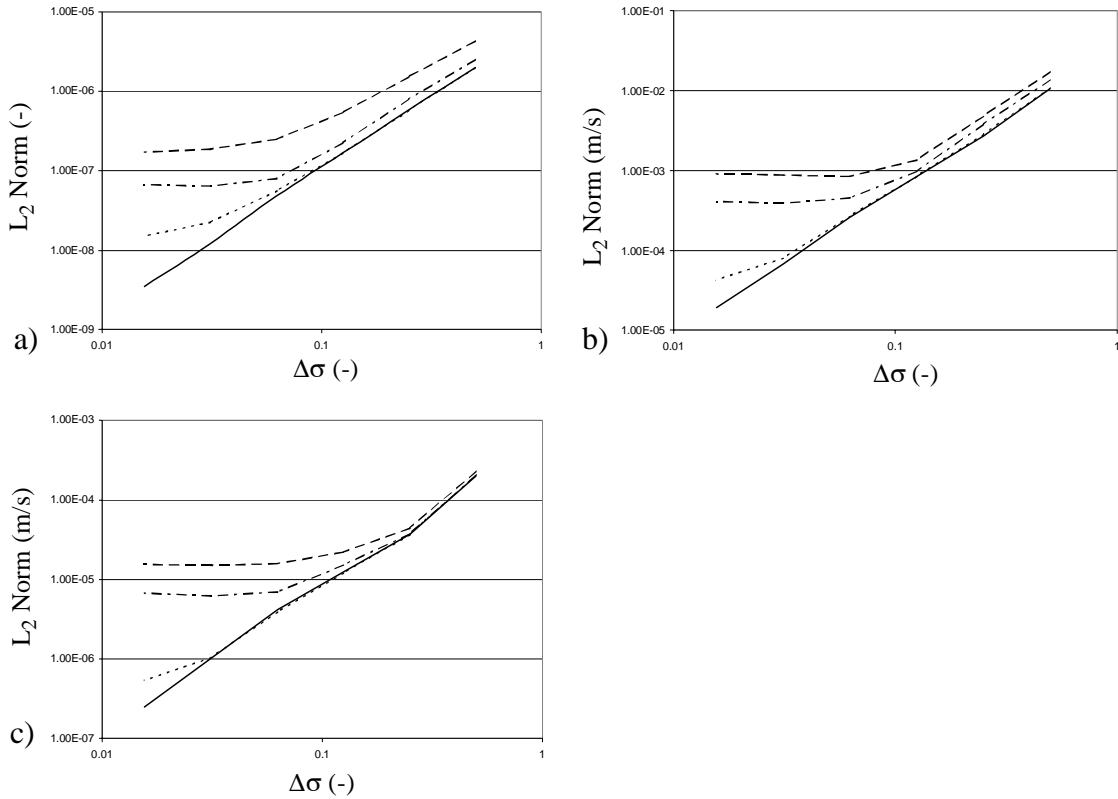
Figure 5.28 Global spatial accuracy results for the seamount test case for vertical resolution (horizontal number of nodes held constant at 65 nodes or $\Delta x = 781$ m): a) BPG, b) horizontal velocity and c) vertical velocity. Long dashes indicate sigma coordinates, dot-dashes indicate the SZS system, solid line indicates the z-coordinates and short dashes or dots indicate the NCOM system.

The number of vertical nodes remains constant at 65 nodes or $\Delta x = 781$ m .

Coarse grid ($\Delta\sigma = 0.25$ or 9 nodes) results for BPG errors are shown in Figure 5.29. In Figure 5.30, we show a plot of the diagnostic density field and the location of the twelve stations. As can be seen, the errors for sigma coordinate system are largest at stations 1 through 6 and 8 through 10 in the bottom layer. If one examines Figure 5.7 in conjunction with Figure 5.8, we find that these are the locations where the bathymetry and density field change rapidly. Thus truncation errors associated with both terms in Equation (5.9) contribute to the BPG errors. In the z-coordinate system, we find the highest errors occur
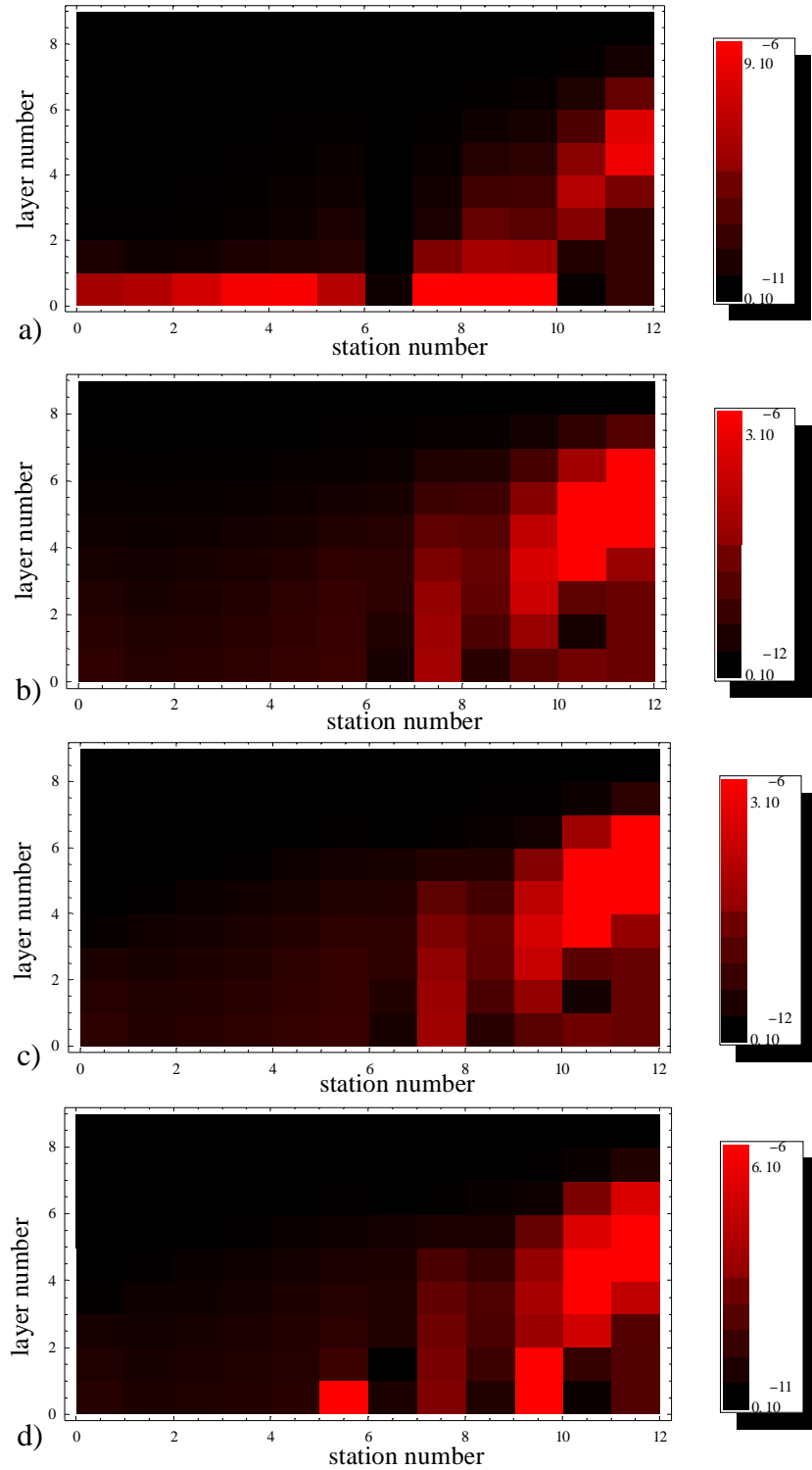
Figure 5.29 BPG error results for the seamount test case for coarse vertical resolution (horizontal number of nodes held constant at 65 nodes or $\Delta x = 781$ m): a) sigma coordinates, b) z-coordinates, c) NCOM system, d) SZS system.

169
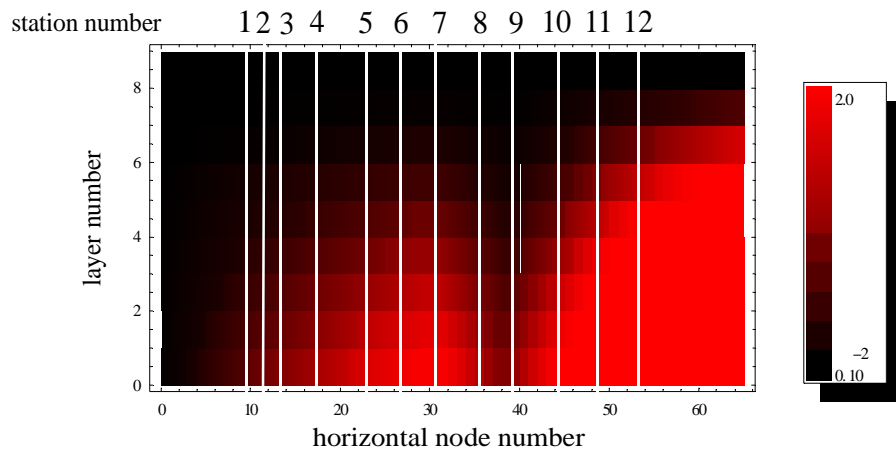
Figure 5.30   Schematic of the density field of the seamount test case for the coarse
vertical resolution with the twelve stations represented by the white
lines (see also Figure 5.7).

in the area where the density field changes rapidly. These areas show high errors because

of the interpolation techniques used in the calculation of the BPG. As before, we note that

the NCOM and SZS system BPG errors show a combination of the patterns for the sigma

coordinates and z-coordinates. We also note that the horizontal and vertical velocity errors

(not shown) are similar to the BPG errors since the driving force is the BPG.

Next, we analyzed the fine grid ($\Delta\sigma = 0.031$ or 65 nodes) results for the BPG

errors, which are shown in Figure 5.31. In Figure 5.32, we show a plot of the diagnostic

density field and the location of the twelve stations. As before, we find that the lowest errors

occur with the z-coordinate system. Results show that the errors for both the sigma

coordinates and z-coordinates increase by half an order of magnitude relative to the coarse

grid results. The sigma coordinate results show BPG errors that are higher in the trough and

crest regions of the seamount (stations 7-10) due to both the evaluation of the gradients of

the pressure term along the sigma coordinates and the coordinate transformation term

(Equation 5.9). In the z-coordinate system, we find the highest errors in the areas where the

170
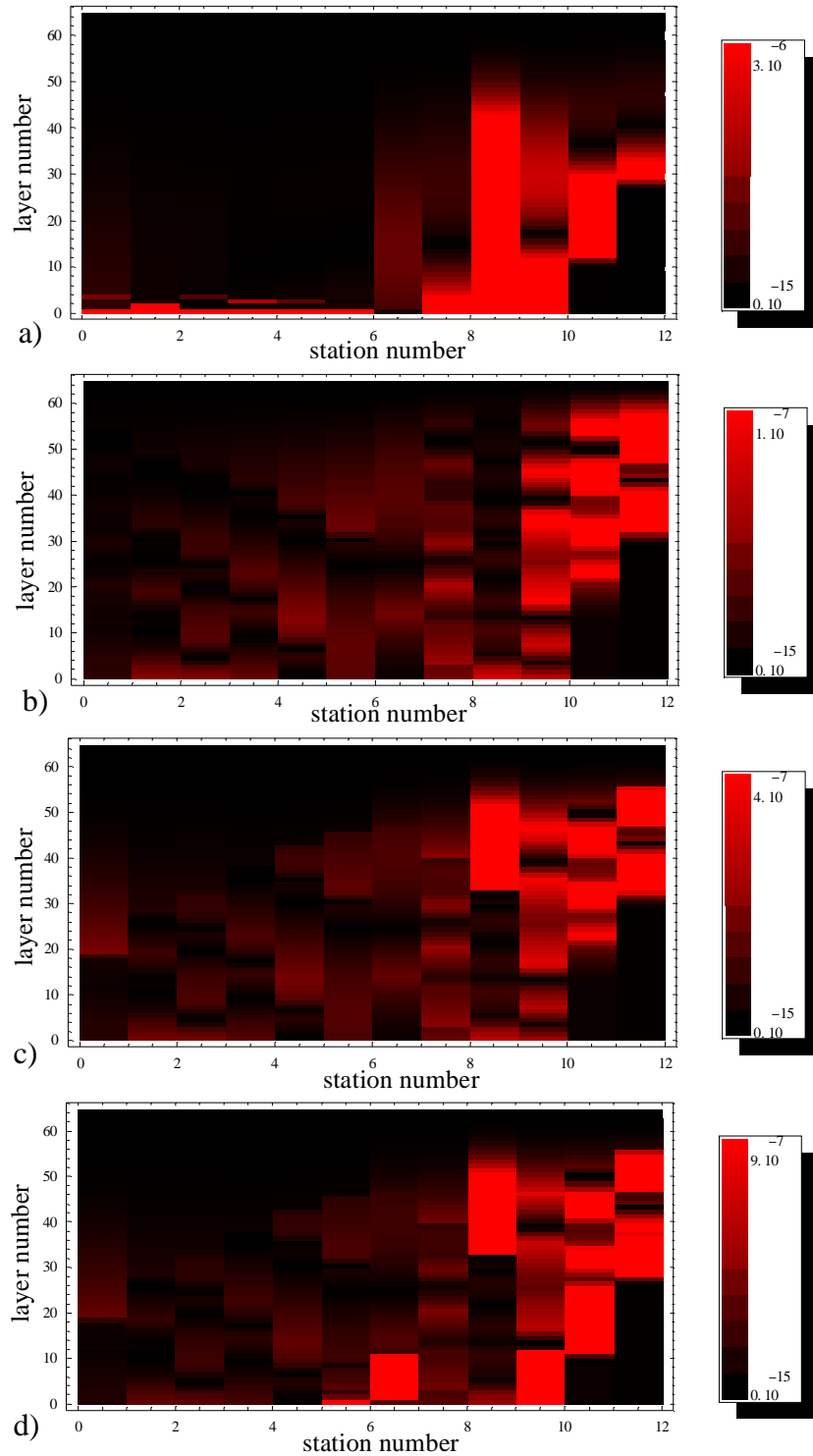
Figure 5.31 BPG errors for the seamount test case for fine vertical resolution (horizontal number of nodes held constant at 65 nodes or $\Delta x = 781$ m): a) sigma coordinates, b) z-coordinates, c) NCOM system, d) SZS system.

171
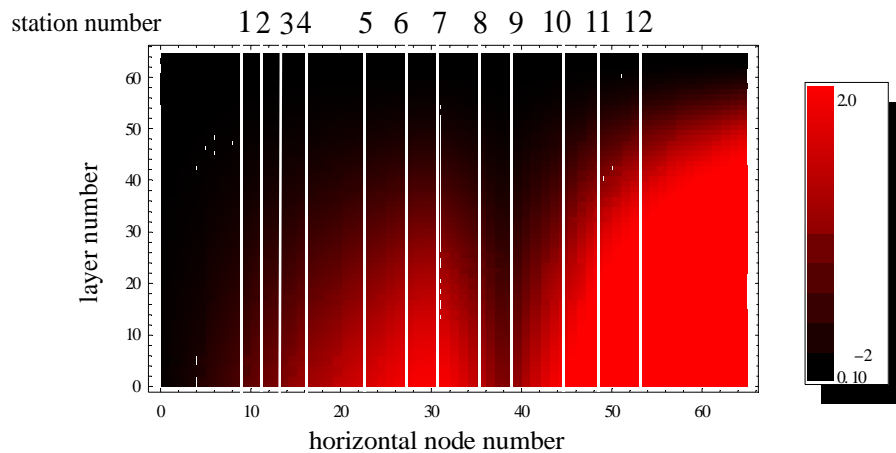
Figure 5.32   Schematic of the density field of the seamount test case for the fine vertical resolution with the twelve stations represented by the white lines (see also Figure 5.7).

density field changes significantly, and some errors occur in regions where we suffer from extrapolation issue at the bottom boundary (stations 7-10). We note again that NCOM and SZS results show a combination of patterns from the sigma coordinates and z-coordinates. The SZS results show how the z-coordinates influence errors in the area over the crest of the seamount. For example, the lower layers of stations 7 through 10 are areas where the sigma coordinate errors are high, but using the z-coordinates in this region for the SZS scheme reduces the errors. Lastly, we note that the horizontal and vertical velocity errors (not shown) are similar to the BPG errors since the driving force is the BPG.

5.6.3.c Horizontal/Vertical Resolution Interplay

Next, we analyzed the interplay of horizontal and vertical resolution on the BPG, horizontal velocity and vertical velocity results (shown in Figures 5.33-5.35, respectively). A matrix of the horizontal and vertical resolutions is given in Table 5.1. Again, note that if the results are unstable then that value is assigned an arbitrary error value (1 for BPG or 1
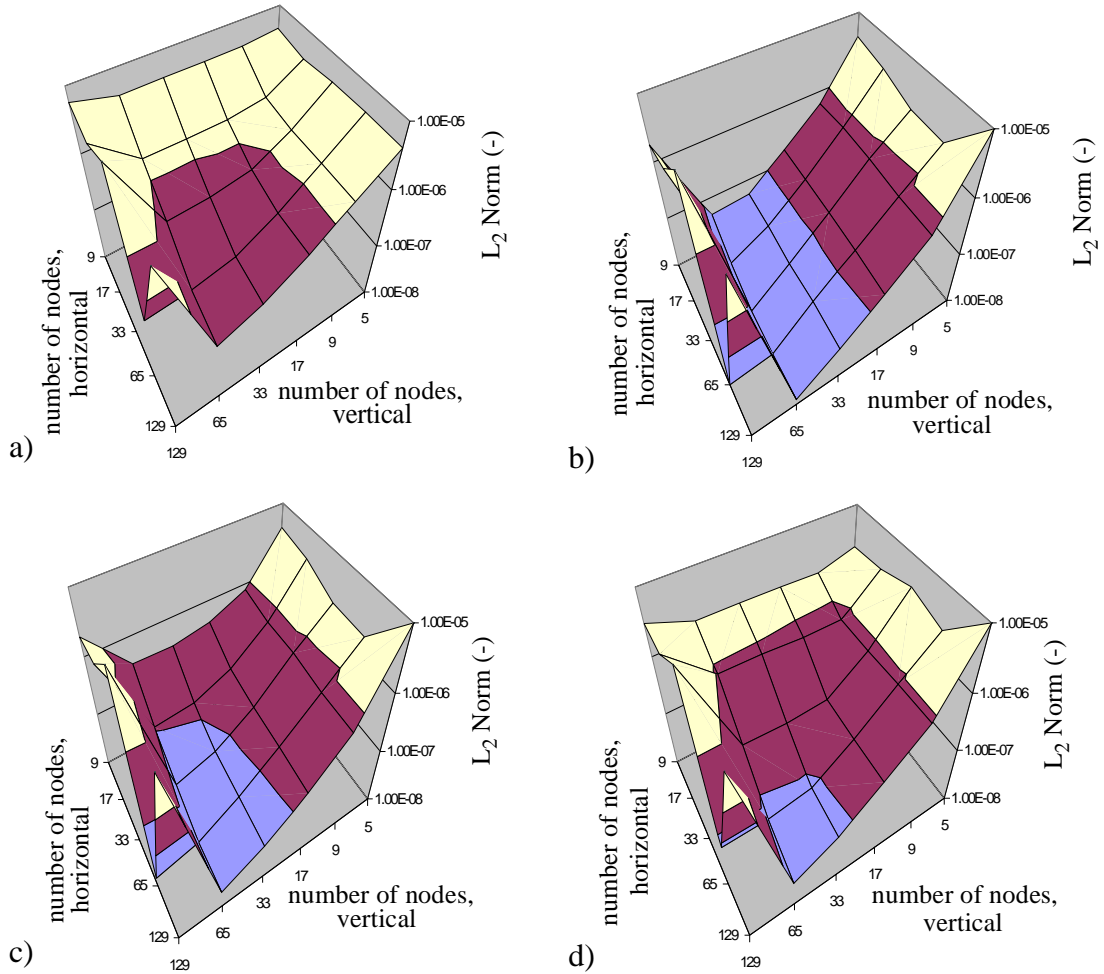
Figure 5.33 BPG errors for the seamount test case for the interplay study. Results are from a) sigma coordinates, b) z-coordinates, c) NCOM system, and d) SZS system.

m/s for velocities) in order to generate the figures (e.g. the simulation using 129 nodes in the horizontal and vertical directions). In Figures 5.33-5.35, the errors within a given figure are shown on the same scale.

From these results, we find that the z-coordinate system produces the least overall error, which is due to the density field being stably stratified, and thus the z-coordinate system more closely coincides with the density profile. The sigma coordinate system shows higher errors than the other coordinate systems used in calculating the BPG, refining the
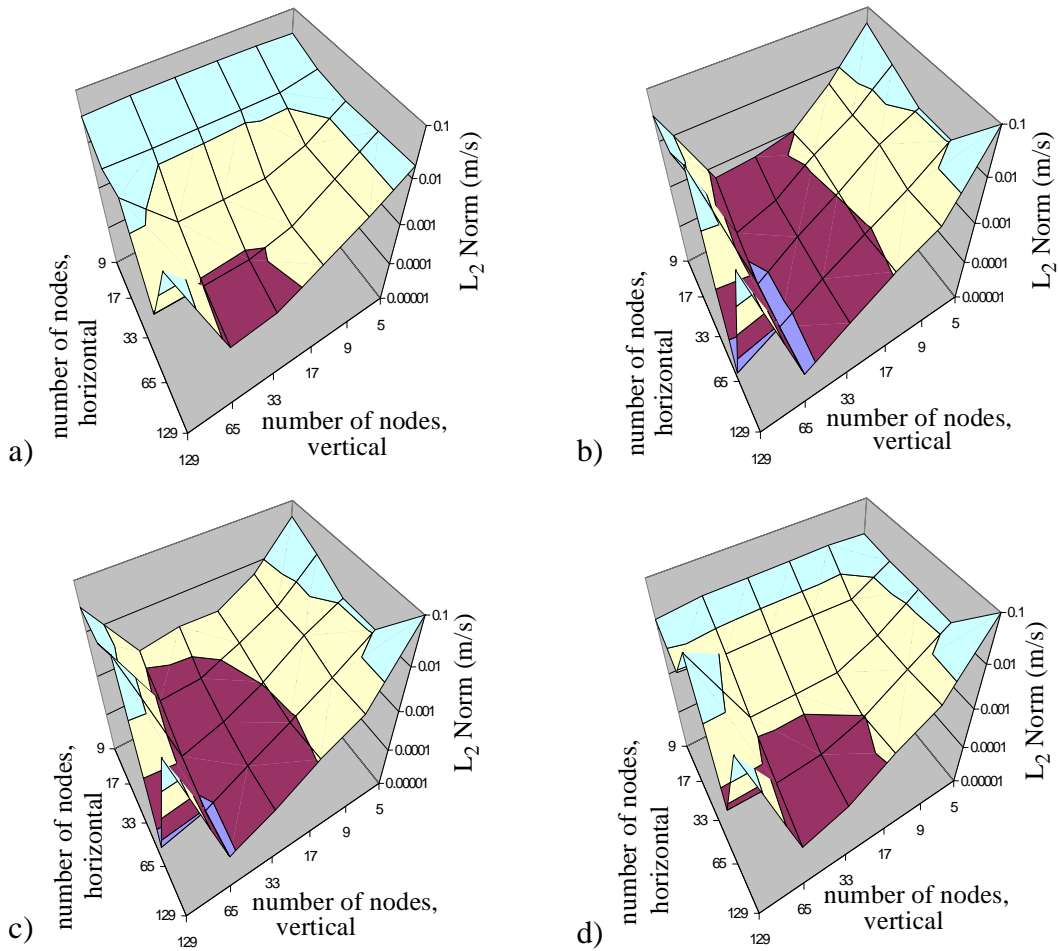
Figure 5.34 Horizontal velocity errors for the seamount test case for the interplay study. Results are from a) sigma coordinates, b) z-coordinates, c) NCOM system, and d) SZS system.

grid decreases these errors but not to the level of the z-coordinates. The NCOM coordinate

system provides similar results to the z-coordinates due to the high number of z-coordinates

used in this system; the SZS coordinate system has results similar to sigma coordinates due

to the high number of sigma coordinates used in this system. Also note that we find similar

behavior in the horizontal and vertical velocity errors.

5.6.3.d Depth for Hybrid Systems

Lastly for this test case, we evaluated the depth at which the hybrid systems switch

174
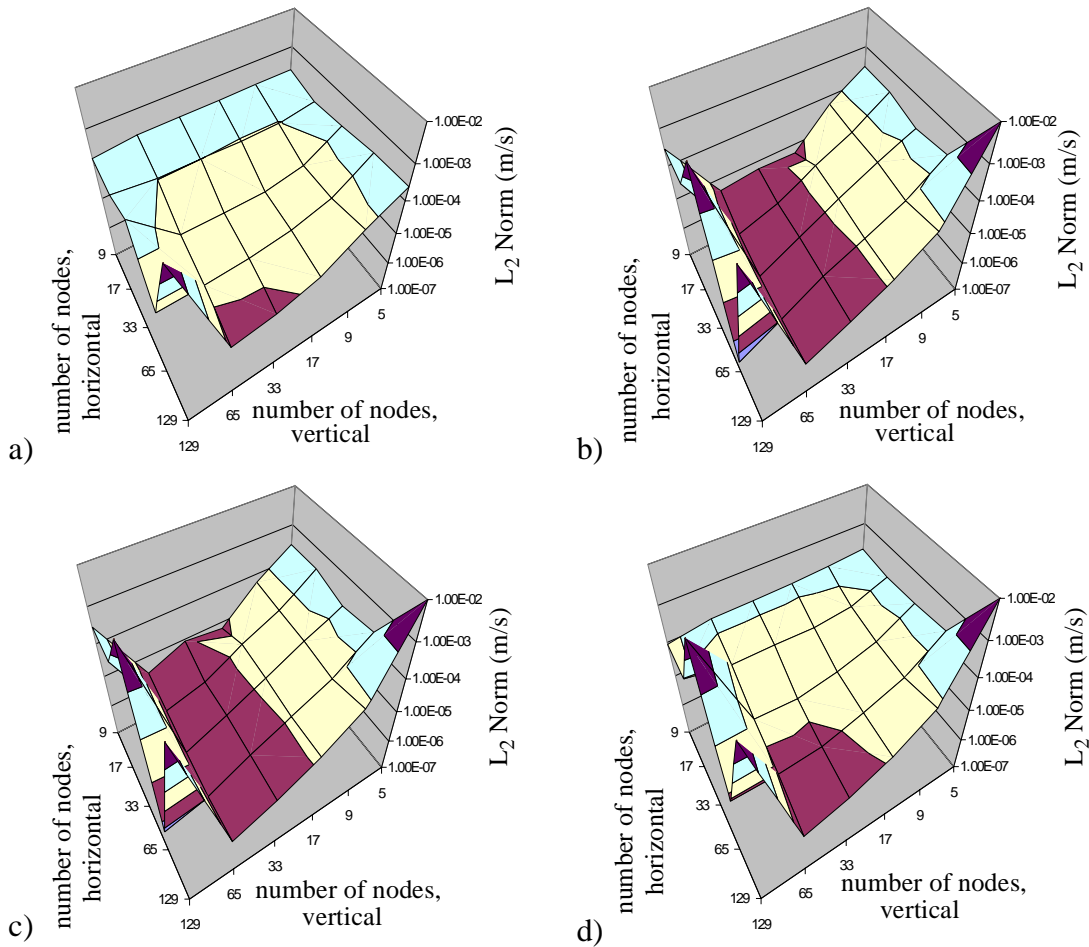
Figure 5.35   Vertical velocity errors for the seamount test case for the interplay study. Results are from a) sigma coordinates, b) z-coordinates, c) NCOM system, and d) SZS system.

coordinate systems. Global accuracy results indicate that the NCOM scheme should switch from sigma coordinates to z-coordinates between 10 m to 30 m for minimal error. For the SZS scheme, the switch from sigma coordinates to z-coordinates should occur between 20 m and 30 m, and the switch back to sigma coordinates should be between 90 m and 100 m in order to minimize errors. These switches correspond to the region above and below the rapid change in the density field. In short, z-coordinates should be used through layered fields in order to minimize error.

5.7 Conclusions

Herein, we present results from an assessment of how the vertical coordinate system used to calculate the BPG and resolution (horizontal/vertical) impacts simulation results. This study uses a 2D laterally-averaged model to investigate these changes. Evidence thus far indicates that the z-coordinate system for calculating the BPG minimizes the error. However, two of the test cases used in this chapter are more favorable for the z-coordinate system. An analysis of the spatial error distribution shows that results from the z-coordinates have highest errors in areas where the density field changes rapidly (interpolation issues) and also has problems when the horizontal resolution is too coarse to address the "running into the ground" problem. Results from simulations with sigma coordinates show that errors occur due to the stretching of the coordinate system, and if the grid resolution is not fine enough in the horizontal, the errors associated with the coordinate transformation term begin to influence the results. The hybrid systems show improvements over the results from the pure sigma coordinates and tend to obtain results that are near the dominate coordinate system. Interplay results show that the errors from sigma coordinates are influenced both by the addition of horizontal and vertical resolution; whereas the errors in the z-coordinates tend to be impacted more by the addition of vertical resolution rather than the addition of horizontal resolution.

Chapter 6. Future Work

The following sections outline future work in each of the topical areas that formed the basis of this dissertation.

6.1 Implicit Time-Marching Algorithm

The implicit time-marching algorithm is currently being implemented into the production code of ADCIRC and studies on this algorithm are complete. Thus there are no plans for any additional analyses of this algorithm.

6.2 Form of the Momentum Equation

This portion of the dissertation work has also been implemented into the production code of ADCIRC. However during this implementation, several new issues arose that must be addressed in the near future. These issues apply to the lateral stress (last terms in Equations (2.2) and (2.3)) and advective terms (second terms in Equations (2.2) and (2.3)) in the two governing equations, GWC and momentum.

Lateral stress terms, which model momentum dissipation, arise from the time averaging of the advective terms in the momentum equation and the viscous term in the original Navier-Stokes equations [87]. The viscous term represents the averaged effects of molecular motions; however, this is a scale not resolved by the equations utilized in ocean

flows. The time-averaged advective terms in the momentum equation represent the turbulent Reynolds stresses, which describe the averaged effects of momentum transfer due to the turbulent fluctuations [87]. These turbulent or high frequency fluctuations in the flow field tend not to be modeled explicitly, so a turbulence closure model, based on constitutive laws, is needed to describe these fluctuations in terms of the dependent variable [60].

Lateral stress terms tend to be used to help stabilize the numerical solution; however, they also represent physical processes which cannot be represented by the scale of the spatial and temporal grids (called "subgrid scale" processes) [41]. These processes range from molecular diffusion and viscosity to larger scale eddies [41]. The turbulence closure models used to evaluate these terms range from the simple, which only use a single parameter to model dissipation, to the complex, which use coupled differential transport equations to describe the distribution of turbulent momentum [2]. In the simplest model, a single parameter, referred to as the eddy viscosity, is defined and is typically selected to be a constant value over the entire domain. This type of formulation works well for depth-averaged flows in large water bodies [2] because there is not much need for additional numerical stability and the small scale processes do not play a significant role in the circulation. However, for widely-varying flow regimes, such as those that exist in the near shore region where small scale processes can influence circulation and numerical stability, more complex closure models are required. For these applications, the eddy viscosity parameter is allowed to vary in space or time; the functional dependence ranges from empirical rules that express eddy viscosity as a function of some static information, such as grid spacing, to equations that actually model momentum dissipation [2]. An example of this more complex formulation is the so-called k-ε model, a two equation formulation

where k is the turbulent kinetic energy and ε is the dissipation rate of k. The k-ε model is frequently utilized in areas that have small-scale turbulent features, such as flows near river beds [2]. Other formulations that fall between the two extremes include mixing-length models and one-equation formulations, such as the k-equation model [2].

Currently, ADCIRC uses the simplest lateral stress closure model, where constant eddy viscosity parameter is used over the entire domain. Future work will look at continuing the use of the eddy viscosity parameter but expressing the lateral stresses in terms of either flux or velocity, as follows. For the GWC equation, we plan to investigate five forms of the lateral stress terms: 1) one that uses flux and elevation (default method in ADCIRC); 2) one that is flux-based and non-symmetric; 3) one that is velocity-based and non-symmetric; 4) one that is flux-based and symmetric; and 5) one that is velocity-based and symmetric. For the momentum equations, we will investigate four forms of the lateral stress term: 1) one that is velocity-based and non-symmetric (default method in ADCIRC); 2) one that is flux-based and non-symmetric; 3) one that is velocity-based and symmetric; and 4) one that is flux-based and symmetric. Lastly, we will also investigate using the Smagorinsky formulation for obtaining the eddy viscosity parameter, which is spatially-varying.

Another issue is with the form of the advective terms between the governing equations. Recall from Chapter 4, that we investigated both the consistent form of the advective terms, which means that these terms utilize the same form (e.g., both conservative), and the inconsistent form of the advective term, which means that these terms utilize a different form (e.g., conservative and non-conservative). We found that the best results occur when using the consistent form of the advective terms. Future work will

179

analyze the advective term in the conservative momentum equation to determine if it should be evaluated as it appears naturally in the equation or in an expanded form (derivatives expanded using the product rule).

To investigate these two issues, we will utilize two domains, an idealized inlet and Beaufort Inlet in North Carolina. These two domains offer diverging and converging flow fields around the inlet entrances; such flow regimes are often characterized by high advection and turbulence. Figure 6.1 shows the idealized inlet using a resolution of 250 m
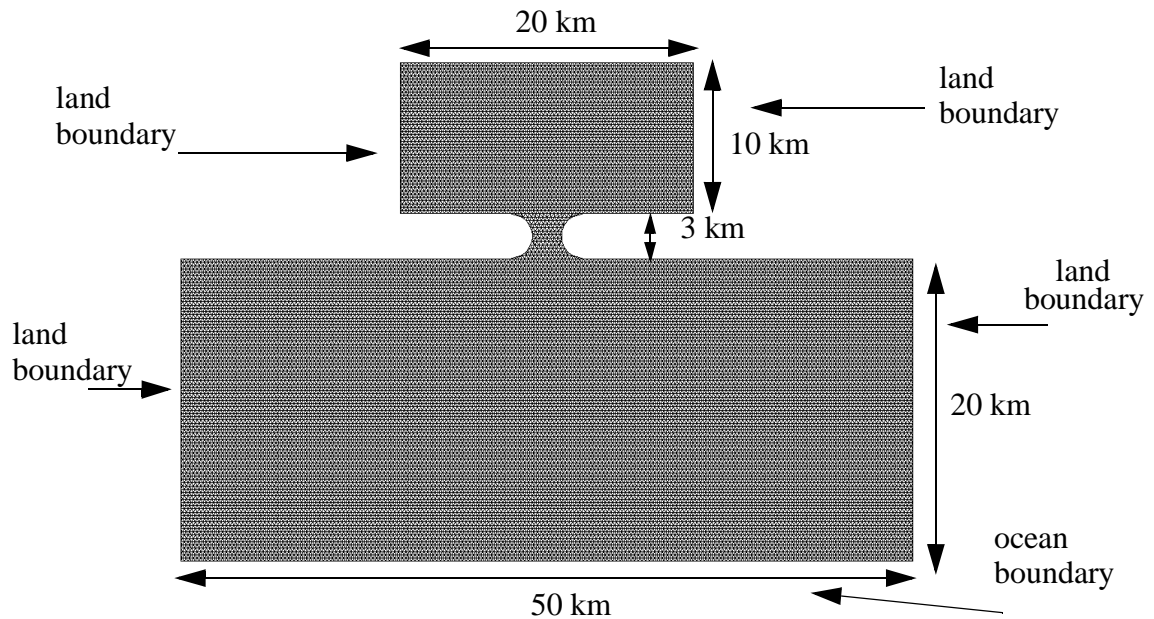
Figure 6.1   Idealized inlet domain (250 m resolution).

on each side of the triangle, which gives a $\lambda/\Delta x$ ratio of 1250 for the M_2 wave. Note equilateral triangles were used throughout (except around the curved inlet) to minimize truncation error. Boundaries are marked on the figure, with either ocean or land indicated. The boundary forcing for the open ocean boundary will be the M_2 tidal constituent with a 0.15 meter amplitude, while the land boundaries are no normal flow. Bathymetry varies from a minimum of 5 m to a maximum of 14 m. The depth in the inlet and in the entrance

to the inlet remains constant at 5 m, while in the larger basin off-shore, the depth varies

linearly from 5 m at the inlet entrance to 14 m near the ocean boundary.

Figure 6.2 shows the coastal North Carolina area and Figure 6.3 shows an
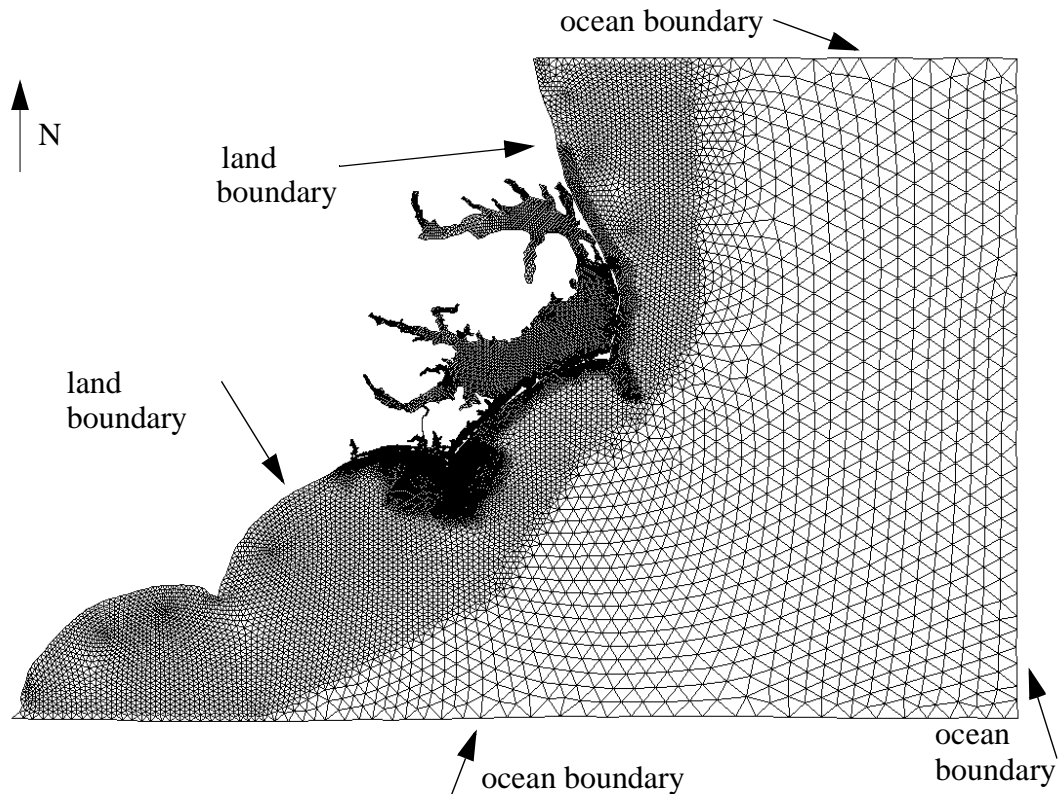
Figure 6.2   Coastal North Carolina area.

enlargement of the Beaufort Inlet area. The domain extends from the tip of Virginia to the

South Carolina border with Georgia, and it includes Cape Fear, Cape Lookout and Cape

Hatteras, North Carolina [58]. A detailed map of the Beaufort Inlet and surrounding areas

is given in Luettich et al. [58]. This domain includes the barrier islands of the North

Carolina shoreline and many of the associated channels. Bathymetry values vary from 5000

m in the deep part of the ocean, which is included in order to more accurately enforce ocean

boundary conditions, to a 2 m depth in the inlet areas. Resolution in the domain ranges from
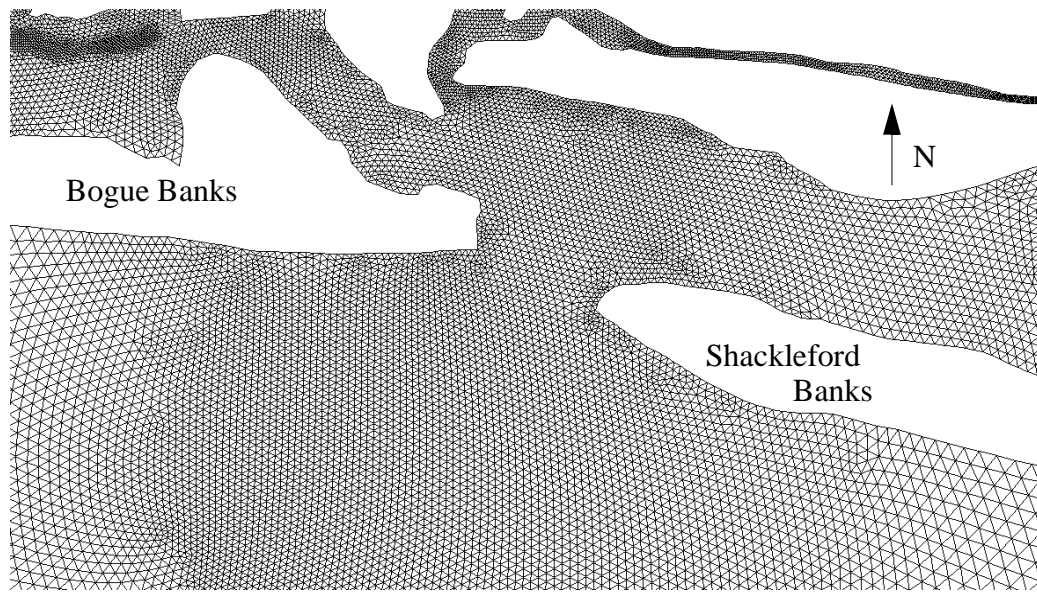
Figure 6.3   Beaufort Inlet, North Carolina.

approximately 25 m in the inlet region to approximately 25 km in the deeper waters. Boundaries are marked in Figure 6.2, with either ocean or land indicated. The boundary forcing of the open ocean boundary consists of 5 tidal constituents, the M_2, S_2, K_1, O_1 and N_2, while the land boundaries are no normal flow.

In order to quantify the impact of the various lateral stress and advective formulations, we will look at the mass conservation, stability and local spatial accuracy. The mass conservation errors will be determined by comparing the accumulation of mass to the net flux of the mass leaving the element or domain by directly integrating the primitive continuity equation, which has been used in previous studies [54]. The development of the mass conservation algorithm is presented in Chapter 4, Section 4.3.1. As mentioned in Chapter 4, we purposely use a finite volume approach for computing mass error because of the diagnostics it provides. To investigate the stability of the algorithms, we will utilize the same procedures presented in Chapter 4, Section 4.3.2 followed by an

additional step to find the maximum allowable time step using the CM equation with the expanded form of the advective term.

Lastly, we will evaluate local spatial accuracy. CAFE [61] plots will be used to quantify changes in local accuracy; a discussion of these plots occurs in references [30,40] and in Chapter 3, Section 3.5.3b. Procedures for this study will follow those presented in Chapters 3 and 4 but will also include an additional evaluation of the results from the CM equation with the expanded form of the advective term. Table 6.1 shows the matrix of the numerical experiments that will be analyzed and details the form of the lateral stress terms used in the GWC and momentum equations. Also note that in Table 6.1, we will analyze each one of the test cases using the three formulations of the advective terms, one using the non-conservative formulation (this will serve as the control for the experiments), one using the conservative formulation with the native form of the advective terms, one using the conservative formulation with the expanded form of the advective terms. Therefore, in this study, 60 different permutations of the lateral stress and advection term formulations will be examined.

Some initial results for the idealized inlet test case have been completed; they look at both global and local mass conservation errors. Results are shown in Table 6.2. To obtain the global and local mass conservation errors, we normalized the errors based on the number of horizontal nodes. We analyzed a small region around the inlet that encompassed the inlet, the entrance to the inlet and a comparable portion of the waters outside the inlet entrance for the local mass conservation errors. From these results, we note that the lowest global and local mass errors are seen with the conservative formulation of the advective terms, either in the native or expanded forms (note the highlighted results). If we divide

Table 6.1 Matrix of numerical experiments.

Test case	Lateral stress term - GWC equation.	Lateral stress term - momentum equation.
1[a]	original formulation	velocity-based (NS[b])
2	original formulation	flux-based (NS)
3	original formulation	velocity-based (S[c])
4	original formulation	flux-based (S)
5	flux-based (NS)	velocity-based (NS)
6	flux-based (NS)	flux-based (NS)
7	flux-based (NS)	velocity-based (S)
8	flux-based (NS)	flux-based (S)
9	velocity-based (NS)	velocity-based (NS)
10	velocity-based (NS)	flux-based (NS)
11	velocity-based (NS)	velocity-based (S)
12	velocity-based (NS)	flux-based (S)
13	flux-based (S)	velocity-based (NS)
14	flux-based (S)	flux-based (NS)
15	flux-based (S)	velocity-based (S)
16	flux-based (S)	flux-based (S)
17	velocity-based (S)	velocity-based (NS)
18	velocity-based (S)	flux-based (NS)
19	velocity-based (S)	velocity-based (S)
20	velocity-based (S)	flux-based (S)

a. Note each test case evaluated the advective terms in non-conservative form, conservative form with the native form of the advective terms, and conservative form with the expanded form of the advective terms.
b. NS - Non symmetric
c. S - Symmetric

Table 6.2 Global and local mass conservation results (lowest errors are in bold).

	Advective term treatment					
	non-conservative formulation		conservative formulation (native)		conservative formulation (expanded)	
Test case	global	local	global	local	global	local
1	1.849	2.815	**1.772**	**2.738**	**1.772**	2.740
2	1.874	2.818	**1.787**	**2.728**	1.788	2.730
3	1.857	2.820	**1.778**	2.746	**1.778**	**2.745**
4	1.874	2.818	**1.787**	**2.728**	1.787	2.730
5	1.849	2.815	**1.772**	**2.738**	1.772	2.740
6	1.874	2.818	**1.787**	**2.728**	1.787	2.729
7	1.857	2.820	**1.778**	2.745	**1.778**	2.745
8	1.874	2.818	**1.787**	**2.728**	1.787	2.729
9	1.849	2.815	**1.772**	**2.738**	1.772	2.740
10	1.874	2.818	**1.787**	**2.728**	1.787	2.729
11	1.874	2.818	**1.778**	2.746	**1.778**	**2.745**
12	1.874	2.818	**1.787**	**2.728**	1.787	2.729
13	1.849	2.815	**1.772**	**2.738**	1.772	2.740
14	1.874	2.818	**1.787**	**2.728**	1.788	2.730
15	1.857	2.820	**1.778**	2.746	**1.778**	**2.745**
16	1.874	2.818	**1.787**	**2.728**	1.788	2.730
17	1.849	2.815	**1.772**	**2.738**	**1.772**	2.740
18	1.874	2.818	**1.787**	**2.728**	1.788	2.730
19	1.857	2.820	**1.778**	2.746	**1.778**	**2.745**
20	1.874	2.818	**1.787**	**2.728**	1.788	2.730

Table 6.2 into the five forms of the lateral stress term used in the GWC equation (see Table 6.1), we find that there is no impact on global or local mass errors (note the results from the first four test cases compared to the second four test cases). When examining the different forms of the advective terms in the equations, we have observed some trends. Keeping with just the non-conservative formulation, we find the lowest global and local errors when using the velocity-based, non-symmetric form of the lateral stress term in the momentum equation (note the values in test cases 1, 5, 9, 13 and 17, first column) regardless of the form of the lateral stress term in the GWC equation.

When looking at the conservative formulation we find that, regardless of the advective term treatment or the form of lateral stress terms in the GWC equation, the lowest global mass errors occur when the lateral stress terms in the momentum equation use the velocity-based, non-symmetric form (note the values in test cases 1, 5, 9, 13 and 17, third and fifth columns). In the local mass balance analysis, the results indicate that the lowest errors exist when the lateral stress terms in the momentum equation use the flux-based, non-symmetric or symmetric forms, regardless of the lateral stress terms in the GWC equation (e.g., note values for even number test cases) and regardless of whether or not the advective terms are native or expanded (fourth column and sixth column).

We plan to use results from the idealized inlet to narrow the number of permutations from 60 down to 10 or less. Then, these will be further tested on the Beaufort Inlet domain.

6.3 Baroclinic Pressure Gradient

Recall from Chapter 5 that the evidence thus far indicates that the z-coordinate system for calculating the BPG provides the lowest error; however, the two of the test cases

used in that chapter were more favorable to the z-coordinate system. Therefore in the future, we will look at other test cases in which the density and bathymetry profiles do not favor the z-coordinate system.

Furthermore, the BPG errors and the interaction of other terms cannot be fully evaluated with diagnostic simulations, so future work will also include making comparisons within the framework of a prognostic model. In order to evaluate prognostic BPG and velocity errors, we plan to look at density and bathymetry profiles that can be validated with results from either laboratory data or from fine grid resolution results. One such laboratory data set is the "dam break" problem [41], which initially has water of two different densities, freshwater and salt water, at rest with a divider between them. When the divider is removed the water is allowed to mix. Laboratory experiments are currently underway to provide the validation data. This data will also provide information in which we can compare the different coordinate systems to one another.

Next, we will investigate the "gravity adjustment problem" [41], which again entails the use of water that has two different densities, e.g. freshwater and salt water, at rest with a divider between them. The salt water resides at the top of the slope so that when the divider is removed, the denser water should move down the bathymetry slope.

Lastly, we will investigate a density field referred to as a salt wedge. The bathymetry in this test case also contains a sloped area where we expect to see salt water intruding into freshwater, as what happens near the mouth of a river. In these latter two test cases, we will utilize a fine grid resolution to provide a "true" solution, as done for some of the accuracy experiments in Chapters 3 and 4.

All of the test cases thus far have used constant mesh spacing. Therefore, future work on the calculation of the BPG needs to analyze test cases with variable grids. Fortunato and Baptista [34] in their studies suggest that the use of these unstructured grids may help address some of the problems seen in the sigma coordinate system. As mentioned earlier in Chapter 5, they provide a set of guidelines; this work will examine these guidelines and offer improvements.

Also, we currently use interpolation to obtain density values between two layers in order to determine the BPG in the z-coordinate system. We will look at alternative interpolation methods. The extrapolation method used to define bottom layer BPG also needs to be assessed.

Lastly based on outcome of future work discussed in Section 6.2, we may decide to change the form of the momentum equation in the 3D ADCIRC model from non-conservative form to conservative form. In 2D (Chapter 4), we have seen that changing the form of the momentum equation decreases local mass conservation errors, which can become an issue when incorporating the transport model needed for prognostic simulations.

Chapter 7. References

1. Aldama AA, Aguilar A, Kolar RL, Westerink JJ. "A Mass Conservation Analysis of the GWCE Formulation." In *Computational Methods in Water Resources XIII, Vol. 2, Computational Methods, Surface Water Systems and Hydrology,* eds. LR Bentley et al., A.A. Balkema, Rotterdam/Brookfield, 2000; 907-912.

2. ASCE Task Committee on Turbulence Models in Hydraulic Computations. "Turbulence Modeling of Surface Water Flow and Transport: Part 1-5." *Journal of Hydraulic Engineers*, **114**, 1988; 969-1073.

3. Aizinger V, Dawson CN. "Discontinuous Galerkin Methods For Two-Dimensional Flow and Transport in Shallow Water." *Advances in Water Resources*, 2002; 67-84.

4. Atkinson JH, Westerink JJ, Hervouet JM. "Similarities Between the Quasi-Bubble and the Generalized Wave Continuity Equation Solutions to the Shallow Water Equations." *International Journal of Numerical Methods in Fluids*, **45**, 2004; 689-714.

5. Becker ML, Luettich RA, Westerink JJ. *A Reconnaissance Modeling Study of Two-Dimensional Tidal Circulation and Sediment Bed Change in the Vicinity of the Cape Fear River Navigation Channel, NC*. Contractors Report, Department of the Army, US Army Corps of Engineers, Waterways Experiment Station, Vicksburg, MS., 2001, 15 p.

6. Beckers JM. "Applications of the GHER 3D General Circulation Model to the Western Mediterranean", *Journal of Marine Systems*, **1**, 1991; 315-322.

7. Beckman A, Haidvogel DB. "Numerical Simulation of Flow Around a Tall Isolated Seamount. Part 1: Problem Formulation and Model Accuracy", *Journal of Physical Oceanography*, **23**, 1993; 1736-1753.

8. Berger RC, Howington M. "Discrete Fluxes and Mass Balance in Finite Elements." *Journal of Hydraulic Research*, **128**, 2002; 87-92.

9. Bijvelds MDJP, van Kester JAThM, Stelling GS. "A Comparison of Two 3D Shallow Water Models Using Sigma-coordinates and z-coordinates in the Vertical Direction." In *Estuarine and Coastal Modeling, Proceedings of the Sixth International Conference*, eds ML Spaulding, HL Butler, American Society of Civil Engineering, 2000; 130-147.

10. Blain CA, Westerink JJ, Luettich RA. "Grid Convergence Studies for the Prediction of Hurricane Storm Surge." *International Journal for Numerical Methods in Fluids*. **26,** 1998; 369-401.

11. Blain CA, Westerink JJ, Luettich RA. "The Influence of Domain Size on the Response Characteristics of a Hurricane Storm Surge Model." *Journal of Geophysical Research*. **99**, 1994; 18467-18479.

12. Blain CA. personal communication, June 2001.

13. Blain CA, Preller RH, Rivera AP. "Tidal Prediction Using the Advanced Circulation Model (ADCIRC) and a Relocatable PC-based System." *Oceanography*, **15**(1), 2002; 77-87.

14. Bleck R. "Finite Difference Equations in Generalized Vertical Coordinates. Part 1: Total Energy Conservation." *Contributions in Atmospheric Physics*, **51**, 1978; 360-372.

15. Blumberg AF, Mellor GL. "A Description of a Three-Dimensional Coastal Ocean Circulation Model." In *Three-Dimensional Coastal Ocean Models*, N. Heaps, Ed., Coastal Estuarine Science, **4**, American Geophysical Union; 1-16.

16. Brouwer, G. "The Creeping Storm." Civil Engineering, June 2003: 46+.

17. Burchard H, Petersen O. "Hybridization Between σ- and z-Co-ordinates for Improving the Internal Pressure Gradient Calculation in Marine Models with Steep Bottom Slopes." *International Journal for Numerical Methods in Fluids*, **25**, 1997; 1003-1023.

18. Casulli V, Cheng RT. "Semi-Implicit Finite Difference Methods for Three-Dimensional Shallow Water Flow." *International Journal for Numerical Methods in Fluids*, **15**, 1992; 629-648.

19. Celia MA, Gray WG. *Numerical Methods for Differential Equations, Fundamental Concepts for Scientific and Engineering Applications*. Prentice Hall, NJ, 1992; 436 pp.

20. Chassignet EP, Smith LT, Halliwell GR, Bleck R. "North Atlantic Simulations with the HYbrid Coordinate Ocean Model (HYCOM): Impact of the Vertical Coordinate Choice, Reference Pressure and Thermobaricity." *Journal of Physical Oceanography*, **33**, 2003; 2504-2526.

21. Chen C, Hedong L. "An Unstructured Grid, Finite-Volume, Three-Dimensional, Primitive Equations Ocean Model: Application to Coastal Ocean and Estuaries." *Journal of Atmospheric and Oceanic Technology*, **20**, 2003; 159-186.

22. Chippada S, Dawson CN, Martinez M, Wheeler M. "A Godunov-Type Finite Volume Method for the System of Shallow Water Equations." *Computer Methods in Applied Mechanics and Engineering*, **151**, 1998; 105-129.

23. Chippada S, Dawson CN, Wheeler MF, Martinez ML. "Parallel Computing for Finite Element Models of Surface Water Flow." In *Computational Methods in Water Resources XI, Volume 2: Computational Methods in Surface Flow and Transport Problems,* eds. AA Aldama et al., 1996; 63-70.

24. Cobb M, Blain CA. "Simulating Wave-Tide Induced Circulation in Bay St. Louis, MS with a Coupled Hydrodynamic-Wave Model." *Marine Technology Science*, **3**, 2000; 1494-1500.

25. Cushman-Roisin B. *Introduction to Geophysical Fluid Dynamics.* Prentice-Hall, New Jersey, 1994; 320 pp.

26. Dawson C, Proft J. "Discontinuous and Coupled Continuous/Discontinuous Galerkin Methods for Shallow Water Equations." *Computer Methods in Applied Mechanics and Engineering*, **191**, 2002; 4721-4746.

27. Dawson C, Proft J. "Coupled Discontinuous and Continuous Galerkin Finite Element Methods for the Shallow Water Equations." *Computer Methods in Applied Mechanics and Engineering*, **193**, 2004; 289-318.

28. Dawson CN, Parr VJ, Wheeler MF. "Issues in Parallel Computation of Flow and Transport in Surface Waters." In *Proceedings of the International Conference on Parallel and Distributed Processing Techniques and Applications*, eds. HR Arabnia, **1**, CSREA Press: Las Vegas, NV, 2000; 21-27.

29. Dresback KM, Kolar RL, Dietrich JC. "On the Form of the Momentum Equation for Shallow Water Models Based on the Generalized Wave Continuity Equation." *Advances in Water Resources*, in press.

30. Dresback KM, Kolar RL, Dietrich JC. "A 2D Implicit Time-Marching Algorithm for Shallow Water Models Based on the Generalized Wave Continuity Equation." *International Journal of Numerical Methods in Fluids*, **45**, 2004; 253-274.

31. Dresback KM, Blain CA, Kolar RL. "Resolution and Algorithmic Influences on the Baroclinic Pressure Gradient in Finite Element Based Hydrodynamic Models." In *Computational Methods in Water Resources XV Volume 2: Computational Methods, Surface Water Systems and Hydrology*, eds. CT Miller et al., 2004; 1755-1766.

32. Dresback KM, Blain CA, Kolar RL. "Methods to Compute Baroclinic Pressure Gradients in FE Models." In *Estuarine and Coastal Modeling, Proceedings of the Seventh International Conference*, eds. ML Spaulding, K Bedford, American Society of Civil Engineers, 2002; 103-119.

33. Dresback KM, Kolar RL. "Implicit Time-Marching Algorithm for Shallow Water Models Based on the Generalized Wave Continuity Equation." *International Journal for Numerical Methods in Fluids*, **36,** 2001; 925-945.

34. Fortunato AB, Baptista AM. "Evaluation of the Horizontal Gradients in Sigma Coordinates in Shallow Water Models." *Atmosphere-Ocean*, **34**(3), 1996; 489-514.

35. Fortunato AB, Baptista AM. "Localized Sigma Coordinates for the Vertical Structure of Hydrodynamic Models." In *Estuarine and Coastal Modeling, Proceedings of the Third International Conference*, eds. ML Spaulding et al., American Society of Civil Engineering, 1994; 323-335.

36. Fortunato AB, Baptista AM. "Vertical Discretization in Tidal Flow Simulations." *International Journal of Numerical Methods in Fluids*, **22**, 1996; 815-834.

37. Gray WG, Lynch DR. "Time-Stepping Schemes for Finite Element Tidal Model Computations." *Advances in Water Resources*, **1**, 1977; 83-96.

38. Gropp W, Lusk E, Skjellum A. *Using MPI Portable Parallel Programming with the Message-Passing Interface*, The MIT Press, Cambridge, Massachusetts, 1999.

39. Hagen SC, Westerink JJ, Kolar RL. "One-dimensional Finite Element Grids Based on a Localized Truncation Error Analysis." *International Journal of Numerical Methods in Fluids.* **32**, 2000; 241-261

40. Hagen SC, Westerink JJ, Kolar RL. *"Two-dimensional, Unstructured Mesh Generation for Tidal Models." International Journal for Numerical Methods in Fluids.* **35**, 2001; 669-686.

41. Haidvogel DB, Beckmann A. *Numerical Ocean Circulation Modeling*, Imperial College Press, London, 1999; 320 pp.

42. Haney RL. "On the Pressure Gradient Force over Steep Topography in Sigma Coordinate Ocean Model." *Journal of Physical Oceanography*, **21**, 1991; 610-619.

43. Hervouet JM. "On Spurious Oscillations in Primitive Shallow Water Equations." In *Computational Methods in Water Resources XIII, Vol. 2, Computational Methods, Surface Water Systems and Hydrology,* eds. LR Bentley et al., A.A. Balkema, Rotterdam/Brookfield, 2000; 929-936.

44. Hughes TJR, Engel G, Mazzei L, Larson MG. "The Continuous Galerkin Method is Locally Conservative." *Journal of Computational Physics*, **163**, 2000; 467-488.

45. Karypis G, Kumar V. *METIS 4.0: Unstructured graph partitioning and sparse matrix ordering system*. Technical report, Dept. of Computer Science and Engineering, Univ. of Minnesota; 1998.

46. Kashiyama K, Saito K, Yoshikawa S. "Massively Parallel Finite Element Method for Large Scale Computation of Storm Surge." In *Computational Methods in Water Resources XI Volume 2: Computational Methods in Surface Flow and Transport Problems*, eds. AA Aldama et al., Computational Mechanics Publication: Southampton; 1996; 79-86.

47. Kinnmark IPE, Gray WG. "An Implicit Wave Equation Model For The Shallow Water Equations." *Advances in Water Resources.* **7**, 1984; 168-171.

48. Kinnmark IPE. *The Shallow Water Wave Equations: Formulations, Analysis and Application (Lecture Notes in Engineering, Vol.15)*, Springer-Verlag, 1986; 187 pp.

49. Kolar RL, Westerink JJ. "A Look Back at 20 Years of GWC-based Shallow Water Models." In *Computational Methods in Water Resources XIII, Vol. 2, Computational Methods, Surface Water Systems and Hydrology,* eds. LR Bentley et al., A.A. Balkema, Rotterdam/Brookfield, 2000; 899-906.

50. Kolar RL, Gray WG, Westerink JJ, Luettich RA. "Shallow Water Modeling in Spherical Coordinates: Equation Formulation, Numerical Implementation and Application." *Journal of Hydraulic Research.* **32**(1), 1994; 3-24.

51. Kolar RL, Gray WG, Westerink JJ. "An Analysis of the Mass Conserving Properties of the Generalized Wave Continuity Equation." In *Computational Methods in Water Resources IX, Vol. 2, Mathematical Modeling in Water Resources,* eds. TF Russell et al., Southampton/London: Computational Mechanics/Elsevier, 1992; 537-544.

52. Kolar RL, Gray WG, Westerink JJ. "Boundary Conditions in Shallow Water Models-An Alternative Implementation for Finite Element Codes." *International Journal for Numerical Methods in Fluids,* **22**(7), 1996; 603-618.

53. Kolar RL, Looper JP, Westerink JJ, Gray WG. "An Improved Time Marching Algorithm for GWC Shallow Water Models." In *Computational Methods in Water Resources XII Volume 2: Computational Methods in Surface Flow and Transport Problems*, eds. VNI Burganos et al., Computational Mechanics Publications: Southampton, 1998; 379-385.

54. Kolar RL, Westerink JJ, Cantekin ME, Blain CA. "Aspects of Nonlinear Simulations using Shallow-Water Models based on the Wave Continuity Equation." *Computer and Fluids*, **23**, 1994; 523-528.

55. Kolar RL, Westerink JJ, Hagen SC. "Truncation Error Analysis of Shallow Water Models Based on the Generalized Wave Continuity Equation." In *Computational Methods in Water Resources IX, Vol. 2, Mathematical Modeling in Water Resources*, eds. AA Aldama et al. Southampton/London: Computational Mechanics/Elsevier, 1996; 215-222.

56. Lee JK, Froehlich DC. *Review of Literature on the Finite-Element Solution of the Equations of Two-Dimensional Surface-Water Flow in the Horizontal Plane*, U.S. Geological Survey Circular 1009, USDOI, Denver, CO, 1986.

57. Luettich RA, Muccino JC, Foreman MGG. "Considerations in the Calculation of Vertical Velocity in Three-Dimensional Circulation Models." *Journal of Atmospheric and Oceanic Technology*, **19**, 2002; 2063-2076.

58. Luettich RA, Hench JL, Fulcher CW, Werner FE, Blanton BO, Churchill JH. "Barotropic Tidal and Wind Driven Larvae Transport in the Vicinity of a Barrier Island Inlet." *Journal of Fisheries Oceanography*, **8**, 1999; 190-209.

59. Luettich RA, Westerink JJ, Scheffner NW. *ADCIRC: An Advanced Three-Dimensional Circulation Model for Shelves, Coasts and Estuaries; Report 1: Theory and Methodology of ADCIRC-2DDI and ADCIRC-3DL*. Technical Report DRP-92-6, Dept. of the Army, USACE, Washington, D.C., 1992.

60. Luettich RA, Westerink JJ. *Formulation and Numerical Implementation of the 2D/3D ADCIRC Finite Element Model Version 43.02*. internal report, 2003; 54 pp.

61. Luettich RA, Westerink JJ. "Continental Shelf Scale Convergence Studies with a Tidal Model." In *Quantitative Skill Assessment for Coastal Ocean Models*, 47, eds. DR Lynch, AM Davies, American Geophysical Union: Washington, DC, 1995; 349-371.

62. Luettich RA, Westerink JJ. *Implementation and Testing of Elemental Flooding and Drying in the ADCIRC Hydrodynamic Model*. Final Report, 8/95, Dept. of the Army, USACE, Washington, D.C. 1995.

63. Luettich RA, Westerink JJ. *Baroclinic Enhancements to the ADCIRC Finite Element Model Version 35.03*. internal report, UNC, Morehead City, NC, 1999.

64. Lynch DR, Gray WG. "A Wave Equation Model for Finite Element Tidal Computations." *Computer and Fluids*. **7**(3), 1979; 207-228.

65. Lynch DR, Holboke MJ. "Normal Flow Boundary Conditions in 3D Circulation Models." *International Journal for Numerical Methods in Fluids*, **25**(10), 1997; 1185-1205.

66. Lynch DR, Werner FE, Greenberg DA, Loder JW. "Diagnostic Model for Baroclinic and Wind-Driven Circulation in Shallow Seas." *Continental Shelf Research*, **12**(1), 1992; 37-64.

67. Lynch DR, Werner FE. "Three-Dimensional Hydrodynamics on Finite Elements. Part II: Non-Linear Time-Stepping Model." *International Journal for Numerical Methods in Fluids*, **12**, 1991; 507-533.

68. Lynch DR. "Three-Dimensional Diagnostic Model for Baroclinic, Wind-Driven and Tidal Circulation in Shallow Seas - FUNDY4 Users' Manual." *Numerical Methods Laboratory Report*, 1990.

69. Martin PJ. *Description of the Navy Coastal Ocean Model Version 1.0*, NRL Report No. NRL/FR/7322-00-9962, 2000, 45 pp.

70. Mellor G.L, Oey LY, Ezer T. "Sigma Coordinate Pressure Gradient Errors and the Seamount Problem." *Journal of Atmospheric and Oceanic Technology*, 15, 1998; 1122-1131

71. Mellor GL, Ezer T, Oey LY. "The Pressure Gradient Conundrum of Sigma Coordinate Ocean Models." *Journal of Atmospheric and Oceanic Technology*, **11**, 1994; 1126-1134.

72. Mellor GL. *Introduction to Physical Oceanography*, Springer-Verlag, 1996; 260 pp

73. Mewis P, Holtz KP. "A Quasi Bubble-Function Approach for Shallow Water Waves." In *Advances in Hydro-Science and Engineering; Proceedings of the First International Conference on Hydro-Science and Engineering*, Washington, DC., **1**, 1993; 768-774.

74. Militello A, Scheffner NW, Bratos S, Brown ME, Fenical S. *Circulation and Transport Modeling, in Study of Navigation Channel Feasibility, Willapa Bay, Kraus, N.C.* Technical Report ERDC-CHL-TR-00-6, U.S. Army Engineer Research and Development Center, Vicksburg, Mississippi, 2000.

75. Muccino JC, Gray WG, Foreman MGG. "Calculation of Vertical Velocity in Three Dimensional Shallow Water Equation, Finite Element Models." *International Journal for Numerical Methods in Fluids*. **25**(7), 1997; 779-802.

76. Partridge PW, Brebbia CA. "Quadratic Finite Elements in Shallow Water Problems." *Journal of Hydraulics Division - ASCE*, **102**, 1976; 1299-1313.

77. Slordal LH. "The Pressure Gradient Force in Sigma Co-ordinate Ocean Models." *International Journal for Numerical Methods in Fluids*, **24**, 1997; 987-1017.

78. Spall MA, Robinson AR. "Regional Primitive Equation Studies of the Gulf Stream Meander and Ring Formation Region." *Journal of Physical Oceanography*, **20**, 1990; 985-1016.

79. Stelling GS, Van Kester JAThM. "On the Approximation of Horizontal Gradients in Sigma Co-ordinates for Bathymetry and Steep Bottom Slopes." *International Journal of Numerical Methods in Fluids*, **18**, 1994; 915-935.

80. Taylor C, Davis JM. "Tidal and Long-Wave Propagation: A Finite Element Approach." *Computer and Fluids*, **3**, 1975; 125-148.

81. Veeramony J, Blain CA. *Barotropic Flow in the Vicinity of an Idealized Inlet - Simulations with the ADCIRC Model*. NRL Report No. NRL/FR/7320-01-9977, 2001, 30 pp.

82. Walters RA, Carey GF. "Numerical Noise in Ocean and Estuarine Models." *Advances in Water Resources*. **7**, 1984; 15-20.

83. Walters RA, Foreman, MGG. "A 3D, Finite Element Model for Baroclinic Circulation on the Vancouver Island Continental Shelf." *Journal of Marine Systems*, **3**, 1992; 507-518.

84. Wang JD, Conner JJ. *Mathematical Modeling of Near Coastal Circulation.* MIT Parsons Laboratory Report #200, Cambridge, MA, 1975.

85. Westerink JJ, Luettich RA, Muccino JC. "Modeling tides in the Western North Atlantic Using Unstructured Graded Grids." *Tellus*, **46A**, 1994; 178-199.

86. Westerink JJ, Luettich RA, Pourtaheri H. *Hurricane Simulations within the Lake Pontchartrain - Gulf of Mexico System; Historical Hindcasts and Design Storms*. Technical Review Board, US Army Corp of Engineers, New Orleans District, 2000.

87. Whitaker S. *Introduction to Fluid Mechanics*. Prentice - Hall, 1968; 457 pp.

Appendix 1. Nomenclature

Symbols

Roman Letters

A	atmospheric forcing
B	vertically-integrated baroclinic pressure gradient
C_r	Courant number, equals $c\Delta t/\Delta x$
C^0	set of continuous functions over Ω whose first derivative is, discontinuous at a finite number of points in Ω
D	momentum dispersion
E_l	lateral eddy viscosity
G	numerical parameter in the generalized wave continuity equation
H	total fluid depth, equals $h + \zeta$
L	symbol for primitive continuity equation
M	lateral stress gradient
M	symbol for primitive momentum equation, non-conservative form
$\mathbf{M}^c$	symbol for primitive momentum equation, conservative form
T	time period for wave period
T	macroscopic stress tensor
U	depth-averaged velocity
W	symbol for the wave continuity equation
W^G	symbol for the generalized wave continuity equation
a	top value for the sigma coordinate mapping ($a = 1$)
b	bottom value for the sigma coordinate mapping ($b = -1$)
b	baroclinic pressure gradient
c	linear wave celerity, equals $\sqrt{gh}$
f	Coriolis parameter, equals $2\Omega\sin\phi$
g	magnitude of gravity $|\mathbf{g}|$
h	bathymetry

i	spatial index
k	time weighting parameter
$\mathbf{m}$	lateral stress gradient
$\mathbf{n}$	unit outward normal vector
p	pressure
p_a	atmospheric pressure
P_s	atmospheric pressure at the sea surface
t	time
u	velocity component in the x-coordinate direction
v	velocity component in the y-coordinate direction
w	velocity component in the z-coordinate direction
$\mathbf{v}$	velocity of the fluid in 2D u, v
$\mathbf{v}_{3D}$	velocity of the fluid in 3D u, v, w
x	Cartesian space coordinate
y	Cartesian space coordinate
z	Cartesian space coordinate
z	depth

Greek Letters

Ω	spatial domain (R^n, for $n = 1$, 2, or 3)
Ω	angular velocity of the earth
α	Earth elasticity factor
ε	lateral eddy viscosity
ζ	surface elevation above the datum
η	Newtonian equilibrium tidal potential
λ	wavelength
ρ	density
ρ_0	reference density
ϕ	latitude (north of the equator positive)
τ	2D bottom friction term, which is determined from either a linear relationship or through the Chezy formulation
τ_b	bottom friction term for the 3D shallow water equations, which is based on the bottom velocity
τ_s	imposed surface stress
$\tau_\mathbf{z}/\rho_0$	vertical stress vector

Special Symbols and Operators

∇ nabla (grad) operator

$\nabla \bullet$ divergence operator

Δ forward difference operator

$\partial/\partial x_\sigma$ partial derivative in the x-direction along the sigma surfaces

$\partial/\partial y_\sigma$ partial derivative in the y-direction along the sigma surfaces

∇_{xy} divergence operator in the x and y-directions

∇_{xy_σ} divergence operator in the x and y-directions along the sigma surfaces

Appendix 2. Derivation of the Sigma Coordinate Transformations

The linear mapping between z-coordinates and sigma coordinates is given by

$$\sigma = a + \left(\frac{a-b}{H}\right)(z - \zeta) \qquad \text{(A2.1)}$$

where a and b are constants, $\sigma = \sigma(x, y, z, t)$, $H = h(x, y) + \zeta(x, y, t)$ and $\zeta = \zeta(x, y, t)$. By rearranging Equation (A2.1), we find the inverse mapping:

$$z = \left(\frac{\sigma - a}{a - b}\right)H + \zeta \qquad \text{(A2.2)}$$

where $z = z(\sigma, x, y, t)$, $H = H(x, y, t)$ and $\zeta = \zeta(x, y, t)$. In the z expression, σ and t are considered independent variables.

Now, we can take derivatives of Equation (A2.2) with respect to the variables shown above. First, we look at the derivative with respect to time:

$$\frac{\partial z}{\partial t} = \frac{\partial}{\partial t}\left[\left(\frac{\sigma(x, y, z, t) - a}{a - b}\right)(h(x, y) + \zeta(x, y, t)) + \zeta(x, y, t)\right] \qquad \text{(A2.3)}$$

$$\frac{\partial z}{\partial t} = \left(\frac{\sigma - a}{a - b}\right)\frac{\partial \zeta}{\partial t} + \frac{\partial \zeta}{\partial t} + \left(\frac{1}{a - b}\right)\frac{\partial \sigma}{\partial t} \qquad \text{(A2.4)}$$

$$0$$

since σ is considered an independent variable. Now, by using a common denominator we

find that the derivative reduces to:

$$\frac{\partial z}{\partial t} = \left(\frac{\sigma - b}{a - b}\right)\frac{\partial \zeta}{\partial t}$$

(A2.5)

Now, we need to evaluate the derivative with respect to the x-direction:

$$\frac{\partial z}{\partial x} = \frac{\partial}{\partial x}\left[\left(\frac{\sigma(x, y, z, t) - a}{a - b}\right)(h(x, y) + \zeta(x, y, t)) + \zeta(x, y, t)\right]$$

(A2.6)

$$\frac{\partial z}{\partial x} = \left(\frac{\sigma - a}{a - b}\right)\frac{\partial h}{\partial x} + \left(\frac{\sigma - a}{a - b}\right)\frac{\partial \zeta}{\partial x} + \frac{\partial \zeta}{\partial x}$$

(A2.7)

Using a common denominator, we obtain the following:

$$\frac{\partial z}{\partial x} = \left(\frac{\sigma - a}{a - b}\right)\frac{\partial h}{\partial x} + \left(\frac{\sigma - b}{a - b}\right)\frac{\partial \zeta}{\partial x}$$

(A2.8)

Next, we evaluate the derivative with respect to the y-direction.

$$\frac{\partial z}{\partial y} = \frac{\partial}{\partial y}\left[\left(\frac{\sigma(x, y, z, t) - a}{a - b}\right)(h(x, y) + \zeta(x, y, t)) + \zeta(x, y, t)\right]$$

(A2.9)

$$\frac{\partial z}{\partial y} = \left(\frac{\sigma - a}{a - b}\right)\frac{\partial h}{\partial y} + \left(\frac{\sigma - a}{a - b}\right)\frac{\partial \zeta}{\partial y} + \frac{\partial \zeta}{\partial y}$$

(A2.10)

Using a common denominator, we obtain the following:

$$\frac{\partial z}{\partial y} = \left(\frac{\sigma - a}{a - b}\right)\frac{\partial h}{\partial y} + \left(\frac{\sigma - b}{a - b}\right)\frac{\partial \zeta}{\partial y}$$

(A2.11)

Next, we evaluate the derivative of σ with respect to the independent variables. In this derivation we utilize the sigma coordinate relationship shown in Equation (A2.1).

$$\frac{\partial \sigma}{\partial z} = \frac{\partial}{\partial z}\left[a + \left(\frac{a-b}{H(x,y,t)}\right)(z(x,y,\sigma,t) - \zeta(x,y,t))\right] \tag{A2.12}$$

$$\frac{\partial \sigma}{\partial z} = \left(\frac{a-b}{H}\right) \tag{A2.13}$$

since H and ζ is independent of z.

Next, we evaluate the derivative for the time derivative:

$$\frac{\partial \sigma}{\partial t} = \frac{\partial}{\partial t}\left[a + \left(\frac{a-b}{H(x,y,t)}\right)(z(x,y,\sigma,t) - \zeta(x,y,t))\right] \tag{A2.14}$$

$$\frac{\partial \sigma}{\partial t} = -\left(\frac{a-b}{H}\right)\frac{\partial \zeta}{\partial t} - \left(\frac{a-b}{H^2}\right)\frac{\partial \zeta}{\partial t}(z - \zeta) \tag{A2.15}$$

$$\frac{\partial \sigma}{\partial t} = -\left(\frac{a-b}{H}\right)\frac{\partial \zeta}{\partial t} - \left(\frac{a-b}{H^2}\right)\frac{\partial \zeta}{\partial t}\left(\left(\frac{\sigma - a}{a-b}\right)H + \zeta - \zeta\right) \tag{A2.16}$$

$$\frac{\partial \sigma}{\partial t} = -\left(\frac{a-b}{H}\right)\frac{\partial \zeta}{\partial t} - \left(\frac{1}{H}\right)\frac{\partial \zeta}{\partial t}(\sigma - a) \tag{A2.17}$$

$$\frac{\partial \sigma}{\partial t} = -\left(\frac{a-b+\sigma-a}{H}\right)\frac{\partial \zeta}{\partial t} \tag{A2.18}$$

$$\frac{\partial \sigma}{\partial t} = -\left(\frac{\sigma - b}{H}\right)\frac{\partial \zeta}{\partial t} \tag{A2.19}$$

Now for the derivative in the x-direction:

$$\frac{\partial \sigma}{\partial x} = \frac{\partial}{\partial x}\left[a + \left(\frac{a-b}{H(x,y,t)}\right)(z(x,y,\sigma,t) - \zeta(x,y,t))\right] \tag{A2.20}$$

$$\frac{\partial \sigma}{\partial x} = \frac{(a-b)}{H}\left(-\frac{\partial \zeta}{\partial x}\right) + \left(\frac{a-b}{H^2}\right)\left(-\frac{\partial H}{\partial x}\right)(z-\zeta) \qquad \text{(A2.21)}$$

$$\frac{\partial \sigma}{\partial x} = \frac{(a-b)}{H}\left(-\frac{\partial \zeta}{\partial x}\right) + \left(\frac{a-b}{H^2}\right)\left(-\frac{\partial H}{\partial x}\right)\left(\left(\frac{\sigma-a}{a-b}\right)H+\zeta-\zeta\right) \qquad \text{(A2.22)}$$

$$\frac{\partial \sigma}{\partial x} = \frac{(a-b)}{H}\left(-\frac{\partial \zeta}{\partial x}\right) + \left(\frac{1}{H}\right)\left(-\frac{\partial H}{\partial x}\right)(\sigma-a) \qquad \text{(A2.23)}$$

$$\frac{\partial \sigma}{\partial x} = \frac{(a-b)}{H}\left(-\frac{\partial \zeta}{\partial x}\right) + \left(\frac{1}{H}\right)\left(-\frac{\partial \zeta}{\partial x}\right)(\sigma-a) + \left(\frac{1}{H}\right)\left(-\frac{\partial h}{\partial x}\right)(\sigma-a) \qquad \text{(A2.24)}$$

$$\frac{\partial \sigma}{\partial x} = \frac{(a-b+\sigma-a)}{H}\left(-\frac{\partial \zeta}{\partial x}\right) + \left(\frac{1}{H}\right)\left(-\frac{\partial h}{\partial x}\right)(\sigma-a) \qquad \text{(A2.25)}$$

$$\frac{\partial \sigma}{\partial x} = \frac{(\sigma-b)}{H}\left(-\frac{\partial \zeta}{\partial x}\right) + \left(\frac{\sigma-a}{H}\right)\left(-\frac{\partial h}{\partial x}\right) \qquad \text{(A2.26)}$$

Following the same steps we find the derivative in the y-direction.

$$\frac{\partial \sigma}{\partial y} = \frac{(\sigma-b)}{H}\left(-\frac{\partial \zeta}{\partial y}\right) + \left(\frac{\sigma-a}{H}\right)\left(-\frac{\partial h}{\partial y}\right) \qquad \text{(A2.27)}$$

Lastly, the derivative in the z-direction is

$$\frac{\partial \sigma}{\partial z} = \frac{(a-b)}{H} \qquad \text{(A2.28)}$$

Now, using the chain rule, we obtain the following for a derivative of a variable, u, in the z-direction.

$$\frac{\partial u(x, y, z, t)}{\partial z} = \frac{\partial u(x, y, \sigma(x, y, z, t), t)}{\partial \sigma}\frac{\partial \sigma(x, y, z, t)}{\partial z} \qquad \text{(A2.29)}$$

$$\frac{\partial u}{\partial z} = \left(\frac{a-b}{H}\right)\frac{\partial u}{\partial \sigma} \qquad (A2.30)$$

We can express the derivatives in z-coordinates as derivatives in sigma coordinates. First, we look at the time derivative term of the momentum equation: $\frac{\partial u}{\partial t}$. By using the chain rule, we obtain the following:

$$\left.\frac{\partial u(x, y, z(x, y, \sigma, t), t)}{\partial t}\right|_z + \frac{\partial u(x, y, z(x, y, \sigma, t), t)}{\partial z}\frac{\partial z}{\partial t} = \left.\frac{\partial u(x, y, \sigma(x, y, z, t), t)}{\partial t}\right|_\sigma \qquad (A2.31)$$

$$\left.\frac{\partial u}{\partial t}\right|_z = \left.\frac{\partial u}{\partial t}\right|_\sigma - \frac{\partial u}{\partial z}\frac{\partial z}{\partial t} \qquad (A2.32)$$

$$\left.\frac{\partial u}{\partial t}\right|_z = \left.\frac{\partial u}{\partial t}\right|_\sigma - \left(\frac{a-b}{H}\right)\frac{\partial u}{\partial \sigma}\left(\frac{\sigma-b}{a-b}\right)\frac{\partial \zeta}{\partial t} \qquad (A2.33)$$

$$\left.\frac{\partial u}{\partial t}\right|_z = \left.\frac{\partial u}{\partial t}\right|_\sigma - \left[\left(\frac{\sigma-b}{a-b}\right)\frac{\partial \zeta}{\partial t}\right]\left(\frac{a-b}{H}\right)\frac{\partial u}{\partial \sigma} \qquad (A2.34)$$

Now, we can look at the derivatives in the sigma coordinates and see if we get the same result.

$$\left.\frac{\partial u(x, y, z(x, y, \sigma, t), t)}{\partial t}\right|_z = \left.\frac{\partial u(x, y, \sigma(x, y, z, t), t)}{\partial t}\right|_\sigma + \frac{\partial u(x, y, \sigma(x, y, z, t), t)}{\partial \sigma}\frac{\partial \sigma}{\partial t} \qquad (A2.35)$$

$$\left.\frac{\partial u}{\partial t}\right|_z = \left.\frac{\partial u}{\partial t}\right|_\sigma + \frac{\partial u}{\partial \sigma}\left(-\left(\frac{\sigma-b}{H}\right)\frac{\partial \zeta}{\partial t}\right) \qquad (A2.36)$$

$$\left.\frac{\partial u}{\partial t}\right|_z = \left.\frac{\partial u}{\partial t}\right|_\sigma - \left(\left(\frac{\sigma-b}{H}\right)\frac{\partial \zeta}{\partial t}\right)\frac{\partial u}{\partial \sigma} \qquad (A2.37)$$

204

which is the same as Equation (A2.34) if you cancel the $a - b$ in that equation.

Next, we look at one of the space derivative terms for the x and y-directions of the momentum equation: $\frac{\partial u}{\partial x}, \frac{\partial u}{\partial y}$. By using the chain rule, we can obtain the following:

$$\frac{\partial u(x, y, z(x, y, \sigma, t), t)}{\partial x}\bigg|_z + \frac{\partial u(x, y, z(x, y, \sigma, t), t)}{\partial z}\frac{\partial z}{\partial x} = \frac{\partial u(x, y, \sigma(x, y, z, t), t)}{\partial x}\bigg|_\sigma \quad \textbf{(A2.38)}$$

$$\frac{\partial u}{\partial x}\bigg|_z + \frac{\partial u}{\partial z}\frac{\partial z}{\partial x} = \frac{\partial u}{\partial x}\bigg|_\sigma \quad \textbf{(A2.39)}$$

$$\frac{\partial u}{\partial x}\bigg|_z = \frac{\partial u}{\partial x}\bigg|_\sigma - \frac{\partial u}{\partial z}\frac{\partial z}{\partial x} \quad \textbf{(A2.40)}$$

For the x-direction, we obtain the following equation:

$$\frac{\partial u}{\partial x}\bigg|_z = \frac{\partial u}{\partial x}\bigg|_\sigma - \left[\left(\frac{\sigma - a}{a - b}\right)\frac{\partial h}{\partial x} + \left(\frac{\sigma - b}{a - b}\right)\frac{\partial \zeta}{\partial x}\right]\left(\frac{a - b}{H}\right)\frac{\partial u}{\partial \sigma} \quad \textbf{(A2.41)}$$

In the y-direction, we obtain the following equation:

$$\frac{\partial u}{\partial y}\bigg|_z = \frac{\partial u}{\partial y}\bigg|_\sigma - \left[\left(\frac{\sigma - a}{a - b}\right)\frac{\partial h}{\partial y} + \left(\frac{\sigma - b}{a - b}\right)\frac{\partial \zeta}{\partial y}\right]\left(\frac{a - b}{H}\right)\frac{\partial u}{\partial \sigma} \quad \textbf{(A2.42)}$$

Now, we determine the derivatives in the x- and y-directions in the sigma coordinate system.

$$\frac{\partial u(x, y, z(x, y, \sigma, t), t)}{\partial x}\bigg|_z = \frac{\partial u(x, y, \sigma(x, y, z, t), t)}{\partial x}\bigg|_\sigma + \frac{\partial u(x, y, \sigma(x, y, z, t), t)}{\partial \sigma}\frac{\partial \sigma}{\partial x} \quad \textbf{(A2.43)}$$

$$\frac{\partial u}{\partial x}\bigg|_z = \frac{\partial u}{\partial x}\bigg|_\sigma + \frac{\partial u}{\partial \sigma}\frac{\partial \sigma}{\partial x} \quad \textbf{(A2.44)}$$

205

For the x-direction, we find the following:

$$\left.\frac{\partial u}{\partial x}\right|_z = \left.\frac{\partial u}{\partial x}\right|_\sigma + \frac{\partial u}{\partial \sigma}\left(\frac{(\sigma-b)}{H}\left(-\frac{\partial \zeta}{\partial x}\right) + \left(\frac{\sigma-a}{H}\right)\left(-\frac{\partial h}{\partial x}\right)\right)$$ (A2.45)

While for the y-direction, we find the following:

$$\left.\frac{\partial u}{\partial y}\right|_z = \left.\frac{\partial u}{\partial y}\right|_\sigma + \frac{\partial u}{\partial \sigma}\left(\frac{(\sigma-b)}{H}\left(-\frac{\partial \zeta}{\partial y}\right) + \left(\frac{\sigma-a}{H}\right)\left(-\frac{\partial h}{\partial y}\right)\right)$$ (A2.46)

which are the same as Equations (A2.41) and (A2.42), if you cancel the $(a-b)$ in the two equations.

Lastly, we looked at the development of the w_σ term, which utilizes the first four terms on the left hand side of the momentum equations in 3D (Equation (A2.47)) and their evaluation in the sigma coordinate system.

$$\left.\frac{\partial u}{\partial t}\right|_z + u\left.\frac{\partial u}{\partial x}\right|_z + v\left.\frac{\partial u}{\partial y}\right|_z + w\left.\frac{\partial u}{\partial z}\right|_z =$$

$$\left.\frac{\partial u}{\partial t}\right|_\sigma - \left[\left(\frac{\sigma-b}{a-b}\right)\frac{\partial \zeta}{\partial t}\right]\left(\frac{a-b}{H}\right)\frac{\partial u}{\partial \sigma} + u\left.\frac{\partial u}{\partial x}\right|_\sigma - u\left[\left(\frac{\sigma-a}{a-b}\right)\frac{\partial h}{\partial x} + \left(\frac{\sigma-b}{a-b}\right)\frac{\partial \zeta}{\partial x}\right]\left(\frac{a-b}{H}\right)\frac{\partial u}{\partial \sigma} +$$

$$v\left.\frac{\partial u}{\partial y}\right|_\sigma - v\left[\left(\frac{\sigma-a}{a-b}\right)\frac{\partial h}{\partial y} + \left(\frac{\sigma-b}{a-b}\right)\frac{\partial \zeta}{\partial y}\right]\left(\frac{a-b}{H}\right)\frac{\partial u}{\partial \sigma} + w\left(\frac{a-b}{H}\right)\frac{\partial u}{\partial \sigma}$$ (A2.47)

We can write it compactly as:

$$\left.\frac{\partial u}{\partial t}\right|_z + u\left.\frac{\partial u}{\partial x}\right|_z + v\left.\frac{\partial u}{\partial y}\right|_z + w\left.\frac{\partial u}{\partial z}\right|_z = \left.\frac{\partial u}{\partial t}\right|_\sigma + u\left.\frac{\partial u}{\partial x}\right|_\sigma + v\left.\frac{\partial u}{\partial y}\right|_\sigma + w_\sigma\left(\frac{a-b}{H}\right)\frac{\partial u}{\partial \sigma}$$ (A2.48)

where

$$w_\sigma = w - \left(\frac{\sigma - b}{a - b}\right)\frac{\partial\zeta}{\partial t} - u\left[\left(\frac{\sigma - a}{a - b}\right)\frac{\partial h}{\partial x} + \left(\frac{\sigma - b}{a - b}\right)\frac{\partial\zeta}{\partial x}\right] - v\left[\left(\frac{\sigma - a}{a - b}\right)\frac{\partial h}{\partial y} + \left(\frac{\sigma - b}{a - b}\right)\frac{\partial\zeta}{\partial y}\right] \quad \textbf{(A2.49)}$$

which is the same as that given in Luettich and Westerink [60].

Appendix 3. Truncation Errors for the Governing Equations

Herein, we examine the truncation errors for the 1D equations of ADCIRC (GWC, NCM and CM equations). To evaluate the truncation errors, we utilize Taylor series expansions of the discrete form of each term shown in the governing equations below:

$$W^G \equiv \frac{\partial^2 \zeta}{\partial t^2} + G\frac{\partial \zeta}{\partial t} - q\frac{\partial G}{\partial x} - \frac{\partial}{\partial x}\left[\frac{\partial(qu)}{\partial x} + (G-\tau)q + gH\frac{\partial \zeta}{\partial x} - \varepsilon\frac{\partial^2 q}{\partial x^2}\right] = 0 \quad \textbf{(A3.1)}$$

$$\mathbf{M} \equiv \frac{\partial(u)}{\partial t} + u\frac{\partial(u)}{\partial x} + \tau u + g\frac{\partial \zeta}{\partial x} - \frac{\varepsilon}{H}\frac{\partial^2 q}{\partial x^2} = 0 \quad \textbf{(A3.2)}$$

$$\mathbf{M}^c \equiv \frac{\partial(q)}{\partial t} + \frac{\partial(qu)}{\partial x} + \tau q + gH\frac{\partial \zeta}{\partial x} - \varepsilon\frac{\partial^2 q}{\partial x^2} = 0 \quad \textbf{(A3.3)}$$

By using the Taylor series, we expand the dependent variables around a common node point for evaluation purposes. The results are then subtracted from the continuum equations in order to obtain the truncation error, that is TE = continuum – discrete approximation .

The discrete form of the equations come from using C^0 linear finite element for the spatial discretization. For the temporal discretization, a three time-level scheme centered at k is used in the GWC equation (Equation (A3.1)) and a two time-level scheme centered at $k + 1/2$ is used in the momentum equations (Equations (A3.2) and (A3.3)). The nonlinear terms in the equations employ an explicit formulation. We utilize exact quadrature rules and

averaged terms are based on an elemental average.

To find the truncation error expressions, we employ *Mathematica*® to expand the Taylor Series to the seventh order terms; however, we report errors only to the leading two orders. In *Mathematica*®, derivatives are shown in both time and space using the following notation: $q^{(0,1)}(j, k)$, where the j indicates the space index, k is the time index and the $(0,1)$ above the dependent variable indicates the order of the derivative in space and time. Thus $q^{(0,1)}(j, k)$ indicates a first derivative in time for the dependent variable, q at node j, time k. Also, note that dt indicates the change in time, while $dx(i + 1)$ and $dx(i)$ indicate the node spacing and i is associated with the element number. Finally, parameters, such as τ or ε, are shown as tau or eddy, respectively. Note: analyses provided herein are only for the interior discrete equations.

Truncation Errors for the Generalized Wave Continuity Equation

First Term - $(\partial^2\zeta)/(\partial t^2)$

$$-\frac{1}{12}\,z^{(0,4)}(j,k)\,dt^2 + \frac{1}{36}\,(dx(j) - dx(j+1))\,z^{(1,4)}(j,k)\,dt^2 - \frac{1}{72}\,(dx(j)^2 - dx(j+1)\,dx(j) + dx(j+1)^2)\,z^{(2,4)}(j,k)\,dt^2 +$$

$$\frac{1}{3}\,(dx(j) - dx(j+1))\,z^{(1,2)}(j,k) - \frac{1}{6}\,(dx(j)^2 - dx(j+1)\,dx(j) + dx(j+1)^2)\,z^{(2,2)}(j,k)$$

Second Term - $G((\partial\zeta)/(\partial t))$

$$-\frac{1}{6}\,G\,z^{(0,3)}(j,k)\,dt^2 + \frac{1}{18}\,G\,(dx(j) - dx(j+1))\,z^{(1,3)}(j,k)\,dt^2 - \frac{1}{36}\,G\,(dx(j)^2 - dx(j+1)\,dx(j) + dx(j+1)^2)\,z^{(2,3)}(j,k)\,dt^2 +$$

$$\frac{1}{3}\,G\,(dx(j) - dx(j+1))\,z^{(1,1)}(j,k) - \frac{1}{6}\,G\,(dx(j)^2 - dx(j+1)\,dx(j) + dx(j+1)^2)\,z^{(2,1)}(j,k)$$

Finite Amplitude Term - part 1 - $gh((\partial^2\zeta)/(\partial x^2))$

$$\frac{1}{3}\,g\,h^{(1,0)}(j,k)\,z^{(1,2)}(j,k)\,dt^2 + \frac{1}{6}\,g\,(dx(j+1) - dx(j))\,z^{(1,2)}(j,k)\,h^{(2,0)}(j,k)\,dt^2 + \frac{1}{3}\,g\,h(j,k)\,z^{(2,2)}(j,k)\,dt^2 +$$

$$\frac{1}{6}\,g\,(dx(j+1) - dx(j))\,h^{(1,0)}(j,k)\,z^{(2,2)}(j,k)\,dt^2 + \frac{1}{12}\,g\,(dx(j)^2 - dx(j+1)\,dx(j) + dx(j+1)^2)\,h^{(2,0)}(j,k)\,z^{(2,2)}(j,k)\,dt^2 +$$

$$\frac{1}{18}\,g\,(dx(j)^2 - dx(j+1)\,dx(j) + dx(j+1)^2)\,z^{(1,2)}(j,k)\,h^{(3,0)}(j,k)\,dt^2 + \frac{1}{9}\,g\,(dx(j+1) - dx(j))\,h(j,k)\,z^{(3,2)}(j,k)\,dt^2 +$$

$$\frac{1}{18}\,g\,(dx(j)^2 - dx(j+1)\,dx(j) + dx(j+1)^2)\,h^{(1,0)}(j,k)\,z^{(3,2)}(j,k)\,dt^2 +$$

$$\frac{1}{36}\,g\,(dx(j)^2 - dx(j+1)\,dx(j) + dx(j+1)^2)\,h(j,k)\,z^{(4,2)}(j,k)\,dt^2 + \frac{1}{2}\,g\,(dx(j+1) - dx(j))\,z^{(1,0)}(j,k)\,h^{(2,0)}(j,k) +$$

$$\frac{1}{2}\,g\,(dx(j+1) - dx(j))\,h^{(1,0)}(j,k)\,z^{(2,0)}(j,k) + \frac{1}{4}\,g\,(dx(j)^2 - dx(j+1)\,dx(j) + dx(j+1)^2)\,h^{(2,0)}(j,k)\,z^{(2,0)}(j,k) +$$

$$\frac{1}{6}\,g\,(dx(j)^2 - dx(j+1)\,dx(j) + dx(j+1)^2)\,z^{(1,0)}(j,k)\,h^{(3,0)}(j,k) + \frac{1}{3}\,g\,(dx(j+1) - dx(j))\,h(j,k)\,z^{(3,0)}(j,k) +$$

$$\frac{1}{6}\,g\,(dx(j)^2 - dx(j+1)\,dx(j) + dx(j+1)^2)\,h^{(1,0)}(j,k)\,z^{(3,0)}(j,k) +$$

$$\frac{1}{12}\,g\,(dx(j)^2 - dx(j+1)\,dx(j) + dx(j+1)^2)\,h(j,k)\,z^{(4,0)}(j,k)$$

Finite Amplitude Term - part 2 - $g((\partial^2(\zeta^2))/(\partial x^2))$

$$\frac{1}{6}\,g\,(dx(j+1) - dx(j))\,zsq^{(3,0)}(j,k) + \frac{1}{24}\,g\,(dx(j)^2 - dx(j+1)\,dx(j) + dx(j+1)^2)\,zsq^{(4,0)}(j,k)$$

Advective Term - conservative form - $(\partial^2(qu))/(\partial x^2)$

$$\frac{1}{3}\,(dx(j+1) - dx(j))\,qu^{(3,0)}(j,k) + \frac{1}{12}\,(dx(j)^2 - dx(j+1)\,dx(j) + dx(j+1)^2)\,qu^{(4,0)}(j,k)$$

Advective Term - non-conservative form part 1 - $\partial(u((\partial\zeta)/\partial t))/(\partial x)$

$-\dfrac{1}{6} z^{(0,3)}(j,k)\,u^{(1,0)}(j,k)\,dt^2 - \dfrac{1}{6}\,u(j,k)\,z^{(1,3)}(j,k)\,dt^2 + \dfrac{1}{12}\,(dx(j)-dx(j+1))\,u^{(1,0)}(j,k)\,z^{(1,3)}(j,k)\,dt^2 +$

$\dfrac{1}{12}\,(dx(j)-dx(j+1))\,z^{(0,3)}(j,k)\,u^{(2,0)}(j,k)\,dt^2 - \dfrac{1}{24}\,(dx(j)^2-dx(j+1)\,dx(j)+dx(j+1)^2)\,z^{(1,3)}(j,k)\,u^{(2,0)}(j,k)\,dt^2 +$

$\dfrac{1}{12}\,(dx(j)-dx(j+1))\,u(j,k)\,z^{(2,3)}(j,k)\,dt^2 - \dfrac{1}{24}\,(dx(j)^2-dx(j+1)\,dx(j)+dx(j+1)^2)\,u^{(1,0)}(j,k)\,z^{(2,3)}(j,k)\,dt^2 -$

$\dfrac{1}{36}\,(dx(j)^2-dx(j+1)\,dx(j)+dx(j+1)^2)\,z^{(0,3)}(j,k)\,u^{(3,0)}(j,k)\,dt^2 -$

$\dfrac{1}{36}\,(dx(j)^2-dx(j+1)\,dx(j)+dx(j+1)^2)\,u(j,k)\,z^{(3,3)}(j,k)\,dt^2 + \dfrac{1}{2}\,z^{(0,2)}(j,k)\,u^{(1,0)}(j,k)\,dt + \dfrac{1}{2}\,u(j,k)\,z^{(1,2)}(j,k)\,dt +$

$\dfrac{1}{4}\,(dx(j+1)-dx(j))\,u^{(1,0)}(j,k)\,z^{(1,2)}(j,k)\,dt + \dfrac{1}{4}\,(dx(j+1)-dx(j))\,z^{(0,2)}(j,k)\,u^{(2,0)}(j,k)\,dt +$

$\dfrac{1}{8}\,(dx(j)^2-dx(j+1)\,dx(j)+dx(j+1)^2)\,z^{(1,2)}(j,k)\,u^{(2,0)}(j,k)\,dt + \dfrac{1}{4}\,(dx(j+1)-dx(j))\,u(j,k)\,z^{(2,2)}(j,k)\,dt +$

$\dfrac{1}{8}\,(dx(j)^2-dx(j+1)\,dx(j)+dx(j+1)^2)\,u^{(1,0)}(j,k)\,z^{(2,2)}(j,k)\,dt +$

$\dfrac{1}{12}\,(dx(j)^2-dx(j+1)\,dx(j)+dx(j+1)^2)\,z^{(0,2)}(j,k)\,u^{(3,0)}(j,k)\,dt +$

$\dfrac{1}{12}\,(dx(j)^2-dx(j+1)\,dx(j)+dx(j+1)^2)\,u(j,k)\,z^{(3,2)}(j,k)\,dt + \dfrac{1}{2}\,(dx(j)-dx(j+1))\,u^{(1,0)}(j,k)\,z^{(1,1)}(j,k) +$

$\dfrac{1}{2}\,(dx(j)-dx(j+1))\,z^{(0,1)}(j,k)\,u^{(2,0)}(j,k) - \dfrac{1}{4}\,(dx(j)^2-dx(j+1)\,dx(j)+dx(j+1)^2)\,z^{(1,1)}(j,k)\,u^{(2,0)}(j,k) +$

$\dfrac{1}{2}\,(dx(j)-dx(j+1))\,u(j,k)\,z^{(2,1)}(j,k) - \dfrac{1}{4}\,(dx(j)^2-dx(j+1)\,dx(j)+dx(j+1)^2)\,u^{(1,0)}(j,k)\,z^{(2,1)}(j,k) -$

$\dfrac{1}{6}\,(dx(j)^2-dx(j+1)\,dx(j)+dx(j+1)^2)\,z^{(0,1)}(j,k)\,u^{(3,0)}(j,k) - \dfrac{1}{6}\,(dx(j)^2-dx(j+1)\,dx(j)+dx(j+1)^2)\,u(j,k)\,z^{(3,1)}(j,k)$

Advective Term - non-conservative form part 2 - $\partial(q((\partial u)/(\partial x)))/(\partial x)$

$-\dfrac{1}{2}\,(dx(j)-dx(j+1))\,u^{(1,0)}(j,k)\,q^{(2,0)}(j,k) + \dfrac{1}{4}\,(dx(j)^2-dx(j+1)\,dx(j)+dx(j+1)^2)\,u^{(2,0)}(j,k)\,q^{(2,0)}(j,k) +$

$\dfrac{1}{2}\,(dx(j+1)-dx(j))\,q^{(1,0)}(j,k)\,u^{(2,0)}(j,k) + \dfrac{1}{6}\,(dx(j)^2-dx(j+1)\,dx(j)+dx(j+1)^2)\,u^{(1,0)}(j,k)\,q^{(3,0)}(j,k) +$

$\dfrac{1}{3}\,(dx(j+1)-dx(j))\,q(j,k)\,u^{(3,0)}(j,k) + \dfrac{1}{6}\,(dx(j)^2-dx(j+1)\,dx(j)+dx(j+1)^2)\,q^{(1,0)}(j,k)\,u^{(3,0)}(j,k) +$

$\dfrac{1}{12}\,(dx(j)^2-dx(j+1)\,dx(j)+dx(j+1)^2)\,q(j,k)\,u^{(4,0)}(j,k)$

GWC Flux Terms - $(G-\tau)((\partial q)/(\partial x))$

$\dfrac{1}{2}\,(G-tau)\,(dx\,(j)-dx\,(j+1))\,q^{(2,0)}(j,k) - \dfrac{1}{6}\,(G-tau)\,(dx\,(j)^2-dx\,(j+1)\,dx\,(j)+dx\,(j+1)^2)\,q^{(3,0)}(j,k)$

Viscous Term - $\varepsilon((\partial^3\zeta)/(\partial x^2\partial t))$

$\dfrac{1}{6}\,eddy\;z^{(2,3)}(j,k)\,dt^2 + \dfrac{1}{18}\,eddy\,(dx\,(j+1)-dx\,(j))\,z^{(3,3)}(j,k)\,dt^2 +$

$\dfrac{1}{72}\,eddy\,(dx\,(j)^2-dx\,(j+1)\,dx\,(j)+dx\,(j+1)^2)\,z^{(4,3)}(j,k)\,dt^2 + \dfrac{1}{3}\,eddy\,(dx\,(j+1)-dx\,(j))\,z^{(3,1)}(j,k) +$

$\dfrac{1}{12}\,eddy\,(dx\,(j)^2-dx\,(j+1)\,dx\,(j)+dx\,(j+1)^2)\,z^{(4,1)}(j,k)$

Truncation Errors for the Non-Conservative Momentum Equation

Accumulation Term - $\partial u / \partial t$

$$-\frac{1}{6}u^{(0,3)}(j,k)\,dt^2 + \frac{1}{18}(dx(j)-dx(j+1))u^{(1,3)}(j,k)\,dt^2 - \frac{1}{36}(dx(j)^2 - dx(j+1)\,dx(j) + dx(j+1)^2)u^{(2,3)}(j,k)\,dt^2 -$$

$$\frac{1}{2}u^{(0,2)}(j,k)\,dt + \frac{1}{6}(dx(j)-dx(j+1))u^{(1,2)}(j,k)\,dt - \frac{1}{12}(dx(j)^2 - dx(j+1)\,dx(j) + dx(j+1)^2)u^{(2,2)}(j,k)\,dt +$$

$$\frac{1}{3}(dx(j)-dx(j+1))u^{(1,1)}(j,k) - \frac{1}{6}(dx(j)^2 - dx(j+1)\,dx(j) + dx(j+1)^2)u^{(2,1)}(j,k)$$

Advective Term - $u(\partial u / \partial x)$

$$\frac{1}{2}(dx(j)-dx(j+1))u^{(1,0)}(j,k)^2 - \frac{1}{2}(dx(j)^2 - dx(j+1)\,dx(j) + dx(j+1)^2)u^{(2,0)}(j,k)\,u^{(1,0)}(j,k) +$$

$$\frac{1}{2}(dx(j)-dx(j+1))u(j,k)\,u^{(2,0)}(j,k) - \frac{1}{6}(dx(j)^2 - dx(j+1)\,dx(j) + dx(j+1)^2)u(j,k)\,u^{(3,0)}(j,k)$$

Bottom Friction Term - τu

$$-\frac{1}{4}\tau\,u^{(0,2)}(j,k)\,dt^2 + \frac{1}{12}\tau\,(dx(j)-dx(j+1))u^{(1,2)}(j,k)\,dt^2 -$$

$$\frac{1}{24}\tau\,(dx(j)^2 - dx(j+1)\,dx(j) + dx(j+1)^2)u^{(2,2)}(j,k)\,dt^2 - \frac{1}{2}\tau\,u^{(0,1)}(j,k)\,dt + \frac{1}{6}\tau\,(dx(j)-dx(j+1))u^{(1,1)}(j,k)\,dt -$$

$$\frac{1}{12}\tau\,(dx(j)^2 - dx(j+1)\,dx(j) + dx(j+1)^2)u^{(2,1)}(j,k)\,dt + \frac{1}{3}\tau\,(dx(j)-dx(j+1))u^{(1,0)}(j,k) -$$

$$\frac{1}{6}\tau\,(dx(j)^2 - dx(j+1)\,dx(j) + dx(j+1)^2)u^{(2,0)}(j,k)$$

Finite Amplitude Term - $g((\partial\zeta)/(\partial x))$

$$-\frac{1}{4}g\,z^{(1,2)}(j,k)\,dt^2 + \frac{1}{8}g\,(dx(j)-dx(j+1))z^{(2,2)}(j,k)\,dt^2 - \frac{1}{24}g\,(dx(j)^2 - dx(j+1)\,dx(j) + dx(j+1)^2)z^{(3,2)}(j,k)\,dt^2 -$$

$$\frac{1}{2}g\,z^{(1,1)}(j,k)\,dt + \frac{1}{4}g\,(dx(j)-dx(j+1))z^{(2,1)}(j,k)\,dt - \frac{1}{12}g\,(dx(j)^2 - dx(j+1)\,dx(j) + dx(j+1)^2)z^{(3,1)}(j,k)\,dt +$$

$$\frac{1}{2}g\,(dx(j)-dx(j+1))z^{(2,0)}(j,k) - \frac{1}{6}g\,(dx(j)^2 - dx(j+1)\,dx(j) + dx(j+1)^2)z^{(3,0)}(j,k)$$

Viscous Term- $(\varepsilon/H)((\partial^2 q)/(\partial x^2))$

$$\frac{1}{4}\text{eddy}\,u^{(2,2)}(j,k)\,dt^2 + \frac{1}{12}\text{eddy}\,(dx(j+1)-dx(j))u^{(3,2)}(j,k)\,dt^2 +$$

$$\frac{1}{48}\text{eddy}\,(dx(j)^2 - dx(j+1)\,dx(j) + dx(j+1)^2)u^{(4,2)}(j,k)\,dt^2 + \frac{1}{2}\text{eddy}\,u^{(2,1)}(j,k)\,dt +$$

$$\frac{1}{6}\text{eddy}\,(dx(j+1)-dx(j))u^{(3,1)}(j,k)\,dt + \frac{1}{24}\text{eddy}\,(dx(j)^2 - dx(j+1)\,dx(j) + dx(j+1)^2)u^{(4,1)}(j,k)\,dt +$$

$$\frac{1}{3}\text{eddy}\,(dx(j+1)-dx(j))u^{(3,0)}(j,k) + \frac{1}{12}\text{eddy}\,(dx(j)^2 - dx(j+1)\,dx(j) + dx(j+1)^2)u^{(4,0)}(j,k)$$

Truncation Errors for the Conservative Momentum Equation

Accumulation Term - $\partial q / \partial t$

$$-\frac{1}{6} q^{(0,3)}(j,k)\,dt^2 + \frac{1}{18}\,(dx(j) - dx(j+1))\,q^{(1,3)}(j,k)\,dt^2 - \frac{1}{36}\,(dx(j)^2 - dx(j+1)\,dx(j) + dx(j+1)^2)\,q^{(2,3)}(j,k)\,dt^2 -$$

$$\frac{1}{2} q^{(0,2)}(j,k)\,dt + \frac{1}{6}\,(dx(j) - dx(j+1))\,q^{(1,2)}(j,k)\,dt - \frac{1}{12}\,(dx(j)^2 - dx(j+1)\,dx(j) + dx(j+1)^2)\,q^{(2,2)}(j,k)\,dt +$$

$$\frac{1}{3}\,(dx(j) - dx(j+1))\,q^{(1,1)}(j,k) - \frac{1}{6}\,(dx(j)^2 - dx(j+1)\,dx(j) + dx(j+1)^2)\,q^{(2,1)}(j,k)$$

Advective Term - $(\partial(qu)/\partial x)$

$$(dx(j) - dx(j+1))\,q^{(1,0)}(j,k)\,u^{(1,0)}(j,k) - \frac{1}{2}\,(dx(j)^2 - dx(j+1)\,dx(j) + dx(j+1)^2)\,q^{(2,0)}(j,k)\,u^{(1,0)}(j,k) -$$

$$\frac{1}{2}\,(dx(j)^2 - dx(j+1)\,dx(j) + dx(j+1)^2)\,q^{(1,0)}(j,k)\,u^{(2,0)}(j,k) +$$

$$\frac{1}{2}\,(dx(j) - dx(j+1))\,(u(j,k)\,q^{(2,0)}(j,k) + q(j,k)\,u^{(2,0)}(j,k)) - \frac{1}{6}\,(dx(j)^2 - dx(j+1)\,dx(j) + dx(j+1)^2)\,u(j,k)\,q^{(3,0)}(j,k) -$$

$$\frac{1}{6}\,(dx(j)^2 - dx(j+1)\,dx(j) + dx(j+1)^2)\,q(j,k)\,u^{(3,0)}(j,k)$$

Bottom Friction Term - τq

$$-\frac{1}{2}\,\text{tau}\,q^{(0,1)}(j,k)\,dt - \frac{1}{4}\,\text{tau}\,q^{(0,2)}(j,k)\,dt^2 + \frac{1}{3}\,\text{tau}\,(dx(j) - dx(j+1))\,q^{(1,0)}(j,k) + \frac{1}{6}\,\text{tau}\,(dx(j) - dx(j+1))\,q^{(1,1)}(j,k)\,dt +$$

$$\frac{1}{12}\,\text{tau}\,(dx(j) - dx(j+1))\,q^{(1,2)}(j,k)\,dt^2 + \frac{1}{36}\,\text{tau}\,(dx(j) - dx(j+1))\,q^{(1,3)}(j,k)\,dt^3 -$$

$$\frac{1}{6}\,\text{tau}\,(dx(j)^2 - dx(j+1)\,dx(j) + dx(j+1)^2)\,q^{(2,0)}(j,k) - \frac{1}{12}\,\text{tau}\,(dx(j)^2 - dx(j+1)\,dx(j) + dx(j+1)^2)\,q^{(2,1)}(j,k)\,dt -$$

$$\frac{1}{24}\,\text{tau}\,(dx(j)^2 - dx(j+1)\,dx(j) + dx(j+1)^2)\,q^{(2,2)}(j,k)\,dt^2$$

Viscous Term - $\varepsilon((\partial^2 q)/(\partial x^2))$

$$\frac{1}{4}\,\text{eddy}\,q^{(2,2)}(j,k)\,dt^2 + \frac{1}{12}\,\text{eddy}\,(dx(j+1) - dx(j))\,q^{(3,2)}(j,k)\,dt^2 +$$

$$\frac{1}{48}\,\text{eddy}\,(dx(j)^2 - dx(j+1)\,dx(j) + dx(j+1)^2)\,q^{(4,2)}(j,k)\,dt^2 + \frac{1}{2}\,\text{eddy}\,q^{(2,1)}(j,k)\,dt +$$

$$\frac{1}{6}\,\text{eddy}\,(dx(j+1) - dx(j))\,q^{(3,1)}(j,k)\,dt + \frac{1}{24}\,\text{eddy}\,(dx(j)^2 - dx(j+1)\,dx(j) + dx(j+1)^2)\,q^{(4,1)}(j,k)\,dt +$$

$$\frac{1}{3}\,\text{eddy}\,(dx(j+1) - dx(j))\,q^{(3,0)}(j,k) + \frac{1}{12}\,\text{eddy}\,(dx(j)^2 - dx(j+1)\,dx(j) + dx(j+1)^2)\,q^{(4,0)}(j,k)$$

Finite Amplitude Term - Part 1 - $gh((\partial\zeta)/(\partial x))$

$$-\frac{1}{4}\,g\,h(j,k)\,z^{(1,2)}(j,k)\,dt^2 + \frac{1}{8}\,g\,(dx(j)-dx(j+1))\,h^{(1,0)}(j,k)\,z^{(1,2)}(j,k)\,dt^2 -$$

$$\frac{1}{16}\,g\,(dx(j)^2 - dx(j+1)\,dx(j) + dx(j+1)^2)\,z^{(1,2)}(j,k)\,h^{(2,0)}(j,k)\,dt^2 + \frac{1}{8}\,g\,(dx(j)-dx(j+1))\,h(j,k)\,z^{(2,2)}(j,k)\,dt^2 -$$

$$\frac{1}{16}\,g\,(dx(j)^2 - dx(j+1)\,dx(j) + dx(j+1)^2)\,h^{(1,0)}(j,k)\,z^{(2,2)}(j,k)\,dt^2 -$$

$$\frac{1}{24}\,g\,(dx(j)^2 - dx(j+1)\,dx(j) + dx(j+1)^2)\,h(j,k)\,z^{(3,2)}(j,k)\,dt^2 - \frac{1}{2}\,g\,h(j,k)\,z^{(1,1)}(j,k)\,dt +$$

$$\frac{1}{4}\,g\,(dx(j)-dx(j+1))\,h^{(1,0)}(j,k)\,z^{(1,1)}(j,k)\,dt - \frac{1}{8}\,g\,(dx(j)^2 - dx(j+1)\,dx(j) + dx(j+1)^2)\,z^{(1,1)}(j,k)\,h^{(2,0)}(j,k)\,dt +$$

$$\frac{1}{4}\,g\,(dx(j)-dx(j+1))\,h(j,k)\,z^{(2,1)}(j,k)\,dt - \frac{1}{8}\,g\,(dx(j)^2 - dx(j+1)\,dx(j) + dx(j+1)^2)\,h^{(1,0)}(j,k)\,z^{(2,1)}(j,k)\,dt -$$

$$\frac{1}{12}\,g\,(dx(j)^2 - dx(j+1)\,dx(j) + dx(j+1)^2)\,h(j,k)\,z^{(3,1)}(j,k)\,dt + \frac{1}{2}\,g\,(dx(j)-dx(j+1))\,h^{(1,0)}(j,k)\,z^{(1,0)}(j,k) -$$

$$\frac{1}{4}\,g\,(dx(j)^2 - dx(j+1)\,dx(j) + dx(j+1)^2)\,z^{(1,0)}(j,k)\,h^{(2,0)}(j,k) + \frac{1}{2}\,g\,(dx(j)-dx(j+1))\,h(j,k)\,z^{(2,0)}(j,k) -$$

$$\frac{1}{4}\,g\,(dx(j)^2 - dx(j+1)\,dx(j) + dx(j+1)^2)\,h^{(1,0)}(j,k)\,z^{(2,0)}(j,k) -$$

$$\frac{1}{6}\,g\,(dx(j)^2 - dx(j+1)\,dx(j) + dx(j+1)^2)\,h(j,k)\,z^{(3,0)}(j,k)$$

Finite Amplitude Term - Part 2 - $(g/2)((\partial(\zeta^2))/(\partial x))$

$$-\frac{1}{8}\,g\,zsq^{(1,2)}(j,k)\,dt^2 + \frac{1}{16}\,g\,(dx(j)-dx(j+1))\,zsq^{(2,2)}(j,k)\,dt^2 -$$

$$\frac{1}{48}\,g\,(dx(j)^2 - dx(j+1)\,dx(j) + dx(j+1)^2)\,zsq^{(3,2)}(j,k)\,dt^2 - \frac{1}{4}\,g\,zsq^{(1,1)}(j,k)\,dt + \frac{1}{8}\,g\,(dx(j)-dx(j+1))\,zsq^{(2,1)}(j,k)\,dt -$$

$$\frac{1}{24}\,g\,(dx(j)^2 - dx(j+1)\,dx(j) + dx(j+1)^2)\,zsq^{(3,1)}(j,k)\,dt + \frac{1}{4}\,g\,(dx(j)-dx(j+1))\,zsq^{(2,0)}(j,k) -$$

$$\frac{1}{12}\,g\,(dx(j)^2 - dx(j+1)\,dx(j) + dx(j+1)^2)\,zsq^{(3,0)}(j,k)$$

From these truncation errors, we can prove that the GWC equation is first-order accurate in time if the advective terms are in non-conservative form, while it is second-order accurate in time if the advective terms are in conservative form. In space, the GWC equation is first-order accurate for variable spacing; while, it is second-order accurate for constant spacing. For the NCM and CM equations, we found that they are first-order accurate in time and space if we use variable spacing, while it is second-order accurate in space if we use constant spacing. Also, both momentum equations become second-order accurate in time if the equations are linearized.

Appendix 4. Derivation of the Analytical Solution for the BPG Test Case

For the analytical solution to this simplified baroclinic problem, we followed the same procedures and assumptions as Luettich and Westerink did in their paper on baroclinic additions [63]. Briefly, the problem uses a idealized basin that is 48 km long with 51 horizontal nodes ($\Delta x = 960\ \text{m}$) and 21 vertical nodes ($\Delta \sigma = 0.05$). A constant bathymetry of 10 m depth ("flat bottom") is used throughout the domain. We utilize land boundary conditions on both ends of the idealized basin so there is a no normal flow.

The first step is to find the horizontal velocity using the x-direction momentum equation. Note that there is no flow in the y-direction, so the y-direction momentum equation is omitted. Equation (2.8) from Chapter 2 is the starting point of the derivation.

$$\cancel{\frac{\partial u}{\partial t}} + u\cancel{\frac{\partial u}{\partial x}} + v\cancel{\frac{\partial u}{\partial y}} + w\cancel{\frac{\partial u}{\partial z}} - \cancel{fv} = -g\frac{\partial[\zeta + \cancel{P_a/(g\rho_0)} - \cancel{\alpha\eta}]}{\partial x} + \frac{\partial}{\partial z}\left(\frac{\tau_{zx}}{\rho_0}\right) - b_x + \cancel{m_x} \qquad \textbf{(A4.1)}$$

where we assume steady-state, linear, no Coriolis forcing and no lateral stress. Therefore, we obtain the following simplified momentum balance:

$$-g\frac{\partial\zeta}{\partial x} + \frac{\partial}{\partial z}\left(\frac{\tau_{zx}}{\rho_0}\right) - b_x = 0 \qquad \textbf{(A4.2)}$$

where the b_x is determined from the following

$$b_x = g\left(\frac{\partial}{\partial x}\left(\int_z^0 \left(\frac{\rho' - \rho_0}{\rho_0}\right) dz\right)\right) \qquad \text{(A4.3)}$$

Note that in Equation (A4.3), we assume ζ varies little from the datum so that the upper

limit of integration is 0, not ζ. In Equation (A4.3), ρ_0 is constant and ρ' is a function of

x only for this problem so the equation becomes

$$b_x = g\left(\frac{\partial \rho}{\partial x}\int_z^0 dz\right) \qquad \text{(A4.4)}$$

where $\rho = \frac{\rho'}{\rho_0}$. Now if we evaluate the integral we obtain:

$$b_x = -gz\frac{\partial \rho}{\partial x} \qquad \text{(A4.5)}$$

Substituting b_x into Equation (A4.2), we obtain

$$-g\frac{\partial \zeta}{\partial x} + \frac{\partial}{\partial z}\left(\frac{\tau_{zx}}{\rho_0}\right) + gz\frac{\partial \rho}{\partial x} = 0 \qquad \text{(A4.6)}$$

Rearranging the equation, we find

$$\frac{\partial}{\partial z}\left(\frac{\tau_{zx}}{\rho_0}\right) = -gz\frac{\partial \rho}{\partial x} + g\frac{\partial \zeta}{\partial x} \qquad \text{(A4.7)}$$

Now substituting in $\frac{\tau_{zx}}{\rho_0} = E_z\frac{\partial u}{\partial z}$ and assuming the vertical eddy viscosity parameter E_z

remains constant, Equation (A4.7) becomes

$$E_z\frac{\partial^2 u}{\partial z^2} = -gz\frac{\partial \rho}{\partial x} + g\frac{\partial \zeta}{\partial x} \qquad \text{(A4.8)}$$

If we integrate both sides of Equation (A4.8) with respect to z, we obtain:

$$E_z \frac{\partial u}{\partial z} = -g\left(\frac{\partial \rho}{\partial x}\left(\frac{z^2}{2}\right)\right) + g\frac{\partial \zeta}{\partial x}z + C_1 \tag{A4.9}$$

where C_1 is the first constant of integration, which can be determined from the top boundary condition: $E_z \frac{\partial u}{\partial z}\Big|_{z=0} = 0$ (no surface stress).

$$E_z \frac{\partial u}{\partial z}\Big|_{z=0} = -g\left(\frac{\partial \rho}{\partial x}\left(\frac{(0)^2}{2}\right)\right) + g\frac{\partial \zeta}{\partial x}(0) + C_1 \tag{A4.10}$$

Evaluating the equation above we find the first constant of integration is

$$0 = 0 + C_1 \Rightarrow C_1 = 0 \tag{A4.11}$$

Therefore, we obtain

$$E_z \frac{\partial u}{\partial z} = -g\left(\frac{\partial \rho}{\partial x}\left(\frac{z^2}{2}\right)\right) + g\frac{\partial \zeta}{\partial x}z \tag{A4.12}$$

Now integrating Equation (A4.12) gives us the following:

$$u(z) = -\frac{g}{E_z}\left(\frac{\partial \rho}{\partial x}\left(\frac{z^3}{6}\right)\right) + \frac{g}{E_z}\frac{\partial \zeta}{\partial x}\left(\frac{z^2}{2}\right) + C_2 \tag{A4.13}$$

where C_2 is the second constant of integration, which can be determined from the bottom boundary condition: $E_z \frac{\partial u}{\partial z}\Big|_{z=-h} = ku(-h)$, i.e. linear slip at the bottom. Using Equations (A4.12) and (A4.13), we find

$$E_z \frac{\partial u}{\partial z}\Big|_{z=-h} = -g\left(\frac{\partial \rho}{\partial x}\left(\frac{(-h)^2}{2}\right)\right) + g\frac{\partial \zeta}{\partial x}(-h) \tag{A4.14}$$

$$k \times u(-h) = -\frac{g}{E_z}\left(\frac{\partial \rho}{\partial x}\left(\frac{(-h)^3}{6}\right)\right)k + \frac{g}{E_z}\frac{\partial \zeta}{\partial x}\left(\frac{(-h)^2}{2}\right)k + kC_2 \tag{A4.15}$$

Equating Equations (A4.14) and (A4.15), we get:

$$-g\left(\frac{\partial \rho}{\partial x}\left(\frac{h^2}{2}\right)\right)-g\frac{\partial \zeta}{\partial x}(h) = \frac{g}{E_z}\left(\frac{\partial \rho}{\partial x}\left(\frac{-kh^3}{6}\right)\right) + \frac{g}{E_z}\frac{\partial \zeta}{\partial x}\left(\frac{kh^2}{2}\right) + kC_2 \tag{A4.16}$$

Solving Equation (A4.16) for the second constant of integration gives

$$C_2 = -g\left(\frac{\partial \rho}{\partial x}\left(\frac{h^2}{2k}\right)\right)-g\frac{\partial \zeta}{\partial x}\left(\frac{h}{k}\right) - \frac{g}{E_z}\left(\frac{\partial \rho}{\partial x}\left(\frac{-h^3}{6}\right)\right) - \frac{g}{E_z}\frac{\partial \zeta}{\partial x}\left(\frac{h^2}{2}\right) \tag{A4.17}$$

Thus, substituting Equation (A4.17) into Equation (A4.13) for C_2 we obtain

$$u(z) = -\frac{g}{E_z}\left(\frac{\partial \rho}{\partial x}\left(\frac{z^3}{6}\right)\right) + \frac{g}{E_z}\frac{\partial \zeta}{\partial x}\left(\frac{z^2}{2}\right)-g\left(\frac{\partial \rho}{\partial x}\left(\frac{h^2}{2k}\right)\right)-g\frac{\partial \zeta}{\partial x}\left(\frac{h}{k}\right) -$$

$$\frac{g}{E_z}\left(\frac{\partial \rho}{\partial x}\left(\frac{-h^3}{6}\right)\right) - \frac{g}{E_z}\frac{\partial \zeta}{\partial x}\left(\frac{h^2}{2}\right) \tag{A4.18}$$

By rearranging Equation (A4.18), we find

$$u(z) = -\frac{g}{6E_z}\left(\frac{\partial \rho}{\partial x}(z^3 + h^3)\right) + \frac{g}{2E_z}\frac{\partial \zeta}{\partial x}(z^2 - h^2)-\frac{gh}{k}\left(\frac{\partial \rho}{\partial x}\left(\frac{h}{2}\right)-g\frac{\partial \zeta}{\partial x}\right) \tag{A4.19}$$

For a closed basin at steady-state, the depth-averaged velocity (U) is zero, thus we can integrate Equation (A4.19) from 0 to $-h$ to obtain an expression for $\frac{\partial \zeta}{\partial x}$.

$$\frac{\partial \zeta}{\partial x} = -\frac{\partial \rho}{\partial x}\left(\frac{3h}{8}\right)\left(\frac{4E_z + kh}{3E_z + kh}\right) \tag{A4.20}$$

$$\frac{\partial \zeta}{\partial x} = -\frac{\partial \rho}{\partial x}\left(\frac{h}{2}\right)\left(\frac{12E_z + 3kh}{12E_z + 4kh}\right) \qquad \textbf{(A4.21)}$$

$$\frac{\partial \zeta}{\partial x} = \underbrace{-\frac{\partial \rho}{\partial x}\left(\frac{h}{2}\right)\left(\frac{1+\dfrac{kh}{4E_z}}{1+\dfrac{kh}{3E_z}}\right)}_{\beta} \qquad \textbf{(A4.22)}$$

which the same as found in Luettich and Westerink's baroclinic paper [63]. For constant parameters, depth and density gradient, this gives $\zeta(x) = \beta x + \alpha$. The mass balance for the closed basin requires $\zeta(L/2) = 0 \Rightarrow \alpha = \beta(L/2)$ so $\zeta(x) = \beta(x - (L/2))$. Now to determine the final form for $u(z)$, we substitute in the results from Equation (A4.22) into Equation (A4.19).

$$u(z) = -\frac{g}{6E_z}\left(\frac{\partial \rho}{\partial x}(z^3 + h^3)\right) + \frac{g}{2E_z}\frac{\partial \zeta}{\partial x}(z^2 - h^2) - \frac{gh}{k}\left(\left(\frac{\partial \rho}{\partial x}\right)\left(\frac{h}{2}\right) - g\left(\frac{\partial \zeta}{\partial x}\right)\right) \qquad \textbf{(A4.23)}$$

To verify this is indeed a solution, we need to ensure it satisfies the original differential equation and the top and bottom boundary conditions, along with the depth-averaged results.

First, we will look at the top boundary condition is $E_z\dfrac{\partial u}{\partial z}\Big|_{z=0} = 0$. The top boundary condition from the $u(z)$ equation, given in Equation (A4.23), is obtained by taking a derivative of this equation and then rearranging it to get $E_z\dfrac{\partial u}{\partial z}$:

$$\frac{\partial u}{\partial z} = -\frac{g}{6E_z}\left(\frac{\partial \rho}{\partial x}(3z^2)\right) + \frac{g}{2E_z}\frac{\partial \zeta}{\partial x}(2z) \qquad \textbf{(A4.24)}$$

$$E_z\frac{\partial u}{\partial z} = -\frac{g}{2}\left(\frac{\partial \rho}{\partial x}(z^2)\right) + g\frac{\partial \zeta}{\partial x}(z) \tag{A4.25}$$

Now if we evaluate Equation (A4.25) at the top boundary conditions, we find

$$E_z\frac{\partial u}{\partial z}\bigg|_{z=0} = 0 \tag{A4.26}$$

therefore the top boundary condition is met.

Next check the bottom boundary condition where $E_z\frac{\partial u}{\partial z}\bigg|_{z=-h} = ku(-h)$. If we evaluate Equation (A4.25) and Equation (A4.23) at the bottom boundary then we obtain:

$$-\frac{g}{2}\left(\frac{\partial \rho}{\partial x}((-h)^2)\right) + g\frac{\partial \zeta}{\partial x}(-h) = -\frac{gk}{6E_z}\left(\frac{\partial \rho}{\partial x}((-h)^3 + h^3)\right) + \frac{gk}{2E_z}\frac{\partial \zeta}{\partial x}((-h)^2 - h^2) -$$

$$g\left(\frac{\partial \rho}{\partial x}\left(\frac{h^2}{2}\right)\right) - g\left(\frac{\partial \zeta}{\partial x}\right)(h) \tag{A4.27}$$

Evaluating and rearranging Equation (A4.27), we find

$$-g\frac{\partial \rho}{\partial x}\left(\frac{h^2}{2}\right) - g\frac{\partial \zeta}{\partial x}(h) = -g\frac{\partial \rho}{\partial x}\left(\frac{h^2}{2}\right) - g\frac{\partial \zeta}{\partial x}(h) \tag{A4.28}$$

$$0 = 0 \tag{A4.29}$$

therefore the bottom boundary condition is met.

Next, we need to verify that the depth-averaged velocity is zero, i.e.

$$U = \int_{-h}^{0} u(z)dz = 0 \tag{A4.30}$$

Substituting in the $u(z)$ equation, given in Equation (A4.23), and evaluating the integral we obtain the following equations.

$$U = \int_{-h}^{0}\left(-\frac{g}{6E_z}\left(\frac{\partial\rho}{\partial x}(z^3 + h^3)\right) + \frac{g}{2E_z}\frac{\partial\zeta}{\partial x}(z^2 - h^2) - g\left(\frac{\partial\rho}{\partial x}\left(\frac{h^2}{2k}\right)\right) - g\left(\frac{\partial\zeta}{\partial x}\right)\left(\frac{h}{k}\right)\right)dz \quad \textbf{(A4.31)}$$

$$U = -\frac{g}{6E_z}\left(\frac{\partial\rho}{\partial x}\left(\frac{z^4}{4} + h^3z\right)\right) + \frac{g}{2E_z}\frac{\partial\zeta}{\partial x}\left(\frac{z^3}{3} - h^2z\right) - g\left(\frac{\partial\rho}{\partial x}\left(\frac{h^2 z}{2k}\right)\right) - g\left(\frac{\partial\zeta}{\partial x}\right)\left(\frac{hz}{k}\right)\Bigg|_{-h}^{0} \quad \textbf{(A4.32)}$$

After evaluating the integral, we obtain the following

$$U = \frac{g}{6E_z}\frac{\partial\rho}{\partial x}\left(\frac{h^4}{4}\right) - \frac{g}{6E_z}\frac{\partial\rho}{\partial x}(h^4) + \frac{g}{2E_z}\frac{\partial\zeta}{\partial x}\left(\frac{h^3}{3}\right) - \frac{g}{2E_z}\frac{\partial\zeta}{\partial x}(h^3)$$

$$-g\left(\frac{\partial\rho}{\partial x}\left(\frac{h^3}{2k}\right)\right) - g\left(\frac{\partial\zeta}{\partial x}\right)\left(\frac{h^2}{k}\right) \quad \textbf{(A4.33)}$$

Rearranging Equation (A4.33), we find

$$U = -\frac{g}{E_z}\frac{\partial\rho}{\partial x}\left(\frac{h^4}{8}\right) - \frac{g}{E_z}\frac{\partial\zeta}{\partial x}\left(\frac{h^3}{3}\right) - g\left(\frac{\partial\rho}{\partial x}\left(\frac{h^3}{2k}\right)\right) - g\left(\frac{\partial\zeta}{\partial x}\right)\left(\frac{h^2}{k}\right) \quad \textbf{(A4.34)}$$

Now, if we substitute in the value of $\frac{\partial\zeta}{\partial x}$, given in Equation (A4.20), we find that

$$U = -\frac{g}{E_z}\frac{\partial\rho}{\partial x}\left(\frac{h^4}{8}\right) - \frac{g}{E_z}\left(-\frac{\partial\rho}{\partial x}\left(\frac{3h}{8}\right)\left(\frac{4E_z + kh}{3E_z + kh}\right)\right)\left(\frac{h^3}{3}\right) - g\left(\frac{\partial\rho}{\partial x}\left(\frac{h^3}{2k}\right)\right) -$$

$$g\left(-\frac{\partial\rho}{\partial x}\left(\frac{3h}{8}\right)\left(\frac{4E_z + kh}{3E_z + kh}\right)\right)\left(\frac{h^2}{k}\right) \quad \textbf{(A4.35)}$$

Simplifying Equation (A4.35) shows the following result

$$U = -\frac{\partial \rho}{\partial x}\left(\frac{h^4}{8}\frac{g}{E_z}\right) - \frac{\partial \rho}{\partial x}\left(\frac{gh^3}{2k}\right) + \frac{\partial \rho}{\partial x}\left(\frac{7gh^4}{8(3E_z + kh)}\right) +$$

$$\frac{\partial \rho}{\partial x}\left(\frac{3E_z gh^3}{2k(3E_z + kh)}\right) + \frac{\partial \rho}{\partial x}\left(\frac{gh^5 k}{8E_z(3E_z + kh)}\right) \tag{A4.36}$$

Now, if we find the common denominator for Equation (A4.36), we have the following

$$U = -\frac{\partial \rho}{\partial x}\left(\frac{(3E_z + kh)kgh^4}{8kE_z(3E_z + kh)}\right) - \frac{\partial \rho}{\partial x}\left(\frac{4E_z(3E_z + kh)gh^3}{8kE_z(3E_z + kh)}\right) + \frac{\partial \rho}{\partial x}\left(\frac{7kgh^4 E_z}{8kE_z(3E_z + kh)}\right) +$$

$$\frac{\partial \rho}{\partial x}\left(\frac{4E_z(3E_z gh^3)}{8kE_z(3E_z + kh)}\right) + \frac{\partial \rho}{\partial x}\left(\frac{gh^5 k^2}{8kE_z(3E_z + kh)}\right) \tag{A4.37}$$

$$U = -\frac{\partial \rho}{\partial x}\left(\frac{3E_z kgh^4 + k^2 gh^5 + 12E_z^2 gh^3 + 4E_z kgh^4}{24kE_z^2 + 8E_z k^2 h}\right) -$$

$$\frac{\partial \rho}{\partial x}\left(\frac{-7E_z kgh^4 - 12E_z^2 gh^3 - k^2 gh^5}{24kE_z^2 + 8E_z k^2 h}\right) \tag{A4.38}$$

All terms cancel, i.e.,

$$U = -\frac{\partial \rho}{\partial x}\left(\frac{0}{24kE_z^2 + 8E_z k^2 h}\right) \tag{A4.39}$$

so $U = 0$ and therefore the depth-averaged condition is met.

Lastly, we need to determine if $u(z)$, given in Equation (A4.23), satisfies the original equation.

$$u(z) = -\frac{g}{6E_z}\left(\frac{\partial\rho}{\partial x}(z^3 + h^3)\right) + \frac{g}{2E_z}\frac{\partial\zeta}{\partial x}(z^2 - h^2) - g\left(\frac{\partial\rho}{\partial x}\left(\frac{h^2}{2k}\right)\right) - g\left(\frac{\partial\zeta}{\partial x}\right)\left(\frac{h}{k}\right)$$ (A4.40)

Starting from Equation (A4.25), we find

$$E_z\frac{\partial^2 u}{\partial z^2} = -g\left(\frac{\partial\rho}{\partial x}(z)\right) + g\frac{\partial\zeta}{\partial x}$$ (A4.41)

Rearranging Equation (A4.41), we obtain

$$E_z\frac{\partial^2 u}{\partial z^2} + g\left(\frac{\partial\rho}{\partial x}(z)\right) - g\frac{\partial\zeta}{\partial x} = 0$$ (A4.42)

where $E_z\frac{\partial^2 u}{\partial z^2} = \frac{\partial}{\partial z}\left(\frac{\tau_{zx}}{\rho_0}\right)$ and $b_x = -gz\frac{\partial\rho}{\partial x}$. If we substitute these expressions back in, we get the following equation, which is the same as the original equation (Equation (A4.2)).

$$-g\frac{\partial\zeta}{\partial x} + \frac{\partial}{\partial z}\left(\frac{\tau_{zx}}{\rho_0}\right) - b_x = 0$$ (A4.43)

Thus $u(z)$, as expressed in Equation (A4.23), must be a solution.

If we do a similar check with the solution presented by Luettich and Westerink in their baroclinic paper (shown in Equation (A4.44)), we find that the solution obtains the

$$u(z) = -\frac{g}{6E_z}\left(\frac{\partial\rho}{\partial x}\left(z^3 + \frac{h^3}{4}\right)\right) + \frac{g}{2E_z}\frac{\partial\zeta}{\partial x}\left(z^2 - \frac{h^2}{3}\right)$$ (A4.44)

same value for $\frac{\partial\zeta}{\partial x}$ (shown in Equation (A4.20)). Now, we need to determine if it satisfies the top boundary condition of $E_z\frac{\partial u}{\partial z}\bigg|_{z=0} = 0$.

$$E_z \frac{\partial u}{\partial z} = -\frac{g}{2}\left(\frac{\partial \rho}{\partial x}(z^2)\right) + g\frac{\partial \zeta}{\partial x}(z) \tag{A4.45}$$

$$E_z \frac{\partial u}{\partial z}\bigg|_{z=0} = 0 \tag{A4.46}$$

We also checked the bottom boundary condition of $E_z \frac{\partial u}{\partial z}\big|_{z=-h} = ku(-h)$. Using Equation (A4.44) at the bottom boundary, we find:

$$-\frac{g}{2}\left(\frac{\partial \rho}{\partial x}((-h)^2)\right) + g\frac{\partial \zeta}{\partial x}(-h) = -\frac{gk}{6E_z}\left(\frac{\partial \rho}{\partial x}\left((-h)^3 + \frac{h^3}{4}\right)\right) + \frac{gk}{2E_z}\frac{\partial \zeta}{\partial x}\left((-h)^2 - \frac{h^2}{3}\right) \tag{A4.47}$$

Evaluating and rearranging Equation (A4.47) gives

$$-\frac{g}{2}\left(\frac{\partial \rho}{\partial x}((-h)^2)\right) + g\frac{\partial \zeta}{\partial x}(-h) = -\frac{gk}{6E_z}\left(\frac{\partial \rho}{\partial x}\left(-\frac{3h^3}{4}\right)\right) + \frac{gk}{2E_z}\frac{\partial \zeta}{\partial x}\left(\frac{2h^2}{3}\right) \tag{A4.48}$$

$$-g\frac{\partial \rho}{\partial x}\left(\frac{h^2}{2}\right) - g\frac{\partial \zeta}{\partial x}(h) = \frac{g}{2E_z}\frac{\partial \rho}{\partial x}\left(\frac{h^3 k}{4}\right) + \frac{g}{E_z}\frac{\partial \zeta}{\partial x}\left(\frac{h^2 k}{3}\right) \tag{A4.49}$$

Substituting in the value of $\frac{\partial \zeta}{\partial x}$, given in Equation (A4.20), we find that

$$-g\frac{\partial \rho}{\partial x}\left(\frac{h^2}{2}\right) + g\left(\frac{\partial \rho}{\partial x}\left(\frac{3h^2}{8}\right)\left(\frac{4E_z + kh}{3E_z + kh}\right)\right) =$$

$$\frac{g}{2E_z}\left(\frac{\partial \rho}{\partial x}\left(\frac{h^3 k}{4}\right)\right) - \frac{g}{E_z}\left(\frac{\partial \rho}{\partial x}\left(\frac{3h}{8}\right)\left(\frac{4E_z + kh}{3E_z + kh}\right)\left(\frac{h^2 k}{3}\right)\right) \tag{A4.50}$$

$$-g\frac{\partial \rho}{\partial x}\left(\frac{h^2}{2}\right) + g\left(\frac{\partial \rho}{\partial x}\left(\frac{12E_z h^2 + 3kh^3}{24E_z + 8kh}\right)\right) =$$

$$g\left(\frac{\partial \rho}{\partial x}\left(\frac{h^3 k}{8E_z}\right)\right) - g\left(\frac{\partial \rho}{\partial x}\left(\frac{12E_z h^3 k + 3k^2 h^4}{E_z(72E_z + 24kh)}\right)\right) \qquad \textbf{(A4.51)}$$

Now, if we find the common denominator for Equation (A4.51), we have the following

$$-g\frac{\partial \rho}{\partial x}\left(\frac{4E_z(72E_z + 24kh)h^2}{8E_z(72E_z + 24kh)}\right) + g\left(\frac{\partial \rho}{\partial x}\left(\frac{24E_z(12E_z h^2 + 3kh^3)}{8E_z(72E_z + 24kh)}\right)\right) =$$

$$g\left(\frac{\partial \rho}{\partial x}\left(\frac{(72E_z + 24kh)h^3 k}{8E_z(72E_z + 24kh)}\right)\right) - g\left(\frac{\partial \rho}{\partial x}\left(\frac{8(12E_z h^3 k + 3k^2 h^4)}{8E_z(72E_z + 24kh)}\right)\right) \qquad \textbf{(A4.52)}$$

$$-g\frac{\partial \rho}{\partial x}\left(\frac{288E_z^2 h^2 + 96E_z kh^3 - 288E_z^2 h^2 - 72E_z kh^3}{8E_z(72E_z + 24kh)}\right) =$$

$$g\frac{\partial \rho}{\partial x}\left(\frac{72E_z h^3 k + 24k^2 h^4 - 96E_z h^3 k - 24k^2 h^4}{8E_z(72E_z + 24kh)}\right) \qquad \textbf{(A4.53)}$$

All terms cancel, i.e.,

$$0 = 0 \qquad \textbf{(A4.54)}$$

Thus the bottom boundary condition is met.

Next, we need to verify that the depth-averaged velocity is zero, i.e.

$$U = \int_{-h}^{0} u(z)dz = 0$$

Substituting in the $u(z)$ equation, given in Equation (A4.44), and evaluating the integral we obtain the following equation.

$$U = -\frac{g}{6E_z}\left(\frac{\partial \rho}{\partial x}\left(\frac{z^4}{4} + \frac{h^3}{4}z\right)\right) + \frac{g}{2E_z}\frac{\partial \zeta}{\partial x}\left(\frac{z^3}{3} - \frac{h^2}{3}z\right)\Bigg|_{-h}^{0} \tag{A4.55}$$

After evaluating the integral, we obtain the following

$$U = -\frac{g}{6E_z}\left(\frac{\partial \rho}{\partial x}\left(\frac{h^4}{4} - \frac{h^4}{4}\right)\right) + \frac{g}{2E_z}\frac{\partial \zeta}{\partial x}\left(\frac{-h^3}{3} + \frac{h^3}{3}\right) \tag{A4.56}$$

All terms cancel, so

$$U = 0 \tag{A4.57}$$

therefore the depth-averaged condition is met.

Lastly, we need to determine if $u(z)$ satisfies the original equation.

$$u(z) = -\frac{g}{6E_z}\left(\frac{\partial \rho}{\partial x}\left(z^3 + \frac{h^3}{4}\right)\right) + \frac{g}{2E_z}\frac{\partial \zeta}{\partial x}\left(z^2 - \frac{h^2}{3}\right) \tag{A4.58}$$

Thus we take two derivatives of Equation (A4.58) with respect to z

$$E_z\frac{\partial^2 u}{\partial z^2} + g\left(\frac{\partial \rho}{\partial x}(z)\right) - g\frac{\partial \zeta}{\partial x} = 0 \tag{A4.59}$$

where $E_z\dfrac{\partial^2 u}{\partial z^2} = \dfrac{\partial}{\partial z}\left(\dfrac{\tau_{zx}}{\rho_0}\right)$ and $b_x = -gz\dfrac{\partial \rho}{\partial x}$. If we substitute these expressions back in Equation (A4.59), we get Equation (A4.43), which is the same as the original equation. Thus $u(z)$, as expressed in Equation (A4.44), must be a solution.

Therefore, both forms of $u(z)$ must be solutions (Equations (A4.23) and (A4.44)) to this problem and must be equal to one another. If we equate the two equations, we end up with the following:

$$-\frac{g}{6E_z}\left(\frac{\partial\rho}{\partial x}\left(z^3+\frac{h^3}{4}\right)\right)+\frac{g}{2E_z}\frac{\partial\zeta}{\partial x}\left(z^2-\frac{h^2}{3}\right)=$$

$$-\frac{g}{6E_z}\left(\frac{\partial\rho}{\partial x}(z^3+h^3)\right)+\frac{g}{2E_z}\frac{\partial\zeta}{\partial x}(z^2-h^2)-\frac{gh}{k}\left(\left(\frac{\partial\rho}{\partial x}\right)\left(\frac{h}{2}\right)-g\left(\frac{\partial\zeta}{\partial x}\right)\right) \tag{A4.60}$$

Evaluating and rearranging Equation (A4.60), we obtain the following:

$$-\frac{g}{6E_z}\left(\frac{\partial\rho}{\partial x}\right)z^3-\frac{g}{6E_z}\left(\frac{\partial\rho}{\partial x}\right)\frac{h^3}{4}+\frac{g}{2E_z}\left(\frac{\partial\zeta}{\partial x}\right)z^2-\frac{g}{2E_z}\left(\frac{\partial\zeta}{\partial x}\right)\frac{h^2}{3}=$$

$$-\frac{g}{6E_z}\left(\frac{\partial\rho}{\partial x}\right)z^3-\frac{g}{6E_z}\left(\frac{\partial\rho}{\partial x}\right)h^3+\frac{g}{2E_z}\left(\frac{\partial\zeta}{\partial x}\right)z^2-\frac{g}{2E_z}\left(\frac{\partial\zeta}{\partial x}\right)h^2-g\left(\frac{\partial\rho}{\partial x}\right)\frac{h^2}{2k}-g\left(\frac{\partial\zeta}{\partial x}\right)\frac{h}{k} \tag{A4.61}$$

$$\frac{g}{6E_z}\left(\frac{\partial\rho}{\partial x}\right)\frac{3h^3}{4}+\frac{g}{2E_z}\left(\frac{\partial\zeta}{\partial x}\right)\frac{2h^2}{3}=-g\left(\frac{\partial\rho}{\partial x}\right)\frac{h^2}{2k}-g\left(\frac{\partial\zeta}{\partial x}\right)\frac{h}{k} \tag{A4.62}$$

$$\frac{g}{2E_z}\left(\frac{\partial\rho}{\partial x}\right)\frac{h^3}{4}+\frac{g}{E_z}\left(\frac{\partial\zeta}{\partial x}\right)\frac{h^2}{3}=-g\left(\frac{\partial\rho}{\partial x}\right)\frac{h^2}{2k}-g\left(\frac{\partial\zeta}{\partial x}\right)\frac{h}{k} \tag{A4.63}$$

Now substituting in the value of $\frac{\partial\zeta}{\partial x}$, given in Equation (A4.20), we find the following:

$$\frac{g}{2E_z}\left(\frac{\partial\rho}{\partial x}\right)\frac{h^3}{4}-\frac{g}{E_z}\left(\frac{\partial\rho}{\partial x}\left(\frac{3h}{8}\right)\left(\frac{4E_z+kh}{3E_z+kh}\right)\right)\frac{h^2}{3}=-g\left(\frac{\partial\rho}{\partial x}\right)\frac{h^2}{2k}+g\left(\frac{\partial\rho}{\partial x}\left(\frac{3h}{8}\right)\left(\frac{4E_z+kh}{3E_z+kh}\right)\right)\frac{h}{k} \tag{A4.64}$$

$$g\frac{\partial\rho}{\partial x}\left(\frac{h^3}{8E_z}\right)-g\frac{\partial\rho}{\partial x}\left(\frac{12E_zh^3+3kh^4}{E_z(72E_z+24kh)}\right)=-g\frac{\partial\rho}{\partial x}\left(\frac{h^2}{2k}\right)+g\frac{\partial\rho}{\partial x}\left(\frac{12E_zh^3+3kh^4}{24E_zk+8k^2h}\right) \tag{A4.65}$$

Now, if we find the common denominator for Equation (A4.65), we obtain the following

227

$$g\frac{\partial\rho}{\partial x}\left(\frac{h^3(72E_z+24kh)(2k)}{8E_z(72E_z+24kh)(2k)}\right)-g\frac{\partial\rho}{\partial x}\left(\frac{16k(12E_zh^2+3kh^3)}{8E_z(72E_z+24kh)(2k)}\right)=$$

$$-g\frac{\partial\rho}{\partial x}\left(\frac{8E_zh^2(72E_z+24kh)}{8E_z(72E_z+24kh)(2k)}\right)+g\frac{\partial\rho}{\partial x}\left(\frac{48E_z(12E_zh^3+3kh^4)}{8E_z(72E_z+24kh)(2k)}\right) \qquad \textbf{(A4.66)}$$

$$g\frac{\partial\rho}{\partial x}\left(\frac{144E_zh^3k+48k^2h^4-192E_zh^3k-48k^2h^4}{8E_z(72E_z+24kh)(2k)}\right)=$$

$$g\frac{\partial\rho}{\partial x}\left(\frac{-576E_z^2h^2-192E_zh^3k+576E_z^2h^2+144E_zh^3k}{8E_z(72E_z+24kh)(2k)}\right) \qquad \textbf{(A4.67)}$$

All terms cancel, i.e.,

$$0 = 0 \qquad \textbf{(A4.68)}$$

Therefore both forms provide the same results.